Cover image ©2025 Sen Zhang

Constructing Co Cluster Sites for Selective CO₂ Hydrogenation via Phase Segregation from Co-Doped TiO₂ Nanocrystals

scilight

Contents

Article

Size-Controlled Synthesis of Rhodium Nanocatalysts and Applications in Low-Temperature Hydroformylation

Andrew Lamkins [1,2], Charles J. Ward [1,2], Jeffrey T. Miller [3], Ziad Alsudairy [4], Xinle Li [4], Joseph Thuma [1,2], Ruoyu Cui [1,2], Xun Wu [1,2], Levi M. Stanley [1], and Wenyu Huang [1,2,]*

[1] Department of Chemistry, Iowa State University, Ames, IA 50010, USA
[2] Ames Laboratory, U.S. Department of Energy, Ames, IA 50010, USA
[3] Davidson School of Chemical Engineering, Purdue University, West Lafayette, IN 47907, USA
[4] Department of Chemistry, Clark Atlanta University, Atlanta, GA 30314, USA
* Correspondence: whuang@iastate.edu

Abstract: Controlling the size and distribution of metal nanoparticles is one of the simplest methods of tuning the catalytic properties of a material. For a nanocrystal particle, the ratio of edge-to-terrace sites can be critical in determining its catalytic activity and selectivity to desired products. To study these effects, we have developed a simple impregnation method of controlling the dispersion of rhodium atoms at the same metal loading in the range of nanoparticles less than 10 nm. Rh precursor salts are loaded onto inert SBA-15, and increasing the ratio of chloride to acetylacetonate salts improves the dispersion of rhodium atoms to form small Rh nanoparticles. Extensive characterization of the size-controlled catalysts, including XAS and in-situ CO-DRIFTS studies, has been performed to characterize the structure of Rh nanoparticles. Applying these catalysts to the hydroformylation of styrene, we observed that turnover frequency increases with decreasing particle size from 6.4 to 1.6 nm. When applied to hydroformylation reactions, we achieved a high branched product selectivity and successfully demonstrated a route to synthesizing the pain relief drug ibuprofen. This simple method can also synthesize Pt and Pd nanoparticles between 2–10 nm.
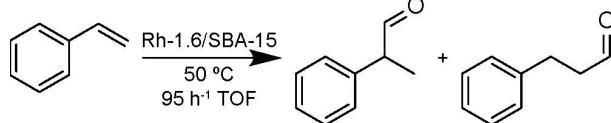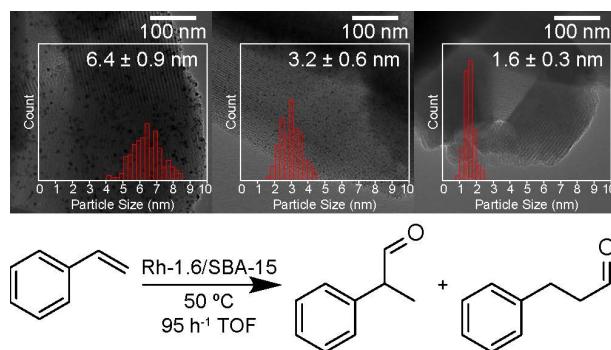
Keywords: heterogeneous catalysis; hydroformylation; EXAFS; infrared spectroscopy; nanoparticle

1. Introduction

The behavior of catalytic systems when varying nanoparticle (NP) size is one of the most studied areas in heterogeneous catalysis [1–10]. An effective method of size control is using capping agents during the synthesis of NPs [7,11], but the capping agents could compete with reactants for coordination to the NPs [12]. Using functional groups to anchor metals to support has the same issue of competitive adsorption [13]. Other methods of controlling NP size, such as inducing defects in the support to stabilize small NPs, are not broadly applicable and can't be used on an inert support like SiO_2. Changing the weight percent (wt.%) of metal on support is another broadly practiced method to alter the size of metal NPs, but it introduces further issues in evaluating catalysts. For example, controlling the space velocity of a reaction is an important factor in comparing catalysts, and differences in metal loading can affect how catalysis data can be interpreted, especially for kinetic studies in a flow reactor [14,15]. When metal loadings on support differ between catalysts, keeping the same amount of metal in the reactor will inevitably change the space velocity. Using catalysts with the same metal loading but different particle sizes is preferable to study the size effect of supported metal nanoparticles on catalysis.

Hydroformylation of olefins to aldehydes (the oxo process) has been a critical industrial reaction since its discovery in 1938 [13,16–18], and is now a vital part of the chemical production industry [19]. Homogeneous rhodium complexes are the prevailing industrial catalysts and are still being studied in modern research [20–22].

However, it is challenging to separate homogeneous catalysts from the reaction mixture, which reduces the overall recyclability of these catalysts [23–25]. The high cost of rhodium causes losses to add up quickly and makes designing alternative catalysts that are easier to recycle of paramount importance [16,20–22,25]. Heterogeneous catalysts, where the active site is at a solid-liquid interface, are far easier to separate than homogenous ones. The superior recyclability of heterogenous catalysts is preferred for industrial applications.

Typical hydroformylation also seeks a high yield to the n-aldehyde (linear) product over the iso-aldehyde (branched) product, though, in the hydroformylation of styrene (Scheme 1), the branched product is also valuable. The branched products of styrene hydroformylation have been used to study the enantioselective properties of catalysts [26]. When considering styrene derivates, such as 1-isobutyl-4-vinylbenzene, as the substrate, the branched aldehyde product from hydroformylation can serve as the precursor for (R/S)-2-(4-(isobutyl)phenyl)propanoic acid, commonly known as ibuprofen. Ibuprofen is a nonsteroidal anti-inflammatory medication that treats conditions such as inflammation-related diseases, pain, fever, and menstrual cramps.
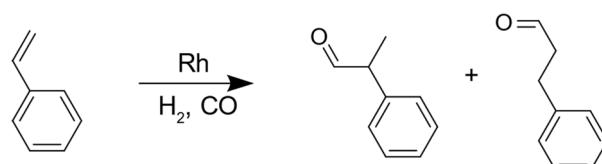
Scheme 1. Hydroformylation of styrene.

Efforts to study the impact of NP size during the hydroformylation of ethylene, 1-hexene, 1-decene, and even formaldehyde have provided insight into changes in activity, chemoselectivity, and regioselectivity in different particle size regimes [10,20,27–30]. In the hydroformylation of small molecules, like ethylene or formaldehyde, a volcano plot of NP size vs aldehyde turnover frequency (TOF) is observed, as the largest particles fail to achieve high activity due to a limited number of edge and corner sites, which are most active for hydroformylation. However, when NP size is too small, they predominantly catalyze the olefin hydrogenation rather than the hydroformylation [28–30]. This is contrasted by hydroformylation reports of larger molecules, which consistently have near 100% chemoselectivity to aldehydes regardless of particle size [12,13,18,27]. Despite the large body of literature on hydroformylation, we have found no reports of a dedicated effort to study the effect of NP size on the hydroformylation of styrene. The impact of NP size was briefly studied previously for Rh supported on silica gel [12]. However, the activity comparison between Rh NPs of different sizes is inconclusive because only the total amount of catalyst was kept constant in catalytic reactions instead of the Rh amount.

In this work, we have developed a general and scalable method for synthesizing metal NP catalysts across various sizes. Chloride ions have been reported to increase the dispersion of metal atoms during reduction from precursor salt to NPs [31]. Using $RhCl_3$ as a precursor leads to Rh NPs of 1.6 ± 0.3 nm, while the acetylacetonate salt gives Rh NPs of 6.4 ± 0.9 nm. By adjusting the ratio between the chloride and acetylacetonate metal precursors impregnated successively in mesoporous silica support, the size of Rh NPs can be controlled between 1.6 and 6.4 nm at the same Rh loading, ~3 wt.%. We employed these Rh-X/SBA-15 (X = particle size, nm) in the low-temperature hydroformylation of styrene. The smallest, Rh-1.6/SBA-15, displayed a TOF four times higher than the homogeneous Wilkinson catalyst while matching the activity of previously reported single-atom catalysts [18]. We successfully performed hydroformylation of 1-isolbutyl-4-vinylbenzene to demonstrate a route to synthesize ibuprofen. Finally, this method of controlling metal NP size is also extended to synthesizing Pt and Pd particles with sizes ranging between ~2 to 10 nm.

2. Materials and Methods

2.1. Materials

Pluronic P123 and styrene (99%) were purchased from Sigma-Aldrich. Rhodium (III) chloride hydrate ($RhCl_3 \cdot xH_2O$, >99%) and rhodium (III) acetylacetonate ($Rh(acac)_3$, 97%) were purchased from Aldrich (Milwaukee, WI, USA). Chloridotris(triphenylphosphine)rhodium(I) (Wilkinson catalyst, >98%) was purchased from TCI (Tokyo, Japan). Syngas (CO:H_2 = 1:1) was purchased from Airgas (Waukesha, WI, USA). 4-isobutylbenzaldehyde (95%) was purchased from Combi Blocks (San Diego, CA, USA).

2.2. SBA-15 Synthesis

4 g of Pluronic P123, 130 mL water, and 20 mL 12.1 M HCl are mixed at 38 °C for 24 h in a 500 mL polypropylene (PP) bottle. 9.11 mL TEOS is added to the bottle quickly, still at 38 °C and with stirring, and allowed to react further for 20 h. The mixture sealed in the PP bottle is then placed in an oven at 100 °C for 24 h under static conditions. After cooling to room temperature, the white solid in the bottle was separated by filtration, washed with water, and further washed with ethanol three times. After drying at room temperature, the solid is calcined at 550 °C for 6 h before being stored in a desiccator until further use. We used a temperature ramping program for the calcination from a previous report [32].

2.3. Rh-X/SBA-15 Synthesis

Rh catalysts are prepared by incipient wetness impregnation [13]. For a typical synthesis of Rh-1.6/SBA-15, 50 µL of 0.3 M $RhCl_3$ aqueous solution is mixed thoroughly in a 1 dram vial with 50 mg SBA-15. After mixing for 5 min, ensuring that no dark regions are visible, the vial is capped and placed in a desiccator for > 8 h. Next, the solid is placed in an oven at 100 °C in air for 2 h to evaporate liquid water. The catalyst is then placed in a tube furnace, ramped at 5 °C/min to 200 °C, and kept for 2 h with 10% H_2 in Ar flowing at 50 mL/min. To synthesize Rh-6.4, the same procedure is followed using $Rh(acac)_3$ dissolved in chloroform. To make Rh-3.2/SBA-15, a 0.15 M solution of $Rh(acac)_3$ chloroform was impregnated first. The same steps are followed until after evaporating the solvent. Then, 0.15 M $RhCl_3$ aqueous solution is impregnated following the same procedure as the synthesis of Rh-1.6/SBA-15. To test if other Cl^- sources can have a similar size control effect, we impregnated 50 µL aqueous solution of 0.9 M KCl to $Rh(acac)_3$/SBA-15, then dried and reduced the sample as before.

2.4. Rh-X/SBA-15 Characterization

Powder X-ray diffraction (PXRD) measurements were collected with a Bruker D8 (Billerica MA, USA) Advance powder diffractometer with a Cu K_α radiation source (40 kV, 40 mA, λ = 1.5406 Å). Transmission electron microscopy (TEM) samples were prepared by drop-casting the catalyst suspension solution onto a carbon-coated copper grid. TEM images were obtained using a JEOL 2100 (Tokyo, Japan) transmission electron microscope operated at 200 kV. Scanning transmission electron microscopy (STEM) experiments were conducted using an FEI Titan Themis (Waltham, MA, USA), an aberration-corrected scanning transmission electron microscope at 200 kV. Inductively coupled plasma mass spectrometry (ICP-MS) measurements were performed using an Agilent 7700 Series spectrometer (Santa Clara, CA, USA). Diffuse reflectance infrared Fourier transformed spectroscopy (DRIFTS) spectra were collected using a Bruker Vertex 80 FTIR (Billerica, MA, USA) with a linearized mercury−cadmium−telluride detector, a Harrick diffuse reflectance accessory, and a Praying Mantis high-temperature reaction chamber. All spectra were obtained at a resolution of 2 cm^{-1} from 1000 to 4000 cm^{-1} under atmospheric pressure. Before measurement, a reducing pretreatment was used to clean catalyst surfaces. Catalysts were treated with 50 mL/min of 10% H_2 in He at 200 °C for 1 h to freshly reduce NPs and remove water. Samples were then cooled to 0 °C while purging with pure He at 20 mL/min. The background was then recorded as the spectrum of the sample under He. CO was flowed at 5 mL/min and diluted with 20 mL/min He for 20 min, after which CO was turned off, and He was kept flowing to flush out free CO. Sample spectra were collected 20 min after turning off CO flow. X-ray absorption spectroscopy (XAS) measurements were performed at beamline 8-ID ISS at the National Synchrotron Light Source II at Brookhaven National Laboratory. Data was collected on the Rh K-edge in fluorescence mode. Scans were performed simultaneously at room temperature and collected with 30 s/scan; 10 scans were taken for each sample and merged for analysis. A Rh_2O_3 reference was also measured. Rh foil was obtained simultaneously with the sample spectra for energy calibration. The fraction of metallic and oxidized Rh was determined by fitting the sample XANES with Rh foil and Rh_2O_3 reference XANES. The k^2-weighted EXAFS data from k = 2.9 to 11.9 Å^{-1} and r = 1.0 to 2.9 Å was fit in R-space using the WinXAS 4.0 software (Thorsten Ressler, Germany). Rh-O and Rh-Rh scattering paths were modeled using FEFF 6.0 software (University of Washington, Seattle, WA, USA). S_0 was determined by fitting Rh foil with 12 Rh-Rh at 2.68 Å. X-ray photoelectron spectroscopy (XPS) experiments were conducted by protecting the samples from air until they were ready for measurements. Samples were analyzed on a Thermo Scientific K-Alpha XPS apparatus (Waltham, MA, USA) equipped with a monochromatic Al K_α source and flood gun for charge compensation. XPS data fitting was conducted using Thermo Avantage software (Avantage 5.9931.0.6755, Thermo Fisher Scientific, Waltham, MA, USA). Temperature programmed reduction (TPR) using hydrogen was done in a fixed bed flow reactor connected to an Agilent 5975 inert mass selective detector, measuring m/z =36.5 ± 0.7. 250 mg of unreduced $RhCl_3$/SBA-15 was placed in the reactor and then heated at 5 °C/min starting at 30 °C for 2.5 h under a 10% H_2 in He flow at 50 mL/min. CO chemisorption was conducted using a Micromeritics 3Flex surface characterization analyzer at 35 °C. Samples

were reduced at 200 °C for 1 h in pure hydrogen flow before analysis. The first isotherm was collected at 200 °C after evacuation for 30 min using a turbomolecular pump. The second isotherm was collected after evacuation at 35 °C for 1 h. The difference between the isotherms extrapolated to zero pressure is the amount of chemisorbed CO. Exposed Rh was calculated using CO/Rh = 1.5.

2.5. Catalytic Testing

In a typical run for hydroformylation, 0.5 mmol of styrene, 0.5 μmol Rh, and 2 mL of toluene were added to a 1-dram vial with a magnetic stir bar. Vials were placed in an aluminum heating block inside a stainless-steel autoclave and sealed. The air inside the autoclave is purged by flushing with syngas 5 times before charging to the reaction pressure of 30 bar. The autoclave is placed in an oil bath pre-heated to the desired temperatures and allowed to react for the specified time. Time starts when the autoclave is placed in the oil. Reaction mixtures were analyzed by gas chromatography (GC). An HP 6890 GC equipped with an HP-5 capillary column (30 m × 0.250 mm × 0.25 μm) and flame ionization detector were used to analyze the mixture after catalysis. Studies of activation energy, selectivity, and catalyst recycle tests were conducted by maintaining the conversion of styrene to less than 15%.

2.6. 1-isobutyl-4-vinylbenzene Synthesis

The 1-isobutyl-4-vinylbenzene was synthesized from 4-isobutylbenzaldehyde using the Wittig reaction according to a previously reported procedure [33].

3. Results and Discussion

A series of Rh NPs were encapsulated in the pores of SBA-15 via an incipient wetness impregnation method. Using $RhCl_3$, $Rh(acac)_3$, or their combination yielded different particle sizes upon reduction. The Rh loadings in all samples are around the target of 3 wt.% (Table 1). Rh-X/SBA-15 catalysts were characterized via TEM and STEM to obtain precise particle sizes based on counting >200 particles. The Rh NPs prepared from pure acetylacetonate, a 50:50 mixture of acetylacetonate and chloride, and pure chloride salts have diameters of 6.4 ± 0.9, 3.2 ± 0.6, and 1.6 ± 0.3 nm, respectively (Figure 1). PXRD results (Figure 2a) agree with STEM, where the crystalline size decreases as increased peak broadening is observed with increased $RhCl_3$ content in the precursor solutions. From the peak width in PXRD patterns of Rh-6.4/SBA-15 and Rh-3.2/SBA-15, we calculated their respective average particle sizes of 6.1 and 3.0 nm using the Debye-Scherrer equation. The PXRD peak broadening of Rh-1.6/SBA-15 is too great for Rh peaks to be clearly observed, as is expected for NPs smaller than 2 nm at this metal loading. The amount of surface-exposed Rh was determined as 18% for Rh-6.4/SBA-15, 30% for Rh-3.2/SBA-15, and 70% for Rh-1.6/SBA-15 according to CO chemisorption. The measured dispersions match well with the predicted values based on average particle sizes for each catalyst.
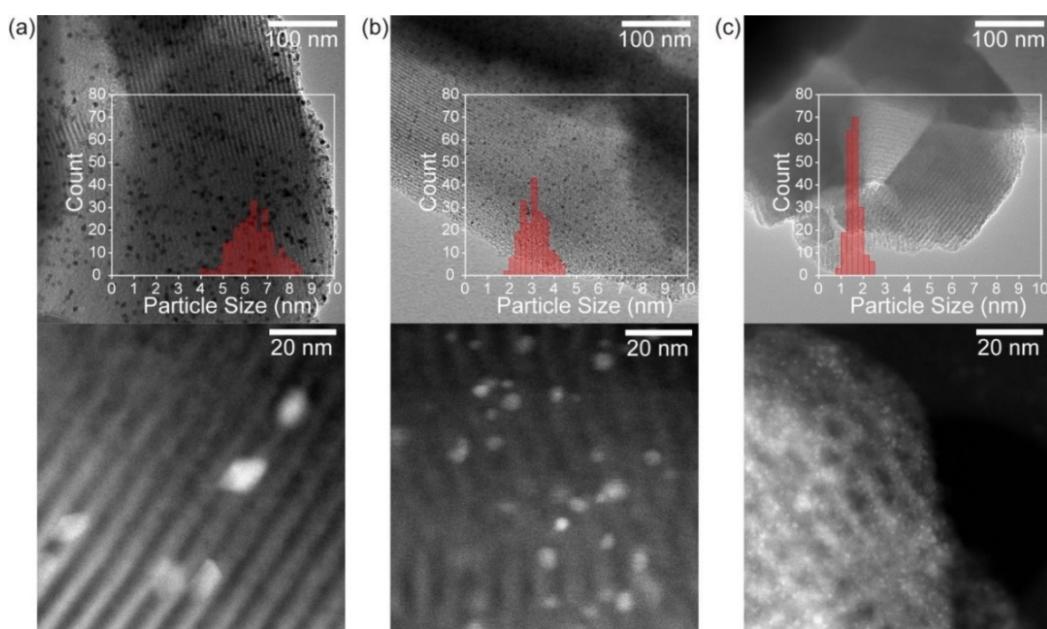

Figure 1. TEM (**top row**) and STEM (**bottom row**) images of SBA-15-supported Rh nanoparticles of different sizes, Rh-X/SBA-15, where X is the averaged Rh particle size: (**a**) X = 6.4 ± 0.9 nm, (**b**) X = 3.2 ± 0.6 nm, and (**c**) X = 1.6 ± 0.3 nm. Insets are histograms of measured particle sizes.
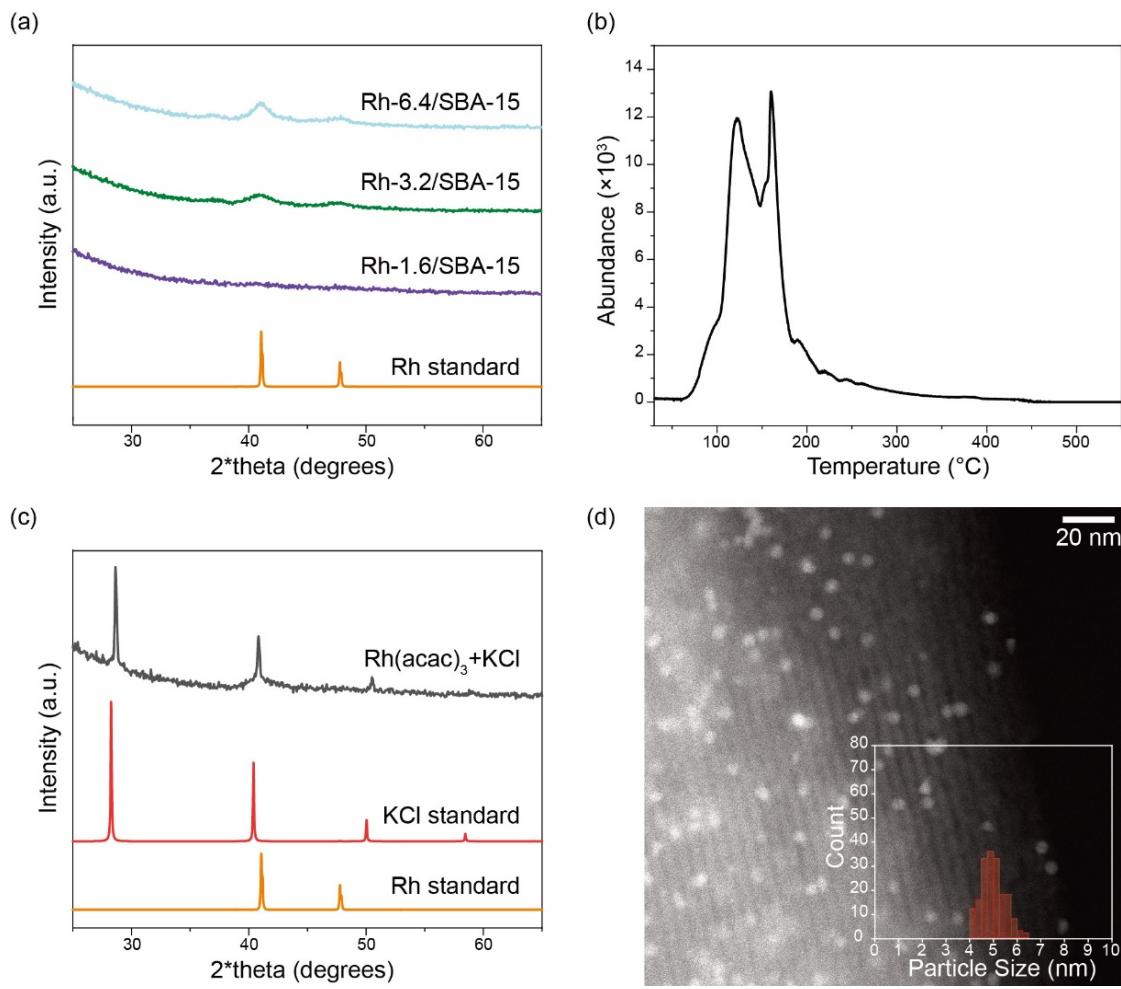
Figure 2. Characterization of the Rh-X/SBA-15 catalysts and the effect of Cl⁻ from KCl on the size of Rh NPs. (**a**) PXRD patterns for each NP size. (**b**) H_2-TPR of unreduced $RhCl_3$/SBA-15. (**c**) PXRD and (**d**) STEM of $Rh(acac)_3$/SBA-15 reduced in the presence of KCl with a ratio of Rh:Cl = 1:3. Inset in (**d**) is the size histogram of Rh NPs. Reduction condition: 10% H_2 in He was flowed at 50 mL/min, starting at 30 °C and ramping at 5 °C/min.

Table 1. Loading of Rh-X/SBA-15 catalysts as measured by ICP-MS.

Catalyst	Actual Loading (Rh wt.%)	Loading after Catalysis (Rh wt.%)
Rh-1.6/SBA-15	3.0 ± 0.1	3.0 ± 0.1
Rh-3.2/SBA-15	3.1 ± 0.1	3.1 ± 0.1
Rh-6.4/SBA-15	3.1 ± 0.2	3.0 ± 0.2

We propose two potential explanations for the disparity in NP size between the two Rh precursor salts. First, the physical differences between the precursor salts could lead to different interactions with the support. In $Rh(acac)_3$, the rhodium atom is capped inside a relatively large organic ligand, which would interact weakly with surface hydroxyls on SBA-15. Weaker interactions of $Rh(acac)_3$ molecules with the support would lead to their higher mobility on the support, enabling faster aggregation. Conversely, $RhCl_3$ can dissociate in an aqueous solution, and interactions between rhodium ions and support hydroxyls could be much stronger, leading to more nucleation centers and smaller particles rather than aggregation during the reduction. The second possibility for the size discrepancy is a change in the mechanism of NP formation induced by Cl⁻ or HCl formed during the reduction step when $RhCl_3$ is loaded into the support. It was previously reported that HCl could redisperse metal atoms in a supported catalyst [31]. A higher ratio of Cl/Pt present during reduction led to higher metal dispersion. However, no mechanistic insights were provided in that report.

If HCl does play a role in forming the smaller particle size, the first possibility would be the prevention of NP nucleation. Another step in NP growth potentially hindered by HCl could be aggregation. Inhibiting diffusion and aggregation or inducing redispersion of aggregated atoms would slow the growth process and result in smaller NPs. To probe the role of HCl in Rh-1.6/SBA-15, we performed H_2-TPR experiments (Figure 2b) measuring the release of m/z = 36.5 (HCl). The first detection of HCl peaks at 130 °C, likely the release of HCl as reduction of

Rh begins. There is a second peak at 170 °C, which we believe could be the desorption of HCl from Rh atoms or NPs. The elution of HCl lasts until 300 °C, which suggests that HCl could facilitate the dispersion of Rh during the reduction at 200 °C. Further work is still needed to identify the exact mechanism, nucleation or redispersion, by which particle size is affected between the chloride and acetylacetonate salts. Still, the identification of HCl desorption indicates that it could play a role in limiting particle growth during reduction. The ability of chloride to promote NP dispersion was also investigated by adding another Cl^- source, KCl, to Rh(acac)$_3$/SBA-15 before the reduction step. PXRD of the reduced sample shows strong diffraction peaks from undecomposed KCl (Figure 2c). Without Cl^-, the reduction of this sample leads to 6.4 ± 0.9 nm Rh NPs. With the inclusion of KCl, we observed a decrease in the average particle size to 4.9 ± 0.6 nm (Figure 2d). This result indicates that KCl is less effective than the Cl^- in RhCl$_3$ in reducing Rh NPs size, possibly due to the physical separation of the Rh^{3+} and Cl^- salts.

The Rh K-edge X-ray absorption near-edge spectrum (XANES) is shown in Figure 3a. The XANES energy is the inflection point of the leading edge; the energy of Rh-6.4/SBA-15 and Rh-3.2/SBA-15 is 23.2200 keV, very close to the foil at 23.2208 keV (Table 2), indicating a high fraction of metallic Rh. For Rh-6.4/SBA-15, the shape of the XANES is also nearly identical to the foil, while in Rh-3.2/SBA-15, there is a slight increase in the white line intensity, the first peak in the XANES spectrum, which indicates partially oxidized Rh NPs. The XANES energy of Rh-1.6/SBA-15 is at 23.2286 keV, indicating these NPs are more highly oxidized. The fraction of metallic and oxidized Rh was determined by fitting the sample XANES with Rh foil and Rh$_2$O$_3$, and the fits are given in Table 2. The fraction of Rh^{3+} in Rh-1.6/SBA-15 and Rh-3.2/SBA-15 was 69% and 37%, respectively, while the fraction of oxidized Rh in Rh-6.4/SBA-15 was too small to detect in these larger particles. The amount of oxidized Rh in Rh-1.6/SBA-15 and Rh-3.2/SBA-15 is close to the dispersion for each catalyst.
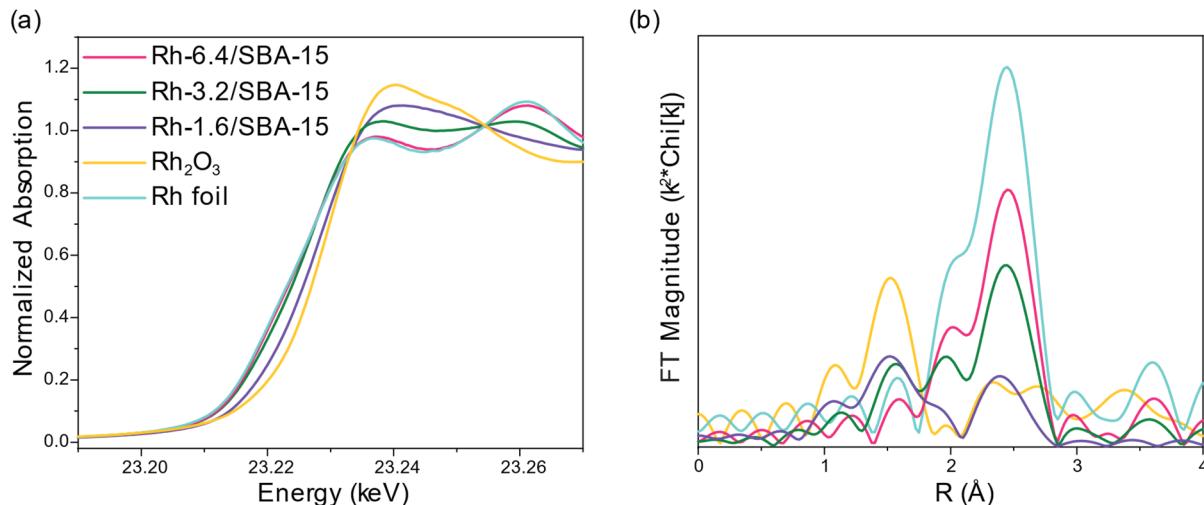
Figure 3. X-ray absorption spectroscopy results for (**a**) X-ray absorption near edge region, and (**b**) Fourier transformation of extended fine structure region.

Table 2. XAS fitting parameters.

Sample	k-Edge Energy (keV)	Rh^{3+} (%)	Rh^0 (%)	Scatter Path	CN	R (Å)	σ^2	E$_0$ (eV)
Rh Foil	23.2208	-	100	Rh-Rh	12	2.69	0.004	0.8
Rh$_2$O$_3$ Standard	23.2305	100	-	Rh-O	6	2.05	0.005	−4.4
Rh-1.6/SBA-15	23.2286	69	31	Rh-O	3.3	2.05	0.005	−1.3
				Rh-Rh	2.0	2.68	0.004	−1.5
Rh-3.2/SBA-15	23.2200	37	63	Rh-O	2.0	2.05	0.005	7.0
				Rh-Rh	5.4	2.69	0.004	2.7
Rh-6.4/SBA-15	23.2200	-	-	Rh-O	-	-	-	-
				Rh-Rh	7.5	2.69	0.004	2.1

The k^2-weighted magnitude of the Fourier transforms of the extended x-ray absorption fine structure (EXAFS) data are shown in Figure 3b. The peaks (phase uncorrected distances) at about 1.0 to 1.9 Å are due to Rh-O scattering, while the multiple peaks from about 1.5 to 3.0 Å are due to Rh-Rh scattering. As the Rh NP size decreases, there is a decrease in the size of the Rh-Rh peak and an increase in the size of the Rh-O peak. The EXAFS fits are given in Table 2. For Rh-6.4/SBA-15, the Rh-Rh coordination number (CN) was 7.5 at a bond distance of 2.69 Å, consistent with metallic Rh NPs. No Rh-O scattering peak is observed in this sample. For Rh-3.2/SBA-15, there are both Rh-O, CN = 2.0 at 2.05 Å, and Rh-Rh, CN = 5.4 at 2.69 Å, peaks indicating partially

oxidized Rh NPs. For Rh-1.6/SBA-15, the Rh-O CN increases to 3.3 at 2.05 Å, and the Rh-Rh CN decreases to 2.0 at 2.68 Å. Two factors contribute to the decrease in Rh-Rh scattering as particle size decreases. First, the Rh coordination number decreases with particle size [34], leading to lower scattering intensity. Second, there is a higher proportion of surface atoms in smaller NPs; thus, a larger fraction of metallic Rh is oxidized as the size decreases.

After the observations of the potential surface oxidation of the catalysts, fresh catalysts were prepared and kept in a strictly oxygen-free environment until they were unsealed for immediate XPS analysis (Figure 4). The deconvoluted Rh 3d XPS spectra of three catalysts revealed the presence of both metallic Rh and Rh oxide species. By quantifying the peak areas, the relative proportions of surface oxide were determined to be 18%, 30%, and 42% for Rh-6.4/SBA-15, Rh-3.2/SBA-15, and Rh-1.6/SBA-15, respectively (Table 3). These findings suggest that the oxidation of Rh occurs rapidly upon exposure to air, agreeing with XAS analyses.
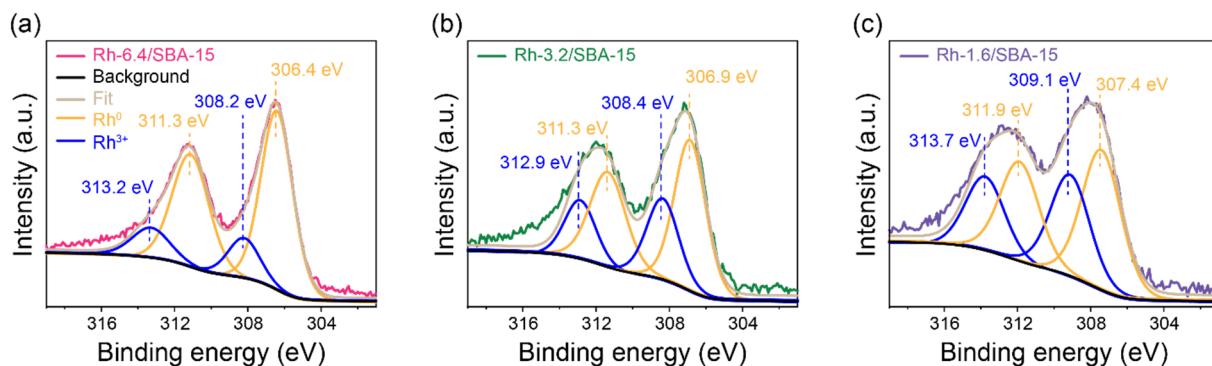

Figure 4. Rh 3d XPS spectra of (**a**) Rh-6.4/SBA-15, (**b**) Rh-3.2/SBA-15, (**c**) Rh-1.6/SBA-15.

Table 3. XPS fitting information.

Catalyst	Rh^{3+} 3d$_{5/2}$ Binding Energy (eV)	Rh^0 3d$_{5/2}$ Binding Energy (eV)	Rh^{3+} 3d$_{5/2}$ Peak Area	Rh^0 3d$_{5/2}$ Peak Area
Rh-1.6/SBA-15	309.1	307.4	0.72	1.00
Rh-3.2/SBA-15	308.4	306.9	0.54	1.00
Rh-6.4/SBA-15	308.2	306.4	0.22	1.00

DRIFTS of adsorbed CO was used to investigate the catalysts' surfaces [35–37]. Since the XAS and XPS showed that these NPs are easily oxidized in air, samples were pretreated with 10% H_2 at 200 °C before performing DRIFTS measurements shown in Figure 5. Rh-1.6/SBA-15 and Rh-3.2/SBA-15 have similar intensities for bridged-bonded CO peaks at ~1900 cm^{-1}, while the linear peak at 2063 cm^{-1} of Rh-3.2/SBA-15 is much smaller. Only linearly adsorbed CO is observed on Rh-6.4/SBA-15 after 10 min of flushing out CO. Once the 20 min were completed, no gaseous CO can be observed, while the amount of adsorbed CO remains the same. CO adsorbed on Rh-6.4/SBA-15 during the experiment was likely much lower than in the other catalysts, leading the bridged and most linear bonded CO to desorb quickly when CO was shut off.

Bridged CO adsorption peaks have previously been attributed to terrace atoms on NP surfaces [38]. The similar peak areas of bridged CO adsorption in Rh-1.6/SBA-15 and Rh-3.2/SBA-15 suggest that these catalysts have only a small difference in the number of terrace atoms on their surfaces. Conversely, the linear adsorption peak has been assigned to adsorption onto corner and edge atoms. The large difference in linearly adsorbed CO corresponds to a much greater number of corners and edges on Rh-1.6/SBA-15 than on Rh-3.2/SBA-15, consistent with smaller NPs. In Rh-1.6/SBA-15 and Rh-3.2/SBA-15, there is a CO vibration peak at 2090 cm^{-1} and a shoulder at 2024 cm^{-1} due to the symmetric and asymmetric stretching of gem-dicarbonyl (geminal) Rh(CO)$_2$. Geminal peaks are characteristic of positive or partially positive Rh atoms, including atomically isolated Rh. These peaks are likely caused by interactions of CO with the edges and corners, causing the particles to redisperse [39]. This does not interfere with hydroformylation reactions, as the syngas is overall reducing for the NPs; also, as demonstrated in Table 1, the catalysts do not leach Rh under the hydroformylation conditions.
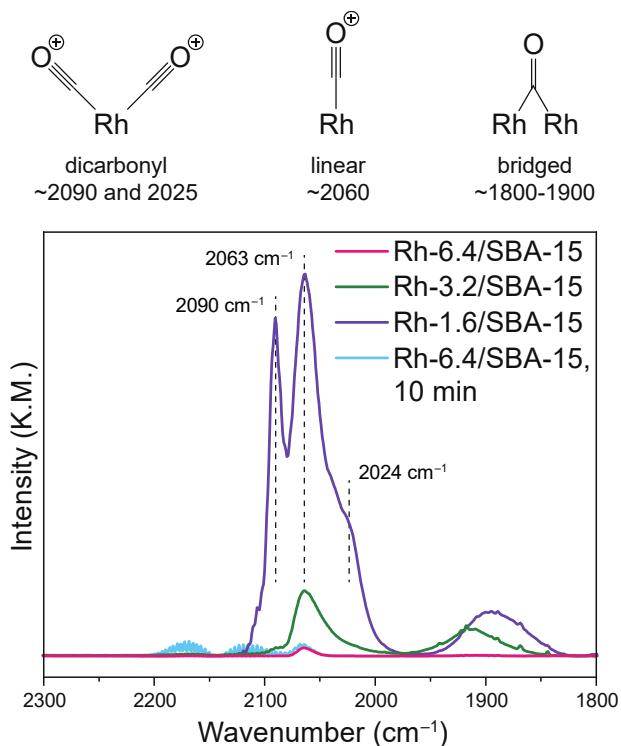
Figure 5. CO-DRIFTS spectra from each of the three materials. 5 mL/min CO diluted with 20 mL/min He was flowed for 20 min, after which time CO was turned off, and the sample was flushed for another 20 min before collecting reported spectra. The additional spectrum of Rh-6.4/SBA-15 is after only 10 min of flushing as indicated, which shows clear gas phase CO.

After characterizing the size-controlled Rh catalysts, the catalytic performance for the hydroformylation of styrene at low temperatures was determined. Hydroformylation is typically performed at 90–110 °C. Because of the high activity of Rh-1.6/SBA-15 with our previously reported conditions [13], we studied low-temperature hydroformylation. To compare the difference in activity, total styrene conversion was kept at ~10% for each catalytic reaction. At 50 °C, Rh-1.6/SBA-15 is approximately 2.5 times more active than Rh-3.2/SBA-15 and five times more active than Rh-6.4/SBA-15 by comparing TOFs (Figure 6a, Table 4), consistent with previous studies of Rh NP size [30]. All three catalysts surpass the performance of the benchmark Wilkinson catalyst. The activation energies were determined using Arrhenius plots within a temperature window of 50–80 °C (Figure 6b). The energy barrier for Rh-1.6/SBA-15 is lower than that of the other catalysts. We attribute the high activity of Rh-1.6/SBA-15 to the increased fraction of lower coordinated edge and corner sites, which turn over more quickly than the terraces on the NPs, matching previously reported trends.

We also studied the impact of the reaction temperature on regioselectivity over Rh-1.6/SBA-15 (Figure 6c). We found that as reaction temperature decreased, the preference toward the production of the branched product increased, agreeing with previous studies on the hydroformylation of various olefins [40]. Additionally, the Wilkinson catalyst gave a similar branched to linear (b/l) ratio as the supported NPs, further confirming the observed regioselectivity is due to reaction conditions and not catalyst structure, as observed previously [18]. We conducted recycle tests of each catalyst by washing it with ethanol post-reaction and then collecting the solid catalyst by centrifugation. The recycle tests show no activity loss upon reusing each catalyst (Figure 6d), agreeing with the ICP-MS results that show no Rh leaching (Table 1).
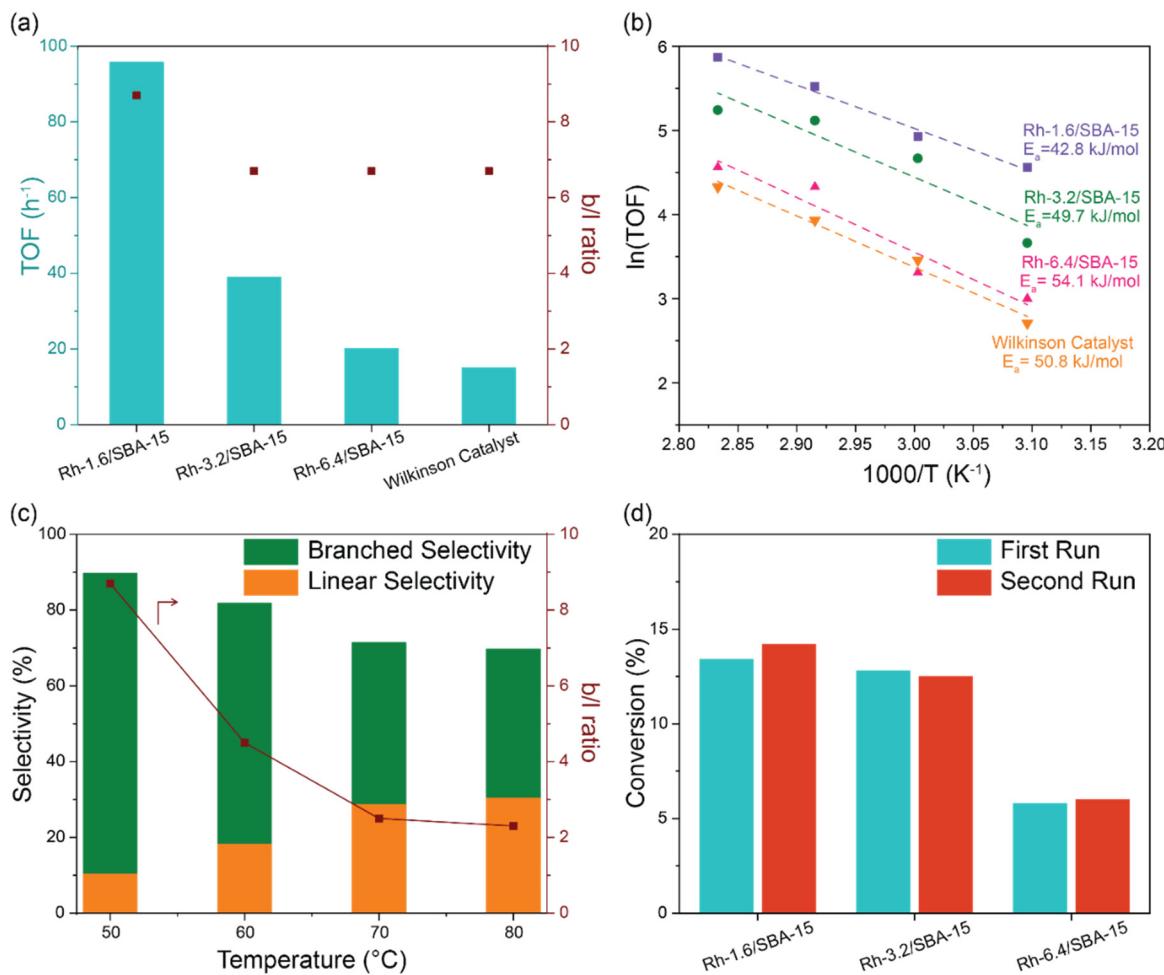
Figure 6. (a) Synthesized and Wilkinson catalysts compared by TOF and branched to linear ratio (b/l) at 50 °C; Rh-1.6/SBA-15, Rh-3.2/SBA-15, and Wilkinson catalyst ran for 2 h, Rh-6.4/SBA-15 ran for 16 h. **(b)** Arrhenius plot calculating activation energy. **(c)** Trend of b/l over Rh-1.6/SBA-15 at ~10% conversion at different temperatures, 60 °C for 1.5 h, 70 °C for 1 h, 80 °C for 0.5 h. **(d)** Recycle tests for all the heterogeneous catalysts. Rh-1.6/SBA-15 ran for 2 h, all others for 16 h. Reaction conditions: 0.5 mmol styrene, 0.5 μmol total Rh, 30 bar syngas, 2 mL toluene.

Table 4. Hydroformylation of styrene over rhodium catalysts.

Entry	Catalyst	Time (h)	Conversion (%)	TOF (h^{-1})	b/l
1	Rh-1.6/SBA-15	2	13.4	95.7	8.7
2	Rh-3.2/SBA-15	2	2.8	38.9	6.8
3	Rh-6.4/SBA-15	16	5.6	20.1	6.8
4	Wilkinson Catalyst	2	3.0	15.0	6.8

Reaction conditions: 0.5 mmol styrene, 0.5 μmol Rh, 2 mL toluene, 30 bar syngas, 50 °C.

After catalysis, we performed CO-DRIFTS on used catalysts to investigate potential changes in the NP structures during catalytic reactions (Figure 7). Previous reports have demonstrated dispersion of rhodium NPs upon exposure to CO [35,41]. The spectra of Rh-3.2/SBA-15 and Rh-6.4/SBA-15 are entirely unchanged, indicating no structural changes in Rh NPs of used catalysts. We again included an earlier spectrum of Rh-6.4/SBA-15 (10 min He purge) as the baseline changes in the latter 10 min of the typical scan. Rh-1.6/SBA-15 no longer has a clearly visible bridged CO peak, indicating a slight decrease in the particle size during the reaction.

Rh NPs of 1 nm and smaller have been reported to lack the bridged CO peak [41]. The symmetric and asymmetric stretching peaks of gem-dicarbonyl (geminal) $Rh(CO)_2$ on Rh-1.6/SBA-15 are also weakened, indicating the number of single atom Rh is also reduced during catalysis.
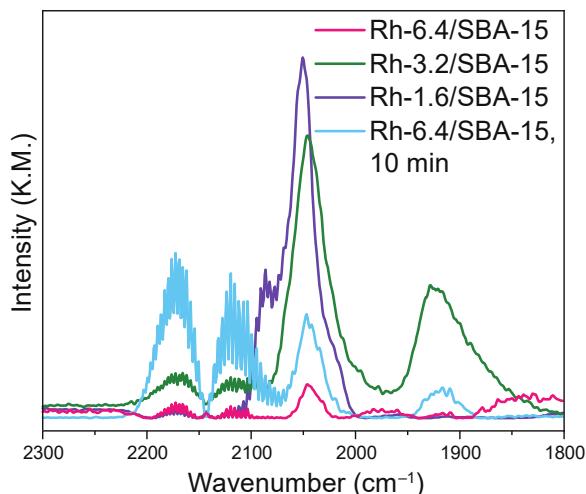

Figure 7. CO-DRIFTS spectra of used catalysts. Reaction conditions: 2.0 mmol styrene, 2.0 μmol total Rh, 30 bar syngas, 8 mL toluene, 2 h, 50 °C. CO-DRIFTS experiments were performed following the same procedures used to obtain spectra in Figure 5.

We evaluated Rh-1.5/SBA-15 for the hydroformylation of 1-isobutyl-4-vinylbenzene, following a previous method by Gao et al. [18] (Scheme 2). After hydroformylation, the resulting branched aldehyde can be further oxidized to make the active ingredient of ibuprofen, which is sold as a racemic mixture. Following the previously reported conditions, we could not match their 92% yield to the branched product in a toluene-water (50:50) mixed solvent. By switching the solvent mixture to pure toluene rather than a 50% mixture with water, we achieved a yield of 92%, with a b/l = 12/1. A possible reason is that the substrate is insoluble in water, and the SBA-15 support likely stays in the aqueous phase due to surface hydroxyls.
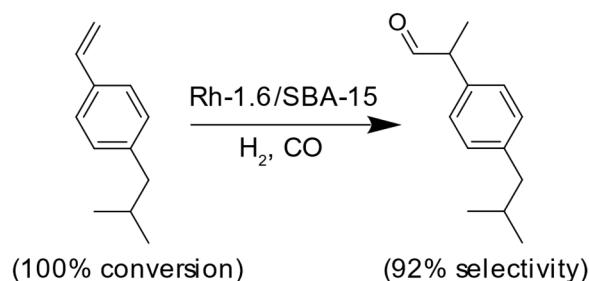
Scheme 2. Reaction scheme for the hydroformylation of 1-isobutyl-4-vinylbenzne. Reaction conditions: 0.4 mmol 1-isobutyl-4-vinylbenzene, 0.5 μmol total Rh, 30 bar syngas, 3 mL toluene, 40 °C, 24 h.

In addition to the control of Rh NP size, the applicability of our synthesis method was demonstrated for other noble metals, e.g., Pt and Pd. Using K_2MCl_4 salts where M = Pt or Pd, we could again achieve high dispersion, with particle sizes <2 nm from PXRD measurements (Figure 8). For the preparation with a mixture of Cl^- and acetylacetonate salts, the peaks were more prominent, though still small, and synthesis with only acetylacetonate salts formed much larger NPs. The NPs formed from platinum (II) acetylacetonate had a Debye-Scherrer particle size of 11 nm, while the $Pd(acac)_2$ salt yielded 8 nm particles. The larger particles from acetylacetonate salts allow for the possibility of controlling the NP size over an increased range depending on the ratio of chloride to acetylacetonate salt.
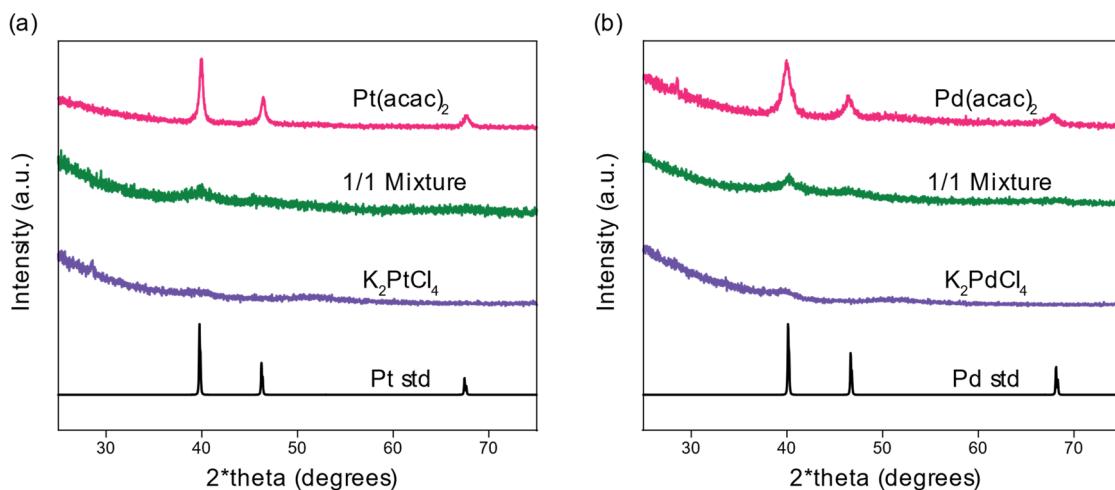
Figure 8. PXRD patterns of (**a**) Pt and (**b**) Pd NPs synthesized according to the method developed for rhodium display a similar trend.

4. Conclusion

Controlling NP sizes while accounting for metal loading and dispersion measurements and keeping the catalysts clean of bulky ligands is a valuable way to study the effect of particle size on reaction systems. We have applied a method of tuning the chloride content by adjusting the ratio of two precursors to affect the particle size of Rh NPs. The size-controlled Rh/SBA-15 catalysts were used to study the size-dependent nature of styrene hydroformylation. Using STEM, we identified a clear trend of NP size increase with decreasing chloride salt content used during the impregnation. PXRD and XAS studies confirmed that the bulk of our material follows that trend. Surface structures of these particles are also characterized by XPS and CO-DRIFTS. When applying these catalysts to hydroformylation, there is a clear activity increase with the decrease of Rh NP size. This reinforces the hypothesis based on small molecule hydroformylation that styrene hydroformylation would depend on particle size. Unlike the hydroformylation of small molecules, where <2 nm NPs tend to hydrogenate olefins, Rh-1.6/SBA-15 was 100% chemoselective to aldehyde products in styrene hydroformylation. This high selectivity and temperature-dependent regioselectivity to the branched aldehyde allowed us to synthesize the branched aldehyde precursor of ibuprofen efficiently. Finally, we demonstrated the applicability of this simple size control method to Pt and Pd, two other essential metals heavily used in catalysis.

Author Contributions: A.L.: conceptualization, methodology, writing—original draft preparation, reviewing and editing, TEM imaging, visualization, investigation; C.J.W.: XAS data collection, writing—reviewing and editing, visualization, software; J.T.M.: XAS data fitting; Z.A.: XPS data collection; X.L.: XPS data fitting; J.T.: organic synthesis; R.C.: STEM imaging; X.W.: STEM imaging; L.M.S.: guiding the organic synthesis; W.H.: conceptualization, guiding the research, writing—reviewing and editing. All authors have read and agreed to the published version of the manuscript.

Data Availability Statement: Raw data will be made available upon reasonable request.

Conflicts of Interest: The authors declare no conflict of interest.

References

1. Xu, L.; Liu, D.; Chen, D.; Liu, H.; Yang, J. Size and Shape Controlled Synthesis of Rhodium Nanoparticles. *Heliyon* **2019**, *5*, e01165. https://doi.org/10.1016/j.heliyon.2019.e01165.

2. Yang, F.; Deng, D.; Pan, X.; Fu, Q.; Bao, X. Understanding Nano Effects in Catalysis. *Natl. Sci. Rev.* **2015**, *2*, 183–201. https://doi.org/10.1093/nsr/nwv024.

3. Cuenya, B.R. Synthesis and Catalytic Properties of Metal Nanoparticles: Size, Shape, Support, Composition, and Oxidation State Effects. *Thin Solid. Films* **2010**, *518*, 3127–3150. https://doi.org/10.1016/j.tsf.2010.01.018.

4. Suchomel, P.; Kvitek, L.; Prucek, R.; Panacek, A.; Halder, A.; Vajda, S.; Zboril, R. Simple Size-Controlled Synthesis of Au Nanoparticles and Their Size-Dependent Catalytic Activity. *Sci. Rep.* **2018**, *8*, 4589. https://doi.org/10.1038/s41598-018-22976-5.

5. Alabdullah, M.; Ibrahim, M.; Dhawale, D.; Bau, J.A.; Harale, A.; Katikaneni, S.; Gascon, J. Rhodium Nanoparticle Size Effects on the CO$_2$ Reforming of Methane and Propane. *ChemCatChem* **2021**, *13*, 2879–2886. https://doi.org/10.1002/cctc.202100063.

6. Chen, M.; Han, Y.; Wei Goh, T.; Sun, R.; V. Maligal-Ganesh, R.; Pei, Y.; Tsung, C.-K.; W. Evans, J.; Huang, W. Kinetics, Energetics, and Size Dependence of the Transformation from Pt to Ordered PtSn Intermetallic Nanoparticles. *Nanoscale* **2019**, *11*, 5336–5345. https://doi.org/10.1039/C8NR10067E.

7. Humphrey, S.M.; Grass, M.E.; Habas, S.E.; Niesz, K.; Somorjai, G.A.; Tilley, T.D. Rhodium Nanoparticles from Cluster Seeds: Control of Size and Shape by Precursor Addition Rate. *Nano Lett.* **2007**, *7*, 785–790. https://doi.org/10.1021/nl070035y.

8. Wang, C.; Li, Y.; Zhang, C.; Chen, X.; Liu, C.; Weng, W.; Shan, W.; He, H. A Simple Strategy to Improve Pd Dispersion and Enhance Pd/TiO$_2$ Catalytic Activity for Formaldehyde Oxidation: The Roles of Surface Defects. *Appl. Catal. B Environ.* **2021**, *282*, 119540. https://doi.org/10.1016/j.apcatb.2020.119540.

9. Wu, X.; Tennakoon, A.; Yappert, R.; Esveld, M.; Ferrandon, M.S.; Hackler, R.A.; LaPointe, A.M.; Heyden, A.; Delferro, M.; Peters, B.; et al. Size-Controlled Nanoparticles Embedded in a Mesoporous Architecture Leading to Efficient and Selective Hydrogenolysis of Polyolefins. *J. Am. Chem. Soc.* **2022**, *144*, 5323–5334. https://doi.org/10.1021/jacs.1c11694.

10. Luo, L.; Li, H.; Peng, Y.; Feng, C.; Zeng, J. Rh-Based Nanocatalysts for Heterogeneous Reactions. *ChemNanoMat* **2018**, *4*, 451–466. https://doi.org/10.1002/cnma.201800033.

11. Zhang, Y.; Grass, M.E.; Kuhn, J.N.; Tao, F.; Habas, S.E.; Huang, W.; Yang, P.; Somorjai, G.A. Highly Selective Synthesis of Catalytically Active Monodisperse Rhodium Nanocubes. *J. Am. Chem. Soc.* **2008**, *130*, 5868–5869. https://doi.org/10.1021/ja801210s.

12. Han, D.; Li, X.; Zhang, H.; Liu, Z.; Li, J.; Li, C. Heterogeneous Asymmetric Hydroformylation of Olefins on Chirally Modified Rh/SiO$_2$ Catalysts. *J. Catal.* **2006**, *243*, 318–328. https://doi.org/10.1016/j.jcat.2006.08.003.

13. Chen, M.; Gupta, G.; Ordonez, C.W.; Lamkins, A.R.; Ward, C.J.; Abolafia, C.A.; Zhang, B.; Roling, L.T.; Huang, W. Intermetallic Nanocatalyst for Highly Active Heterogeneous Hydroformylation. *J. Am. Chem. Soc.* **2021**, *143*, 20907–20915. https://doi.org/10.1021/jacs.1c09665.

14. Munnik, P.; de Jongh, P.E.; de Jong, K.P. Recent Developments in the Synthesis of Supported Catalysts. *Chem. Rev.* **2015**, *115*, 6687–6718. https://doi.org/10.1021/cr500486u.

15. García-Sánchez, J.T.; Valderrama-Zapata, R.; Acevedo-Córdoba, L.F.; Pérez-Martínez, D.; Rincón-Ortiz, S.; Baldovino-Medrano, V.G. Calculation of Mass Transfer Limitations for a Gas-Phase Reaction in an Isothermal Fixed Bed Reactor: Tutorial and Sensitivity Analysis. *ACS Catal.* **2023**, *13*, 6905–6918. https://doi.org/10.1021/acscatal.3c01282.

16. Franke, R.; Selent, D.; Börner, A. Applied Hydroformylation. *Chem. Rev.* **2012**, *112*, 5675–5732. https://doi.org/10.1021/cr3001803.

17. Lang, R.; Li, T.; Matsumura, D.; Miao, S.; Ren, Y.; Cui, Y.-T.; Tan, Y.; Qiao, B.; Li, L.; Wang, A.; et al. Hydroformylation of Olefins by a Rhodium Single-Atom Catalyst with Activity Comparable to RhCl(PPh$_3$)$_3$. *Angew. Chem. Int. Ed.* **2016**, *55*, 16054–16058. https://doi.org/10.1002/anie.201607885.

18. Gao, P.; Liang, G.; Ru, T.; Liu, X.; Qi, H.; Wang, A.; Chen, F.-E. Phosphorus Coordinated Rh Single-Atom Sites on Nanodiamond as Highly Regioselective Catalyst for Hydroformylation of Olefins. *Nat. Commun.* **2021**, *12*, 4698. https://doi.org/10.1038/s41467-021-25061-0.

19. Tudor, R.; Shah, A. Industrial Low Pressure Hydroformylation: Forty-Five Years of Progress for the LP OxoSM Process. *Johns. Matthey Technol. Rev.* **2017**, *61*, 246–256. https://doi.org/10.1595/205651317X695875.

20. Hanf, S.; Alvarado Rupflin, L.; Gläser, R.; Schunk, S.A. Current State of the Art of the Solid Rh-Based Catalyzed Hydroformylation of Short-Chain Olefins. *Catalysts* **2020**, *10*, 510. https://doi.org/10.3390/catal10050510.

21. Liu, Y.; Zhao, J.; Zhao, Y.; Liu, H.-M.; Fu, H.; Zheng, X.; Yuan, M.; Li, R.; Chen, H. Homogeneous Hydroformylation of Long Chain Alkenes Catalyzed by Water Soluble Phosphine Rhodium Complex in CH$_3$OH and Efficient Catalyst Cycling. *RSC Adv.* **2019**, *9*, 7382–7387. https://doi.org/10.1039/C8RA08787C.

22. Wang, P.; Shi, H.; Feng, B.; Zhao, D.; Yang, D. Highly Selective and Recyclable Homogeneous Hydroformylation of Olefins with [Rh(Cod)Cl]$_2$/PPh$_3$ Regulated by Et3N as Additive. *Mol. Catal.* **2023**, *548*, 113459. https://doi.org/10.1016/j.mcat.2023.113459.

23. Evans, D.; Osborn, J.A.; Wilkinson, G. Hydroformylation of Alkenes by Use of Rhodium Complex Catalysts. *J. Chem. Soc. Inorg. Phys. Theor.* **1968**, 3133–3142. https://doi.org/10.1039/J19680003133.

24. Brown, C.K.; Wilkinson, G. Homogeneous Hydroformylation of Alkenes with Hydridocarbonyltris-(Triphenylphosphine)Rhodium(I) as Catalyst. *J. Chem. Soc. Inorg. Phys. Theor.* **1970**, 2753–2764. https://doi.org/10.1039/J19700002753.

25. Bohnen, H.-W.; Cornils, B. Hydroformylation of Alkenes: An Industrial View of the Status and Importance. In *Advances in Catalysis*; Academic Press: Cambridge, MA, USA, 2002; Volume 47, pp. 1–64.

26. Han, D.; Li, X.; Zhang, H.; Liu, Z.; Hu, G.; Li, C. Asymmetric Hydroformylation of Olefins Catalyzed by Rhodium Nanoparticles Chirally Stabilized with (R)-BINAP Ligand. *J. Mol. Catal. Chem.* **2008**, *283*, 15–22. https://doi.org/10.1016/j.molcata.2007.12.008.

27. Bruss, A.J.; Gelesky, M.A.; Machado, G.; Dupont, J. Rh(0) Nanoparticles as Catalyst Precursors for the Solventless Hydroformylation of Olefins. *J. Mol. Catal. Chem.* **2006**, *252*, 212–218. https://doi.org/10.1016/j.molcata.2006.02.063.

28. McClure, S.M.; Lundwall, M.J.; Goodman, D.W. Planar Oxide Supported Rhodium Nanoparticles as Model Catalysts. *Proc. Natl. Acad. Sci. USA* **2011**, *108*, 931–936. https://doi.org/10.1073/pnas.1006635107.

29. Yang, Q.; Wang, P.; Li, C.; Wang, B.; Zheng, Y.; Feng, Y.; Miao, Z.; Li, M.; Wang, M.-Y.; Huang, S.; et al. Unravelling Structure Sensitivity in Heterogeneous Hydroformylation of Aldehyde over Rh. *Chem. Eng. J.* **2024**, *481*, 148529. https://doi.org/10.1016/j.cej.2024.148529.

30. Hanaoka, T.; Arakawa, H.; Matsuzaki, T.; Sugi, Y.; Kanno, K.; Abe, Y. Ethylene Hydroformylation and Carbon Monoxide Hydrogenation over Modified and Unmodified Silica Supported Rhodium Catalysts. *Catal. Today* **2000**, *58*, 271–280. https://doi.org/10.1016/S0920-5861(00)00261-3.

31. Barbier, J.; Bahloul, D.; Marecot, P. Reduction of Pt/Al$_2$O$_3$ Catalysts: Effect of Hydrogen and of Water and Hydrochloric Acid Vapor on the Accessibility of Platinum. *J. Catal.* **1992**, *137*, 377–384. https://doi.org/10.1016/0021-9517(92)90165-E.

32. Zhao, D.; Feng, J.; Huo, Q.; Melosh, N.; Fredrickson, G.H.; Chmelka, B.F.; Stucky, G.D. Triblock Copolymer Syntheses of Mesoporous Silica with Periodic 50 to 300 Angstrom Pores. *Science* **1998**, *279*, 548–552. https://doi.org/10.1126/science.279.5350.548.

33. Greenhalgh, M.D.; Thomas, S.P. Iron-Catalyzed, Highly Regioselective Synthesis of α-Aryl Carboxylic Acids from Styrene Derivatives and CO2. *J. Am. Chem. Soc.* **2012**, *134*, 11900–11903. https://doi.org/10.1021/ja3045053.

34. Marinkovic, N.S.; Sasaki, K.; Adzic, R.R. Determination of Single- and Multi-Component Nanoparticle Sizes by X-ray Absorption Spectroscopy. *J. Electrochem. Soc.* **2018**, *165*, J3222. https://doi.org/10.1149/2.0281815jes.

35. Asokan, C.; Xu, M.; Dai, S.; Pan, X.; Christopher, P. Synthesis of Atomically Dispersed Rh Catalysts on Oxide Supports via Strong Electrostatic Adsorption and Characterization by Cryogenic Infrared Spectroscopy. *J. Phys. Chem. C* **2022**, *126*, 18704–18715. https://doi.org/10.1021/acs.jpcc.2c05426.

36. Yang, C.; Garl, C.W. Infrared Studies of Carbon Monoxide Chemisorbed on Rhodium. *J. Phys. Chem.* **1957**, *61*, 1504–1512. https://doi.org/10.1021/j150557a013.

37. Chen, M.; Yan, Y.; Gebre, M.; Ordonez, C.; Liu, F.; Qi, L.; Lamkins, A.; Jing, D.; Dolge, K.; Zhang, B.; et al. Thermal Unequilibrium of PdSn Intermetallic Nanocatalysts: From In Situ Tailored Synthesis to Unexpected Hydrogenation Selectivity. *Angew. Chem. Int. Ed.* **2021**, *60*, 18309–18317. https://doi.org/10.1002/anie.202106515.

38. Meng, X.; Yang, Y.; Chen, L.; Xu, M.; Zhang, X.; Wei, M. A Control over Hydrogenation Selectivity of Furfural via Tuning Exposed Facet of Ni Catalysts. *ACS Catal.* **2019**, *9*, 4226–4235. https://doi.org/10.1021/acscatal.9b00238.

39. Marino, S.; Wei, L.; Cortes-Reyes, M.; Cheng, Y.; Laing, P.; Cavataio, G.; Paolucci, C.; Epling, W. Rhodium Catalyst Structural Changes during, and Their Impacts on the Kinetics of, CO Oxidation. *JACS Au* **2023**, *3*, 459–467. https://doi.org/10.1021/jacsau.2c00595.

40. Caiazzo, A.; Settambolo, R.; Uccello-Barretta, G.; Lazzaroni, R. Influence of the Reaction Temperature on the Regioselectivity in the Rhodium-Catalyzed Hydroformylation of Vinylpyrroles. *J. Organomet. Chem.* **1997**, *548*, 279–284. https://doi.org/10.1016/S0022-328X(97)00479-8.

41. Yan, G.; Tang, Y.; Li, Y.; Li, Y.; Nguyen, L.; Sakata, T.; Higashi, K.; Tao, F.F.; Sautet, P. Reaction Product-Driven Restructuring and Assisted Stabilization of a Highly Dispersed Rh-on-Ceria Catalyst. *Nat. Catal.* **2022**, *5*, 119–127. https://doi.org/10.1038/s41929-022-00741-2.

Article

Constructing Co Cluster Sites for Selective CO₂ Hydrogenation via Phase Segregation from Co-Doped TiO₂ Nanocrystals

Xiangru Wei [1], Yizhen Chen [1], Yulu Zhang [1], Liyue Zhang [1], Lu Ma [2], Matthew M. Yung [3], and Sen Zhang [1],*

[1] Department of Chemistry, University of Virginia, Charlottesville, VA 22904, USA
[2] National Synchrotron Light Source II, Brookhaven National Laboratory, Upton, NY 11973, USA
[3] Bioenergy Science and Technology Directorate, National Renewable Energy Laboratory, Denver West Parkway, Golden, CO 80401, USA
* Correspondence: sz3t@virginia.edu

Abstract: This article presents a Co phase segregation strategy for creating stable Co cluster catalytic sites on TiO₂, enabling selective CO₂ hydrogenation to CO. Through oxidative calcination, pre-synthesized Co-doped brookite TiO₂ nanorods transform into a mixed TiO₂ phase, leading to the phase segregation of Co species. The resulting Co clusters, stabilized by strong Co-TiO₂ interactions during reductive CO₂ hydrogenation, effectively suppress the formation of larger nanoparticles. The undercoordinated sites of these clusters promote a high CO production rate with near-unit selectivity, contrasting with Co nanoparticles, which favor CH₄ formation under identical conditions. In-situ diffuse reflectance infrared Fourier transform spectroscopy (DRIFTS) analysis indicates that the weakened CO adsorption on Co clusters is key to their enhanced CO selectivity, highlighting this method as a promising approach for efficient CO₂ utilization.

Keywords: CO₂ hydrogenation; heterogeneous catalysis; cluster sites; selectivity; phase segregation.
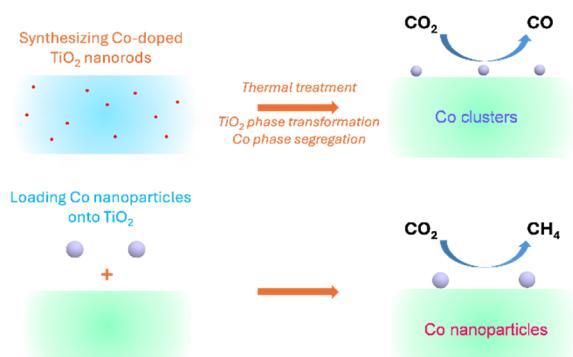
1. Introduction

CO₂ valorization technologies are becoming increasingly critical for mitigating the environmental impact of carbon emission and promoting a circular carbon economy [1,2]. At the heart of this approach is the utilization of CO₂ as a feedstock, along with renewable hydrogen and energy sources, to produce valuable carbon-based chemicals and fuels, reducing reliance on fossil-derived resources [3–5]. Typically, CO₂ hydrogenation at atmospheric pressure proceeds through the reverse water-gas shift (RWGS) reaction ($CO_2 + H_2 \rightarrow CO + H_2O$) and the methanation reaction ($CO_2 + 4H_2 \rightarrow CH_4 + 2H_2O$), yielding CO and CH₄, respectively [6]. There has been significant interest in enhancing selectivity for CO production over CH₄, as CO is a crucial intermediate in the synthesis of liquid hydrocarbons and oxygenated products [6–8].

Research indicates that various metals, including Rh [9–11], Ru [12,13], Ni [14,15] and Pd [16] tend to favor CO production over CH₄ when present as smaller nanoparticles rather than larger ones. For example, Simons et al. [17] investigated Ni catalysts of varying nanoparticle sizes (2−12 nm) supported on silica using operando spectroscopy to explore their structure-sensitivity of CO₂ hydrogenation. They found that the active sites involved in the conversion of CO₂ to CO differ from those responsible for the subsequent hydrogenation of CO to CH₄. While the initial CO₂-to-CO reaction is minimally influenced by nanoparticle size, the hydrogenation of CO to CH₄ is highly sensitive to the structure. Specifically, nanoparticles smaller than 5 nm have a reduced availability of step edges, which are essential for CO dissociation, leading to a significant decrease in methanation activity. Such findings are widely accepted in mechanistic studies of the methanation reaction [18–20], suggesting that CO₂ often first dissociates to CO via the RWGS reaction, with the adsorbed CO serving as a key intermediate in CH₄ formation

through direct C−O bond cleavage or the RWGS + CO-Hydro pathway [21,22]. In the direct C−O bond cleavage pathway, *CO_2 dissociates to *CO and *O, and the resulting *CO undergoes further dissociation to form *O and *C, which is subsequently hydrogenated to CH_4 [23,24]. Alternatively, *CO can be hydrogenated to *HCO, which dissociates into *CH + *O, with *CH eventually being hydrogenated to CH_4 [25,26].

The Co-based catalyst has been widely used for multiple CO_2 hydrogenation reactions, such as methanation [27], methanol synthesis [28], and C−C coupling reactions including Fischer–Tropsch synthesis [29] and higher alcohol synthesis [30]. However, a comprehensive understanding of the structure–property relationships in Co-based catalytic systems for RWGS reaction remains limited, posing challenges for the rational design, optimization, and mechanistic elucidation of these catalysts. Compared to metallic nanoparticles, we envision that smaller clusters, characterized by primarily low coordination sites, hold promise for reducing the likelihood of multi-bound CO adsorption—a crucial step in CH_4 production [31]. To produce these small Co cluster catalysts, we developed a Co phase segregation strategy aimed at limiting nanoparticle formation and enhancing cluster stability. To achieve this, we synthesized Co-doped TiO_2 (Co-TiO_2) nanorods using a one-step colloidal method, where Co atoms are integrated into TiO_2 brookite nanorods through single-site substitution, forming stable Co-O-Ti bonds. X-ray absorption spectroscopy (XAS) and synchrotron X-ray diffraction (SXRD) analyses showed that oxidative calcination induces the phase transformation of brookite TiO_2 while simultaneously promoting Co phase segregation, as illustrated in Figure 1. The robust Co/TiO_2 interactions help stabilize Co clusters, preventing the formation of larger nanoparticles under reductive CO_2 hydrogenation conditions, which results in improved CO selectivity. In-situ diffuse reflectance infrared Fourier transform spectroscopy (DRIFTS) further revealed that the weakened CO adsorption on Co clusters, compared to larger nanoparticles, is a critical factor contributing to the enhanced CO selectivity during CO_2 hydrogenation.
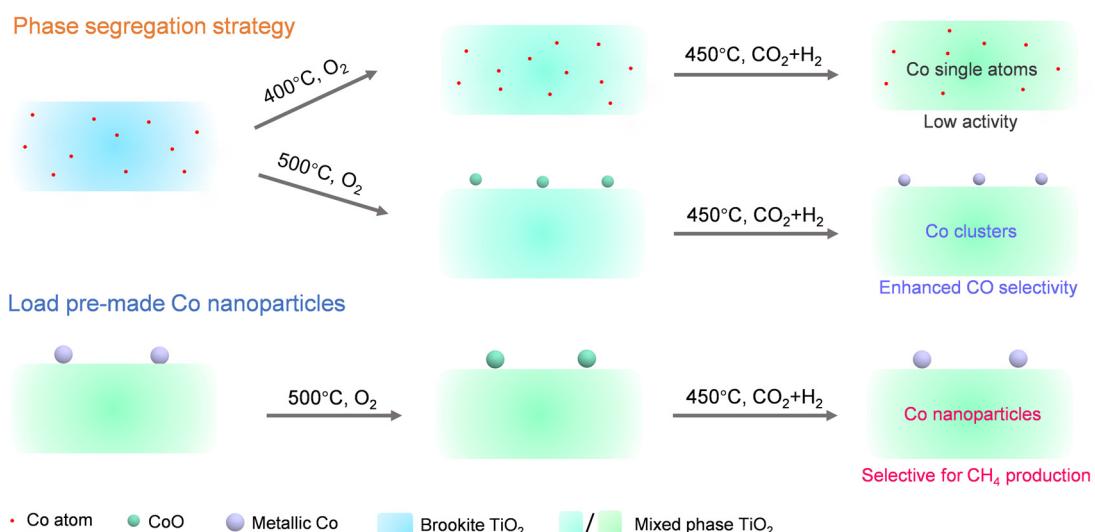
Figure 1. Schematic illustration of the development of Co cluster catalysts for CO production through the segregation of Co from Co-TiO_2. In contrast, depositing Co nanoparticles onto a TiO_2 support results in CH_4 production.

2. Results and Discussion

The Co-TiO_2 nanorods were synthesized through thermal decomposition of titanium chloride ($TiCl_4$) and cobalt oleate precursors in an octadecane (ODE) solution, with oleylamine (OAm) and oleic acid (OAc) as surfactants, following a previously established protocol [32,33]. During high-temperature synthesis, a minor release of water, resulting from the reaction between OAc and OAm, facilitates the controlled hydrolysis of $TiCl_4$. Simultaneously, cobalt oleates decompose, leading to the formation of TiO_2 nanorods doped with Co atoms.

By adjusting the ratio of Co to Ti precursors, Co-TiO_2 nanorods with varying doping concentrations were achieved, reaching a maximum Co doping level of approximately 12%, as reported in our earlier studies [33]. Transmission electron microscopy (TEM, Thermo Fisher Scientific, Waltham, MA, USA) images confirm that Co-TiO_2 nanorods with different Co doping levels retain a consistent nanorod morphology, exhibiting an average diameter of 4.2 ± 0.8 nm and an average length of 35 ± 6 nm (Figures 2a and S1). Synchrotron X-ray diffraction (SXRD, Brookhaven National Laboratory, Upton, NY, USA) analysis (λ = 0.6199 Å) (Figure 2b) reveals the exclusive formation of the brookite phase of TiO_2, as indicated by the characteristic (121) diffraction peak at 12.28° (2θ) (JCPDS file: 96-900-4143), with no interference from anatase or rutile phases. For comparison, Co

nanoparticles (NPs) with an average size of 8.2 ± 2 nm were synthesized (Figure S2a) and subsequently loaded onto a commercial TiO_2 support (P25), yielding the reference sample, Co NPs/TiO_2 (Figure S2b) [34].
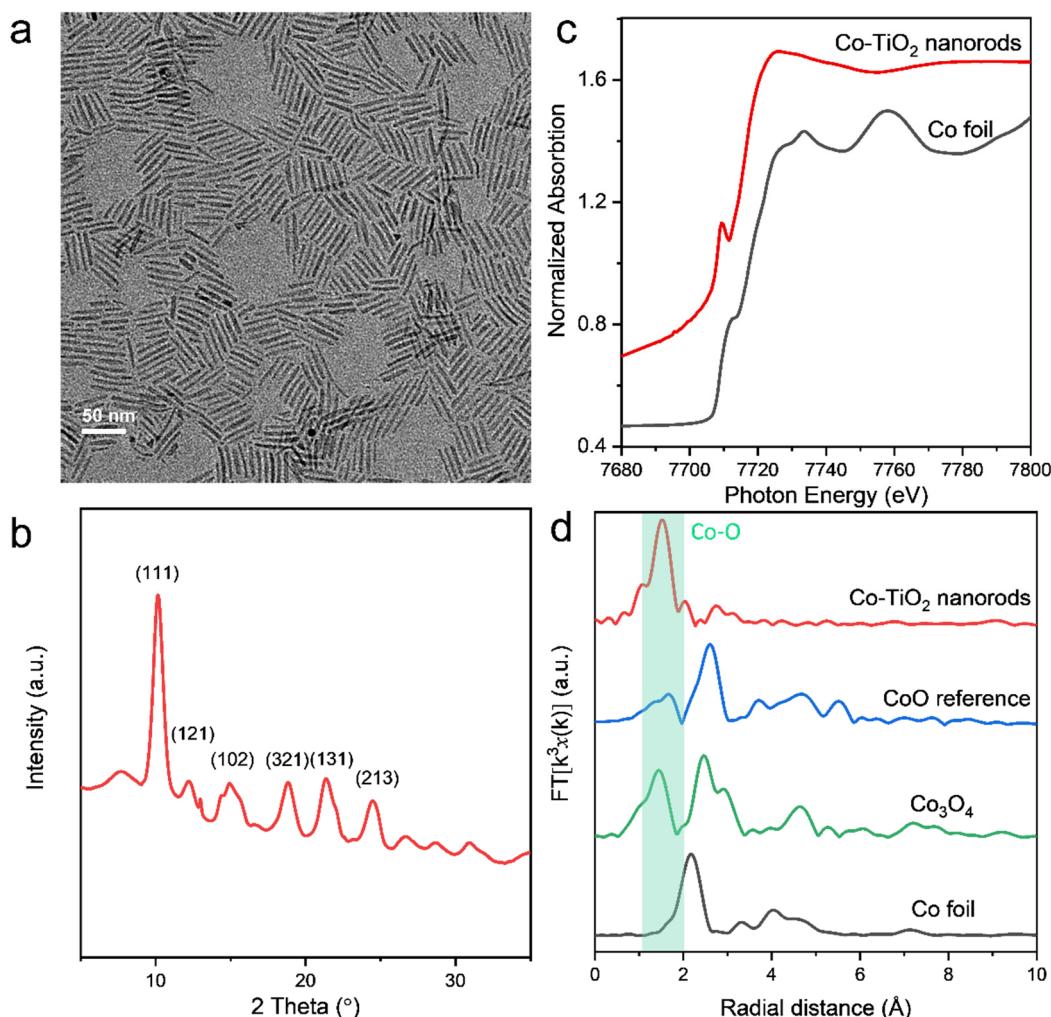
Figure 2. Characterization of as-synthesized Co-TiO_2 (12%) nanorods. (**a**) TEM image, (**b**) synchrotron X-ray diffraction (SXRD) pattern, (**c**) Co K-edge X-ray absorption near-edge structure (XANES) profiles, and (**d**) k^3-weighted Fourier transform of extended X-ray absorption fine structure (EXAFS) spectra of Co-TiO_2 nanorods and reference samples.

The electronic structures, oxidation states, and local bonding environments of the Co species in Co-TiO_2 nanorods were further investigated using Co K-edge X-ray absorption near-edge structure (XANES) and extended X-ray absorption fine structure (EXAFS) spectroscopies. The XANES spectra (Figure 2c) are consistent with previously reported findings, indicating that the oxidation state of Co in the as-synthesized Co-TiO_2 nanorods is predominantly Co^{2+}, distinct from the Co^0 state observed in Co foil [35]. Additionally, the corresponding EXAFS spectra (Figure 2d) of the as-synthesized Co-TiO_2 nanorods exhibit similar characteristics to prior studies [33], confirming that the Co species are primarily isolated Co atoms doped within the TiO_2 matrix, with no detectable contributions from metallic Co or Co oxides.

Prior to catalytic testing, the Co-TiO_2 nanorods were subjected to calcination at various temperatures (400–600 °C) in air for 2 h to remove surfactants from the colloidal nanocrystals and expose the active catalyst surface, yielding Co-TiO_2-x (where x denotes the oxidative calcination temperature). The calcined samples were then reduced in situ under reaction conditions (1 vol.% CO_2 + 4 vol.% H_2 + 95 vol.% N_2) at 450 °C before the study of CO_2 hydrogenation. It was observed that the nanorod morphology was largely preserved after calcination at 400 °C (Figure S3a). However, increasing the temperature to 500 °C resulted in pronounced aggregation, forming irregular nanosheets, with further coalescence observed following calcination at 600 °C (Figure S3b,c).

SXRD analysis suggests that these morphological changes are coupled with phase transitions in TiO_2. As shown in Figure S4, using the representative sample Co-TiO_2-500, the crystallinity of the catalyst is enhanced after calcination, and the brookite phase partially transforms into rutile and anatase. This transformation is evidenced

by the presence of the (110) diffraction peak of rutile at 10.93° (JCPDS file: 96-900-4143) and the (200) diffraction peak of anatase at 18.86° (JCPDS file: 96-900-8214). After reduction under the reaction gas, the intensity of the brookite peaks at 12.28° further diminished, indicating a continued phase transformation from brookite to rutile and anatase. Notably, no diffraction peaks corresponding to cobalt species such as CoO, Co_3O_4, or metallic Co were detected, even in the sample with a high Co doping level (12%) calcined at 500 °C (Figure S4). This indicates that, despite potential Co segregation from the TiO_2 matrix during the calcination process, the Co species do not form large grains with long-range crystalline order. We observed that higher calcination temperatures facilitated phase transitions, with a larger fraction of brookite converting into anatase and rutile when calcined at 600 °C. This process led to a more pronounced mixed-phase composition, as shown in Figure S5.

The CO_2 hydrogenation performance of each catalyst was evaluated over a temperature range of 250 to 500 °C in a fixed-bed reactor. Pure TiO_2 showed no measurable CO_2 conversion under these conditions. As shown in Figure 3a,b, the Co NPs/TiO_2 catalyst predominantly promotes CO_2 methanation, achieving a high CH_4 selectivity of 81.2% at 400 °C. In contrast, the Co-TiO_2-500 catalyst (12% Co) exhibits near-complete selectivity for CO across the entire temperature range. Specifically, at 450 °C and a CO_2 conversion of 40.9%, the CO selectivity reaches 98.7%. This shift in product distribution suggests that the Co-TiO_2 significantly suppresses the deep hydrogenation of CO to CH_4, favoring the production of CO as the primary hydrogenation product [36,37]. As shown in Figure 3c, the Co-TiO_2-500 catalyst maintains its high CO selectivity throughout a 10-h continuous reaction while preserving its morphology (Figure S6). This demonstrates the catalyst's robust stability under CO_2 hydrogenation conditions.

To investigate the effect of Co loading on catalytic performance, Co-TiO_2-500 catalysts with varying Co concentrations but constant Co mass (143 mg of 4.2% Co-TiO_2, 80 mg of 7.5% Co-TiO_2, and 50 mg of 12% Co-TiO_2) were tested. As shown in Figure S7, the catalytic activity and CO selectivity remained largely unaffected by changes in Co loading. However, calcination temperature was found to significantly influence performance, as illustrated in Figure S8. The Co-TiO_2-400 sample exhibits low activity, achieving a CO_2 conversion of only 8.9% at 400 °C. With increasing calcination temperature, CO_2 conversion rates improve, reaching 28.6% and 40.1% for the Co-TiO_2-500 and Co-TiO_2-600 samples, respectively. Simultaneously, the Co-TiO_2-600 catalyst shows a higher CH_4 selectivity (9.9% at 400 °C) compared to other calcined samples.

To elucidate the origins of the distinct catalytic activity and selectivity, EXAFS experiments were performed to monitor structural changes in Co-TiO_2 catalysts exposed to varying calcination temperatures. In the case of the Co-TiO_2-400 sample, the EXAFS spectrum shows a predominant, single Co–O shell, which is consistent with the as-synthesized nanorods, indicating that the atomically dispersed Co structure remains stable at 400 °C (Figure 4a). However, after the calcination at 500 °C in air, phase segregation of the Co species was observed. The Co K-edge EXAFS spectrum of Co-TiO_2-500 showed not only the Co–O pathway but also the presence of multiple shells at higher distance, R (Figure 4a). These shells correspond to Co–O–Co scattering pathways similar to those found in reference materials like Co_3O_4 and CoO [38,39]. Notably, the distinct second and third shells were observed that shifted to a higher R position than the Co–O–Co, suggesting the formation of Co–O–Ti structures due to high-temperature calcination, which implies strong bonding interactions between Co and the TiO_2 support [40,41]. These results suggest that Co species in the Co-TiO_2-500 primarily exist as CoO_x clusters on TiO_2. Moreover, the absence of observable cobalt oxide SXRD peaks, as previously mentioned, further supports the presence of small CoO_x clusters after oxidative calcination [42].

As shown in Figure 4b, the XANES spectrum of the reduced Co-TiO_2-500 sample (under CO_2 hydrogenation conditions) exhibits a decrease in white-line intensity and pre-edge features, indicating the reduction of Co species following the reaction process. The corresponding EXAFS analysis reveals the appearance of a small shell (Figure 4a), consistent with the Co–Co shell in Co foil, further confirming the reduction of CoO_x clusters. Although our ex-situ XAS experiments involved air exposure, which may have caused some oxidation during sample transfer, this subtle change observed in the XAS result suggests that reduced Co metallic clusters are likely the active species under CO_2 hydrogenation conditions. However, due to the small size of the Co clusters, no metallic Co peaks are detected in the SXRD pattern of the reduced Co-TiO_2-500 sample (Figure S4). In contrast, the Co NPs/TiO_2 sample clearly exhibits Co peaks in its XRD pattern (Figure S9), indicating larger Co nanoparticles.
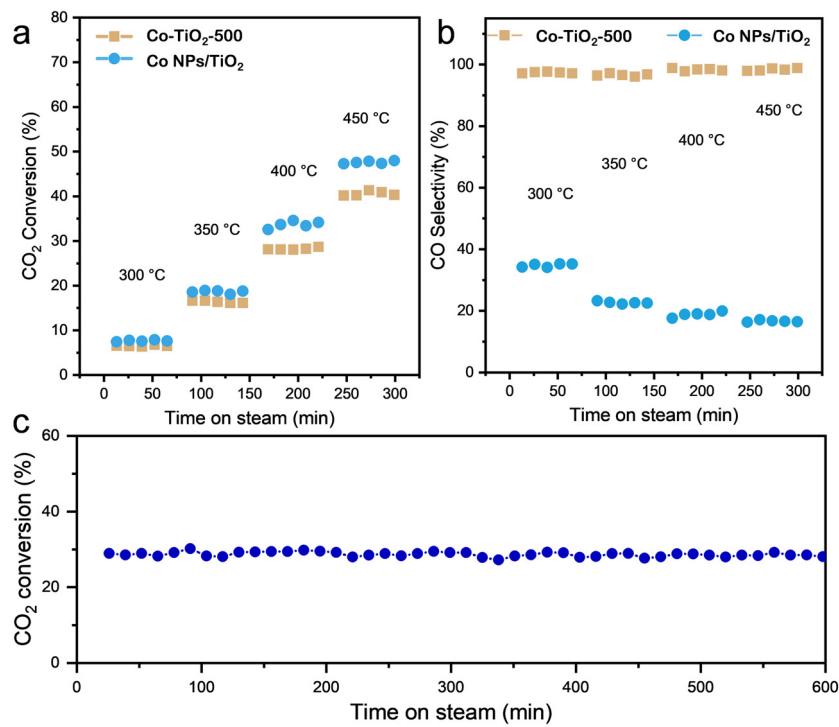
Figure 3. Catalytic performance of Co-TiO$_2$-500 (12%) and Co NPs/TiO$_2$ catalysts. (**a**) CO$_2$ conversion and (**b**) CO selectivity with time on stream at different temperatures. (**c**) Stability test for CO$_2$ hydrogenation over Co-TiO$_2$-500 (12%) catalyst. Reaction conditions: 1 vol % CO$_2$ + 4 vol % H$_2$ + 95 vol % N$_2$ with a space velocity of ~30,000 mL g$_{cat}^{-1}$ h^{-1} at ambient pressure, 400 °C.
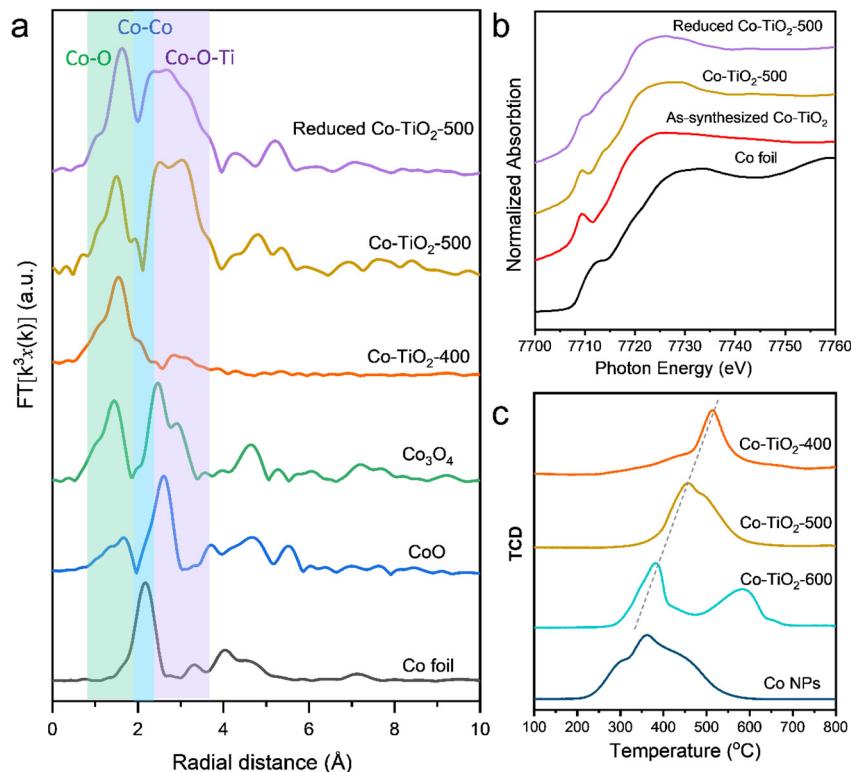
Figure 4. (**a**) k^3-weighted Fourier transform of EXAFS and (**b**) XANES spectra of the catalysts and reference samples. (**c**) H$_2$-TPR profiles of the catalysts.

The phase segregation of Co from the Co-TiO$_2$ support is a critical process in forming the desirable cluster structure. Unlike catalysts prepared through post-loading methods, the strong interaction between the TiO$_2$ support and Co species effectively limits the size of segregated Co, stabilizing them in a cluster state under CO$_2$

hydrogenation conditions and preventing their growth into larger particles. As a result, the Co-TiO$_2$-500 catalyst achieves near-unit selectivity for CO production. Even with further intensified Co segregation and potential aggregation into nanoparticles at 600 °C, the Co-TiO$_2$-600 catalyst continues to exhibit much higher selectivity for CO over CH$_4$ than Co NPs/TiO$_2$.

H$_2$ temperature-programmed reduction (H$_2$-TPR) was performed to investigate the interaction strength between Co and the TiO$_2$ support (Figure 4c). The Co NPs/TiO$_2$ catalyst exhibits a broad reduction peak between 200 and 500 °C. The peak at 200–350 °C can be attributed to the reduction of Co^{3+} to Co^{2+}, while the peak at 350–500 °C corresponds to the reduction of Co^{2+} to Co^0 (both in the surface and inner layers) [43]. In comparison, the Co reduction temperatures for the Co-TiO$_2$-400 catalyst are significantly higher, indicating the limited reducibility of single-site Co dopant in TiO$_2$ matrix [44]. The Co phase segregation from TiO$_2$ matrix, as demonstrated by the shift of the reduction peak to lower temperatures in Co-TiO$_2$-500 and Co-TiO$_2$-600 catalyst. In the Co-TiO$_2$-600 catalyst, a reduction peak around 390 °C, associated with CoO$_x$ reduction, is observed, along with an additional peak at 590 °C, which may be attributed to the formation of CoTiO$_3$ at high temperature [45].

In-situ diffuse reflectance infrared Fourier transform spectroscopy (DRIFTS) studies were conducted under steady-state CO$_2$ hydrogenation conditions on both Co-TiO$_2$-500 and Co NPs/TiO$_2$ catalysts to further understand the origins of their differing selectivities. As shown in Figure 5, upon introducing the reaction gas mixture (1 vol.% CO$_2$, 4 vol.% H$_2$, and 95 vol.% N$_2$) at 300 °C, symmetric OCO stretching of bicarbonate (HCO$_3^-$) and carbonate (CO$_3^{2-}$) species (1565 cm^{-1}, 1362 cm^{-1}) are immediately observed on the surfaces of both catalysts, indicating the interaction between CO$_2$ and hydroxyl groups on TiO$_2$ [46]. On the Co NPs/TiO$_2$ catalyst, a band at 1965 cm^{-1} appears, corresponding to multi-bound CO on hollow Co sites (Figure 5a, at 1 min). Simultaneously, methane formation is detected, evidenced by the emergence of C–H bonds (3013 cm^{-1}) [26]. As the reaction progressed, the intensities of the CO and C–H bands increase (Figure 5a, at 5–60 min), signifying an accelerating CO$_2$ methanation reaction. Additionally, weak and unchanged bands associated with formate (HCOO$^-$) species at 2962 and 2878 cm^{-1} are observed, suggesting that formate is not a reaction intermediate [47]. In contrast, when the same experiment was performed on Co-TiO$_2$ (Figure 5b), CO is detected as the primary product after the introduction of the reactant gas. However, no CO band appears in the DRIFTS spectrum, indicating that CO immediately desorbs from the catalyst as the final product. The absence of C–H bands further confirms that the hydrogenation of CO to methane is strongly suppressed in the Co-TiO$_2$ system (Figure 5b).

The in-situ DRIFTS results suggest that differences in CO interaction strength may account for the selectivity variations between the two catalysts. On Co-TiO$_2$, rapid CO desorption prevents further hydrogenation to methane, making CO the dominant product. Previous studies on Ni catalysts for CO$_2$ hydrogenation have shown that smaller Ni nanoparticles reduce CH$_4$ selectivity. Similarly, our previous work on NiP$_x$ demonstrated that phosphorization of Ni suppressed strong CO adsorption at the hollow sites of metallic Ni surfaces, thereby promoting high selectivity for CO [48]. In the present study, the weak CO adsorption is likely due to the lack of long-range lattice ordering in Co clusters, which eliminates multi-bound CO adsorption, as indicated by the DRIFTS results. In contrast, the Co NPs/TiO$_2$ catalyst, with its stronger CO adsorption, enables further hydrogenation of CO to CH$_4$. Additionally, while CoO$_x$ clusters are more easily reduced than atomically dispersed Co, they are still less reducible than surface Co in nanoparticles, which may limit their ability to activate H$_2$ for CO$_2$ methanation [49].
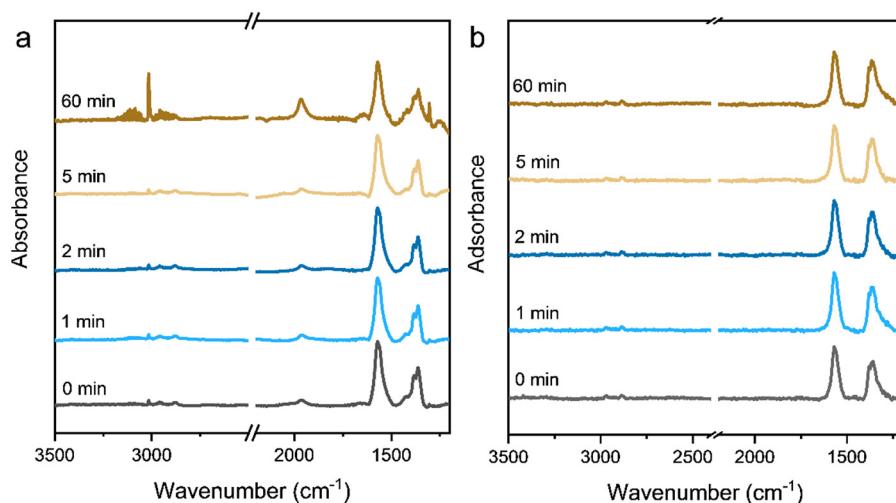

Figure 5. DRIFTS spectra of (**a**) Co NPs/TiO$_2$ and (**b**) Co-TiO$_2$-500 (12%) in CO$_2$ hydrogenation reaction gas with a flow rate of 10 mL min^{-1} at 300 °C for 0−60 min.

3. Conclusions

In summary, we have developed a phase segregation strategy to achieve high CO selectivity in CO_2 hydrogenation through the formation of Co clusters on TiO_2. A thorough structural analysis, including SXRD, XANES, and H_2-TPR, confirms that Co phase segregation from Co-TiO_2 occurs during high-temperature calcination, leading to the formation of small Co clusters. Compared to Co nanoparticles, our structural and catalytic performance data have demonstrated that Co clusters exhibit significantly higher selectivity for CO production. This improved activity and selectivity are attributed to their weaker interaction with the key reaction intermediate *CO, which reduces multi-bound CO adsorption, thereby suppressing methanation and greatly enhancing CO selectivity. We anticipate that this catalyst design strategy can be applied to develop highly efficient supported catalysts for selective CO_2 hydrogenation and other reactions.

Supplementary Materials: The additional data and information can be downloaded at: https://www.sciltp.com/journals/mi/2025/1/585/s1. Experimental section. Figure S1: TEM images of Co-TiO_2 and TiO_2 nanorods with different doping level. Figure S2: TEM images of as-synthesized Co NPs and Co NPs/TiO_2. Figure S3: TEM images of Co-TiO_2 after calcination at different temperature. Figure S4: XRD patterns of Co-TiO_2 after calcination at 500 °C and after catalytic reaction at 450 °C and the Bragg positions for anatase, brookite, and rutile TiO_2 respectively. Figure S5: XRD pattern of Co-TiO_2 after calcination at 600 °C and the Bragg positions for anatase and rutile TiO_2, respectively. Figure S6: TEM image of Co-TiO_2-500 after the stability test. Figure S7: Catalytic data of Co-TiO_2-500 with different doping level. Figure S8: Catalytic data of Co-TiO_2 treated with different calcination conditions. Figure S9: XRD patterns of Co NPs/TiO_2 after catalytic reaction at 400 °C and the Bragg positions for cobalt, anatase TiO_2, and rutile TiO_2. References [32–34,50] are cited in the supplementary materials.

Author Contributions: X.W.: conceptualization, methodology, investigation, data curation, validation, writing—original draft, writing—reviewing and editing; Y.C.: investigation, data curation, writing—reviewing and editing; Y.Z.: data curation, writing—reviewing and editing; L.Z.: data curation, writing—reviewing and editing; L.M.: methodology, data curation, writing—reviewing and editing; M.M.Y.: conceptualization, methodology, writing—reviewing and editing; S.Z.: conceptualization, methodology, resources, supervision, writing, reviewing, and editing. All authors have read and agreed to the published version of the manuscript.

Data Availability Statement: The data that support the findings of this study are available from the corresponding author, S.Z, upon reasonable request.

Conflicts of Interest: The authors declare no conflict of interest.

References

1. Ra, E.C.; Kim, K.Y.; Kim, E.H.; Lee, H.; An, K.; Lee, J.S. Recycling carbon dioxide through catalytic hydrogenation: recent key developments and perspectives. *ACS Catal.* **2020**, *10*, 11318–11345. https://doi.org/10.1021/acscatal.0c02930.

2. Tackett, B.M.; Gomez, E.; Chen, J.G., Net reduction of CO_2 via its thermocatalytic and electrocatalytic transformation reactions in standard and hybrid processes. *Nature Catal.* **2019**, *2*, 381–386. https://doi.org/10.1038/s41929-019-0266-y.

3. Roy, S.; Cherevotan, A.; Peter, S.C. Thermochemical CO_2 hydrogenation to single carbon products: scientific and technological challenges. *ACS Energy Lett.* **2018**, *3*, 1938–1966. https://doi.org/10.1021/acsenergylett.8b00740.

4. Ye, R.P.; Ding, J.; Gong, W.; Argyle, M.D.; Zhong, Q.; Wang, Y.; Russell, C.K.; Xu, Z.; Russell, A.G.; Li, Q.; et al. CO_2 hydrogenation to high-value products via heterogeneous catalysis. *Nat. Commun.* **2019**, *10*, 5698. https://doi.org/10.1038/s41467-019-13638-9.

5. Orege, J.I.; Wei, J.; Ge, Q.; Sun, J. Spinel-structured nanocatalysts: New opportunities for CO_2 hydrogenation to value-added chemicals. *Nano Today* **2023**, *51*, 101914. https://doi.org/10.1016/j.nantod.2023.101914.

6. Len, T.; Luque, R. Addressing the CO_2 challenge through thermocatalytic hydrogenation to carbon monoxide, methanol and methane. *Green Chem.* **2023**, *25*, 490–521. https://doi.org/10.1039/d2gc02900f.

7. Cheng, K.; Li, Y.; Kang, J.; Zhang, Q.; Wang, Y. Selectivity control by relay catalysis in CO and co_2 hydrogenation to multicarbon compounds. *Acc. Chem. Res.* **2024**, *57*, 714–725. https://doi.org/10.1021/acs.accounts.3c00734.

8. Yang, H.; Zhang, C.; Gao, P.; Wang, H.; Li, X.; Zhong, L.; Wei, W.; Sun, Y. A review of the catalytic hydrogenation of carbon dioxide into value-added hydrocarbons. *Catal. Sci. Technol.* **2017**, *7*, 4580–4598. https://doi.org/10.1039/C7CY01403A.

9. Liao, W.; Yue, M.; Chen, J.; Wang, Z.; Ding, J.; Xu, Y.; Bai, Y.; Liu, X.; Jia, A.; Huang, W.; et al. Decoupling the interfacial catalysis of CeO_2-supported rh catalysts tuned by CeO_2 morphology and Rh particle size in CO_2 hydrogenation. *ACS Catal.* **2023**, *13*, 5767–5779. https://doi.org/10.1021/acscatal.3c00512.

10. Karelovic, A.; Ruiz, P. CO_2 hydrogenation at low temperature over Rh/γ-Al_2O_3 catalysts: Effect of the metal particle size

on catalytic performances and reaction mechanism. *Appl. Catal. B Environ.* **2012**, *113–114*, 237–249. https://doi.org/10.1016/j.apcatb.2011.11.043.

11. An, Z.; Ma, N.; Xu, Y.; Yang, H.; Zhao, H.; Wu, L.; Tan, L.; Zou, C.; Meng, F.; Zhang, B.; et al. Shape dependency of CO_2 hydrogenation on ceria supported singly dispersed Ru catalysts. *J. Catal.* **2024**, *429*, 115245. https://doi.org/10.1016/j.jcat.2023.115245.

12. Chen, M.; Liu, L.; Chen, X.; Qin, X.; Li, K.; Zhang, J.; Bao, X.; Ma, L.; Zhang, C. Effects of Ru particle size over TiO_2 on the catalytic performance of CO_2 hydrogenation. *Appl. Surf. Sci.* **2024**, *654*, 159460. https://doi.org/10.1016/j.apsusc.2024.159460.

13. Li, S.; Xu, Y.; Wang, H.; Teng, B.; Liu, Q.; Li, Q.; Xu, L.; Liu, X.; Lu, J. Tuning the CO_2 hydrogenation selectivity of rhodium single-atom catalysts on zirconium dioxide with alkali ions. *Angew. Chem. Int. Ed.* **2023**, *62*, e202218167. https://doi.org/10.1002/anie.202218167.

14. Galhardo, T.S.; Braga, A.H.; Arpini, B.H.; Szanyi, J.; Goncalves, R.V.; Zornio, B.F.; Miranda, C.R.; Rossi, L.M. Optimizing active sites for high CO selectivity during CO_2 hydrogenation over supported nickel catalysts. *J. Am. Chem. Soc.* **2021**, *143*, 4268–4280. https://doi.org/10.1021/jacs.0c12689.

15. Vogt, C.; Groeneveld, E.; Kamsma, G.; Nachtegaal, M.; Lu, L.; Kiely, C.J.; Berben, P.H.; Meirer, F.; Weckhuysen, B.M. Unravelling structure sensitivity in CO_2 hydrogenation over nickel. *Nat. Catal.* **2018**, *1*, 127–134. https://doi.org/10.1038/s41929-017-0016-y.

16. Cao, F.; Song, Z.; Zhang, Z.; Xiao, Y.S.; Zhang, M.; Hu, X.; Liu, Z.W.; Qu, Y. Size-controlled synthesis of Pd nanocatalysts on defect-engineered CeO_2 for CO_2 hydrogenation. *ACS Appl. Mater. Interfaces* **2021**, *13*, 24957–24965. https://doi.org/10.1021/acsami.1c05722.

17. Simons, J.F.M.; de Heer, T.J.; van de Poll, R.C.J.; Muravev, V.; Kosinov, N.; Hensen, E.J.M. Structure sensitivity of CO_2 hydrogenation on Ni revisited. *J. Am. Chem. Soc.* **2023**, *145*, 20289–20301. https://doi.org/10.1021/jacs.3c04284.

18. Zhang, R.; Wang, X.; Wang, K.; Wang, H.; Song, S.; Zhang, H. Effects of metal size on supported catalysts for CO_2 hydrogenation. *Mater. Chem. Front.* **2023**, *7*, 6411–6426. https://doi.org/10.1039/d3qm00384a.

19. Adhikari, D.; Whitcomb, C.A.; Zhang, W.; Zhang, S.; Davis, R.J. Revisiting the influence of Ni particle size on the hydrogenation of CO_2 to CH_4 over Ni/CeO_2. *J. Catal.* **2024**, *438*, 115708. https://doi.org/10.1016/j.jcat.2024.115708.

20. Niu, K.; Chen, L.; Rosen, J.; Björk, J. CO_2 hydrogenation with high selectivity by single Bi atoms on MXenes enabled by a concerted mechanism. *ACS Catal.* **2024**, *14*, 1824–1833. https://doi.org/10.1021/acscatal.3c04480.

21. Swallow, J.E.N.; Jones, E.S.; Head, A.R.; Gibson, J.S.; David, R.B.; Fraser, M.W.; van Spronsen, M.A.; Xu, S.; Held, G.; Eren, B.; et al. Revealing the role of CO during CO_2 hydrogenation on Cu surfaces with In Situ soft X-Ray spectroscopy. *J. Am. Chem. Soc.* **2023**, *145*, 6730–6740. https://doi.org/10.1021/jacs.2c12728.

22. Kattel, S.; Liu, P.; Chen, J.G. Tuning selectivity of CO_2 hydrogenation reactions at the metal/oxide interface. *J. Am. Chem. Soc.* **2017**, *139*, 9739–9754. https://doi.org/10.1021/jacs.7b05362.

23. Zhang, J.; Yang, Y.; Liu, J.; Xiong, B. Mechanistic understanding of CO_2 hydrogenation to methane over Ni/CeO_2 catalyst. *Appl. Surf. Sci.* **2021**, *558*, 149866. https://doi.org/10.1016/j.apsusc.2021.149866.

24. Yang Lim, J.; McGregor, J.; Sederman, A.J.; Dennis, J.S. Kinetic studies of CO_2 methanation over a $Ni/\gamma-Al_2O_3$ catalyst using a batch reactor. *Chem. Eng. Sci.* **2016**, *141*, 28–45. https://doi.org/10.1016/j.ces.2015.10.026.

25. Song, J.; Chen, B.; Bian, J.; Cai, Y.; Ali, S.; Cai, D.; Zheng, B.; Huang, J.; Zhan, G. $ZnZrO_x$ nanoparticles derived from metal–organic frameworks as superior catalysts to boost CO_2 hydrogenation to methanol. *ACS Appl. Nano Mater.* **2024**, *7*, 19677–19687. https://doi.org/10.1021/acsanm.4c03801.

26. Li, K.; Li, X.; Li, L.; Chang, X.; Wu, S.; Yang, C.; Song, X.; Zhao, Z.-J.; Gong, J. Nature of catalytic behavior of cobalt oxides for CO_2 hydrogenation. *JACS Au* **2023**, *3*, 508–515. https://doi.org/10.1021/jacsau.2c00632.

27. Struijs, J.J.C.; Muravev, V.; Verheijen, M.A.; Hensen, E.J.M.; Kosinov, N. Ceria-supported cobalt catalyst for low-temperature methanation at low partial pressures of CO_2. *Angew. Chem. Int. Ed. Engl.* **2023**, *62*, e202214864. https://doi.org/10.1002/anie.202214864.

28. Wang, L.; Guan, E.; Wang, Y.; Wang, L.; Gong, Z.; Cui, Y.; Meng, X.; Gates, B.C.; Xiao, F.-S. Silica accelerates the selective hydrogenation of CO_2 to methanol on cobalt catalysts. *Nat. Commun.* **2020**, *11*, 1033. https://doi.org/10.1038/s41467-020-14817-9.

29. Rahmati, M.; Safdari, M.S.; Fletcher, T.H.; Argyle, M.D.; Bartholomew, C.H. Chemical and thermal sintering of supported metals with emphasis on cobalt catalysts during Fischer-Tropsch synthesis. *Chem. Rev.* **2020**, *120*, 4455–4533. https://doi.org/10.1021/acs.chemrev.9b00417.

30. Liu, S.; He, Y.; Fu, W.; Chen, J.; Ren, J.; Liao, L.; Sun, R.; Tang, Z.; Mebrahtu, C.; Zeng, F. Hetero-site cobalt catalysts for higher alcohols synthesis by CO_2 hydrogenation: A review. *J. CO_2 Util.* **2023**, *67*, 102322. https://doi.org/10.1016/j.jcou.2022.102322.

31. Miyazaki, R.; Belthle, K.S.; Tüysüz, H.; Foppa, L.; Scheffler, M. Materials genes of CO_2 hydrogenation on supported cobalt catalysts: An artificial intelligence approach integrating theoretical and experimental data. *J. Am. Chem. Soc.* **2024**,

146, 5433–5444. https://doi.org/10.1021/jacs.3c12984.

32. Zhang, Z.; Wu, Q.; Johnson, G.; Ye, Y.; Li, X.; Li, N.; Cui, M.; Lee, J.D.; Liu, C.; Zhao, S.; et al. Generalized synthetic strategy for transition-metal-doped brookite-phase TiO_2 nanorods. *J. Am. Chem. Soc.* **2019**, *141*, 16548–16552. https://doi.org/10.1021/jacs.9b06389.

33. Liu, C.; Qian, J.; Ye, Y.; Zhou, H.; Sun, C.-J.; Sheehan, C.; Zhang, Z.; Wan, G.; Liu, Y.-S.; Guo, J.; et al. Oxygen evolution reaction over catalytic single-site Co in a well-defined brookite TiO_2 nanorod surface. *Nat. Catal.* **2021**, *4*, 36–45. https://doi.org/10.1038/s41929-020-00550-5.

34. Wu, L.; Li, Q.; Wu, C.H.; Zhu, H.; Mendoza-Garcia, A.; Shen, B.; Guo, J.; Sun, S. Stable Cobalt nanoparticles and their monolayer array as an efficient electrocatalyst for oxygen evolution reaction. *J. Am. Chem. Soc.* **2015**, *137*, 7071–7074. https://doi.org/10.1021/jacs.5b04142.

35. Liu, Q.; Jiang, Y.; Yan, W.; Sun, Z.; Pan, Z.; Yao, T.; Wu, Z.; Wei, S. Co-doped rutile TiO_2-δthin films studied by XANES and first principles calculations. *J. Phys. Conf. Ser.* **2009**, *190*, 012107. https://doi.org/10.1088/1742-6596/190/1/012107.

36. Bao, S.; Yang, L.; Fu, H.; Qu, X.; Zheng, S. Fine Ru-Ru_2P heterostructure enables highly active and selective CO_2 hydrogenation to CO. *ACS Catal.* **2024**, *14*, 18134–18144. https://pubs.acs.org/doi/full/10.1021/acscatal.4c05369.

37. Zhou, X.; Price, G.A.; Sunley, G.J.; Copéret, C. Small cobalt nanoparticles favor reverse water-gas shift reaction over methanation under CO_2 hydrogenation conditions. *Angew. Chem. Int. Ed. Engl.* **2023**, *62*, e202314274. https://doi.org/10.1002/ange.202314274.

38. Yan, Y.; Liu, C.; Jian, H.; Cheng, X.; Hu, T.; Wang, D.; Shang, L.; Chen, G.; Schaaf, P.; Wang, X.; et al. Substitutionally dispersed high-oxidation CoO_x clusters in the lattice of rutile TiO_2 triggering efficient Co-Ti cooperative catalytic centers for oxygen evolution reactions. *Adv. Funct. Mater.* **2020**, *31*, 2009610. https://doi.org/10.1002/adfm.202009610.

39. Zhou, T.; Xu, W.; Zhang, N.; Du, Z.; Zhong, C.; Yan, W.; Ju, H.; Chu, W.; Jiang, H.; Wu, C.; et al. Ultrathin cobalt oxide layers as electrocatalysts for high-performance flexible Zn-Air batteries. *Adv. Mater.* **2019**, *31*, e1807468. https://doi.org/10.1002/adma.201807468.

40. Mori, K.; Jida, H.; Kuwahara, Y.; Yamashita, H. CoO_x-decorated CeO_2 heterostructures: Effects of morphology on their catalytic properties in diesel soot combustion. *Nanoscale* **2020**, *12*, 1779–1789. https://doi.org/10.1039/c9nr08899g.

41. Wang, X.; Du, L.Y.; Du, M.; Ma, C.; Zeng, J.; Jia, C.J.; Si, R. Catalytically active ceria-supported cobalt-manganese oxide nanocatalysts for oxidation of carbon monoxide. *Phys. Chem. Chem. Phys.* **2017**, *19*, 14533–14542. https://doi.org/10.1039/c7cp02004j.

42. Savereide, L.; Gosavi, A.; Hicks, K.E.; Notestein, J.M. Identifying properties of low-loaded CoO_x/CeO_2 via X-ray absorption spectroscopy for NO reduction by CO. *J. Catal.* **2020**, *381*, 355–362. https://doi.org/10.1016/j.jcat.2019.11.016.

43. Li, J.; Lu, G.; Wu, G.; Mao, D.; Guo, Y.; Wang, Y.; Guo, Y. Effect of TiO_2 crystal structure on the catalytic performance of Co_3O_4/TiO_2 catalyst for low-temperature CO oxidation. *Catal. Sci. Technol.* **2014**, *4*, 1268–1275. https://doi.org/10.1039/c3cy01004j.

44. Platero, F.; Todorova, S.; Aoudjera, L.; Michelin, L.; Lebeau, B.; Blin, J.L.; Holgado, J.P.; Caballero, A.; Colon, G. Cobalt stabilization through mesopore confinement on TiO_2 support for Fischer-Tropsch reaction. *ACS Appl. Energy Mater.* **2023**, *6*, 9475–9486. https://doi.org/10.1021/acsaem.3c01432.

45. Lima, T.M.; Castelblanco, W.N.; Rodrigues, A.D.; Roncolatto, R.E.; Martins, L.; Urquieta-González, E.A. CO oxidation over Co-catalysts supported on silica-titania—The effects of the catalyst preparation method and the amount of incorporated Ti on the formation of more active Co^{3+} species. *Appl. Catal. A Gen.* **2018**, *565*, 152–162. https://doi.org/10.1016/j.apcata.2018.08.006.

46. Li, W.H.; Zhang, G.H.; Jiang, X.; Liu, Y.; Zhu, J.; Ding, F.S.; Liu, Z.M.; Guo, X.W.; Song, C.S. CO_2 hydrogenation on unpromoted and M-promoted Co/TiO_2 catalysts (M = Zr, K, Cs): Effects of crystal phase of supports and metal-support interaction on tuning product distribution. *ACS Catal.* **2019**, *9*, 2739–2751. https://doi.org/10.1021/acscatal.8b04720.

47. Deng, K.X.; Lin, L.L.; Rui, N.; Vovchok, D.; Zhang, F.; Zhang, S.H.; Senanayake, S.D.; Kim, T.; Rodriguez, J.A. Studies of CO_2 hydrogenation over cobalt/ceria catalysts with in situ characterization: The effect of cobalt loading and metal-support interactions on the catalytic activity. *Catal. Sci. Technol.* **2020**, *10*, 6468–6482. https://doi.org/10.1039/d0cy00962h.

48. Wei, X.; Johnson, G.; Ye, Y.; Cui, M.; Yu, S.-W.; Ran, Y.; Cai, J.; Liu, Z.; Chen, X.; Gao, W.; et al. Surfactants used in colloidal synthesis modulate Ni nanoparticle surface evolution for selective CO_2 hydrogenation. *J. Am. Chem. Soc.* **2023**, *145*, 14298–14306. https://doi.org/10.1021/jacs.3c02739.

49. Li, X.Y.; Lin, J.; Li, L.; Huang, Y.K.; Pan, X.L.; Collins, S.E.; Ren, Y.J.; Su, Y.; Kang, L.L.; Liu, X.Y.; et al. Controlling CO_2 hydrogenation selectivity by metal-supported electron transfer. *Angew. Chem.-Int. Ed.* **2020**, *8*, 19983–19989. https://doi.org/10.1002/anie.202003847.

50. Ravel, B.; Newville, M. ATHENA, ARTEMIS, HEPHAESTUS: data analysis for X-ray absorption spectroscopy using IFEFFIT. *J. Synchrotron Radiat.* **2005**, *12*, 537–541

Article

Intrinsically Multi-Color Device Based on Dynamic Cooperation of Molecular Switches and Metal Ions

Min Li, Shuo Wang *, Ruipeng Shen, Yigui Xie, Yu-Mo Zhang, and Sean Xiao-An Zhang *

State Key Laboratory of Supramolecular Structure and Materials, College of Chemistry, Jilin University, Changchun 130012, China
* Correspondence: wangshuo@jlu.edu.cn (S.W.); seanzhang@jlu.edu.cn (S.X.-A.Z.)

Abstract: Multi-color electrochromic material is a long-expected and extremely challenging material, which is important for electrochromic technology to be applied in adaptive camouflage, augmented reality, transparent display, etc. Here, an intrinsically multi-color indirect-electrochromic material based on supramolecular interactions of unusual multi-state molecular switch and metal ion was developed, combining the advantages of multi-state of molecular switch and chemical stability of metal ion. Related prototype device, with transparent intrinsic colorless, magenta, cyan and various mixed colors, have been explored and demonstrated. The mechanism was based on the dynamic coordination of multiple metal ions and single-molecular-dual-switches within fragile supramolecular clusters. Wherein, the color and lightness could be controlled simply by the bias applied, with abilities such as transmittance change (41%), coloring time (7.8 s), coloration efficiency (>100 cm^2/C), and reversibility (>600 test cycles, no abnormal changes). The prototype device was fabricated to show the potential to be used in low energy consumption display.
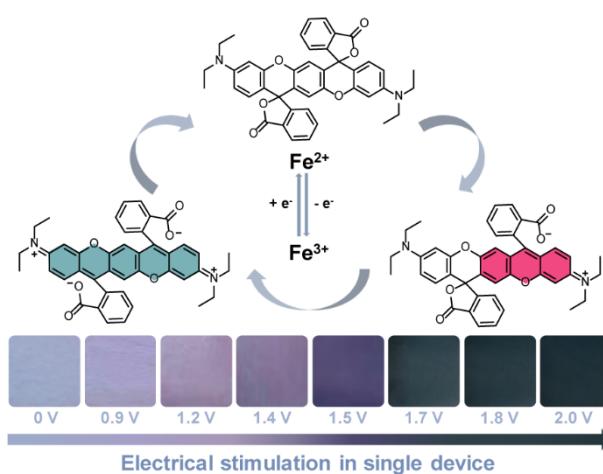
Keywords: electrochromism; intrinsic multi-color device; leuco dye; metal ion; dynamic coordination

Electrical stimulation in single device

1. Introduction

Electrochromic (EC) materials have the unique property of optical change after redox reaction [1]. They have been partially applied in scenarios like rearview mirror and smart window in cars and airplanes [2,3]. Compared to the common single-color change, EC materials with multi-color change are very beneficial and required. The emerging multi-color ability is becoming more and more important for EC materials to be applied in broader fields, such as adaptive camouflage [4–9], augmented reality [10,11], transparent display [12–15], optical information encryption [16] and so on. Related multi-color electrochromic device (ECD) has been extensively studied and developed so far. Many of them were developed through the combination of multiple kinds of single-color EC materials or by lateral/vertical arrangement of them. Hereinto, multi-color EC materials have broad development prospects in related ECD. These materials show multi-color under different bias, obviously no complex combination or arrangement of single-color EC materials are needed to develop more ideal multi-color ECD.

Known multi-color EC materials need multi-redox states to cause structural change to result in multi-color, researchers developed them so far through the following ways. For single compound, many pleasant colors were developed by finely designed molecules with multi-redox-state. Impressive various multi-color EC materials were developed through this way, like viologen (derivative) [17–20], vanadium oxide [12,21] and methyl ketone (derivative) [22]. Through the tailoring of different EC blocks, the ECDs also show multi-color electrochromism of the blocks, like the copolymerization of triphenylamine and viologen [23], the co-assembling of tungsten oxide and vanadium oxide [24]. This method cleverly combines the advantages of different EC blocks. Besides, by

constructing the trilayer film structure driven by discharging/self-charging mechanism, intrinsic multi-color electrochromism can also be realized [25]. And the hybrid materials of metal ion and ligand have also realized intrinsic multi-color electrochromism. It's realized through the mixture of different metal ion centers like Os^{2+}, Co^{2+}, Fe^{2+}, Ru^{2+} and pyridine derivatives [26,27], or by forming supramolecular polymer of them [7]. Wherein multi metal ion centers offer multi states of metal-to-ligand charge transfer (MLCT) to realize multi-color electrochromism. In addition, interesting structural color has also been induced into ECD to realize multi-color, like the localized surface plasmon resonance (LSPR) of silver nanoparticles [28,29] and Fabry-Perot (F-P) nanocavity of metal tungsten [30]. Structural color provided novel perspective of EC mechanism and materials with rich colors.

It should acknowledge that these preliminary works have demonstrated various useful methods and unique multi-color transformation functional attributes. They have greatly expanded the available methods and development prospects in this field. However, ideal multi-color EC materials are still challenging due to the traditional ways' technical barriers such as EC mechanisms, complex synthesis and fabrication processes. Development of a simple and effective method to achieve high molar absorptivity and multiple colors of organic small molecules for the preparation of more ideal EC materials has been long-awaited.

Based on this challenge, we developed herein a new EC material with intrinsic multi-color, based on dynamic coordination of multiple ions and multi-state-molecular-switches. Unlike common direct EC materials, their chromophores undergo direct color change due to redox reactions, the electrochromism in this work is indirect way of color change. Herein, multi-valance metal ion was used as redox center to provide multi-valence state. Meanwhile, the relevant color switching unit is the cis-ABPX with multi-color states, which has recently been discovered and demonstrated by admirable research groups [31,32] and possesses unique other properties. The color change of this EC system is introduced indirectly by redox of metal ions first and then dynamic coordination of multiple related metal ions with the cis-ABPXs. This special design brought many advantages, the redox center was inexpensive and chemically very stable, and the color-switching unit was easily synthesized and modified. In addition, the EC system is endowed with high molar absorbance coefficient cis-ABPX, thereby achieving high coloration efficiency (CE). Here, adjustable Fe^{2+} was used as an example, to act as the expected redox center to dynamically coordinate with the dual-switchable rhodamine derivative cis-ABPX. The colors of the EC system could be finely regulated under different bias. Compared with previous work, this work realized multi-color electrochromism within single molecular switch, and the multiple colors and their absorption intensity could be precisely controlled at the same time by voltage in this work.

The color regulation of cis-ABPX was systematically explored, and how to distinguish different color states from chemical stimulus to electrical stimulus was demonstrated. Then its EC mechanism based on dynamic cooperation was given. Thereafter, by optimizing the fabrication process of ECDs, prototype ECDs were fabricated to demonstrate their multi-color ability. The ECD was possible to switch between colorless, magenta, cyan and various mixed colors with different metal ions and cis-ABPXs condensed states. Those intrinsic color changes were purely realized in single pixel of above complex, without traditional pixel arrangement in vertical or lateral way. The success and gains from this exploration based on dynamically coordinated single-molecule multicolor changes may inspire and motivate more researchers to adopt similar strategies to accelerate the development of intrinsic EC materials, and future application in transparent displays and many other low-energy application scenarios.

2. Experimental Part

2.1. Materials and Instruments

4-diethylamino-ketoacid (99%), methyl sulfonic acid (MSA, 99%), anhydrous sodium carbonate (A.R.), anhydrous sodium sulfate (A.R.), $FeCl_3$ (95%), $FeCl_2$ (99%), trifluoroacetic acid (TFA, 99%), p-benzoquinone (BQ, 98%), hydroquinone (HBQ, 99%), propylene carbonate (PC, 99.5%) were purchased from Energy Chemical Company (Shanghai, China). Polymethyl methacrylate (PMMA, *M*w: ~100,000), chromatographic pure acetonitrile, dichloromethane, methanol, tetrahydrofuran (THF) and tetrabutylammonium hexafluorophosphate (TBAPF$_6$, 98%) were purchased from Aladdin Reagent. Trichloromethane was purchased from China National Pharmaceutical Group Corporation. TBAPF$_6$ was recrystallized three times in ethanol and dried under vacuum overnight at 80 °C.

^{1}H NMR spectra were obtained on a AS 400 400M (Q.NE Instruments Ltd., Wuhan, China) and referenced to tetramethyl silane (TMS) as an internal standard. Ultraviolet-visible absorption spectra were obtained on the double-beam UV-2600i spectrophotometer (Shimadzu, Suzhou, China) or SPECORD 210 PLUS (Analytikjena, Jena, Germany). High-resolution mass spectra (HRMS) were measured on Agilent 1290-microTOF-Q II. MALDI-

TOF mass spectrometry were measured on a Brucker Autoflex speed TOF. Fourier Transform infrared spectroscopy (FT-IR) was measured on a Vertex 80/80 V FT-IR spectrometer, which used LN-MCT Mid DC detector in the range of 4000–400 cm^{-1} wave numbers. Unless otherwise mentioned, the electrochemical experiments were measured using the SP-150 Electrochemical Workstation (Bio-Logic) at room temperature.

2.2. Synthesis of cis-ABPX

cis-ABPX was synthesized according to Uchiyama et al.'s work [30]. The synthesis route of cis-ABPX is shown as Figure S1. Both 4-diethylamino-ketoacid (620 mg, 2.0 mmol) and HBQ (110 mg, 1.0 mmol) were placed in a 15 mL pressure tube. MSA (5 mL) was added and heated at 110 °C for 4 h. After cooling to room temperature, the reaction mixture was added to saturated sodium carbonate aqueous solution, then the solution was extracted with CH_2Cl_2 for 3 times, and then dried with anhydrous sodium sulfate. The solvent was evaporated to form dark purple solid. The crude product was purified by silica gel chromatography and eluted with CH_2Cl_2/MeOH (100:1) to obtain product, which was pink powder, with yield of 24.0%. The product was characterized by nuclear magnetic resonance (NMR) spectroscopy (Figure S2), high-resolution mass spectrometry (HRMS, Figure S3) and MALDI-TOF mass spectrometry (Figure S4). More details about NMR and mass spectrometry are provided in supporting information.

2.3. Preparation of the Solution

The electrochromic solution was a mixture of cis-ABPX (13.28 mg), $FeCl_2$ (6.3 mg), TBAPF$_6$ (75 mg), PMMA (150 mg) and PC (75 mg) in 1.0 mL THF and was stirred for 2 h. The conducting solution was a mixture of PMMA (1.94 g), TBAPF$_6$ (0.97 g) and PC (0.97 g) in 15 mL acetonitrile and was stirred for 2 h. The ion storage solution was a mixture of PMMA (1.94 g), TBAPF$_6$ (0.97 g), PC (0.97 g), BQ (0.16 g) and HBQ (0.33 g) in 30 mL acetonitrile and was stirred for 2 h.

2.4. Device Fabrication

The transparent electrochromic film was spin-coated (2000 r.p.m., 15 s) on the first ITO electrode. The ion storage film was coated on the second ITO electrode and the height of the scraper was set to 1300 μm and 1400 μm, respectively. The conducting film was then coated on the top of the ion storage film and the height of the scraper was set to 1500 μm, 1600 μm, 1700 μm, 1700 μm, 1800 μm, 1800 μm, respectively. Both ITO electrodes were assembled together.

2.5. Visible Absorption Spectrum Test

All in-situ absorption spectra during the voltage stimulation were tested in a cell of in situ three-electrode system under room temperature (25 °C), with TBAPF$_6$ as the electrolyte. Air was used as reference for the measurements, and the optical path of the sample cell was 1 mm.

2.6. Calculation of the CE and the Response Time

CE is defined as the change in absorbance (ΔA) obtained by injecting a certain amount of charge per unit area. The CE herein was tested in ECD and calculated according to the formula: CE = ΔA/Q. Air is used as a reference for absorption measurements. In Figure 4c, the conversion of A and T was achieved according to the formula: A = Lg (1/T).

The response time denotes as the time required for an electrochromic material or device to complete 90% of its optical modulation. For Figure 4c, with "bleached state to colored state" switching, the response time can be divided into coloring time (t_1) and fading time (t_2).

3. Results and Discussion

To realize intrinsic multi-color electrochromism in single pixel, the rhodamine derivative cis-ABPX was chosen as the coloring unit in our EC system. cis-ABPX is a sensitive molecular switch, and due to its molecular tautomerization, it has color changing in response to external stimuli, including protonation effect, photochromism and piezochromism [33]. Two lactone rings of cis-ABPX brought it multi-state ability, under the treatment of proton (TFA) in the solution, several absorption peaks appeared due to the opening of two spirolactone rings (Figure 1a), the spectral change here was in agreement with the pioneers [30], and its structure change was proved by ^{1}H-NMR (Figure S5). cis-ABPX formed monocation to show magenta under the stimulation of proton, and then formed dication to show cyan under more amount of proton (Figure 1a). It's always more difficult to form

dication than monocation of it, which meant its state/color could be distinguished by the amount of proton. But cis-ABPX needed extreme amount of proton to form dication to show cyan, even 600,000 eq. was needed to reach maximum coloration.
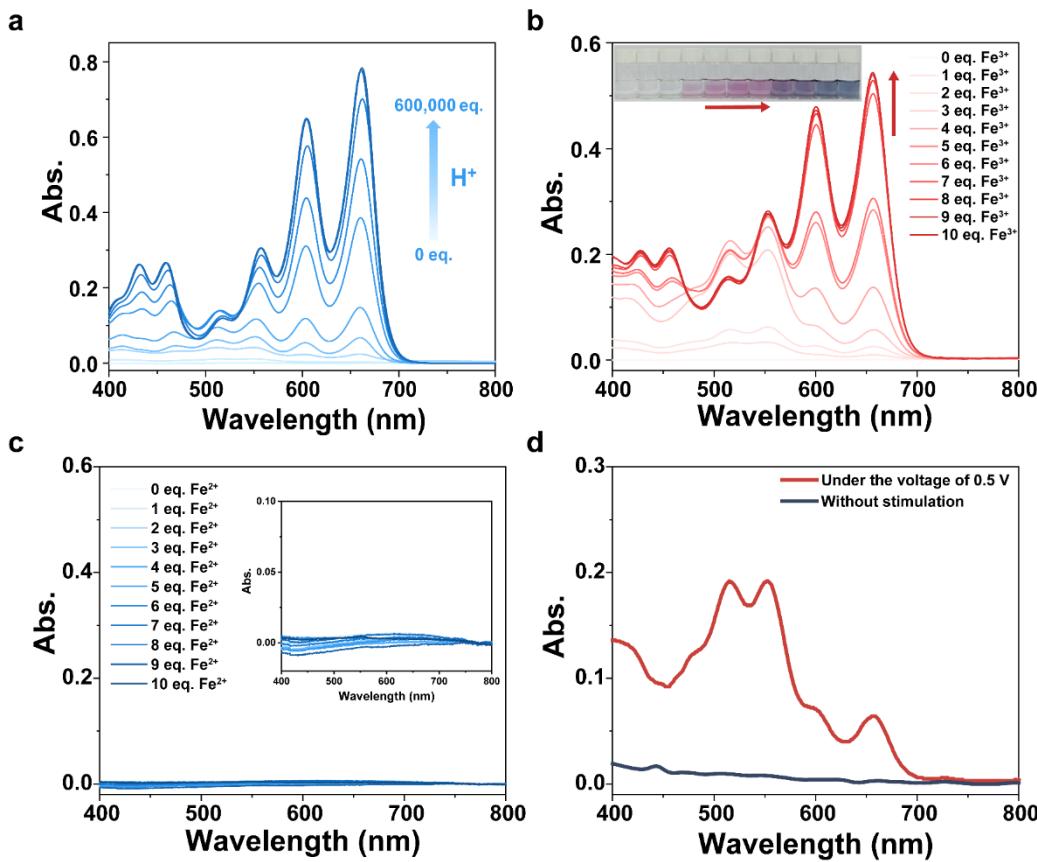

Figure 1. Feasibility of electrochromism. (**a**) Absorption spectra of cis-ABPX treated with various equivalents of TFA. The concentration of cis-ABPX was 1.0×10^{-5} mol/L in CHCl₃. (**b**) Absorption spectra and corresponding photos (inset) of cis-ABPX treated with different equivalent FeCl₃. The concentration of cis-ABPX was 1.0×10^{-5} mol/L in CH₂Cl₂+CH₃CN (*v:v* = 1:1). (**c**) Absorption spectra of cis-ABPX with various amounts of Fe^{2+}. The concentration of the solution is 1.0×10^{-5} mol/L in CH₂Cl₂+CH₃CN (*v:v* = 1:1). (**d**) The absorption spectra of "cis-ABPX & FeCl₂" without stimulation (dark blue curve) and under the voltage of 0.5 V (red curve). The concentration of cis-ABPX and FeCl₂ were 1.0×10^{-4} mol/L in CH₂Cl₂+CH₃CN (*v:v* = 1:1).

Further, the titration experiment of cis-ABPX & Fe^{3+} was performed (Figure 1b), to find Fe^{3+} could also distinguish the colored state of cis-ABPX. The color of the solution changed from colorless to magenta, then to purple and gradually to cyan with the increasing equivalent of Fe^{3+}. And surprisingly only 9 eq. of Fe^{3+} was needed to reach maximum coloration. The change progress of the absorption and fluorescence spectra were similar with the proton stimulation one (Figures 1a and S6), which indicated the lactone rings of cis-ABPX were gradually opened through coordination with Fe^{3+}. But Fe^{2+} could not achieve similar effect, the color of the mixture solution of Fe^{2+} & cis-ABPX was colorless (Figure 1c). And the results of infrared (IR) spectroscopy experiment (Figure S7) demonstrated the interaction of cis-ABPX and Fe^{3+} further. cis-ABPX had an alkane amine C-N stretching vibration peak of at 1072cm⁻¹. The C-O-C stretching vibration peak of xanthene at 1207 cm⁻¹ and the C-C stretching vibration peak of alkane at 1239 cm⁻¹. Compared with the IR spectra of cis-ABPX or cis-ABPX & Fe^{2+}, cis-ABPX & Fe^{3+} had an asymmetric C-O-C stretching vibration peak at 1105 cm⁻¹. The C-N stretching vibration peak of the tertiary amine at 1304 cm⁻¹ disappeared and the C=N stretching vibration peak appeared at 1649 cm⁻¹. Due to the influence of O⁻, the stretching vibration of carboxylic acid C=O moved towards the low wave number (1717 cm⁻¹). Besides, the coordination numbers have been tested by Jobs' plot (Figure S8). It can be found that the coordination ratio between cis-ABPX⁺ & FeCl₃ was ca. 2:3 and cis-ABPX²⁺ & FeCl₃ was ca. 1:4. In our assumption, multiple Fe^{3+} surrounded cis-ABPX⁺ and cis-ABPX²⁺, forming an dynamically ionic stabilized molecular aggregate (possibly a fragile "supramolecular cluster/cage") [34], which not only can stabilize the configuration of cis-ABPX⁺ and cis-ABPX²⁺, but also can reduce their electrostatic repulsion. Unfortunately, due to this dynamic fragility, such supramolecular aggregates can easily undergo dynamic structural changes, it is

difficult to capture quickly by suitable testing equipment, so the inference of the dynamic structure of the "supramolecular cluster/cage" is still in the theoretical stage. We expect more researchers to join us in solving this technical problem, improve the capture speed and progress of the test instrument, and have a deeper understanding of the material structure. These results all indicated that Fe^{3+} could interact with cis-ABPX and open the lactone ring of it to change the spectra and color through the coordination interaction.

There existed difference between the interaction of Fe^{3+} & cis-ABPX and Fe^{2+} & cis-ABPX, which indicated the colors of the mixture solution of Fe^{n+} & cis-ABPX may be regulated through the electrical stimulation to develop indirect EC material. The in-situ spectro-electro-chemistry test was performed. The mixture solution of cis-ABPX and Fe^{2+} showed change in visible spectrum after treated with 0.5 V (Figure 1d), but this spectrum change was not observed in their individual solution (Figure S9). The spectra of the mixture solution demonstrated the feasibility of electrochromism here.

The states of cis-ABPX could be distinguished by the concentration of Fe^{3+}, and electrochemical experiments were conducted to determine its EC ability further. As Figure 2a shows, the oxidation potential of $FeCl_2$ was 0.27 V, while cis-ABPX had no redox signal at this stage. The oxidation potential ensured that $FeCl_2$ was oxidized before cis-ABPX, then in-situ spectro-electro-chemistry tests were conducted. The mixture solution of Fe^{2+} & cis-ABPX was nearly colorless, after applying 0.5 V, Fe^{2+} was gradually oxidized to Fe^{3+}. Then after coordination, the lactone rings of cis-ABPX were gradually opened, so the color of the mixture solution changed to magenta then to cyan. Correspondingly the absorption intensity increased at various absorption peaks, mainly located at 514 nm, 553 nm and 659 nm (Figure 2b), which was similar to cis-ABPX treated with proton (Figure 1a). However, these results were not seen in their individual solution (Figure S9). The EC mechanism based on Fe^{2+} and cis-ABPX was illustrated in Figure 2c. As the applied bias rising, Fe^{2+} began to be oxidized to Fe^{3+} to make cis-ABPX color gradually, and the absorbance of the mixture solution gradually increased. Then the color was bleached when the reduction of Fe^{3+} began. The color state of the EC system was dependent on the dynamic coordination of Fe^{n+} and cis-ABPX, and could be distinguished by the bias applied.
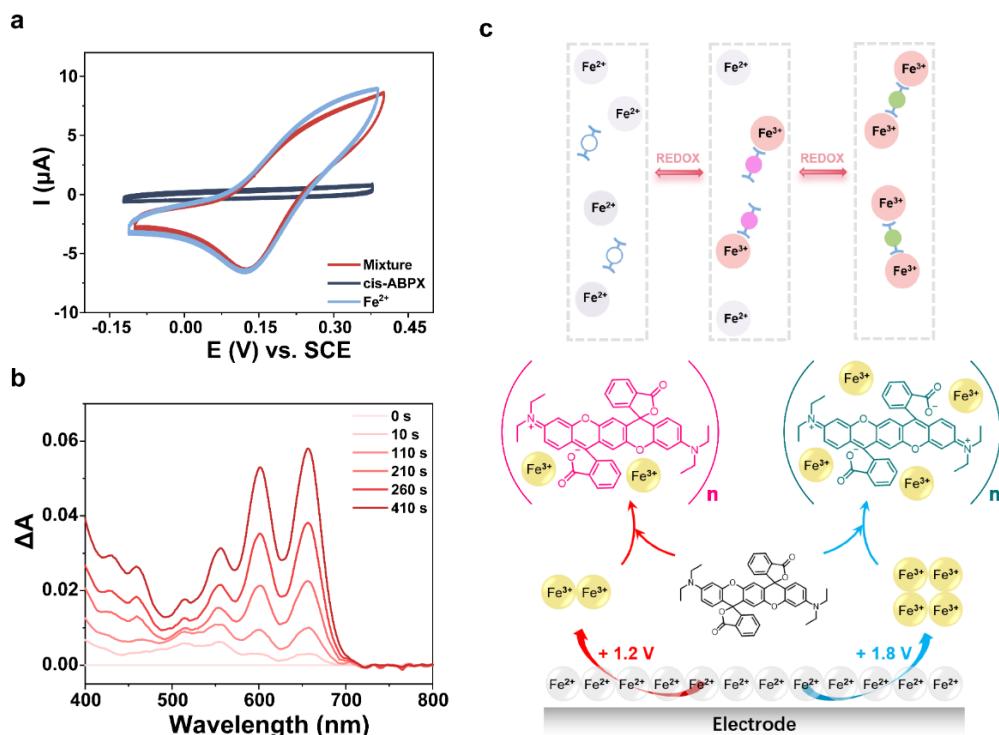
Figure 2. Investigation of the electrochromic mechanism. (**a**) The cyclic voltammetry curve of cis-ABPX, $FeCl_2$ and their mixture at 100 mV/s. The concentration of the solution was 2.0×10^{-3} mol/L in $CH_2Cl_2 + CH_3CN$ (*v:v* = 1:1). (**b**) The absorption spectra of "cis-ABPX + $FeCl_2$" under the voltage of 0.5 V versus Ag with different time. The concentration of cis-ABPX and $FeCl_2$ were 2.0×10^{-4} mol/L in $CH_2Cl_2 + CH_3CN$ (*v:v* = 1:1). (**c**) Illustration of the mechanism of EC processes based on cis-ABPX and Fe^{n+}.

To explore its color regulation ability further, the ECD was fabricated using the conventional "sandwich" structure (Figure 3a). The electrochromic layer was spin-coated on one indium tin oxide (ITO) glass, and ion storage layer and ion conducting layer were blade-coated on another ITO glass, then the two ITO glasses were

assembled together to fabricate the ECD (details in Experimental Part). The ECD exhibited magenta (1.2 V) and cyan (1.8 V) under different bias, then recovered to its nearly colorless state under reverse bias (Figure 3b). These results indicated the ability of Fe^{n+} to regulate the states of cis-ABPX still worked in ECD. To improve the EC performance of the device, the ratio of Fe^{2+} as redox agent and cis-ABPX as coloring agent in electrochromic layer was optimized. The molar ratio cis-ABPX:Fe^{2+} = 4:1 was selected for further experiment, because of the largest transmittance change (ΔT) at both 553 nm and 659 nm and the limitation of cis-ABPX solubility. It seemed that Fe^{3+} could cooperate with multiple cis-ABPX molecules in device. Then, the other components (PMMA, PC, $TBAPF_6$) in three layers were adjusted to optimize the EC performance. PMMA here was used as polymer matrix, PC was used as plasticizer and $TBAPF_6$ was used as electrolyte, their contents affected T_0 and ΔT of the device. Finally, the molar ratio PC:$TBAPF_6$ = 1:1 (PMMA = 50 wt%) was selected because of its largest ΔT and relatively high T_0.
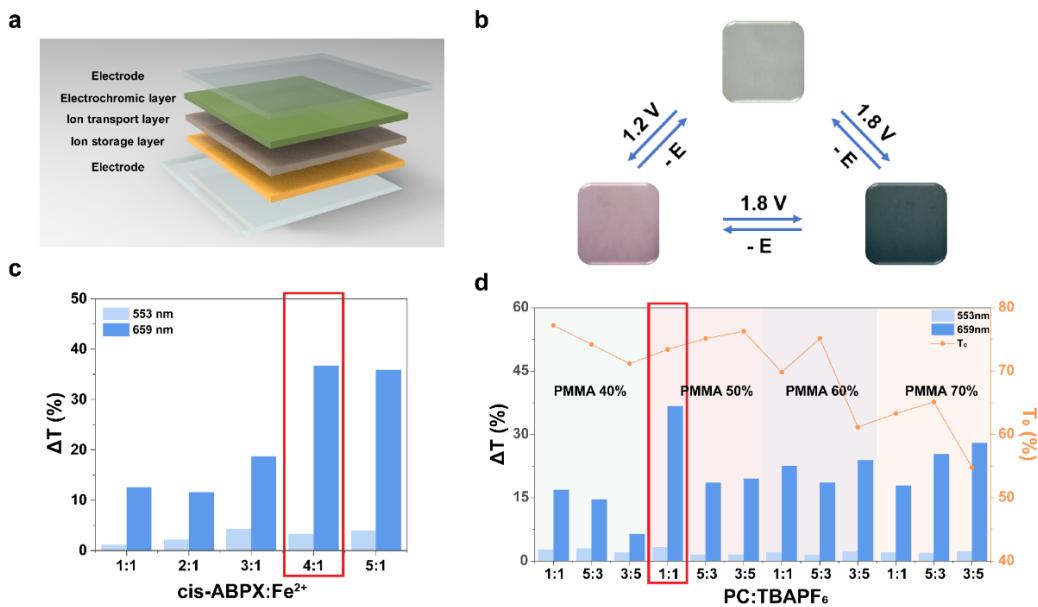

Figure 3. The optimization of the ECD. (**a**) The illustration of the ECD structure. (**b**) The photos of the device under different voltages. (**c**) The ΔT of the device made with different ratios of cis-ABPX/$FeCl_2$ with fixed concentration of $FeCl_2$ (5.0×10^{-3} mol/L) under the voltage of 1.2 V, 2 s (553 nm) and 1.8 V, 2 s (659 nm). (**d**) The ΔT and T_0 of the device with different ratios of propylene carbonate and $TBAPF_6$ and different ratios of PMMA used in the electrochromic layer under the voltage of 1.2 V, 2 s (553 nm) and 1.8 V, 2 s (659 nm).

With the optimized ratio of components, the ECD was fabricated for the further tests. When different voltages were applied to the device, the transmittance of the device changed in different wavelength ranges (Figure 4a). When 1.2 V was applied, the change of transmittance mainly occurred at 500–600 nm, and the color of the corresponding device changed from colorless to magenta. Correspondingly, when 1.8 V was applied, the change of transmittance mainly occurred at 400–500 nm and 600–700 nm, and the color of the device became cyan. Colorless, magenta, cyan and their mixture could be distinguished and regulated finely by the voltage applied, as shown in Figure 4b. The CIE L * a * b * values of corresponding process in Figure 4b were listed in Table S1. The color differences were calculated to show all greater than 2, indicating the differences in Figure 4b were obvious and could be distinguished by human eyes. It took the device 7.8 s/12.3 s to color/bleach under stimulation of 1.8 V/−0.8 V respectively (Figures 4c and S10). And the ECD exhibited high CE of 185 cm^2/C (Figure 4d) at 659 nm, indicating that this ECD exhibited large optical modulation under the same quantity of electric charge. The ECD could maintain the colored state for 77.1 s under open circuit with the attenuation of ΔT less than 10% (Figure S11), which has the potential to design energy-saving device. The reversibility of its coloring-bleaching cycles was measured by applying 1.7 V/−0.9 V to evaluate the service life of this ECD, ΔT showed no abnormal changes after 600 cycles (Figure S12).
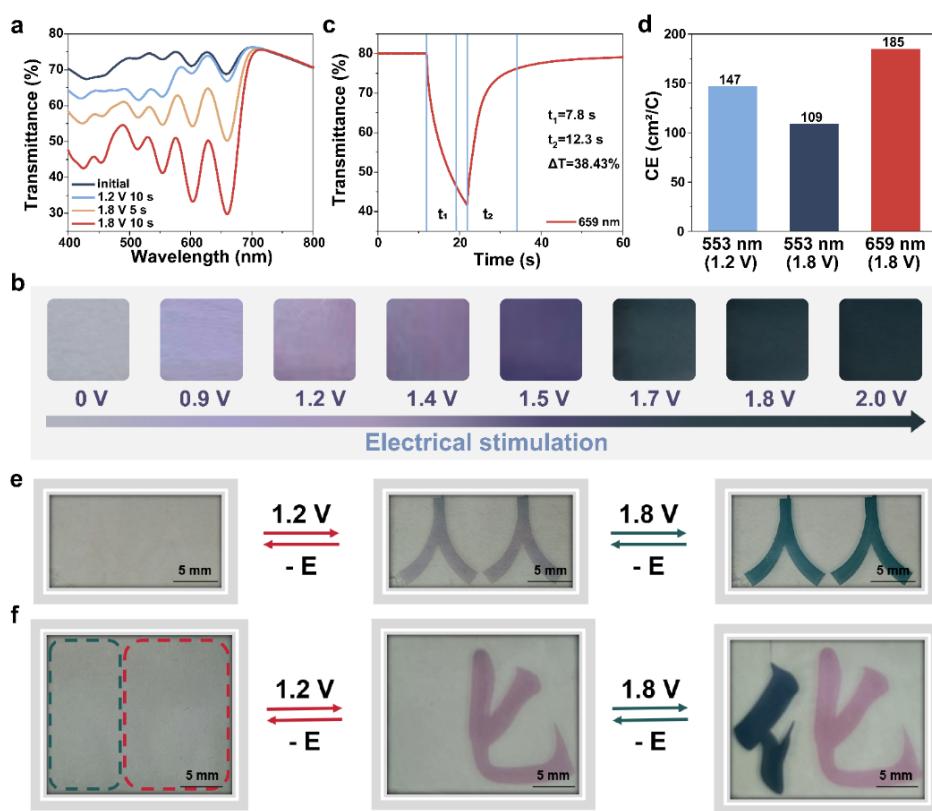
Figure 4. Investigation of the performance of the ECD. (**a**) The transmission spectrum of the ECD fabricated with optimal components. (**b**) Photos of the ECD treated with different voltage for 10 s. (**c**) The transmittance change at 659 nm of the ECD under the voltage of 1.8 V/−0.8 V (t_1 and t_2 corresponding to the time that takes to modulate the device transmittance from 0% to 90% of the transmittance change ratio during the coloring or fading process). (**d**) The CE of the ECD under different voltages and wavelengths. (**e,f**) The photos of the prototype ECDs under different bias (1.2 V, 30 s; 1.8 V, 15 s).

To demonstrate its intrinsic multi-color EC ability in single pixel device, prototype ECDs were fabricated (Figure 4e,f) by laser-etched ITO glass and layer-by-layer coating, the pattern was etched on the ITO glass. The color of the ECD could switch from its initial transparent colorless state to magenta state under 1.2 V, and to cyan under 1.8 V, which indicated the ability of multi-color electrochromism in single pixel (Figure 4e). Furthermore, the color of the device at different area could be switched independently. As shown in Figure 4f, after 1.2 V/1.8 V were applied to the magenta/cyan box area, the pattern showed respectively to form the Chinese character.

4. Conclusion

In conclusion, transparent colorless, magenta, cyan and various mixed color states were produced in single pixel ECD with condensed supramolecular cluster of multiple metal ions and cis-ABPX molecules and could be switched finely under different bias. This color change was based on the dynamic cooperation of multi-valent metal ion and multi-color-state molecular switch, realized intrinsic multi-color electrochromism in single cell. The EC mechanism was demonstrated by titration tests and in-situ spectro-electro-chemistry tests. The components of device were optimized and the prototype device was fabricated to demonstrate its intrinsic multi-color display ability. The low cost EC material developed here was suitable for use in low consumption reflective mode display device, and the success and grain of related exploration of intrinsically multi-color materials may probably inspire more researches to develop various other surprising applications.

state devices under the voltage of 1.2 V/−0.8 V (a) and 1.8 V/-0.8 V (b) (t₁ and t₂ corresponding to the time that takes to modulate the device transmittance from 0% to 90% of the transmittance change ratio during the coloring or fading process); Figure S11. The transmittance of ECD at 553 nm under stimulation of 1.2 V, power off 84.5 s, −0.8 V (a) and 1.8 V, power off 95.6 s, −1.0 V (b). (c) The transmittance of ECD at 659 nm under stimulation of 1.8 V, power off 77.1 s. −1.0 V; Figure S12. The ΔT of the ECD at 659 nm under stimulation of 1.7 V/−0.9 V for >600 test cycles, no abnormal changes; Table S1. The CIE L*a*b* values of the device treated with different voltages.

Author Contributions: M.L., S.W., Y.-M.Z. and S.X.-A.Z. conceived and designed this project. M.L. and S.W. wrote the original draft, S.W., Y.-M.Z. and S.X.-A.Z. revised the original draft. M.L. performed the experiments. M.L., S.W., Y.-M.Z. and S.X.-A.Z. conducted the data analysis. R.S. provided suggestions for data analysis. Y.X. provided advice for methodological. All authors have read and agreed to the published version of the manuscript.

Data Availability Statement: The data that support the findings of this study are available from the corresponding author upon reasonable request.

Conflicts of Interest: The authors declare that there is no conflict of interest regarding the publication of this article.

References

1. Beaujuge, P.M.; Ellinger, S.; Reynolds, J.R. The Donor–Acceptor Approach Allows a Black-to-Transmissive Switching Polymeric Electrochrome. *Nat. Mater.* **2008**, *7*, 795.

2. Rosseinsky, D.R.; Mortimer, R.J. Electrochromic Systems and the Prospects for Devices. *Adv. Mater.* **2001**, *13*, 783.

3. Grätzel, M. Ultrafast Colour Displays. *Nature* **2001**, *409*, 575.

4. Yu, H.; Qi, M.; Wang, J.; Yin, Y.; He, Y.; Meng, H.; Huang, W. A Feasible Strategy for the Fabrication of Camouflage Electrochromic Fabric and Unconventional Devices. *Electrochem. Commun.* **2019**, *102*, 31.

5. Yu, H.; Shao, S.; Yan, L.; Meng, H.; He, Y.; Yao, C.; Xu, P.; Zhang, X.; Hu, W.; Huang, W. Side-Chain Engineering of Green Color Electrochromic Polymer Materials: Toward Adaptive Camouflage Application. *J. Mater. Chem. C* **2016**, *4*, 2269.

6. Fu, H.; Yan, S.; Yang, T.; Yin, M.; Zhang, L.; Shao, X.; Dong, Y.; Li, W.; Zhang, C. New Dual Conjugated Polymer Electrochromic Device with Remarkable Yellow-to-Green Switch for Adaptive Camouflage. *Chem. Eng. J.* **2022**, *438*, 135455.

7. Sarmah, S.; Kashyap, S.S.; Bera, M.K. Dual Redox-Responsive Os/Ru-Based Alternated Heterobimetallic Supramolecular Polymer as a Multicolor Electrochromic Material for Camouflage Devices. *ACS Appl. Electron. Mater.* **2023**, *5*, 1738.

8. Laschuk, N.O.; Ebralidze, I.I.; Easton, E.B.; Zenkina, V.O. Post-Synthetic Color Tuning of the Ultra-Effective and Highly Stable Surface-Confined Electrochromic Monolayer: Shades of Green for Camouflage Materials. *ACS Appl. Mater. Interfaces* **2021**, *13*, 39573.

9. Zhao, G.; Wang, W.; Wang, X.; Xia, X.; Gu, C.; Tu, J. A Multicolor Electrochromic Film Based on a SnO₂/V₂O₅ Core/Shell Structure for Adaptive Camouflage. *J. Mater. Chem. C* **2019**, *7*, 5702.

10. Gu, C.; Yan, Y.; He, J.; Pu, D.; Chen, L.; Zhang, Y.-M.; Zhang, S.X.-A. Transparent and Energy-Efficient Electrochromic AR Display with Minimum Crosstalk Using the Pixel Confinement Effect. *Device* **2023**, *1*, 100126.

11. Kim, G.W.; Kim, Y.C.; Ko, I.J.; Park, J.H.; Bae, H.W.; Lampande, R.; Kwon, J.H. High-Performance Electrochromic Optical Shutter Based on Fluoran Dye for Visibility Enhancement of Augmented Reality Display. *Adv. Opt. Mater.* **2018**, *6*, 1701382.

12. Zhang, W.; Li, H.; Yu, W.W.; Elezzabi, A.Y. Transparent Inorganic Multicolour Displays Enabled by Zinc-Based Electrochromic Devices. *Light Sci. Appl.* **2020**, *9*, 121.

13. Wang, B.; Zhao, F.; Zhang, W.; Li, C.; Hu, K.; Carnio, B.N.; Liu, L.; Yu, W.W.; Elezzabi, A.Y.; Li, H. Inhibiting Vanadium Dissolution of Potassium Vanadate for Stable Transparent Electrochromic Displays. *Small Sci.* **2023**, *3*, 2300046.

14. Wang, Y.; Shen, R.; Wang, S.; Chen, Q.; Gu, C.; Zhang, W.; Yang, G.; Chen, Q.; Zhang, Y.-M.; Zhang, S.X.-A. A See-through Electrochromic Display via Dynamic Metal-Ligand Interactions. *Chem* **2021**, *7*, 1308.

15. Wang, Y.; Shen, R.; Wang, S.; Zhang, Y.; Zhang, S.X. Dynamic Metal–Ligand Interaction of Synergistic Polymers for Bistable See-Through Electrochromic Devices. *Adv. Mater.* **2022**, *34*, 2104413.

16. Zhao, F.; Zhao, J.; Zhang, Y.; Wang, X.; Wang, W. Self-powered quasi-solid-state electrochromic devices for optical information encryption. *J. Mater. Chem. C* **2021**, *9*, 7958.

17. Alesanco, Y.; Viñuales, A.; Palenzuela, J.; Odriozola, I.; Cabañero, G.; Rodriguez, J.; Tena-Zaera, R. Multicolor Electrochromics: Rainbow-Like Devices. *ACS Appl. Mater. Interfaces* **2016**, *8*, 14795.

18. Zhuang, Y.; Li, J.; Zhu, M.; Li, F.; Liu, S.; Zhao, Q. Electrochromism and Electrofluorochromism Based on Viologen Derivative with 1,10-Phenanthroline Moiety for Multicolor Large-Area and Patterned Display. *Adv. Mater. Technol.* **2023**, *8*, 2301092.

19. Choi, Y.; Kim, K.-W.; In, Y.R.; Tang, X.; Kim, P.; Quy, V.H.V.; Kim, Y.M.; Lee, J.; Choi, C.; Jung, C.; et al. Multicolor, Dual-Image, Printed Electrochromic Displays Based on Tandem Configuration. *Chem. Eng. J.* **2022**, *429*, 132319.

20. Song, R.; Li, G.; Zhang, Y.; Rao, B.; Xiong, S.; He, G. Novel Electrochromic Materials Based on Chalcogenoviologens for Smart Windows, E-Price Tag and Flexible Display with Improved Reversibility and Stability. *Chem. Eng. J.* **2021**, *422*, 130057.

21. Tong, Z.; Lv, H.; Zhang, X.; Yang, H.; Tian, Y.; Li, N.; Zhao, J.; Li, Y. Novel Morphology Changes from 3D Ordered Macroporous Structure to V_2O_5 Nanofiber Grassland and Its Application in Electrochromism. *Sci. Rep.* **2015**, *5*, 16864.

22. Zhang, Y.-M.; Wang, X.; Zhang, W.; Li, W.; Fang, X.; Yang, B.; Li, M.; Zhang, S.X.-A. A Single-Molecule Multicolor Electrochromic Device Generated through Medium Engineering. *Light Sci. Appl.* **2015**, *4*, e249.

23. Kim, K.-W.; Lee, J.K.; Tang, X.; Lee, Y.; Yeo, J.; Moon, H.C.; Lee, S.W.; Kim, S.H. Novel Triphenylamine Containing Poly-Viologen for Voltage-Tunable Multi-Color Electrochromic Device. *Dyes Pigment.* **2021**, *190*, 109321.

24. Wang, J.-L.; Liu, J.-W.; Sheng, S.-Z.; He, Z.; Gao, J.; Yu, S.-H. Manipulating Nanowire Assemblies toward Multicolor Transparent Electrochromic Device. *Nano Lett.* **2021**, *21*, 9203.

25. Xue, W.; Zhang, Y.; Liu, F.; Dou, Y.; Yan, M.; Wang, W. Self-powered flexible multicolor electrochromic devices for information displays. *Research* **2023**, *6*, 0227.

26. Laschuk, N.O.; Ahmad, R.; Ebralidze, I.I.; Poisson, J.; Easton, E.B.; Zenkina, O.V. Multichromic Monolayer Terpyridine-Based Electrochromic Materials. *ACS Appl. Mater. Interfaces* **2020**, *12*, 41749.

27. Malik, N.; Lahav, M.; van der Boom, M.E. Electrochromic Metallo–Organic Nanoscale Films: A Molecular Mix and Match Approach to Thermally Robust and Multistate Solid-State Devices. *Adv. Electron. Mater.* **2020**, *6*, 2000407.

28. Tsuboi, A.; Nakamura, K.; Kobayashi, N. A Localized Surface Plasmon Resonance-Based Multicolor Electrochromic Device with Electrochemically Size-Controlled Silver Nanoparticles. *Adv. Mater.* **2013**, *25*, 3197.

29. Tsuboi, A.; Nakamura, K.; Kobayashi, N. Multicolor Electrochromism Showing Three Primary Color States (Cyan–Magenta–Yellow) Based on Size- and Shape-Controlled Silver Nanoparticles. *Chem. Mater.* **2014**, *26*, 6477.

30. Wang, Z.; Wang, X.; Cong, S.; Chen, J.; Sun, H.; Chen, Z.; Song, G.; Geng, F.; Chen, Q.; Zhao, Z. Towards Full-Colour Tunability of Inorganic Electrochromic Devices Using Ultracompact Fabry-Perot Nanocavities. *Nat. Commun.* **2020**, *11*, 302.

31. Wu, M.; Li, Y.; Yuan, W.; De Bo, G.; Cao, Y.; Chen, Y. Cooperative and Geometry-Dependent Mechanochromic Reactivity through Aromatic Fusion of Two Rhodamines in Polymers. *J. Am. Chem. Soc.* **2022**, *144*, 17120.

32. Shirasaki, Y.; Okamoto, Y.; Muranaka, A.; Kamino, S.; Sawada, D.; Hashizume, D.; Uchiyama, M. Fused-Fluoran Leuco Dyes with Large Color-Change Derived from Two-Step Equilibrium: *Iso*-Aminobenzopyranoxanthenes. *J. Org. Chem.* **2016**, *81*, 12046.

33. Li, A.; Chu, N.; Huang, L.; Han, L.; Geng, Y.; Xu, S.; Pan, L.; Cui, H.; Xu, W.; Ma, Z. Remarkable responsive behaviors of iso-aminobenzopyranoxanthenes: Protonation effect, photochromism and piezochromism. *Dye. Pigment.* **2019**, *162*, 831.

34. Gu, C.; Wang, X.; Jia, A.-B.; Zheng, H.; Zhang, W.; Wang, Y.; Li, M.; Zhang, Y.-M.; Zhang, S.X.-A. A strategy of stabilization via active energy-exchange for bistable electrochromic displays. *CCS Chem.* **2021**, *4*, 2757.

Article

High-Yield, Environmentally-Friendly, and Sustainable Synthesis of Silver Nanowires Using Tannic Acid and Their Application in Conductive Ink Preparation: Economic Analysis and Rheological Investigation

Sina Kaabipour [1], Finley Neal [2], and Shohreh Hemmati [2],*

[1] School of Chemical Engineering, Oklahoma State University, Stillwater, OK 74078, USA
[2] School of Mathematics and Natural Sciences, The University of Southern Mississippi, Hattiesburg, MS 39406, USA
* Correspondence: shohreh.hemmati@usm.edu

Abstract: Silver nanowires (AgNWs) have garnered significant attention during the past decade thanks to their applications in conductive inks used for electronic applications. The polyol process, widely used for AgNW synthesis, is known for its effectiveness in producing high aspect ratio and high yield nanowires. However, this process suffers from drawbacks such as high energy consumption and use of unsustainable reagents derived from non-renewable resources, which makes its large-scale utilization and economic feasibility challenging. In

contrast, green synthesis methods offer potential solutions by employing environmentally friendly and cost-effective approaches. In this study, we offer a high-yield (90%) approach for the inexpensive, environmentally friendly, and sustainable synthesis of AgNWs, and show that the production cost per grams of AgNWs can be reduced by 31.72% compared to the polyol process. In addition, we investigate the rheological behavior of the synthesized AgNW-based conductive ink under screen printing and direct writing conditions using flow sweep, peak hold, and frequency sweep tests. The rheological behavior of the AgNW-based conductive ink provides valuable information regarding its use for various printing applications. The conductive ink demonstrated a shear-thinning thixotropic behavior for all silver nanostructure contents (2, 5, 10, and 20 wt.%), and all temperatures (25, 30, and 40 °C). It was observed that direct writing is better suited for printing inks with low colloidal content due to its lower shear rate, whereas screen printing is more effective for high-content, high-viscosity inks because it utilizes higher shear rates. The proposed cheaper and more sustainable method can serve as a promising alternative for industrial conductive ink manufacturing for printed electronic appliances such as printed circuit boards (PCBs) and flexible transparent conductive films (TCFs).
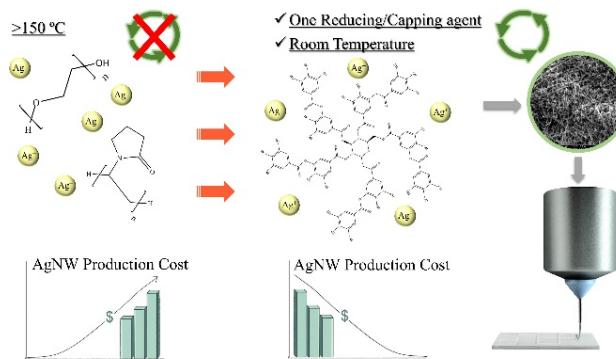
Keywords: silver nanowires; green chemistry; sustainability; rheology; conductive ink; screen printing; direct writing

1. Introduction

The development of metal-based colloidal conductive inks has gained significant attention for the manufacturing cost-effective, versatile, and flexible transparent conductive films (TCFs). These films have a wide range of applications, including wearable health-monitoring devices, supercapacitors, photodetectors, and solar cells, to name a few [1–4]. Indium tin oxide (ITO) is the most commonly used material for TCFs, due to its excellent optical transmittance (>90%) and its low sheet resistance (<10 Ω/square) [5]. However, its brittleness and energy-intensive manufacturing process limit its use in flexible electronics [5,6]. As an alternative, silver nanowire (AgNW)-based conductive inks have emerged as promising candidates for TCFs due to their superior electrical conductivity, high transmittance, and durability under bending stress [7,8]. The interconnected nanowire

networks facilitate electron flow, reducing sheet resistance and enabling flexibility. However, challenges remain, particularly in the synthesis and printing of AgNW-based inks.

The polyol process is the most common method for synthesizing AgNWs, which has also been extensively investigated and further optimized over the past years [9–11]. However, it is energy-intensive, requiring high temperatures (>150 °C), and relies on reagents such as ethylene glycol (EG) and polyvinylpyrrolidone (PVP), which are derived from fossil fuels. EG, in particular, poses environmental concerns due to its toxicity to aquatic life [12]. Furthermore, scaling up the polyol process is challenging and results in high production costs, raising questions about its economic feasibility.

Printing AgNW-based conductive patterns also presents difficulties. Achieving high-quality patterns, with sharp lines, high resolution, and minimal surface roughness requires careful optimization of ink rheology, including shear-thinning behavior and viscosity, as well as the composition of the ink, which typically includes binders, solvents, and nanostructured fillers.

Among the various printing methods, screen printing is widely used due to its simplicity, fine resolution, and scalability. The ink undergoes shear stress as it is forced through a mesh onto a substrate, with shear rates typically ranging from 0.1–200 1/s depending on mesh size and squeegee movement [13–17]. Rapid viscosity recovery after shear stress is crucial for maintaining sharp-edged lines [18,19]. While screen printing is versatile, it often results in significant material wastage. Inkjet printing, on the other hand, enables high-resolution patterning by depositing ink droplets tens of micrometers in diameter onto a substrate [20,21]. This method requires inks with low viscosity (1–30 cP) to prevent nozzle clogging [22,23]. However, the high aspect ratio of AgNWs can still pose clogging issues, often necessitating nanowire shortening via sonication [24]. The direct writing approach, a mechanized process typically involving 3D printing instrument, offers cost-effective and customizable printing solutions. It requires inks with intermediate viscosity to ensure smooth flow and shape retention after deposition [25]. Despite its advantages, direct writing is limited by its relatively low resolution and thicker pattern lines, which are unsuitable for miniaturized circuits.

In all printing processes, the timescale for viscosity recovery significantly influences line sharpness and film leveling [18]. The "Stretched Exponential" model [26,27] describes this transition (Equation (1)), where viscosity recovery is influenced by factors such as nanostructure content and aspect ratio. Studies have shown that higher AgNW content and aspect ratios improve viscosity recovery and printing performance.

$$\eta = \eta_0 + (\eta_\infty - \eta_0)(1 - \exp(-\frac{t}{\tau})^r) \qquad (1)$$

where η is the viscosity at time t, η_0 is the viscosity at the high shear rate, η_∞ is the viscosity at the low shear rate, τ is the transition characteristic time, and r is a dimensionless constant, which is equal to one in most cases. The values for η_0 and η may be obtained using the peak hold test (applying a step increase to the shear rate followed by a decrease to the initial shear rate to mimic the ink charging sequence [28]).

Hemmati et al. [18] investigated the characteristic recovery time using the same equation (Equation (1)) by testing inks with different commercially available AgNW content. They found that the characteristic time decreased (reaching as low as 20.9 s) with an increase in the Ag nanostructure content (up to 6 wt.%). In another study, Liang et al. [19] also investigated the rheological behavior of the AgNW ink by measuring the viscosity recovery percentage after an applied shear stress, for different AgNW compositions. They showed that for a medium AgNW composition of 6.6 wt.%, a maximum viscosity recovery percentage of 59.4% can be obtained after 10 s of a step change in shear rate (from 200 to 0.1 1/s). After 50 s, the viscosity recovery percentage increased to 85.9%. However, for a higher content of AgNW (7.3 wt.%), 58.5% of the initial viscosity value was obtained. This behavior was attributed to the high viscosity of the ink at higher AgNW content [19,29].

For high-precision ink printing, three criteria are key: (1) The ink's viscosity should be suitable for smooth printing, avoiding droplet formation or nozzle blockage. (2) The ink should quickly recover its viscosity after extrusion to maintain shape. (3) Shrinkage during drying should be minimized using a high colloid volume, with high-aspect-ratio silver nanowires (AgNWs) to prevent nozzle clogging. [25,30–34].

AgNWs synthesized through the polyol process, initially developed in 2001, [9] have been widely used for the preparation of conductive ink. However, to the best of our knowledge, the large-scale green and sustainable synthesis of AgNWs and their applications in conductive ink preparation have not been extensively studied. To address the limitations of conventional synthesis methods, we previously developed a room-temperature process for synthesizing AgNWs using tannic acid as both a reducing and capping agent. This green and sustainable method eliminates the need for high temperatures and additional capping agents. However, the yield (~50%) and application of these AgNWs remain limited. This study builds upon our prior work, focusing on the large-scale, sustainable synthesis of AgNWs and their integration into conductive inks for advanced TCF manufacturing.

2. Methodology

2.1. Materials

Silver nitrate (AgNO$_3$, MW: 169.87 g/mol, product number: S0139), tannic acid (C$_{76}$H$_{52}$O$_{46}$, MW: 1701.2 g/mol, product number: 403040), nitric acid (HNO$_3$, 70% ACS reagent, MW: 63.01 g/mol, product number: 438073), and sodium carboxymethyl cellulose (CMC, MW~90,000 g/mol, product number: 419273) were purchased from Sigma Aldrich (St. Louis, MO, USA). Dispex ultra FA 4416 was purchased from BASF© (Florham Park, NJ, USA) as the dispersing agent and was used for conductive ink preparation. Deionized water (DIW, ASTM type II) was used as the solvent to prepare aqueous AgNO$_3$ and tannic acid solutions, as well as the conductive ink.

2.2. Synthesis and Isolation of AgNWs

For AgNWs synthesis with high throughput compared to our previously published study (5 mM tannic acid and AgNO$_3$ solutions), aqueous tannic acid and AgNO$_3$ solutions (both 20 mL, 100 mM each) were prepared. The pH of the tannic acid solution was adjusted to 1.25 by adding HNO$_3$. The tannic acid solution was then added to a 100 mL round glass flask, and the AgNO$_3$ solution was added dropwise. The reaction was continued at room temperature for 4 h. The flask was exposed to white fluorescent light at 676 LUX during the whole reaction because it assists the reduction process [35]. After the synthesis process was completed, the AgNWs suspension was centrifuged 4 times in DIW at 5000 rpm, with the supernatant being removed after each centrifugation step.

2.3. Scanning Electron Microscopy (SEM) Characterization

AgNWs were characterized by the FEI Quanta 600 (Stillwater, OK, USA) field-emission gun Environmental Scanning Electron Microscope at the Oklahoma State University microscopy laboratory. To do the characterization, 100 μL of the AgNWs suspension was pipetted onto smooth carbon tabs taped to aluminum pins. The samples were then kept at dry and room temperature conditions for 24 h to allow the samples to dry. The pins containing the AgNWs were then put on sample holders in the SEM instrument for characterization.

2.4. Conductive Ink Preparation

The AgNW-based conductive ink was prepared by mixing the AgNWs suspended in DIW, CMC, and the Dispex Ultra FA 4416 dispersing agent. The ink was prepared at different AgNWs weight percentages (2, 5, 10, and 20 wt.%), while the weight percentage of CMC and the dispersing agent were both kept at 6 wt.%. The combination of AgNWs and other nanostructures, aside from nanowires, was used for conductive ink preparation.

2.5. Rheological Tests

To investigate the rheological properties of the prepared conductive ink, the ink sample was analyzed using a TA Instrument's© Discovery HR-10 Rheometer (New Castle, DE, USA). To do so, a 25 mm geometry was used, and three main tests were performed including flow sweep, peak hold, and frequency sweep tests. After geometry definition and test setup, the ink sample was poured onto the sample holder disk (peltier plate) and trapped between the geometry and the disk. The trim gap (gap set for trimming the sample prior to the rheological test) was 1050 μm and the test gap (gap set for rheological testing) was 1000 μm. A 3-min soak time was allowed for the ink to reach the desired temperature.

2.6. Conductive Ink Printing Rheological Simulation

To simulate the ink printing process using screen printing, the peak hold test was performed using the rheometer. In the first step of the peak hold test, the ink was subjected to a low shear rate of 0.1 1/s for 40 s to simulate ink at rest. In the second step, the ink was subjected to a high shear rate of 400 1/s for 20 s to simulate ink under printing shear stress. In the third step, the shear rate was reduced back to 0.1 1/s for 100 s to simulate ink at resting condition after printing. To simulate the ink printing process using the direct writing method, a laboratory-made 3D printer (Figure 1) was considered as the model printer for the purpose of simulation, and its specifications were considered the direct printing simulation process. The 3D printer extruder operated based on a syringe and piston system. To initiate the printing process, the syringe would be loaded by conductive ink, with the ink being pushed manually by the piston to reach the printing needle tip. The syringe inner diameter was set at 12 mm, the main tube inner diameter was set at 3.5 mm, and the needle diameter was set 0.69 mm. To operate the

printer, the Repetier Host software can be used, which utilizes Gcode to define printing properties, such as the extruder movement rate, the flowrate, and the writing pattern.
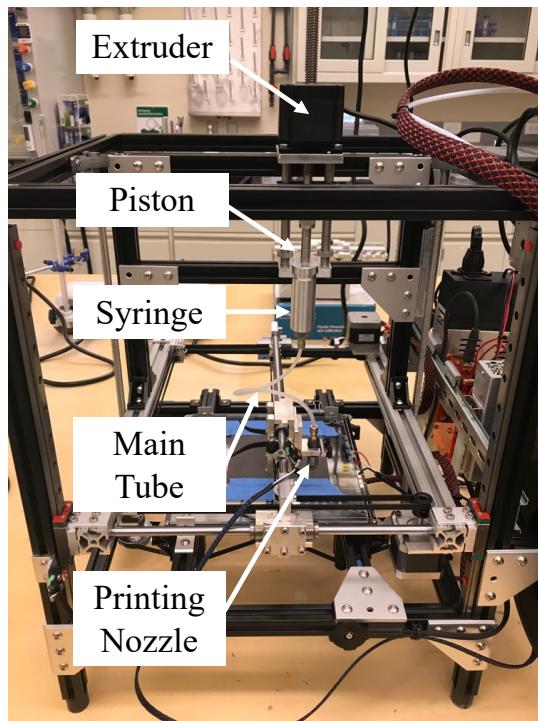

Figure 1. Laboratory-made 3D printer that its specifications were used for conductive inks printing process simulation.

3. Results and Discussion

3.1. Synthesis of AgNWs

We previously investigated the green synthesis of AgNWs using tannic acid and AgNO$_3$ at room temperature, as well as the effect of various factors such as light, Ag$^+$ ion and tannic acid concentration ratio, and pH [35,36]. In such cases, AgNWs were synthesized at moderate yield using both batch and continuous millifluidic processes (yield of 50 and 82%, respectively). We demonstrated that light is a significant factor in controlling the reduction rate of Ag$^+$ ions by tannic acid, and the fact that the reduction rate can be increased by increasing the pH and increasing the light intensity of UV-visible white fluorescent lamp. We also demonstrated that it is imperative that the ratio of tannic acid concentration to Ag$^+$ concentration is maintained at 1 to assist with the anisotropic growth of nanostructures that leads to the formation of nanowires [35]. The process by itself has several advantages, which are the minimal use of energy—due to the reaction being performed at room temperature—using a single-step process and just one reducing agent, which can also act as a capping and stabilizing agent, and using a sustainable and environmentally friendly reducing/capping agent, thereby decreasing chemical waste production. Despite all these advantages, the overall productivity of that process was limited and not feasible for preparation of conductive ink, which requires high silver nanostructure content, because AgNO$_3$ was used at a mere concentration of 5 mM. In the current study, we were able to produce AgNWs with an approximate yield of 90% using AgNO$_3$ and tannic acid at a much higher concentration (100 mM each) (Figure 2). This yield was higher compared to the yield acquired by both batch and millifluidic processes (~50 and 82%, respectively) previously synthesized at 5 mM of AgNO$_3$ and tannic acid. This was done by adjusting both the pH and light to control the reduction kinetics in a manner that leads to a controlled anisotropic growth process. Furthermore, acquiring such a high yield at lower concentrations was more difficult for two main reasons. The first issue is the increased sensitivity to experimental conditions. When the concentration is too low, the reaction can become highly sensitive to temperature, pH, and reducing agent/precursor concentration, which may ultimately lead to non-uniform morphologies and low yield. The second issue is the increased risk of contamination. When the concentration of the precursor (in this case, AgNO$_3$) is too low, the amount of impurities and contaminants in the reaction may be relatively large compared to concentration of Ag$^+$; therefore, interfering with the reaction in a disruptive manner. If favorable experimental parameters at high precursor/reducing agent concentration are discovered, such two challenges can be minimized. The reduction rate increases with an increase in the concentration of Ag$^+$ ions. However, reducing the pH to a

highly acidic value of 1.25 significantly decreases the reduction rate, offsetting the increase caused by the high Ag^+ concentration. Deviating from a pH of 1.25, either lower or higher, results in a reduced yield of AgNWs.
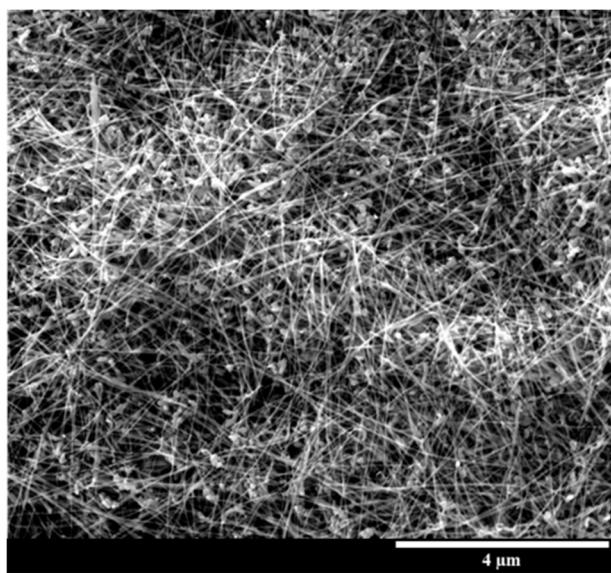

Figure 2. SEM image of silver nanowires (AgNWs) synthesized by tannic acid at room temperature. Average nanowire diameter: 32.9 ± 8.2 nm. Average nanowire length: 9.8 ± 4.1 μm.

3.2. Economic Analysis

To assess the economic feasibility of the tannic acid-mediated and polyol processes, the costs of the metal precursor ($AgNO_3$), reducing agent (tannic acid/ethylene glycol), capping agent (polyvinylpyrrolidone (PVP)), and electricity consumption by the hotplate were considered. To determine the cost of materials needed for a typical polyol process, a previous reference [37] was studied and the amounts of materials used in grams were initially documented. Then the cost per gram of materials were collected from the Sigma Aldrich website based on the product number associated with each material, considering the largest volumes available because it would be the most likely scenario for large-scale operations. For electricity consumption, the hotplates were assumed to have a range of power consumption from 300–1500 Watts, with the cost of electricity in the industry sector standing at 8.21 cents per KWh by the end of October 2024 according to the U.S Energy Information Administration (EIA) [38]. As a result, the minimum and maximum power consumption costs were calculated, and the average was used. In the case of a room-temperature process, such as the tannic acid-mediated synthesis, it would not be realistic to account for the total power consumption of the hotplate, because only magnetic stirring is active, which is estimated to account for about 5% of the total power consumption, nearly negligible compared to the power consumed by heating. However, the light usage should be considered for the tannic acid-mediated process because it relies on UV-Visible illumination by white fluorescent lamps which are 25 W strong.

To calculate the total grams of AgNWs synthesized in a typical polyol process, the amount of Ag^+ ions at the end of the reaction (performed according to Hemmati et al.'s [37] publication) was identified using a spectrophotometric technique we used in one of our previous publications [35]; which was followed by the calculation of the Ag^0 produced in the process as shown in Equation (2).

$$Ag^0(g) \; produced = initial \; Ag^+(g) - final \; Ag^+(g) \qquad (2)$$

where the initial Ag^+ is known and the final Ag^+ is calculated by the spectrophotometric identification technique. The same technique was used to calculate the amount of Ag^0 produced by the tannic acid process. The conversion rate ($Ag^0 \; produced/initial \; Ag^+ \times 100\%$) calculated based on the data from Equation (2) stands at 83.64% for the polyol process and 32.12% for the tannic acid- mediated process. Based on the materials and energy consumption costs, the production cost per gram of AgNWs can be calculated. For the tannic acid-mediated synthesis process, a correction factor of 10/9 (100%/90%) is considered due to its yield standing at 90%. Since this value is typically 99% or higher for the polyol process, it was neglected. Table 1 compares production cost per gram of AgNWs for the polyol process and the tannic acid-mediated process. The production cost is broken down into materials and electricity consumption costs for each process. The sum of these costs is then converted to $/g of AgNWs, taking into account the yield and conversion rates of each process. For brevity, only the electricity, materials, and total production costs, and grams of AgNWs produced per process are included. Reader

can refer to the supplemental Excel file for more information and to see how these conversions are specifically made.

Table 1. Comparison of the production costs ($/grams of AgNWs) between polyol process and the tannic acid-mediated process.

Method	Energy (Electricity) Consumption Cost per Process ($)	Materials Cost per Process ($)	Grams of AgNWs Produced per Process	Production Cost $/g of AgNWs
Our method (tannic acid-mediated synthesis)	0.02	2.18	0.0689	35.59
Hemmati et al. [37] (2017)	0.11	1.88	0.0382	52.12

As demonstrated in Table 1, the production cost per gram of AgNWs is lower in the tannic acid-mediated synthesis compared to the conventional polyol process. Although the production cost depends on the very specifics of a synthesis process, it can be reduced 31.72% by using the tannic acid-mediated process. Despite having a lower conversion rate of the tannic acid-mediated synthesis process compared to the polyol process, the tannic acid-mediated process is much cheaper and is environmentally friendly, making its industrial applications simpler and more feasible compared to the conventional polyol process.

3.3. Rheological Analysis

When investigating the rheological behavior of a printable nanostructure-based conductive ink, 6 main factors should be considered, including viscosity, shear rate, weight percentage and morphology of the nanostructures, solvent, temperature, and more importantly the printing conditions [25,28,39–42]. The first three were discussed in the introduction section. The effect of solvent is also important because solvents with higher surface tension tend to increase the viscosity of the ink. Temperature is another important factor because higher temperatures can reduce the viscosity of the conductive ink while lower temperatures can increase it. This characteristic can be beneficial in the printing process as it allows for fine-tuning the rheological behavior of the ink to match the requirements of the printing process by temperature adjustments. Lastly, for the sake of proper rheological measurements, the specific printing condition needs to be considered. Printing conditions such as printing speed, ink flowrate, width/diameter of printing nozzle, and width/diameter of flow channel can affect the rheological behavior of the ink during the printing process. Based on previous tests with our laboratory-made printer, the overall viscosity of the ink (at rest) should be more than 5 Pa.s. Lower viscosities may result in nozzle drip, which leads to an inconsistent printed pattern. Higher viscosities can be used; however, this depends on the colloidal content and the concentration of the binder. One should note that there is no defined viscosity range for printing applications, and the required viscosity and shear rate is application specific.

3.3.1. Rheological Behavior of AgNW-Based Conductive Ink and the Effect of Silver (Ag) Nanostructure Content

Flow Sweep Test

To investigate the rheological behavior of the ink, the first test was the flow sweep test. This test shows the overall viscosity of the ink change with respect to shear rates and determines whether the ink has shear-thinning or shear-thickening behavior. A conductive ink that is used for screen printing or direct printing applications should have a shear thinning characteristic. Figure 3 shows the viscosity of the ink vs. shear rate for concentration of 2, 5, 10, and 20 wt.% of Ag nanostructures at room temperature (25 °C). As demonstrated, for all Ag nanostructure contents, the viscosity of the ink decreases with increase in shear rate, indicating the shear-thinning behavior of the ink. However, the decline in viscosity is more pronounced for the ink with higher Ag nanostructure content, whereas it is less pronounced for the ink with lower silver nanostructure content.
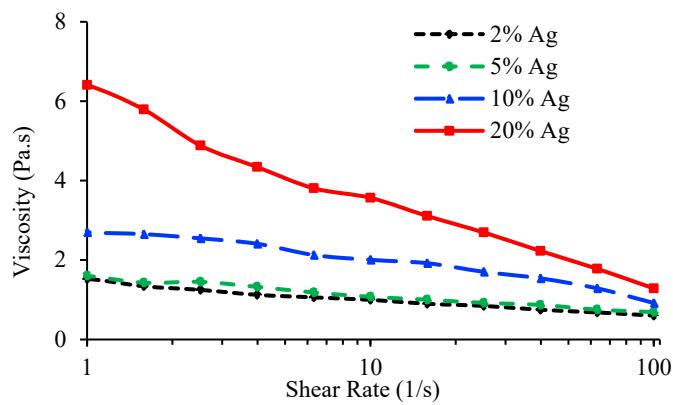
Figure 3. Flow sweep test for conductive ink with different silver nanostructure contents.

Frequency Sweep Test

The frequency sweep test was performed to analyze the viscoelastic behavior of the ink, and to extract valuable information about the effect of colloidal forces and the interaction of nanostructures. Two main variables are provided by the frequency sweep test including storage modulus and loss modulus. The storage modulus (G′) is a measure of the elastic behavior of the ink while the loss modulus (G″) is a measure of the viscous behavior of the ink. Figure 4 shows the frequency sweep test results, demonstrating storage and loss modulus vs. angular frequency for different Ag nanostructure contents at room temperature (25 °C). Both loss and storage modulus increase with increasing the Ag nanostructure content. This means that the resistance of the ink to deformation increases as the Ag nanostructure content increases. However, for all Ag nanostructure contents, and for the whole angular frequency spectrum, the loss modulus is more than the storage modulus, meaning that the viscous effect is dominant compared to the elastic effect. A more detailed analysis of the viscous/elastic effect can be provided by describing the tan delta variable (tan δ) as shown in Equation (3).
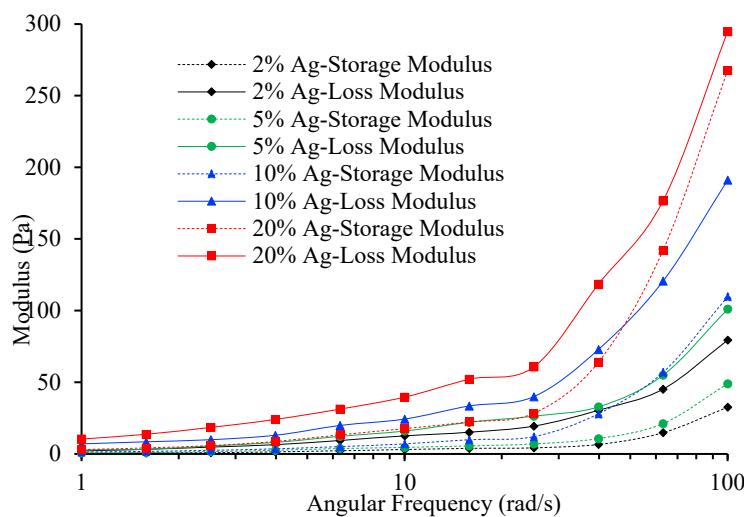
Figure 4. Frequency sweep test for conductive ink with different silver nanostructure contents.

$$tan\delta = \frac{G''}{G'} \tag{3}$$

where G″ (Pa) is the loss modulus and G′ (Pa) is the storage modulus. Thus, a higher tan δ accounts for a stronger viscous behavior while a lower tan δ accounts for a stronger elastic behavior. Figure 5A shows tan δ vs. angular frequency for different Ag nanostructure contents. As demonstrated, tan δ decreases overall for all Ag nanostructure contents, meaning that the elastic effects become stronger at higher frequencies. This is because at lower frequencies, nanostructures have more time to move within the binder matrix, which can result in a more viscous response, while at higher frequencies, nanostructures have less time to move within binder matrix due to

the high oscillation factor, which ultimately results in a more elastic response. The more the Ag nanostructure content, the lower the tan δ at high frequencies, meaning that the elastic response becomes stronger as the Ag nanostructure content increases.
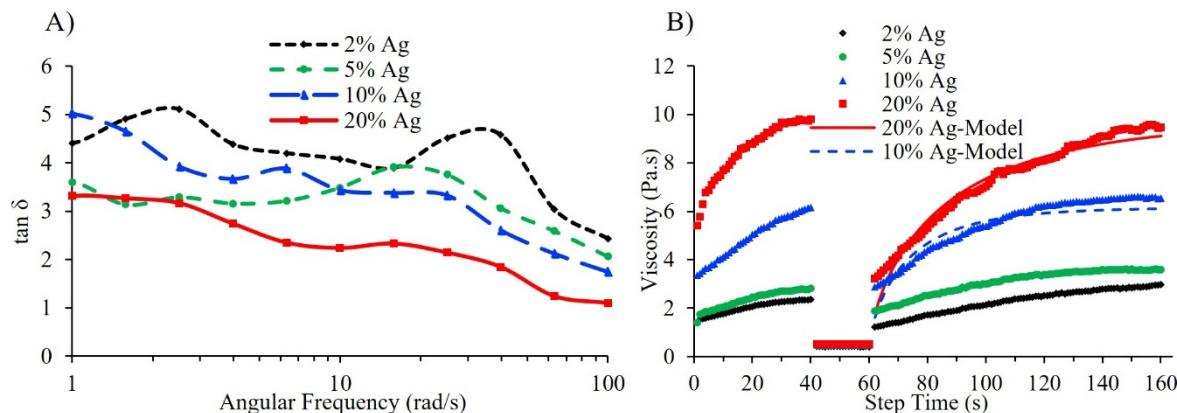
Figure 5. (**A**) tan δ (ratio of viscous modulus to elastic modulus) for conductive ink with different silver nanostructure contents. (**B**) Peak hold test for conductive ink with different silver nanostructure contents (high shear rate = 400 1/s and low shear rate = 0.1 1/s).

Nevertheless, for all Ag nanostructure contents and for the whole angular frequency spectrum, tan δ is higher than one, meaning that the viscous response is still dominant compared to the elastic response even for the highest angular frequencies. There is a "cross-over frequency" where the value of G′ equalizes G″, and tan δ becomes equal to 1. After this frequency, the elastic response will be more dominant rather than the viscous response. However, this frequency was not reached in the range of angular frequency used in this study.

Peak Hold Test: High-Shear Rate Printing

In the peak hold test, the ink is first subjected to a low shear rate, simulating ink at rest, and then subjected to a high shear rate, simulating ink under increased stress during printing, and then back to the low shear rate, simulating ink at rest or recovery after printing. This test is very useful for printing applications such as screen printing, inkjet printing, and direct writing or 3D printing because it can simulate the flow of the ink during the printing process, and therefore determines whether the ink is suitable for such applications. The peak hold test was performed for the inks with Ag nanostructures content of 2, 5, 10, and 20 wt.%. The sample was first subjected to low shear rate at 0.1 1/s for 40 s, followed by high shear rate at 400 1/s for 20 s, and then back to 0.1 1/s for 100 s. Figure 5B shows the peak hold test results for different Ag nanostructure contents at room temperature (25 °C). As demonstrated, the overall viscosity of the ink increases as the Ag nanostructure content is increased. However, it takes longer for the higher Ag nanostructure content ink to retain its original viscosity. By using the build-up structure model (Equation (1)), the characteristic time for transition can be identified. Table 2 shows the characteristic times of transition for Ag nanostructure contents of 10 and 20 wt.%. The characteristic time for transition in the case of 20 wt.% Ag nanostructure content is almost twice of that of 10 wt.% Ag nanostructure content, which explains the longer time for viscosity retention. For 2 and 5 wt.% of Ag nanostructure contents, the structure build-up model did not provide a statistically significant R^2 value, and therefore could not fit the data. One possible reason for this may be the high shear rate; because high shear rates—particularly for low colloidal content—can cause structural deformation in the ink, which causes the experimental data to deviate from the structure build-up model. Nevertheless, in both 2, and 5 wt.% Ag nanostructure contents, the viscosity retains its original value (viscosity just before being subjected to the higher shear rate) in less than 60 s compared to 100 s for the 20 wt.% Ag nanostructure content. We used the 400 1/s shear rate, as a significantly high shear rate value to observe the thixotropic behavior of the ink at very high shear. The relatively long transition time caused by the 400 1/s shear rate suggests that this value may not be a proper shear rate in the printing process. When the shear rate increases, it also makes it harder for the ink to retain its original structure. Therefore, in this case, a lower shear rate is required to allow for a rapid transition.

Table 2. Stretched Exponential model parameters from the structure build-up model for 10 and 20 wt.% silver nanostructure contents.

Ag nanostructure content	10%	20%
Characteristic time τ (s)	13.75	27.04
r (dimensionless constant)	0.78	0.73
R^2	0.91	0.97

3.3.2. Effect of Temperature

Flow Sweep Test

The flow sweep test was repeated at 30 and 40 °C to observe the change in viscosity and shear-thinning behavior of the ink with respect to temperature. The frequency sweep, and the peak hold tests were done for the 20 wt.% Ag nanostructure content because 20 wt.% Ag nanostructure content was the most favorable condition for the direct writing application. Figure 6A shows the viscosity with respect to shear rate at 25, 30, and 40 °C. The curve for 25 °C is the Same provided in Figure 3. As demonstrated, the viscosity decreases by increasing the temperature. The decline in viscosity with respect to increasing shear rate is more rapid at lower temperatures; this behavior is similar to that of lower Ag nanostructure content ink.
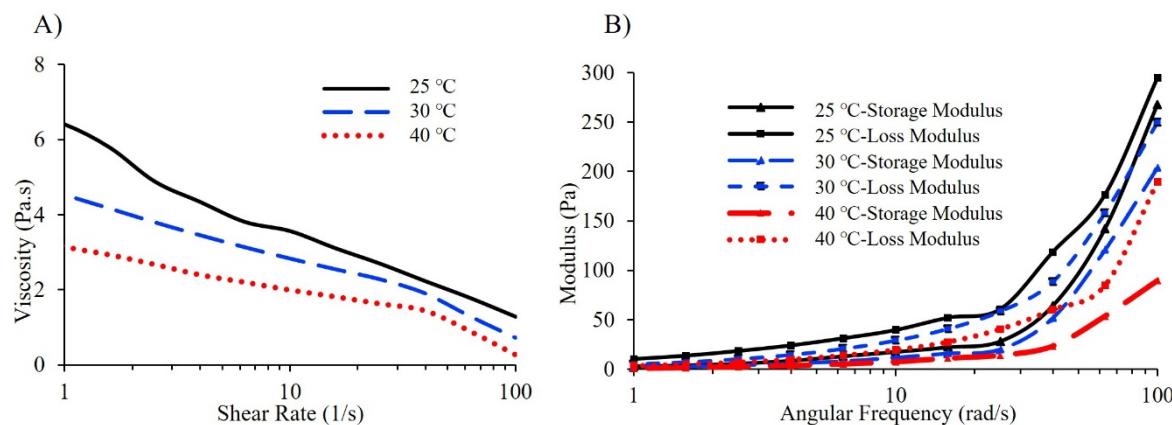
Figure 6. (**A**) Flow sweep test for conductive ink with 20 wt.% silver nanostructure content at different temperatures. (**B**) Frequency sweep test for conductive ink with 20 wt.% silver nanostructure content at different temperatures.

Frequency Sweep Test

The frequency sweep test was performed at 30 and 40 °C to observe the viscoelastic behavior of the ink. Figure 6B shows the storage and loss modulus of the ink with respect to angular frequency for different temperatures. As shown, both storage and loss modulus decrease as the temperature increases. With increasing temperature, overall resistance of the ink to deformation decreases. This is an important phenomenon and should be considered for printing processes at other temperatures than that of room temperature. To analyze the dominance of either the storage or loss modulus, tan δ with respect to angular frequency for all temperatures should be considered, and Figure 7A shows this comparison. As demonstrated, for all temperatures, tan δ decreases by increasing angular frequency, which means that the elastic response becomes more dominant at higher frequencies. However, there is a noticeable difference between the curves. After the frequency of approximately 4 rad/s, tan δ for inks at 30 and 40 °C surpasses the one at room temperature, meaning that at low frequencies, the viscous response is more dominant in the case of lower temperatures, while at higher frequencies, the elastic response is more dominant. This phenomenon occurs because at higher temperatures, the nanostructures can move slightly easier, and therefore allows the ink to maintain its viscous response.
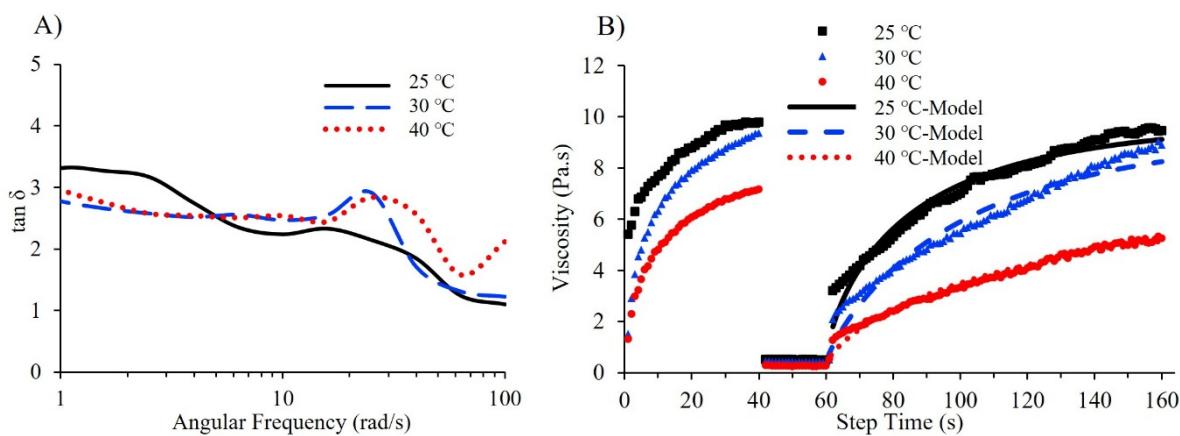
Figure 7. (**A**) Tan δ (ratio of viscous modulus to elastic modulus) for conductive ink with 20 wt.% silver nanostructure content at different temperatures. (**B**) Peak hold test for conductive ink with 20 wt.% silver nanostructure content at different temperatures (high shear rate = 400 1/s and low shear rate = 0.1 1/s).

Peak Hold Test: High-Shear Rate Printing

Similar to the peak hold test performed for different Ag nanostructure contents at room temperature, the peak hold test was performed to observe the shear thinning thixotropic behavior of the ink at different temperatures. Figure 7B shows the peak hold test results for the viscosity sketched with respect to time at different temperatures. In all cases, the ink experiences a relatively high transition time to retain its original viscosity. To compare the characteristic times for transition, the build-up structure model was used to fit the data for three temperatures. Table 3 shows the model parameters for all temperatures.

Table 3. Stretched Exponential model parameters from the structure build-up model for different temperatures.

Temperature	25 °C	30 °C	40 °C
Characteristic time τ (s)	27.04	42.37	75.72
r (dimensionless constant)	0.73	0.86	0.73
R^2	0.97	0.96	0.98

3.3.3. Printing Simulation: Low-Shear Rate Printing

To simulate the printing process, the situation that the ink undergoes inside the printer needs to be analyzed in detail. In a syringe-piston system, where the ink is squeezed through a cylindrical tube, the shear rate for a shear-thinning material can be calculated by the Rabinowitsch-Mooney correction relation as shown in Equation (4) [43].

$$\dot{\gamma}_w = \frac{Q}{\pi r^3}[3 + \frac{1}{n}] \tag{4}$$

where Q is the flowrate inside the tube (mm³/s), r is the tube radius (mm), $\dot{\gamma}_w$ is the shear rate at the wall of the tube (1/s), and n is the dimensionless power law index, which will be derived from the power-law as shown in Equation (5).

$$\sigma = k\dot{\gamma}^n \tag{5}$$

where σ is the shear stress (pa), $\dot{\gamma}$ is the shear rate (1/s), k is the consistency index (pa.s), and n is the power-law index. The power-law equation relates shear rate and shear stress for a non-Newtonian fluid. In the case of $n = 1$, the fluid is Newtonian, in the case of $n > 1$, the fluid has a shear-thickening behavior, and in the case of $n < 1$, the fluid has a shear-thinning behavior. The rheometer was used to simulate the printing process by performing the peak hold test on the AgNW-based ink, with 20 wt.% Ag nanostructure content. To do so, n should be calculated by fitting the power-law equation (Equation (5)) with the experimental data. Figure 8A shows shear stress vs. shear rate for the experimental data (obtained by flow sweep test with the rheometer) and the fitted model. After calculating n, Equation (4) was used to calculate the shear rate inside the main tube of the printer. With n being equal to 0.58, the shear rate was 22.24 1/s inside the main tube. After the shear rate is calculated, the peak hold test can be performed using the calculated shear rate value. It was assumed that the printing process has already reached a steady state. It was also assumed that the shear rate within the nozzle and tube fittings can be neglected compared to the shear rate within the main tube. This assumption was made because the time the ink is

under shear stress inside the nozzle and tube fittings is a fraction of a second, and therefore negligible compared to 34.53 s in the main tube. Therefore, a consistent shear rate of 22.24 1/s was used for the high-shear rate step in the peak hold test, which lasted for 34.53 s. The low shear rate, simulating the ink at rest, was considered as 0.1 1/s. The first low-shear rate step lasted for 40 s, and the second low-shear rate step lasted for 100 s. The test was done at room temperature as the printing process is also performed at room temperature. Figure 8B shows the peak hold test performed for the ink with 20 wt.% silver nanostructure content. As demonstrated, after undergoing stress at 22.24 1/s for 34.53 s, the ink follows smooth transition back to its original viscosity. The structure build-up model was used to fit the experimental data after high shear rate removal. The characteristic time for transition in this case was equal to 1.78 s, which is significantly lower compared to the one previously calculated for 20 wt.%-Ag nanostructure-content ink, undergoing 400 1/s shear rate. This suggests that the low shear rate of 22.24 1/s allows for a rapid and smooth transition during the ink printing process.
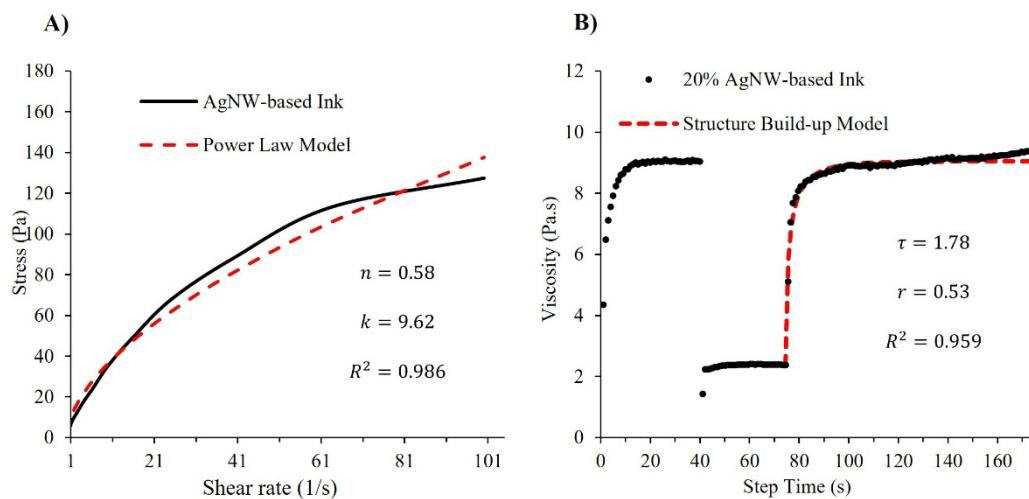

Figure 8. (**A**) Shear stress vs. shear rate, and the fitted power-law model for the tannic acid-synthesized AgNWs-based conductive ink (result obtained by the flow sweep test). Ag nanostructure content: 20 wt.%. (**B**) Peak hold test for tannic acid-synthesized AgNWs-based conductive ink with Ag nanostructure content of 20 wt.% (high shear rate = 22.24 1/s and low shear rate = 0.1 1/s).

4. Conclusions

This study presents a high-yield (90%), environmentally friendly, and cost-effective method for synthesizing AgNWs at room temperature. The synthesis process involved the use of tannic acid and silver nitrate, with the reaction being moderated by UV-visible light emission. Additionally, the approach demonstrated sustainability as a key feature. It was demonstrated that the production cost per gram of AgNWs can be decreased by at least 31.72% compared to the polyol process. Such a reduction in cost greatly enables the utilization of AgNWs in the realm of large-scale conductive ink manufacturing. The use of white fluorescent light for small-scale synthesis of AgNWs may face challenges when scaled up due to varying light intensity and distribution. Future work could focus on optimizing light delivery in larger reactors to ensure consistent reaction conditions. Furthermore, the rheological behavior of AgNW-based conductive ink for printing applications was investigated by performing rheological tests at different contents of silver nanostructure and temperatures. The conductive ink demonstrated a shear-thinning thixotropic behavior for all silver nanostructure contents (2, 5, 10, and 20 wt.%), and all temperatures (25, 30, and 40 °C). Three general rheological tests were performed, namely, the flow sweep, frequency sweep, and peak hold tests. The flow sweep test revealed the shear-thinning behavior of the ink, indicating a decrease in viscosity with increasing shear rates. This decline in viscosity was more pronounced for higher silver nanostructure contents and lower temperatures. The frequency sweep test illustrated the viscoelastic behavior of the ink and its overall resistance to deformation. The results demonstrated that higher silver nanostructure contents led to increased storage and loss modulus in the ink, resulting in greater resistance to deformation. It was demonstrated that, in general, the viscous response dominates over the elastic response, regardless of the silver nanostructure content and temperature. However, with higher silver nanostructure contents, the elastic response becomes more pronounced, particularly with increasing oscillation frequency. Additionally, at 25 °C, the ink exhibits a stronger viscous response at lower oscillation frequencies compared to the behavior observed at 30 and 40 °C. At higher oscillation frequencies, the elastic response was more dominant for the ink at 25 °C compared to 30 and 40 °C.

The peak hold tests indicated that the time for viscosity and shape retention after exposure to high shear rate (400 1/s) was longer for ink samples with higher silver nanostructure contents and higher temperatures. Finally, to simulate the direct writing process, a peak hold test was conducted on the environmentally friendly AgNW-based ink using a custom laboratory printer. The ink exhibited a smooth transition in retaining its structure after being subjected to the shear rate of 22.24 1/s during printing process. This transition occurred much more rapidly when using the direct writing procedure compared to the ink subjected to a high shear rate of 400 1/s. This indicates that direct writing is better suited for printing the ink with low colloidal content due to its lower shear rate, whereas screen printing is more favorable for printing high-content and high-viscosity ink due to its utilization of high shear rates. In conclusion, the cost-effective synthesis of AgNWs proves to be extremely valuable for large-scale production of conductive ink. This is supported by both the economic analysis and the rheological tests conducted on the prepared conductive ink.

References

1. Hasan, M.M.; Hossain, M.M. Nanomaterials-patterned flexible electrodes for wearable health monitoring: A review. *J. Mater. Sci.* **2021**, *56*, 14900–14942. https://doi.org/10.1007/s10853-021-06248-8.

2. Manjakkal, L.; Núñez, C.G.; Dang, W.; Dahiya, R. Flexible self-charging supercapacitor based on graphene-Ag-3D graphene foam electrodes. *Nano Energy* **2018**, *51*, 604–612. https://doi.org/10.1016/j.nanoen.2018.06.072.

3. Lin, C.H.; Fu, H.C.; Cheng, B.; Tsai, M.L.; Luo, W.; Zhou, L.; Jang, S.H.; Hu, L.; He, J.H. A flexible solar-blind 2D boron nitride nanopaper-based photodetector with high thermal resistance. *NPJ 2D Mater. Appl.* **2018**, *2*, 23. https://doi.org/10.1038/s41699-018-0070-6.

4. Tseberlidis, G.; Trifiletti, V.; Le Donne, A.; Frioni, L.; Acciarri, M.; Binetti, S. Kesterite solar-cells by drop-casting of inorganic sol–gel inks. *Sol. Energy* **2020**, *208*, 532–538. https://doi.org/10.1016/j.solener.2020.07.093.

5. Lee, S.; Jang, J.; Park, T.; Park, Y.M.; Park, J.S.; Kim, Y.K.; Lee, H.K.; Jeon, E.C.; Lee, D.K.; Ahn, B.; et al. Electrodeposited silver nanowire transparent conducting electrodes for thin-film solar cells. *ACS Appl. Mater. Interfaces* **2020**, *12*, 6169–6175. https://doi.org/10.1021/acsami.9b17168.

6. Gonzalez-Garcia, L.; Maurer, J.H.M.; Reiser, B.; Kanelidis, I.; Kraus, T. Ultrathin gold nanowires for transparent electronics: Breaking barriers. *Procedia Eng.* **2016**, *141*, 152–156. https://doi.org/10.1016/j.proeng.2015.08.1120.

7. Yang, X.; Du, D.; Wang, Y.; Zhao, Y. Silver nanowires inks for flexible circuit on photographic paper substrate. *Micromachines* **2018**, *10*, 22. https://doi.org/10.3390/mi10010022.

8. Yang, L.; Xu, X.; Yuan, Y.; Li, Z.; He, S. Meter-scale transparent conductive circuits based on silver nanowire networks for rigid and flexible transparent light-emitting diode screens. *Opt. Mater. Express* **2019**, *9*, 4483–4496. https://doi.org/10.1364/OME.9.004483.

9. Sun, Y.; Gates, B.; Mayers, B.; Xia, Y. Crystalline silver nanowires by soft solution processing. *Nano Lett.* **2002**, *2*, 165–168. https://pubs.acs.org/doi/10.1021/nl010093y.

10. Parente, M.; Van Helvert, M.; Hamans, R.F.; Verbroekken, R.; Sinha, R.; Bieberle-Hütter, A.; Baldi, A. Simple and fast high-yield synthesis of silver nanowires. *Nano Lett.* **2020**, *20*, 5759–5764. https://doi.org/10.1021/acs.nanolett.0c01565.

11. Shi, Y.; He, L.; Deng, Q.; Liu, Q.; Li, L.; Wang, W.; Xin, Z.; Liu, R. Synthesis and applications of silver nanowires for transparent conductive films. *Micromachines* **2019**, *10*, 330. https://doi.org/10.3390/mi10050330.

12. Staples, C.A.; Williams, J.B.; Craig, G.R.; Roberts, K.M. Fate, effects and potential environmental risks of ethylene glycol: A review. *Chemosphere* **2001**, *43*, 377–383. https://doi.org/10.1016/S0045-6535(00)00148-X.

13. Zeng, P.; Tian, B.; Tian, Q.; Yao, W.; Li, M.; Wang, H.; Feng, Y.; Liu, L.; Wu, W. Screen-printed, low-cost, and patterned flexible heater based on Ag fractal dendrites for human wearable application. *Adv. Mater. Technol.* **2019**, *4*, 1800453. https://doi.org/10.1002/admt.201800453.

14. Faddoul, R.; Reverdy-Bruas, N.; Blayo, A. Formulation and screen printing of water based conductive flake silver pastes onto green ceramic tapes for electronic applications. *Mater. Sci. Eng. B Solid-State Mater. Adv. Technol.* **2012**, *177*, 1053–1066. https://doi.org/10.1016/j.mseb.2012.05.015.

15. Ke, S.H.; Xue, Q.W.; Pang, C.Y.; Guo, P.W.; Yao, W.J.; Zhu, H.P.; Wu, W. Printing the ultra-long Ag nanowires inks onto the flexible textile substrate for stretchable electronics. *Nanomaterials* **2019**, *9*, 686. https://doi.org/10.3390/infrastructures4020020.

16. Li, W.; Yang, S.; Shamim, A. Screen printing of silver nanowires: Balancing conductivity with transparency while maintaining flexibility and stretchability. *NPJ Flex. Electron.* **2019**, *3*, 13. https://doi.org/10.1038/s41528-019-0057-1.

17. He, X.; Shen, G.; Xu, R.; Yang, W.; Zhang, C.; Liu, Z.; Chen, B.; Liu, J.; Song, M. Hexagonal and square patterned silver nanowires/PEDOT composite grids by screen printing for uniformly transparent heaters. *Polymers* **2019**, *11*, 468. https://doi.org/10.3390/polym11030468.

18. Hemmati, S.; Barkey, D.P.; Gupta, N. Rheological behavior of silver nanowire conductive inks during screen printing. *J. Nanoparticle Res.* **2016**, *18*, 249. https://doi.org/10.1007/s11051-016-3561-4.

19. Liang, J.; Tong, K.; Pei, Q. A water-based silver-nanowire screen-print ink for the fabrication of stretchable conductors and wearable thin-film transistors. *Adv. Mater.* **2016**, *28*, 5986–5996. https://doi.org/10.1002/adma.201600772.

20. Patil, P.; Patil, S.; Kate, P.; Kulkarni, A.A. Inkjet printing of silver nanowires on flexible surfaces and methodologies to improve the conductivity and stability of the printed patterns. *Nanoscale Adv.* **2021**, *3*, 240–248. https://doi.org/10.1039/d0na00684j.

21. Huang, Q.; Al-Milaji, K.N.; Zhao, H. Inkjet printing of silver nanowires for stretchable heaters. *ACS Appl. Nano Mater.* **2018**, *1*, 4528–4536. https://doi.org/10.1021/acsanm.8b00830.

22. Lee, H.H.; Chou, K.S.; Huang, K.C. Inkjet printing of nanosized silver colloids. *Nanotechnology* **2005**, *16*, 2436–2441. https://doi.org/10.1088/0957-4484/16/10/074.

23. Liu, Z.; Su, Y.; Varahramyan, K. Inkjet-printed silver conductors using silver nitrate ink and their electrical contacts with conducting polymers. *Thin Solid Films* **2005**, *478*, 275–279. https://doi.org/10.1016/j.tsf.2004.11.077.

24. Finn, D.J.; Lotya, M.; Coleman, J.N. Inkjet printing of silver nanowire networks. *ACS Appl. Mater. Interfaces* **2015**, *7*, 9254–9261. https://doi.org/10.1021/acsami.5b01875.

25. Kuzmenko, V.; Karabulut, E.; Pernevik, E.; Enoksson, P.; Gatenholm, P. Tailor-made conductive inks from cellulose nanofibrils for 3D printing of neural guidelines. *Carbohydr. Polym.* **2018**, *189*, 22–30. https://doi.org/10.1016/j.carbpol.2018.01.097.

26. Barnes, H.A. Thixotropy—A review. *J. Nonnewton Fluid Mech.* **1997**, *70*, 1–33. https://doi.org/10.1016/S0377-0257(97)00004-9.

27. Mallik, S. Study of the Time-Dependent Rheological Behaviour of Lead-Free Solder Pastes and Flux Mediums Used for Flip-Chip Assembly Applications. Ph.D. Thesis, University of Greenwich, London, UK, 2009.

28. Hemmati, S.; Barkey, D.P.; Gupta, N.; Banfield, R. Synthesis and characterization of silver nanowire suspensions for printable conductive media. *ECS J. Solid State Sci. Technol.* **2015**, *4*, 3075–3079. https://doi.org/10.1149/2.0121504jss.

29. Rudež, R.; Pavlič, J.; Bernik, S. Preparation and influence of highly concentrated screen-printing inks on the development and characteristics of thick-film varistors. *J. Eur. Ceram. Soc.* **2015**, *35*, 3013–3023. https://doi.org/10.1016/j.jeurceramsoc.2015.04.035.

30. Smay, J.E.; Gratson, G.M.; Shepherd, R.F.; Cesarano, J.; Lewis, J.A. Directed colloidal assembly of 3D periodic structures. *Adv. Mater.* **2002**, *14*, 1279–1283. https://doi.org/10.1002/1521-4095(20020916)14:18<1279::AID-ADMA1279>3.0.CO;2-A.

31. Nair, N.M.; Daniel, K.; Vadali, S.C.; Ray, D.; Swaminathan, P. Direct writing of silver nanowire-based ink for flexible transparent capacitive touch pad. *Flex. Print. Electron.* **2019**, *4*, 045001. https://doi.org/10.1088/2058-8585/ab4b04.

32. Martin, G.D.; Hoath, S.D.; Hutchings, I.M. Inkjet printing—The physics of manipulating liquid jets and drops. *J. Phys. Conf. Ser.* **2008**, *105*, 012001. https://doi.org/10.1088/1742-6596/105/1/012001.

33. Yan, P.; Brown, E.; Su, Q.; Li, J.; Wang, J.; Xu, C.; Zhou, C.; Lin, D. 3D Printing Hierarchical Silver Nanowire Aerogel with Highly Compressive Resilience and Tensile Elongation through Tunable Poisson's Ratio. *Small* **2017**, *13*, 1701756. https://doi.org/10.1002/smll.201701756.

34. Compton, B.G.; Lewis, J.A. 3D-printing of lightweight cellular composites. *Adv. Mater.* **2014**, *26*, 5930–5935. https://doi.org/10.1002/adma.201401804.

35. Kaabipour, S.; Hemmati, S. Green, sustainable, and room-temperature synthesis of silver nanowires using tannic acid—Kinetic and parametric study. *Colloids Surfaces A Physicochem. Eng. Asp.* **2022**, *641*, 128495. https://doi.org/10.1016/j.colsurfa.2022.128495.

36. Kaabipour, S.; Hemmati, S. Continuous, green, and room-temperature synthesis of silver nanowires in a helically-coiled millifluidic reactor. *Colloids Surfaces A Physicochem. Eng. Asp.* **2023**, *659*, 130806. https://doi.org/10.1016/j.colsurfa.2022.130806.

37. Hemmati, S.; Barkey, D.P. Parametric study, sensitivity analysis, and optimization of polyol synthesis of silver nanowires. *ECS J. Solid State Sci. Technol.* **2017**, *6*, 132–137. https://doi.org/10.1149/2.0141704jss.

38. U.S Energy Information Administration (2024). Available online: https://www.eia.gov/electricity/monthly/epm_table_grapher.php?t=epmt_5_6_a (accessed on 5 January 2025).

39. Hong, H.; Jiyong, H.; Moon, K.S.; Yan, X.; Wong, C.P. Rheological properties and screen printability of UV curable conductive ink for flexible and washable E-textiles. *J. Mater. Sci. Technol.* **2021**, *67*, 145–155. https://doi.org/10.1016/j.jmst.2020.06.033.

40. Dzisah, P.; Ravindra, N.M. Modeling of Rheological Properties of Metal Nanoparticle Conductive Inks for Printed Electronics. In *TMS 2021 150th Annual Meeting & Exhibition Supplemental Proceedings*; Springer International Publishing: Berlin/Heidelberg, Germany, 2021; pp. 964–979. https://doi.org/10.1007/978-3-030-65261-6_86.

41. Yoon, I.S.; Oh, Y.; Kim, S.H.; Choi, J.; Hwang, Y.; Ju, B.K. 3D Printing of Self-Wiring Conductive Ink with High Stretchability and Stackability for Customized Wearable Devices. *Adv. Mater. Technol.* **2019**, *4*, 1900363. https://doi.org/10.1002/admt.201900363.

42. Hatala, M.; Gemeiner, P.; Hvojnik, M.; Mikula, M. The effect of the ink composition on the performance of carbon-based conductive screen printing inks. *J. Mater. Sci. Mater. Electron.* **2019**, *30*, 1034–1044. https://doi.org/10.1007/s10854-018-0372-7.

43. Ahmed, S.F.; Hasan, A.R. Rheology of low-rank coal-water slurries at both high and low shear rates. *Fuel* **1993**, *72*, 763–769. https://doi.org/10.1016/0016-2361(93)90077-F.

Article

Efficient Synthesis of Liquid Photonic Crystal by Electrically-Driven Colloid Concentration

Xiaodong Lu [1,†], Huimin Zhu [1,†], Sheng Chen [1], Ximeng Lv [1], and Jianping Ge [1,2,*]

[1] State Key Laboratory of Petroleum Molecular & Process Engineering, Shanghai Key Laboratory of Green Chemistry and Chemical Processes, School of Chemistry and Molecular Engineering, East China Normal University, Shanghai 200062, China

[2] Institute of Eco-Chongming, Shanghai 202162, China

* Correspondence: jpge@chem.ecnu.edu.cn

† These authors contributed equally to this work.

Abstract: Liquid photonic crystal (LPC) is a promising new material in the field of sensing, display, printing, and coating due to its unique fluidity, metastability, and reversibility in colloidal assembly. However, it is a big challenge to prepare LPC materials in an efficient, controllable, and eco-friendly way. In this work, an electrically-driven colloid concentration process was developed for the efficient synthesis of LPC. The key for the synthesis was that the electrophoretic process produced a locally concentrated but "agglomeration-free" colloidal

solution, which spontaneously turned to LPC after being kept standing for a few minutes. The synthesis possessed good universality and reproducibility for LPCs composed of different particles and solvents. Its efficiency could be improved by tuning the particles' surface charge, the dielectric constant and viscosity of the solvent, as well as the external field conditions. More importantly, it could be developed into a large-scale and green process without chemical wastes compared to the previous synthetic methods.
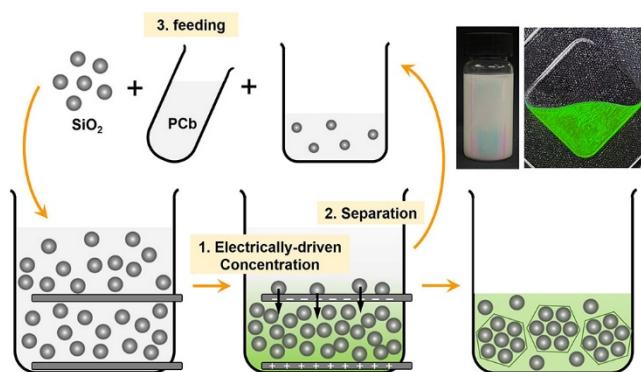
Keywords: liquid photonic crystal; electrically-driven concentration; agglomeration-free; colloidal assembly; green synthesis

1. Introduction

Liquid photonic crystal (LPC) is a colloid-based photonic structure in solution. It can be considered as a mixture of the "solvent-wrapped colloidal microcrystals" and the "saturated colloidal solution" [1–4]. The former crystalline phase renders the colloidal system photonic bandgap and characteristic structural colors. While the latter amorphous phase stabilizes the ordered particle arrangement and retains the fluidity for the system at the same time. The LPC is usually converted from a highly concentrated colloidal solution, where the particles spontaneously precipitate to form colloidal crystals driven by entropy increase. On the other hand, the formed LPC only has a metastable structure so that it easily changes back to the concentrated colloidal solution under external disturbance. The aforementioned fluidity, metastability, and reversible assembly-disassembly make LPC a special colloidal system that arouses great interest in the recent research of photonic crystals.

The LPC materials are widely used in photonic sensing [5–8], optical devices [9–12], and PC synthesis [13–16] due to the above properties. First of all, the LPC is intrinsically a responsive material as its photonic properties and structural color are influenced by many physical and chemical stimuli. For example, Joo and Kang et al. [17] reported an electrically responsive LPC composed of $Fe_3O_4@SiO_2$ particles and solvent propylene carbonate (PCb). The $(Fe_3O_4@SiO_2)$/PCb LPC showed different colors at different voltages because it flexibly changed its interparticle spacing to satisfy the balance between the interparticle net repulsion and electrophoretic packing force applied to the particles. For another instance, Zhu and Ge et al. [8] developed a mesopore detection reagent based

on SiO_2/(ethylene glycol) LPC. The absorption of solvent by mesopore substance changes the bandgap of LPC so that the reflection wavelength change could be used to reveal the pore volume, average pore size, and pore size distribution. Furthermore, the LPC is also a good precursor for the synthesis of solid PC and responsive PC [18–21] on different substrates because it separates the traditional PC synthesis into two steps, which addresses the conflict between synthetic efficiency and PC crystallinity. For example, Li and Shao et al. [14] utilized Polystyrene (PS)/H_2O LPC as the major component of color pastes to construct PC on textile substrates. Benefiting from the pre-assembly of particles in the LPC precursor, the shear-induced coating technique enabled efficient manufacture of large-area PC films with high crystallinity.

In the past decades, great efforts have been made to synthesize LPC in an efficient and controllable way. A traditional method is "waiting" for the spontaneous precipitation of colloidal particles from the colloidal solution [22–24]. Luck et al. [23] prepared PS/H_2O LPC with this method and demonstrated that the liquid's color originated from the ordered arrangement of particles. However, the synthetic efficiency of this method is a big concern, as several hours and even days are usually required for LPC formation. Recently, Ge et al. [4] developed an "evaporation-driven colloid concentration" process to prepare LPCs in different solvents. They well dispersed the particles in a mixing solvent and removed the volatile solvent by thermal treatment, which eventually produced the LPC in the high boiling-point solvent. The synthetic efficiency was significantly improved as the highly concentrated colloidal system led to a larger entropy increase after colloidal assembly and thereby accelerated the formation of LPC. Later, they developed a "liquid-liquid extraction" process [25] to prepare LPC, where the highly concentrated colloidal solution was achieved by extraction of solvent from the well-dispersed but diluted colloidal solution. Compared to the abundant methods to prepare solid PCs on different substrates, the synthetic route of LPC was very limited. The reported methods faced great challenges, such as the low synthetic efficiency, the requirement of high bp solvent, the consumption of large amount of extractant, etc. Therefore, there was an urgent need to develop efficient, universal, and environmentally benign method for LPC synthesis.

In this work, an electrically-driven colloid concentration process was developed for the efficient synthesis of LPC. Based on our previous research experience [4,25], the key point of the LPC synthesis was forming the highly concentrated but "agglomeration-free" colloidal system by controllable operations. The particles for colloidal assembly usually possessed high surface charges, which reminds us that the electrophoresis under an electric field was exactly the suitable process to realize particle concentration without agglomeration. In a typical synthesis, the particles were enriched near the electrode with opposite charges to form a locally concentrated solution, which was separated by the removal of supernatant and kept standing to form LPC spontaneously. In addition to the confirmation of each step in synthesis, we explored the factors influencing the synthesis efficiency, such as the particles' surface charge, the dielectric constant and viscosity of the solvent, and the electric field conditions. The universality and reproducibility of the current synthetic method were also investigated, Finally, a green synthetic process without chemical wastes was proposed to realize large-scale production of LPC materials.

2. Experimental Section

2.1. Materials

Tetraethyl orthosilicate (TEOS, 98%), aqueous ammonia ($NH_3 \cdot H_2O$, 28%), ethanol (EtOH, 99.7%), ammonium persulfate (APS, 99.5%), and isopropyl alcohol (C_3H_8O, 99.7%) were purchased from China National Pharmaceutical Group Co. Ltd. (Sinopharm) Propylene carbonate (PCb, 99%), n-Propanol (C_3H_8O, 99%), cerium(III) nitrate hexahydrate ($Ce(NO_3)_3 \cdot 6H_2O$, 99.5%), and acrylic acid (AA, 99%) were purchased from Aladdin Bio-Chem Technology Co. Ltd. Styrene (St, 99.5%) and ethylene glycol (EG, 99%) were purchased from Belling Technology Co. Ltd. Acetonitrile (C_2H_3N, 81.5%) and polyvinyl pyrrolidone (PVP, Mw = 29,000) were purchased from Sigma-Aldrich Co. Ltd. All chemicals were used as received without further treatment.

2.2. Synthesis of SiO₂ Particles

Monodisperse SiO_2 colloidal particles were prepared by a modified Stöber method. Taking the preparation of SiO_2 particles with a diameter of 180 nm as a typical example, 90 mL of TEOS was added to a mixture containing 1200 mL of EtOH, 48 mL of $NH_3 \cdot H_2O$, and 84 mL of H_2O. The above solution was continuously stirred for 9 h, during which the solution gradually changed from transparent to milky white. After the reaction, the particles were separated by centrifugation and the unreacted TEOS and $NH_3 \cdot H_2O$ were removed. After washing with ethanol 3 times, the SiO_2 particles were dispersed in EtOH for the following synthesis of liquid photonic crystals.

2.3. Synthesis of Polystyrene (PS) Particles

Monodisperse PS particles were prepared using an emulsion polymerization method. In a typical synthesis of PS particles with a diameter of 160 nm, 7 mL of styrene (St), 1 mL of acrylic acid (AA), and 100 mL of distilled water (H_2O) were mixed in a three-neck flask and stirred for 1 h under nitrogen flow. The mixture was then heated to 70 °C by heating mental. Once the temperature was stabilized, 1 mL of ammonium persulfate (APS) aqueous solution (0.1 g/mL) was added to the above mixture to initiate the polymerization. The solution was refluxed under nitrogen at 70 °C for 8 h, after which a milky white colloidal suspension was obtained. The PS particles were separated from the solution by centrifugation and washed with water 3 times. Finally, the PS particles were dispersed in water for the following synthesis of liquid photonic crystals. PS particles with different diameters could be synthesized by a similar process, except for the change of St and AA dosage or the reaction time.

2.4. Synthesis of CeO$_2$ Particles

Monodisperse CeO_2 particles were prepared by a high-temperature polyol process assisted with the SiO_2 nanoparticle seeds. Here, 0.087 g of arginine was added to the mixture of 5.5 mL of TEOS and 87 mL of water, which was continuously stirred under nitrogen protection at 70 °C for 24 h to obtain a transparent solution of SiO_2 nanoparticle seeds with a diameter of 20 nm. For the preparation of CeO_2 particles with a diameter of 130 nm, 24 g of $Ce(NO_3)_3 \cdot 6H_2O$, 12.5 g of PVP, 750 μL of the SiO_2 seed solution, and 100 mL of EG were mixed in a three-neck flask. The mixture was stirred under nitrogen and heated to react at 155 °C for 1 h, during which the transparent solution gradually transformed into a yellow colloidal suspension. After the reaction, the mixture was cooled down to room temperature, and the CeO_2 particles were separated by centrifugation and washed with EtOH three times. Finally, the CeO_2 particles were dispersed in EtOH for the following synthesis of liquid photonic crystals. Its diameter could be controlled by adjusting the dosage of $Ce(NO_3)_3 \cdot 6H_2O$ and PVP in synthesis.

2.5. Construction of the Electrophoretic Cell for Particle Concentration

In the prototype experiment, we used a plastic cuvette equipped with two parallel copper electrodes as the electrophoretic cell for particle concentration. The plastic cuvette was a commonly used consumable with size of 1 cm × 1 cm × 4.5 cm. Two Cu plates were horizontally inserted into the plastic cuvette with interspacing of 0.5 cm or 1 cm. The parallel Cu electrodes were fixed on the cuvette by epoxy adhesives, which also sealed the cuvette to avoid leakage of the solution.

2.6. Preparation of SiO$_2$/EtOH LPC by Electric Field-Assisted Concentration

In a typical process, a diluted SiO_2/EtOH solution with a particle volume fraction of 5% was first prepared by sufficient sonication of particles in solution. The initial particle volume fraction in a specific solvent should be low enough to ensure the generation of agglomeration-free colloidal suspension. Then, 1 mL of the SiO_2/EtOH solution was added to the cuvette with an electrode interspacing of 0.5 cm. After the Cu electrodes were connected to the direct current (DC) power source, a voltage of 8 V was applied to drive the SiO_2 particles moving toward the bottom electrode with a positive charge. After the electrophoresis for several minutes, a concentration gradient formed in the solution, and most of the particles were concentrated at the bottom between the electrodes. Finally, half of the solution above the upper electrode was carefully removed by pipette, leaving behind a concentrated but "agglomeration-free" colloidal solution to produce the LPC spontaneously.

2.7. Large-Scale Synthesis of SiO$_2$/PCb LPC by Green Approaches

The green synthesis of LPC was generally composed of the electrically-driven particle concentration, the separation of the supernatant colloidal solution, and the feeding of dried colloids and solvents. The first two steps were similar to the procedures above. In a typical process, 1 mL of SiO_2/PCb solution with particle volume fraction (f_{SiO2}) of 8.69% (m =177.3 mg) was used as the initial colloidal dispersion. Firstly, the SiO_2 particles in PCb were concentrated around the electrode with a positive charge by the application of an electric field. Secondly, liquid-liquid separation was used to obtain 0.5 mL of LPC and 0.5 mL of supernatant colloidal solution. The mass of SiO_2 particles in the LPC and the supernatant was measured to be 158 mg and 19.3 mg. Thirdly, 0.5 mL of fresh PCb and 158 mg of dry SiO_2 particles were added to the supernatant solution to form the diluted SiO_2/PCb solution for next-round preparation. Through multiple cycles of electrically-driven concentration, separation, and feeding, the f_{SiO2} of the LPC and the supernatant colloidal solution gradually achieved stable values, which were 15.49% and 1.89%, respectively.

2.8. Measurement of the Volume Fraction of Colloidal Particles in Solution

For a typical measurement of the volume fraction of SiO$_2$ particles (f_{SiO2}) in solution, 200 μL of the colloidal solution was taken for centrifugation at 11,000 rpm for 5 min, after which the supernatant solution was carefully removed. Then, the SiO$_2$ particles were placed in an oven at 120 °C and dried for 4 h to completely remove the residual solvent. The mass of the SiO$_2$ particles was accurately measured to determine their volume, which was finally used to calculate the particle volume fraction in the colloidal solution.

Characterizations: The reflection spectra were recorded by an Ocean Optics Maya 2000 Pro spectrometer coupled to a six-around-one reflection probe, where both the incident and reflective angle were fixed at 0°. The morphology and the size of the colloidal particles were characterized by the Hitachi S4800 scanning electron microscope (SEM). The optical microscopy images were collected by an Olympus BXFM reflection-type microscope operated in dark-field mode. The Zeta potential of colloidal particles in the solution was measured by Malvern Zetasizer Nano ZS90 at room temperature.

3. Results and Discussion

In a typical synthesis, the SiO$_2$/EtOH liquid photonic crystal (LPC) was prepared by an "agglomeration-free" concentration under an electric field, the removal of the supernatant colloidal solution, and a spontaneous colloidal assembly in the concentrated solution (Figure 1a). In the step of concentration, a diluted SiO$_2$/EtOH solution with a typical particle volume fraction (f_{SiO2}) of 5% was first loaded to the cuvette equipped with horizontally parallel copper electrode. Here, one electrode was placed at the bottom of the cuvette and the other was fixed at half height of the colloidal solution. According to the simulation of potential distribution, the colloid particles in the upper solution were majorly in Brownian motion and those in the bottom solution would migrate orientationally towards one electrode (Figure 1b). Once a voltage was applied, the negatively charged SiO$_2$ particles moved towards the bottom electrode with opposite charges, which produced a concentrated colloidal solution between two electrodes in a few minutes. In the step of separation, the upper solution containing very few particles was removed in the presence of the electric field, and the bottom solution was left standing to form LPCs with structural colors. Besides the photos for each step, the effective concentration of particles under the electric field could also be confirmed by the change of transmission spectra, where the transmittance of the concentrated solution was lower than that of the initial solution, and the transmittance of the supernatant was higher than the initial (Figure 1c,d).

It should be noted that the key point for the synthesis was the "agglomeration-free" concentration under an electric field. It is extremely difficult to form a highly concentrated colloidal solution without any agglomerations by directly dispersing a large amount of colloidal powder in the solvent. Therefore, the synthesis started from a diluted colloidal solution where the particles could be well dispersed at that low concentration. Then, the electrophoretic conditions were controlled to effectively but gently enrich the particles in the liquid environment. It led to the formation of a concentrated but "agglomeration-free" colloidal system, which was exactly the precondition for the LPCs.

In some cases, multistep concentration under an electric field helped produce LPCs with larger f_{SiO2} and higher crystallinity. Here, we investigated the regulations in the multistep concentration of SiO$_2$/EtOH through the change in f_{SiO2}, the concentration efficiency (f_n/f_{n-1}), and the reflection spectra (Figure 1e–g). As the concentration time increased from 1 to 3, the SiO$_2$ particles were gradually enriched in ethanol and the f_{SiO2} increased from the original 5.8% to 12%, 22%, and 35%, respectively (Table S1). Meanwhile, the concentration efficiency defined as the ratio of f_{SiO2} after and before the concentration decreased from 2.1 to 1.5 probably because the increase in viscosity inhibited the movement of colloidal particles under the same electric field. Along with the three-step synthesis, the reflection wavelength of the as-made LPC blue shifted from 813 nm to 745 nm and 672 nm because the increase of f_{SiO2} significantly decreased the lattice spacing of colloidal crystals. At the same time, the reflection intensity became stronger as the increase of f_{SiO2} also favored the assembly of particles into a more ordered structure. Based on the above experiments, the electrically-driven multistep concentration could be used to prepare LPCs with different bandgaps and structural colors. It was also useful to prepare some LPCs that required a very high f_{SiO2} to achieve the spontaneous colloidal assembly.
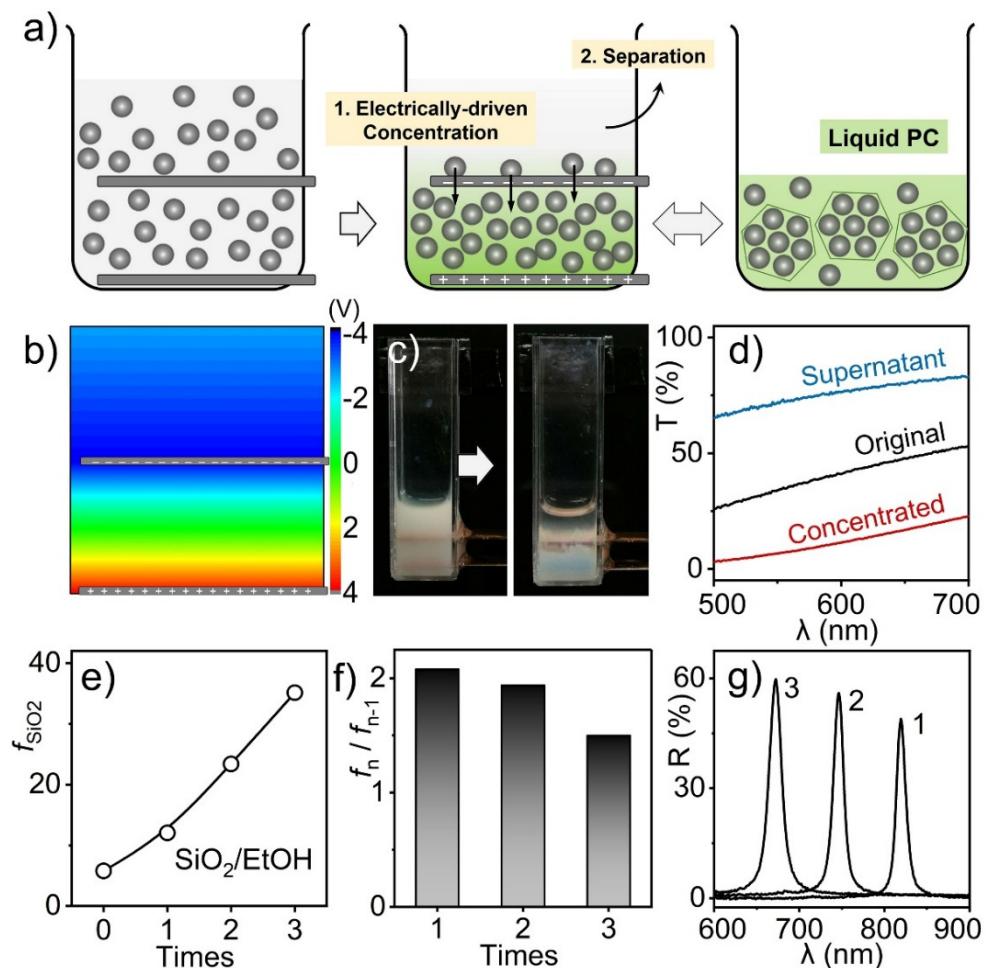
Figure 1. Synthesis of LPC by electrically-driven colloid concentration. (**a**) Scheme for the synthesis of LPC through electrically-driven concentration followed by liquid-liquid separation; (**b**) the simulated distribution of the potential in the solution; (**c**) the photo of the SiO$_2$/EtOH colloidal solution before and after concentration; (**d**) the transmission spectra of the originally diluted colloidal solution, the concentrated colloidal solution, and the supernatant; the evolution of (**e**) the particle volume fraction (f_{SiO2}), (**f**) the concentration factor (f_n/f_{n+1}), and (**g**) the reflection spectra of the generated LPC after 3 times of concentration.

The highly concentrated SiO$_2$/EtOH colloidal solution prepared by electrically-driven concentration exhibited typical characteristics of the liquid photonic crystals. First of all, the SiO$_2$/EtOH LPC was a fluid with two phases coexisted, where the structural color originated from the crystalline phase (Figure 2a–f). As proved by the previous study, the LPC was composed of a crystalline and an amorphous phase, which referred to the solvent-wrapped colloidal crystals and the saturated colloidal dispersion, respectively. These two phases could be directly recognized as the colored and the colorless domains in the microscope image. They could also be confirmed by the difference in their microscale reflection spectra, where the reflection intensity of the crystalline phase was higher. When the LPC was carefully dried in the air, these two phases were retained so one could observe the ordered and disordered particle arrangement in their SEM images. For the second feature, the LPC was a metastable structure, which allowed reversible colloidal assembly and disassembly (Figure 2g–i). In the absence of external disturbance, the SiO$_2$/EtOH colloidal solution spontaneously formed the SiO$_2$/EtOH LPC in several seconds. While the LPC quickly turned back to the colloidal solution if the LPC was mechanically disturbed. When these two processes occurred alternatively, the reflection intensity rose and fell periodically, which indicated that the assembly and disassembly were fully reversible.
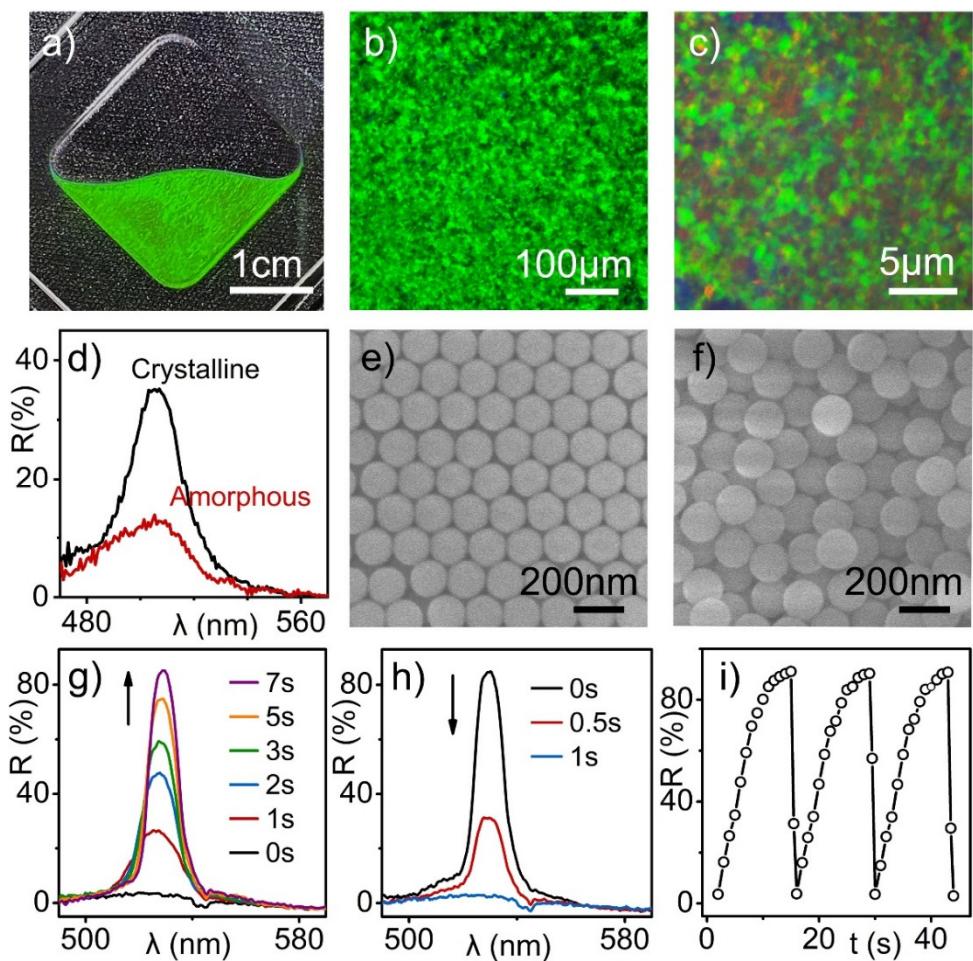
Figure 2. Characteristics of the SiO$_2$/EtOH LPC. (**a–c**) Digital photos and optical microscope images of the SiO$_2$/EtOH LPC; (**d–f**) microscopic reflection spectra of the crystalline and amorphous region of the LPC and the SEM images of the corresponding region after careful drying; (**g–i**) reversible colloidal assembly and disassembly proved by the periodic change of the reflection intensities.

Since the LPC synthesis was achieved by the particle electrophoresis and the electrically-driven colloid concentration, the properties of the colloids and solvent as well as the external field conditions became the key factors to ensure the formation of LPC and improve the synthetic efficiency. For the LPC formation, the solvents were usually polar solvents and the particles had ionizable groups so that the particles could have adequate strong surface charge to realize the colloidal assembly through electrostatic repulsion. Furthermore, the external voltage should be as low as possible to avoid electrochemical reactions during the synthesis. For the synthetic efficiency, one could find solutions in the well-known electrophoresis formula (Equation (1)). In this equation, the particle migration speed (v) is proportional to the particles' surface potential (ζ), the solvent's dielectric constant (ε), and the applied voltage (E). Meanwhile, the speed is inversely proportional to the distance between two electrodes (d) and the solvent's viscosity (η). Therefore, any adjustment that favored the increase of υ would improve the synthetic efficiency (Figure 3a). In the following discussion, we investigated the strategies to improve the efficiency in the aspects of colloidal particles, the solvent medium, and the electric field conditions.

$$v = (\zeta \cdot \varepsilon \cdot E)/(k \cdot \pi \cdot d \cdot \eta) \tag{1}$$

Firstly, the particle with a high surface charge was favorable to the efficiency of LPC synthesis. Here, we dispersed SiO$_2$, polystyrene (PS), or CeO$_2$ particles in EtOH to form a diluted colloidal solution, which was used to prepare LPC via electrically-driven concentration under the same conditions. The particle volume fraction (f_p) was continuously monitored in three concentrations and the total concentration factors (TCF) were calculated to indicate the synthetic efficiency. The experiment suggested that the f_p increased along with the electrically-driven concentration in all cases. The TCF for SiO$_2$/EtOH, PS/EtOH, and CeO$_2$/EtOH solution were then calculated to be 8.7, 6.3, and 3.0, respectively (Figure 3b,c). The decrease in TCF was believed to be tightly related to the surface charge of the particles, where the ζ of SiO$_2$, PS, and CeO$_2$ particles were measured to be −40 mV, −37 mV, and

+30 mV, respectively. Among them, SiO$_2$ particles possessed the highest surface charges, which led to the fastest migration speed, facilitated the concentration of colloids under the electric field, and eventually improved the synthetic efficiency.
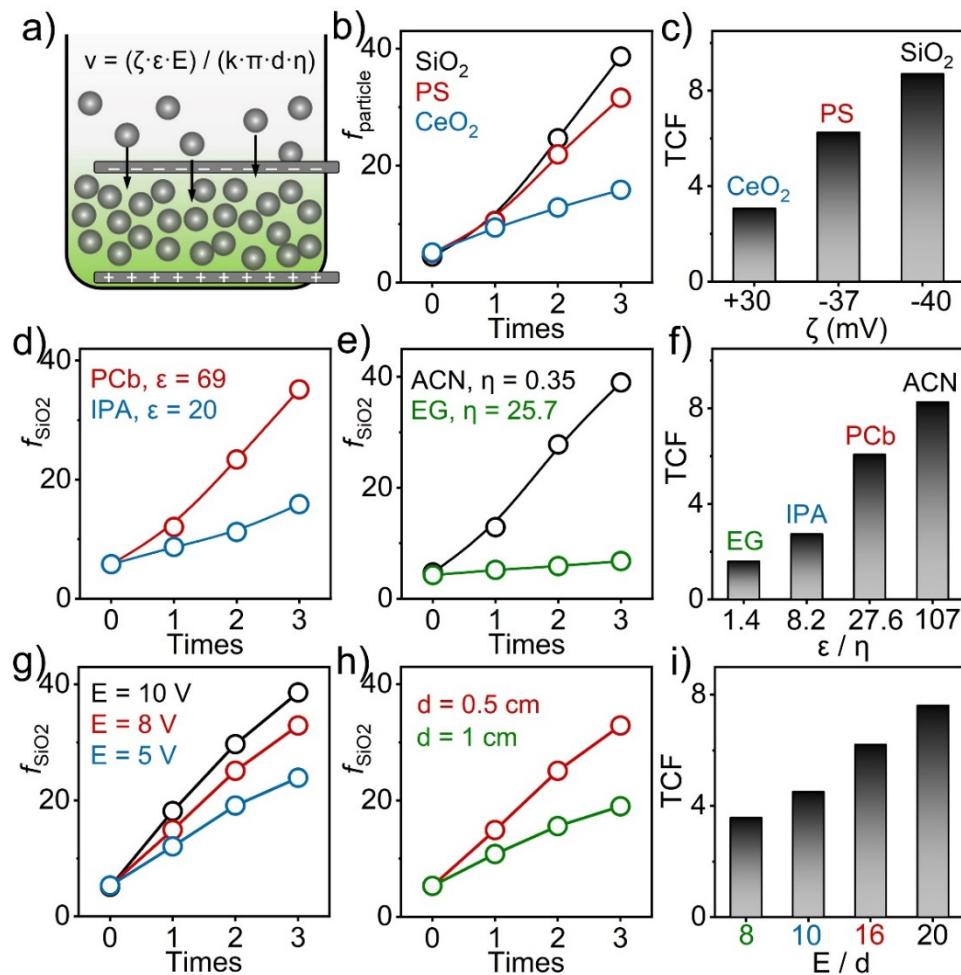

Figure 3. Factors influencing the synthetic efficiency. (**a**) Schematic diagram showing that the efficiency of LPC synthesis was determined by the particle migration speed; (**b**,**c**) evolution of the particle volume fraction in 3 times of concentration and the total concentration factor (TCF) for the ethanol solution of CeO$_2$, PS, and SiO$_2$ particles with different zeta potentials (ζ); (**d**–**f**) evolution of the f_{SiO2} for four colloidal solutions composed of different solvents and the independence of TCF upon the ratio of dielectric constant and viscosity (ε/η); (**g**–**i**) evolution of the f_{SiO2} under different electric field conditions and the independence of TCF upon the ratio of the external voltage and the electrode spacing (E/d).

Secondly, the solvent with a high dielectric constant and low viscosity also favored the efficiency of LPC synthesis. Here, we designed SiO$_2$/propylene carbonate (PCb) and SiO$_2$/isopropyl alcohol (IPA) diluted solutions for LPC synthesis under the same condition, where PCb and IPA possessed close viscosities (η = 2.50, 2.43) but different dielectric constants (ε = 69.0, 19.9) (Figure 3d, Table S2). After three rounds of electrically-driven concentration, the f_{SiO2} in PCb (35.1%) was much higher than that in IPA (15.9%), which suggested that a large dielectric constant accelerated the migration of colloidal particles and then improved the concentration efficiency. Similarly, we designed SiO$_2$/acetonitrile (ACN) and SiO$_2$/ethylene glycol (EG) solutions for LPC synthesis, where ACN and EG had close dielectric constants (ε = 37.5, 37.0) but different viscosities (η = 0.35, 25.7) (Figure 3e). After three continuous concentrations, the f_{SiO2} in ACN (39.0%) was much higher than that in EG (6.8%), which suggested that a low viscosity decreased the resistance of particle migration in solvent and thereby improved the concentration efficiency. Since every solvent had different ε and η, one could combine their influence with the ε/η ratio according to Equation (1) (Figure 3f). When the 4 SiO$_2$ colloidal systems were compared in the concentration efficiency, the TCF exactly increased with the increasing of the ε/η ratios, which again demonstrated the high dielectric constant and low viscosity favored the synthetic efficiency.

Thirdly, the efficiency of LPC synthesis could be improved by the application of a strong electric field. Here, we took the SiO$_2$/PCb solution for electrically-driven concentration and investigated the influence of the external voltage (E) and the electrode spacing (d) (Figure 3g,h). As the applied voltage increased from 5 V to 10 V, the f_{SiO2} after three rounds of concentration increased from 26% to 35%. In parallel control experiments, the f_{SiO2} after concentration increased from 24% to 28% when the electrode spacing decreased from 1 cm to 0.5 cm. When the above tests were arranged in the order of increasing E/d ratio, one could find that their TCF increased with the strength of the electric field (Figure 3i). It confirmed that a strong electric field was favorable to the fast migration of particles and the higher concentration efficiency. It should be noted that a voltage higher than 10 V was not acceptable as it caused particle agglomerations around the electrode. An electrode spacing smaller than 5 mm was not preferred either because it brought challenges to the liquid-liquid separation and decreased the production yield of the LPCs. In a word, the electrically-driven concentration method was suitable for preparing LPCs composed of highly charged particles and solvents with large dielectric constant and low viscosity. A voltage of 8 V, an electrode spacing of 0.5 cm, and a 10-min concentration could be the optimized conditions for most synthesis in the current work.
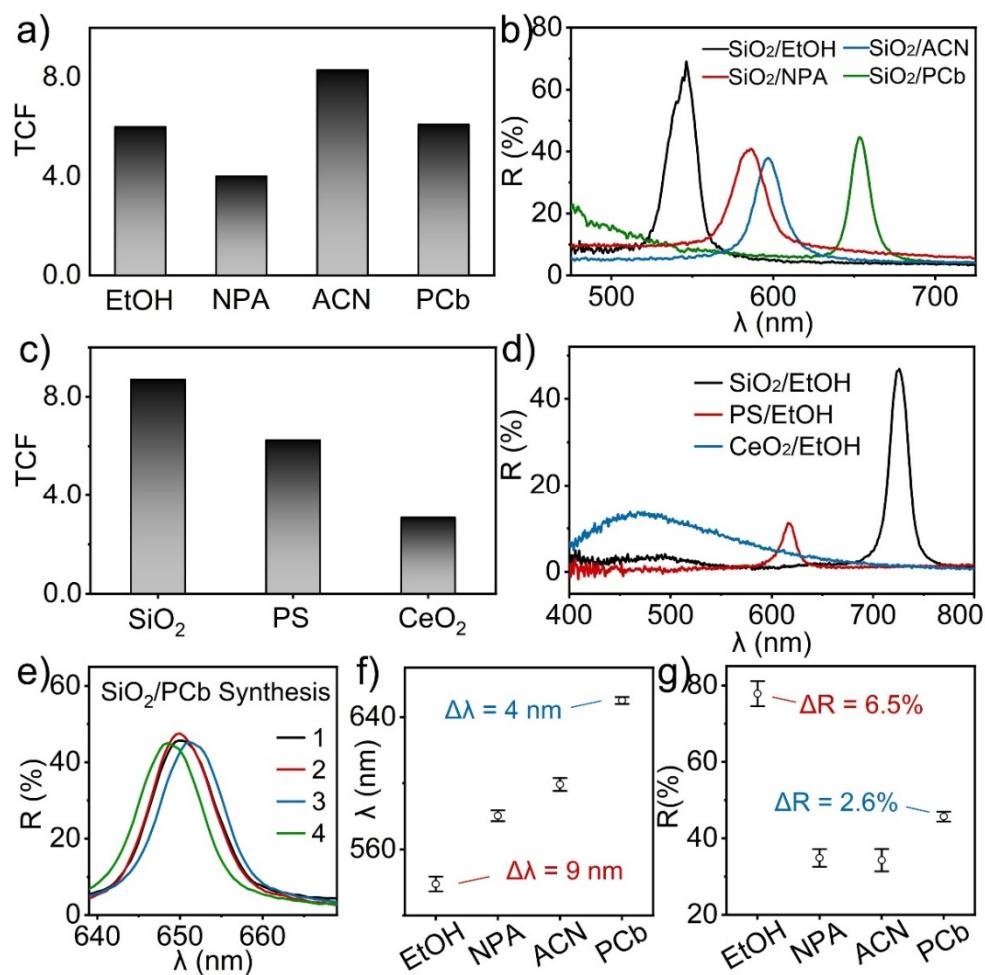
Figure 4. Universality and reproducibility of the synthetic method. (a–d) TCF values when synthesizing LPCs composed of different colloidal particles or solvents and the reflection spectra of the generated LPCs; (**e**) the reflection spectra of four SiO$_2$/PCb LPC samples prepared in different batches; (**f,g**) the deviation of λ and R for the LPCs prepared in different batches.

The electrically-driven colloid concentration was a convenient and universal method for the synthesis of LPCs composed of different particles and solvents. For example, this method was feasible for the synthesis of LPCs composed of SiO$_2$ particles and various solvents, including ethanol (EtOH), n-propanol (NPA), acetonitrile (ACN), and propylene carbonate (PCb) (Figure 4a,b). Starting with the same initial f_{SiO2} around 5.5%, the SiO$_2$ particles in all systems could be effectively concentrated by 3 cycles of electrophoresis, which could be proved by their TCFs around 4 to 5. The agglomeration-free concentration led to the formation of SiO$_2$/EtOH, SiO$_2$/NPA, SiO$_2$/ACN, and SiO$_2$/PCb LPCs, which was confirmed by the strong reflection peaks at different wavelengths due to the different particle fraction and different refractive indices. Furthermore, this method was also applicable to

LPCs composed of ethanol and different colloids, including SiO_2, PS, and CeO_2 (Figure 4c,d). The formation of SiO_2/EtOH, PS/EtOH, and CeO_2/EtOH LPCs was supported by their reflection spectra and TCF values after 3 cycles of electrically-driven concentration. The low crystallinity of the CeO_2/EtOH LPC was related to the relatively low surface charge of CeO_2 particles and thereby the low concentration efficiency under the electric field. It could be improved by enhancing the field strength or increasing the concentration times.

In addition to the universality, the current synthetic method also possessed satisfactory reproducibility in parallel productions (Figure 4e–g). Here, the syntheses of SiO_2/EtOH, SiO_2/NPA, SiO_2/ACN, and SiO_2/PCb LPCs were performed 4 times on different days, and the corresponding reflection spectra were recorded and compared to examine the reproducibility. The LPCs prepared in parallel batches had very close compositions and bandgap structures, which could be confirmed by the 4 reflection peaks with very close wavelengths and intensities. A little fluctuation in the reflection signal might originate from the evaporation of solvent during the synthesis, which slightly changed the particle volume fraction and eventually altered the lattice constant and the crystallinity of the generated LPCs. In our experiments, the synthesis of SiO_2/PCb LPC showed a smaller deviation than the other syntheses, which could be explained by its high boiling point and low volatility. Nevertheless, the reproducibility was satisfactory and it might be improved when the synthesis scale was further amplified.
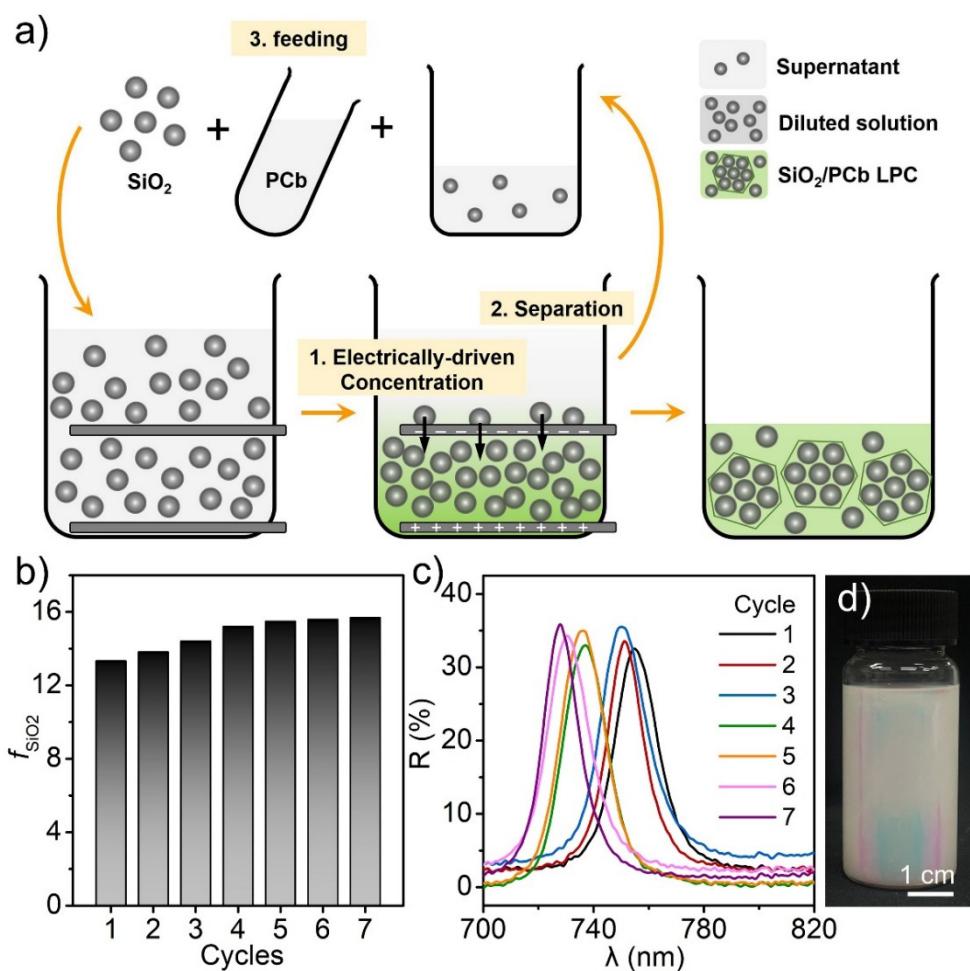
Figure 5. Large-scale and green synthesis of LPC. (a) Green synthetic route based on the electrically-driven concentration, liquid-liquid separation, and the feeding of colloids and solvent; **(b)** evolution of the f_{SiO2} in 7 times of closed-loop synthesis and **(c)** the reflection spectra of the corresponding LPC prepared by this method; **(d)** the photo of the concentrated SiO_2/PCb colloidal solution, which transforms into LPCs later.

Through the recycling of the supernatant colloidal solution from separation, the current method could be developed into a large-scale synthetic process for green production of LPC materials (Figure 5a). Taking the synthesis of SiO_2/PCb LPC as an example, the 1st round LPC product was achieved by an electrically-driven colloid concentration followed by a liquid-liquid separation of the supernatant colloidal solution. Since the supernatant solution contained a few SiO_2 particles (f_{SiO2} = 1.89%) and half of the PCb solvent, it could be mixed with the supplied PCb and SiO_2 powders to form a new "diluted colloidal solution" for the next round electrically-

driven concentration. With the joining of the feeding step, the whole synthesis became a closed loop, which continuously produced LPC materials on a large scale without wasting the colloids and solvent. In the practical experiment, the f_{SiO2} of the LPCs produced in each cycle gradually increased to a stable value ($f_{SiO2} = 15.49\%$), and the reflection of the LPC blue shifted to a stable wavelength accordingly, both of which confirmed the large-scale production of LPC material with a stable composition and optical property (Figure 5b–d). Unlike the traditional synthesis of LPCs based on evaporation-driven colloid concentration and liquid-liquid extraction, the current synthesis fully utilizes the source material and realizes zero emission in production.

4. Conclusions

In summary, an electrically-driven colloid concentration process was developed for the efficient synthesis of liquid photonic crystals (LPC). Colloidal particles first migrated towards the electrode with opposite charges and formed a locally concentrated but "agglomeration-free" solution. After removing the supernatant by liquid-liquid separation, the concentrated colloidal solution spontaneously formed LPC in the absence of external disturbance. Multiple concentrations could be performed to produce LPCs with larger f_{SiO2} and higher crystallinity. The as-prepared colloidal system exhibited typical characteristics of LPC including two-phase coexistence, structural color, metastable structure, and reversible colloidal assembly and disassembly. The "electrically-driven concentration" method was suitable for preparing LPCs composed of highly charged particles and solvents with large dielectric constant and low viscosity, as these conditions favored fast particle migration under the electric field. The voltage was set around 8 V to maintain the high efficiency and avoid electrochemical reactions. This method exhibited good universality and reproducibility for the synthesis of LPCs composed of different particles and solvents. More importantly, it could be developed into a large-scale and green synthetic process without chemical wastes through the recycling of the supernatant colloidal solution, which guaranteed the supply of responsive LPC material for related applications.

References

1. Chen, Y.; Zhang, C.B.; Zheng, Q.F.; Chen, Y. Separation-Cooperated Assembly of Liquid Photonic Crystals from Polydisperse Particles. *Chem. Commun.* **2018**, *54*, 13937–13940.

2. Guo, J.J.; Zhang, Y.L.; Li, X.Y.; Zhang, X.; Huang, Y.; Yu, M.L.; Shao, J.Z. Electrostatic Fence Induced Assembly of Low-Concentration Colloidal Nanospheres to Form Liquid Photonic Crystals. *J. Colloid Interface Sci.* **2025**, *679*, 1084–1094.

3. Kim, S.H.; Park, J.G.; Choi, T.M.; Manoharan, V.N.; Weitz, D.A. Osmotic-Pressure-Controlled Concentration of Colloidal Particles in Thin-Shelled Capsules. *Nat. Commun.* **2014**, *5*, 3068.

4. Yang, D.P.; Ye, S.Y.; Ge, J.P. Solvent Wrapped Metastable Colloidal Crystals: Highly Mutable Colloidal Assemblies Sensitive to Weak External Disturbance. *J. Am. Chem. Soc.* **2013**, *135*, 18370–18376.

5. Cai, J.Y.; Luo, W.; Pan, J.J.; Li, G.; Pu, Y.Y.; Si, L.Y.; Shi, G.P.; Shao, Y.X.; Ma, H.R.; Guan, J.G. Glucose-Sensing Photonic Nanochain Probes with Color Change in Seconds. *Adv. Sci.* **2022**, *9*, 2105239.

6. Hu, Y.; Tian, Z.Q.; Ma, D.K.; Qi, C.Z.; Yang, D.P.; Huang, S.M. Smart Colloidal Photonic Crystal Sensors. *Adv. Colloid Interface Sci.* **2024**, *324*, 103089.

7. Zhang, Y.X.; Ge, J.P. Liquid Photonic Crystal Detection Reagent for Reliable Sensing of Cu^{2+} in Water. *RSC Adv.* **2020**, *10*, 10972–10979.

8. Zhu, B.T.; Fu, Q.Q.; Chen, K.; Ge, J.P. Liquid Photonic Crystals for Mesopore Detection. *Angew. Chem. Int. Ed.* **2018**, *57*, 252–256.

9. Liu, Y.F.; Hou, X.Y.; Song, Y.L.; Li, M.Z. Bioinspired Reflective Display Based on Photonic Crystals. *Interdiscip. Mater.* **2024**, *3*, 54–73.

10. Liu, T.; Lin, H.Y.; Hou, D.X.; Wang, J.X.; Zeng, S.S.; Che, C.C.; Wu, X.J.; Guo, J.B. Electrically-Triggered Oblique Helicoidal Cholesterics with a Single-Layer Architecture for Next-Generation Full-Color Reflective Displays. *Adv. Funct. Mater.* **2024**, *34*, 2408855.

11. Shen, T.Z.; Perera, K.N.A.; Masud, A.R.; Priyadharshana, P.; Park, J.Y.; Wang, Q.H.; Hong, S.H.; Song, J.K. A Dual-Frequency Photonic Crystal Nanocolloid with Hue- and Brightness-Tunable Structural Colors. *Cell Rep. Phys. Sci.* **2023**, *4*, 101343.

12. Ran, X.X.; Ren, J.; Zhang, S.F.; Wu, Y.; Wu, S.L. Multicolor Electrochromic Display and Patterned Device Based on Hollow-SiO_2-Supported WO_3 Photonic Crystals. *ACS Appl. Mater. Interfaces* **2023**, *15*, 41763–41771.

13. Li, S.; Xiao, Y.S.; Shan, G.H.; Li, P.C.; Jia, L.X. Efficient Preparation of Single-Sided Structural Color Fabrics with Asymmetric Wettability, Angle-Dependence and Patternability Based on Liquid Photonic Crystals. *Dye. Pigment.* **2023**, *215*, 111302.

14. Li, Y.C.; Fan, Q.S.; Wang, X.H.; Liu, G.J.; Chai, L.Q.; Zhou, L.; Shao, J.Z.; Yin, Y.D. Shear-Induced Assembly of Liquid Colloidal Crystals for Large-Scale Structural Coloration of Textiles. *Adv. Funct. Mater.* **2021**, *31*, 2010746.

15. Wang, X.H.; Liang, X.H.; Li, Y.C.; Li, X.Y.; Liu, G.J.; Hu, M.G.; Liu, Y.J.; Huang, Y.; Zhou, L.; Zhou, W.L.; et al. Chameleon-Inspired Structural Coloration of Textiles with Non-Close-Packed Photonic Crystals for High Color Saturation and Color Fastness. *Chem. Eng. J.* **2024**, *483*, 149053.

16. Zhang, X.; Yin, T.; Ge, J.P. Thermochromic Photonic Crystal Paper with Integrated Multilayer Structure and Fast Thermal Response: A Waterproof and Mechanically Stable Material for Structural-Colored Thermal Printing. *Adv. Mater.* **2024**, *36*, 2309344.

17. Lee, I.; Kim, D.; Kal, J.; Baek, H.; Kwak, D.; Go, D.; Kim, E.; Kang, C.; Chung, J.; Jang, Y.; et al. Quasi-Amorphous Colloidal Structures for Electrically Tunable Full-Color Photonic Pixels with Angle-Independency. *Adv. Mater.* **2010**, *22*, 4973–4977.

18. Hu, Y.; Yang, D.P.; Ma, D.K.; Huang, S.M. Extremely Sensitive Mechanochromic Photonic Crystals with Broad Tuning Range of Photonic Bandgap and Fast Responsive Speed for High-Resolution Multicolor Display Applications. *Chem. Eng. J.* **2022**, *429*, 132342.

19. Hu, Y.; Yang, D.P.; Ma, D.K.; Huang, S.M. Liquid, Transparent, and Antideformable Thermochromic Photonic Crystals for Displays. *Adv. Opt. Mater.* **2022**, *10*, 2200769.

20. Li, Y.; Long, Y.; Yang, G.Q.; Tung, C.H.; Song, K. Tunable Amplified Spontaneous Emission Based on Liquid Magnetically Responsive Photonic Crystals. *J. Mater. Chem. C* **2019**, *7*, 3740–3743.

21. Li, Z.W.; Yin, Y.D. Stimuli-Responsive Optical Nanomaterials. *Adv. Mater.* **2019**, *31*, 1807061.

22. Clark, N.A.; Hurd, A.J.; Ackerson, B.J. Single Colloidal Crystals. *Nature* **1979**, *281*, 57–60.

23. Luck, W.A.P.; Stranski, I.N. Kristallstrukturen Aus Nichtmolekularen Bausteinen. *Phys. Blätter* **1967**, *23*, 304–313.

24. Yethiraj, A.; van Blaaderen, A. A Colloidal Model System with An Interaction Tunable from Hard Sphere to Soft and Dipolar. *Nature* **2003**, *421*, 513–517.

25. Wang, C.; Zhang, X.; Zhu, H.M.; Fu, Q.Q.; Ge, J.P. Liquid-Liquid Extraction: A Universal Method to Synthesize Liquid Colloidal Photonic Crystals. *J. Mater. Chem. C* **2020**, *8*, 989–995.

Perspective

Noble-Metal Nanocrystals: From Synthesis to Biomedical Applications

Yidan Chen [1], Emily Yan [2], and Younan Xia [2,*]

[1] School of Materials Science and Engineering, Georgia Institute of Technology, Atlanta, GA 30332, USA
[2] Wallace H. Coulter Department of Biomedical Engineering, Georgia Institute of Technology and Emory University, Atlanta, GA 30332, USA
* Correspondence: younan.xia@bme.gatech.edu

Abstract: Noble metals hold promises for a variety of biomedical applications due to their unique physical and biochemical properties. To unlock this potential, a significant amount of research has been dedicated to the controlled synthesis of noble-metal nanocrystals over the past two decades, with a particular emphasis on the production of Au and Ag nanocrystals with diverse and well-controlled shapes. The successful synthesis of noble-metal nanocrystals with tunable sizes, shapes, and morphologies allows researchers to explore their use in a range of biomedical applications, including contrast enhancement for an array of bioimaging modalities, facilitating stimuli-responsive drug delivery, and functioning as antimicrobial or anticancer agents.
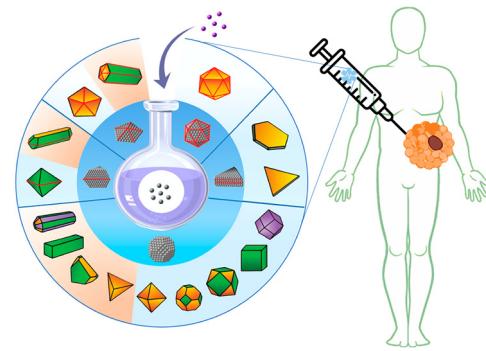
1. Introduction

Noble metals refer to ruthenium (Ru), rhodium (Rh), palladium (Pd), osmium (Os), iridium (Ir), platinum (Pt), and gold (Au). They are considered "noble" due to their resistance to corrosion and thus natural occurrence in the elemental form. Sometimes, silver (Ag), copper (Cu), and mercury (Hg) are also included as noble metals, albeit these elements typically occur in nature as sulfides. Noble metals have found widespread use in catalysis, electronics, photonics, and plasmonics. The increasingly efficient synthesis of noble-metal nanocrystals also renders new opportunities in a spectrum of biomedical applications [1], including sensing, imaging, diagnostics, controlled release, targeted drug delivery, advanced therapy, and antimicrobial coating. As a major advantage over other types of materials, the surface of noble-metal nanocrystals can be robustly modified with organic ligands to increase their biocompatibility, alter their biodistribution in vivo, and/or entail additional functionalities, such as targeting specific biomarkers overexpressed on the surface of malignant cells.

When used as nanocrystals, their properties and thus figures of merit in various applications can be tuned by optimizing their size, shape, and morphology or by varying the composition in the case of an alloy [1]. For nanocrystals based on Au, Ag, and Cu, they possess remarkable optical properties due to their ability to efficiently absorb and scatter light in the visible and near-infrared (NIR) regions, enabling applications in the context of localized surface plasmon resonance (LSPR) and surface-enhanced Raman spectroscopy (SERS). LSPR refers to the collective oscillation of conductive-band electrons upon excitation by light, whereas SERS enhances the sensitivity of Raman spectroscopy by leveraging the enhancement of local electric field to amplify the Raman scattering cross-section of molecules near the surface of nanocrystals. Both LSPR and SERS have facilitated the development of advanced biosensing techniques and imaging modalities, enhancing our ability to detect biomarkers and resolve malignant tissues.

Noble-metal nanocrystals have also shown promise in theranostics, a research theme that aims to integrate diagnosis with therapy. In theranostics, nanocrystals can serve as both imaging and therapeutic agents, making it feasible to simultaneously visualize and eradicate malignant cells. One such imaging modality is photoacoustic

tomography (PAT), which relies on optical absorption to generate ultrasound signals upon excitation by a pulsed laser. The exceptional absorption capability of Au-based nanocrystals positions them as a class of superior contrast agents for PAT [2]. In parallel, Au-based nanocrystals have been extensively explored as photothermal transducers for localized hyperthermia treatment. In this case, the heat derived from photothermal conversion can be used to destroy malignant cells and pathogens at the diseased site without affecting the surrounding healthy tissues. Position emission tomography (PET) is a non-invasive modality that relies on the positrons emitted from a radioactive isotope (e.g., ^{64}Cu) to produce gamma rays when they interact with tissues, allowing for the monitoring of physiological activities and measurement of changes in metabolic processes. To this end, Au-Cu alloy nanocrystals can be directly utilized as a radioactive tracer for PET when some of the ^{63}Cu atoms are substituted with ^{64}Cu.

2. Colloidal Synthesis of Noble-Metal Nanocrystals

Solution-phase synthesis is the most versatile and robust route for producing noble-metal nanocrystals (Figure 1a) [3]. The synthesis typically starts with the generation of metal atoms through the chemical reduction or thermal decomposition of a salt precursor. The concentration of the atoms continues to increase until it reaches the threshold for homogeneous nucleation. At this point, the atoms aggregate to generate small clusters, commonly referred to as nuclei, followed by their growth and evolution into seeds with well-defined internal structures [3,4]. For noble metals, the seeds generally adopt one of the following four internal structures: single-crystal, singly-twinned, multiply-twinned, and stacking-fault-lined [4]. The internal structure, in conjunction with kinetic and thermodynamic factors during the subsequent growth step, ultimately determines the shape taken by the nanocrystals. In general, one needs to optimize the precursor, reducing agent, capping agent, and stabilizer (including both the type and concentration) to obtain nanocrystals uniform in terms of both shape and size. Over the past decades, extensive research has been conducted to elucidate the mechanistic details involved in solution-phase syntheses and the protocols for reproducibly producing nanocrystals with controlled shapes, with a focus on those made of Au, Ag, Cu, Pd, Pt, and their alloys. Readers should consult the most recent literature to find the updated protocols.

Polycrystalline Au nanoparticles (AuNPs) with a quasi-spherical shape can be conventionally prepared by reducing HAuCl$_4$ in a solution phase (Figure 1b) [2]. Two of the established protocols were originally developed by Turkevich and Brust, respectively. In the Turkevich method, HAuCl$_4$ is reduced with sodium citrate in water at an elevated temperature (e.g., 100 °C). The size of the resulting AuNPs is mainly determined by the molar ratio between the reactants. A study by Peng and coworkers demonstrated that relatively uniform particles with sizes in the range of 20−40 nm could be obtained using this simple method [5]. As for the Brust method, it entails transferring the HAuCl$_4$ precursor into an organic solvent such as toluene and controlling the growth of the AuNPs with a thiol-based capping agent (e.g., 1-dodecanethiol) to obtain particles below 10 nm in size [2].

Unlike the quasi-spherical nanoparticles, Au nanospheres (AuNSs) can be made with a single-crystal structure while assuming a spherical shape that gives a circular projection under transmission electron microscopy (Figure 1c) [2]. To this end, our group developed a facile route for synthesizing AuNSs by utilizing Au clusters capped with hexadecyltrimethylammonium bromide (CTAB) as the initial seeds for a repeated growth process [6,7]. In a typical protocol, the initial seeds are mixed with a precursor such as HAuCl$_4$, a capping agent based on hexadecyltrimethylammonium chloride (CTAC), and a reductant such as ascorbic acid (AA) in water at room temperature. Through meticulous control of the reaction conditions, uniform AuNSs with tunable diameters in the range of 5−150 nm were consistently produced [6,7].

Another popular class of Au nanocrystals is nanorods (NRs), characterized by a distinctive anisotropic structure (Figure 1d). Among the various methods developed for AuNR synthesis, seed-mediated growth stands out due to its simplicity in procedure, readily tunable aspect ratio for the product, and high yield of NRs with a narrow size distribution. While specific chemicals and protocols may differ among various methods of seed-mediated growth, they typically involve two stages: the initial preparation of citrate-capped Au seeds by reducing HAuCl$_4$ precursor with a strong reductant such as NaBH$_4$ in water, followed by their introduction into a growth medium [8]. The growth medium usually consists of the precursor, a surface capping agent (e.g., CTAB) to stabilize the colloid and initiate/guide the anisotropic growth, and a moderately strong reductant such as AA [8]. To increase the uniformity and purity of the products, it is critical to introduce AgNO$_3$ or an aromatic additive like 5-bromosalicylic acid or 2,6-dihydroxybenzoic acid [2].

Characterized by their well-defined sharp corners, Ag nanocubes (Figure 1e) have received increasing attention in recent years for their applications in both LSPR and SERS [9]. Our group pioneered the one-pot polyol synthesis of Ag nanocubes by employing ethylene glycol (EG) as both the solvent and reductant [10]. Subsequently,

improved protocols were developed to yield large volumes of uniform Ag nanocubes with edge lengths up to 250 nm by switching the precursor from the commonly used $AgNO_3$ to CF_3COOAg [11], introducing a trace amount of Na_2S or NaHS to manipulate initial nucleation [12], and/or selectively removing the twinned seeds through the use of O_2/Cl^- (NaCl or KCl) to initiate oxidative etching [13].

As a more cost-effective alternative to Au and Ag nanocrystals due to the high abundance of Cu in Earth's crust [14], Cu nanocubes (Figure 1f) also exhibit tunable LSPR in the visible and NIR regions. The colloidal synthesis of Cu nanocubes is comparatively more challenging than that of Au and Ag nanocrystals due to the lower reduction potential of Cu and greater susceptibility to oxidation. In addition to one-pot methods, seed-mediated growth has been developed as a viable route for producing Cu nanocubes with controllable sizes. In one study, for example, 5-nm AuNSs were utilized as seeds to synthesize Au@Cu core-shell nanocubes with a uniform edge length tunable from 20−30 nm. The presence of the Au seeds effectively lowered the activation energy barrier to nucleation while increasing the conversion of the $CuCl_2$ precursor [15].
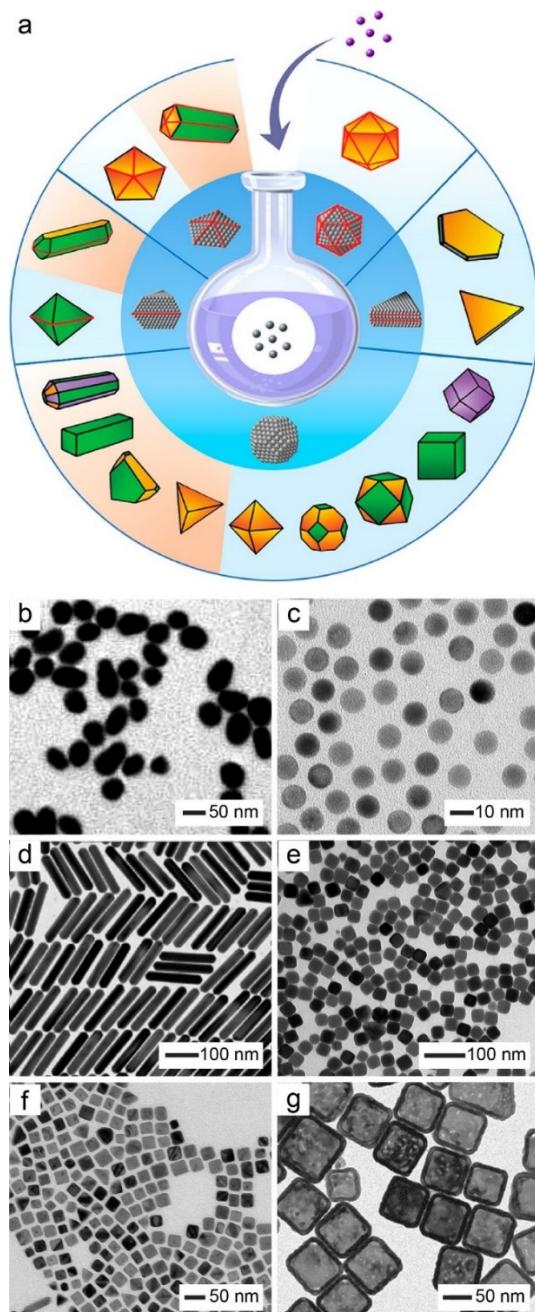
Figure 1. Colloidal synthesis of noble-metal nanocrystals. (**a**) Schematic showing the generation of nanocrystals with diverse and controllable shapes. (**b–g**) TEM images of various types of noble-metal nanocrystals: (**b**) Au nanoparticles; (**c**) Au nanospheres; (**d**) Au nanorods; (**e**) Ag nanocubes; (**f**) Au@Cu core-shell nanocubes; and (**g**) Au nanocages. (**a**) Reproduced with permission from [3]. Copyright 2023 Americal Chemical Society. (**b**) Reproduced with permission from [5]. Copyright 2007 Americal Chemical Society. (**c**) Reproduced with

Gold nanocages (AuNCs) represent a class of hollow nanocrystals characterized by ultrathin and porous walls, which are composed of either pure Au or Au-based alloys [18]. The pores in the walls can be engineered to create an "open or close" gating mechanism, allowing for controlled, on-demand release of a payload. The primary method for generating AuNCs involves the galvanic replacement reaction between Ag nanocubes and $HAuCl_4$ in water, a spontaneous reaction driven by the more positive standard reduction potential of $AuCl_4^-/Au$ (1.00 V) relative to that of Ag^+/Ag (0.80 V). One can conveniently produce AuNCs by titrating aqueous $HAuCl_4$ into an aqueous mixture containing Ag nanocubes and poly(vinyl pyrrolidone) (PVP). As Ag atoms are gradually oxidized and dissolved, Au atoms are formed and deposited on the surface of the nanocubes to generate AuNCs. When Ag nanocubes with sharp corners are used, the initial oxidation and dissolution of Ag occur on the side faces to generate small pinholes, which then act as anodes for further oxidation and dissolution. Meanwhile, the resultant Au atoms are conformally deposited on the side faces. As the reaction proceeds, the pinholes are closed due to atomic diffusion and direct Au deposition, leading to the formation of Au–Ag alloy nanoboxes. Subsequent removal of Ag from the walls through a dealloying process generates AuNCs with porous walls (Figure 1g). The size, shape, and wall thickness of the AuNCs can all be tailored by changing the Ag templates, introducing a proper surface capping agent (e.g., PVP), and varying the amount of $HAuCl_4$. As such, one can increase the diversity of AuNCs and enhance their optical and photothermal properties. When applied to in vivo studies, the size and shape of the AuNCs impact both their biodistribution and therapeutic efficiency.

3. Examples of Applications

Noble metals have been employed as therapeutic agents since ancient times. Recent studies of their distinctive physical and biochemical attributes, in conjunction with advancements in controlling their colloidal synthesis (as illustrated in Section 2), have reignited interest in employing their nanocrystals for a range of biomedical applications. Notable examples include their use as antimicrobial agents and as active components in diagnostics and cancer treatment.

Due to its wide accessibility and rapid responsiveness, point-of-care (POC) diagnosis holds increasing significance in the modern healthcare industry. When conjugated with ligands targeting specific analytes, AuNPs have found extensive use in POC diagnosis, spanning infectious virus detection, diabetes monitoring, pregnancy tests, cardiovascular disease assessment, and cancer screening [19]. Enabled by their unique LSPR properties, AuNPs can be detected using a variety of methods, including colorimetric, fluorescence, and SERS. For instance, commercial pregnancy tests use AuNPs conjugated with antibodies of hCG, a hormone excreted during early pregnancy [20], to create a red test line for the indication of a positive result (Figure 2a) [21]. Similarly, during the COVID-19 pandemic, AuNP-based molecular diagnostic kits were developed to enable rapid and cost-effective screening of infected individuals [22]. In this case, instead of antibodies, the AuNPs were functionalized with antisense oligonucleotides (ASOs) to target the N-gene of SARS-CoV-2, the virus responsible for the pandemic. The agglomeration of ASO-capped AuNPs in the presence of SARS-CoV-2 triggers a discernible color change from purple to blue, which can be easily observed by the naked eye (Figure 2b).

The LSPR properties of Au nanostructures have also been put to work for other biomedical applications. Researchers have demonstrated that the LSPR peaks of Au nanostructures could be precisely tuned to cover the entire visible and NIR regions by varying their sizes and morphologies, with the latter being particularly effective [18]. For instance, a remarkable redshift of the LSPR peaks was observed for AuNRs as their aspect ratios were increased while maintaining a constant width (Figure 3a) [23]. Similarly, AuNCs exhibited precisely tunable LSPR peaks into the NIR region when the wall thickness was adjusted by controlling the degree of galvanic replacement reaction (Figure 3b) [2]. Of particular importance for biomedical applications are Au nanostructures with LSPR peaks in the window of 650−900 nm, where water, blood, and soft tissues exhibit optical transparency, facilitating deep penetration for effective imaging and treatment [18].
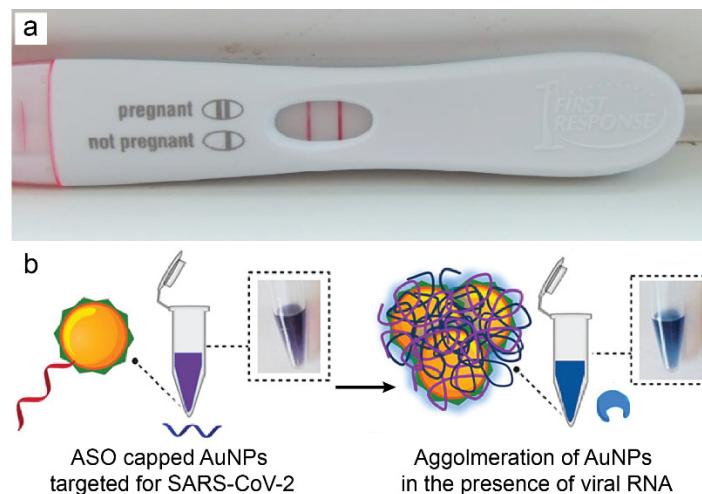
Figure 2. Use of Au nanoparticles as a colorant for point-of-care diagnosis. (**a**) Formation of red test lines in a commercial pregnancy test kit through the accumulation of Au nanoparticles. (**b**) Color change in a solution detectable by the naked eye due to the agglomeration of Au nanoparticles in the presence of SARS-CoV-2 RNA. (**a**) Adapted from [21]. (**b**) Reproduced with permission from [22]. Copyright 2020 American Science Society.
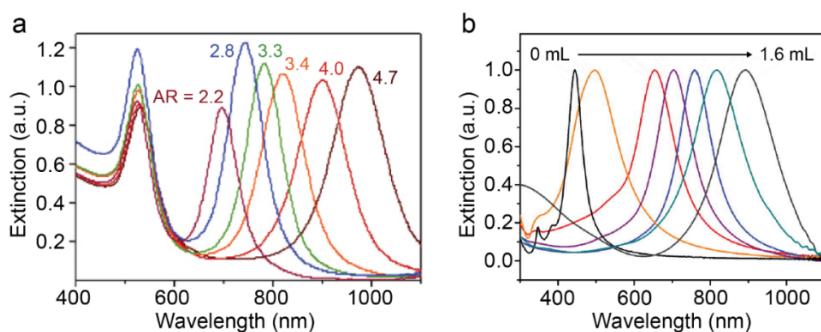
Figure 3. Tunable LSPR property of Au nanocrystals. The UV-vis-NIR spectra were recorded from aqueous suspensions of (**a**) Au nanorods with different aspect ratios (ARs) and (**b**) Au nanocages prepared by titrating different amounts of HAuCl4 (volume = 0−1.6 mL). (**a**) Reproduced with permission from [24]. Copyright 2006 the Royal Society of Chemistry. (**b**) Reproduced with permission from [25]. Copyright 2011 Wiley-VCH.

With their LSPRs tuned to the proper wavelength, the strong absorption of AuNCs has been harnessed for diverse theranostic applications, including optical imaging, controlled release, and drug delivery. In one study, AuNCs were used to actively target subcutaneous tumor tissue in mice, leading to pronounced enhancement in PAT imaging [26]. Specifically, the surface of the nanocages was conjugated with poly(ethylene glycol) (PEG) chains terminated in [Nle4, d-Phe7]-α-melanocyte-stimulating hormone ([Nle4, d-Phe7]-α-MSH)—a peptide capable of binding to receptors on melanoma cells (Figure 4a). After intravenous injection of [Nle4, d-Phe7]-α-MSH-AuNCs, PA images were recorded at 0, 3 and 6 h, respectively. The images in Figure 4b–d clearly indicate the gradual accumulation of the AuNCs inside the tumor to greatly enhance the PA signal.
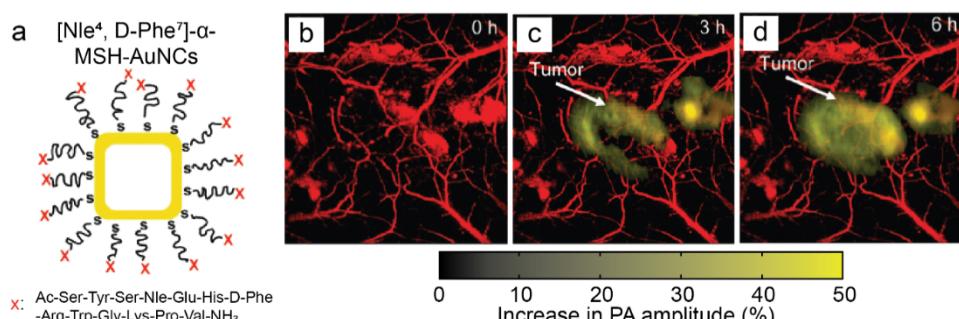
Figure 4. Use of Au nanocage as a contrast agent for photoacoustic (PA) imaging. (**a**) Schematic of the [Nle4,d-Phe7]-α-MSH-AuNCs. MSH: Melanocyte Stimulating Hormone. (**b–d**) PA images of the melanoma tissue

recorded at different time points (0, 3, and 6 h) post injection of [Nle4,d-Phe7]-α-MSH-AuNCs, with yellow and red corresponding to the melanoma and the surrounding vasculature. Reproduced with permission from [26]. Copyright 2010 Americal Science Society.

The strong NIR absorption of AuNCs also facilitates photothermal conversion for application in stimuli-triggered release. To this end, control can be achieved through two methods: either attaching gating polymer brushes to the surface of the AuNCs or filling the interior with a phase-change material (PCM), a substance that undergoes solid-to-liquid phase transition upon melting. In one approach, our group employed poly(N-isopropylacrylamide) (pNIPAAm)—a thermal-responsive polymer—to seal the pores on AuNCs [27]. As the local temperature increases due to the photothermal heating enabled by AuNCs, the polymer chains contract to allow the payloads to freely diffuse out through the pores. In another approach, our group loaded the cavity of the AuNCs with a PCM based on lauric acid. For the treatment of hypoxic cancer, 2,2′-azobis[2-(2-imidazolin-2-yl)propane] dihydrochloride (AIPH) was added into the PCM to generate AIPH–PCM–AuNCs (Figure 5a) [28]. Upon exposure to an NIR laser, the AuNCs were heated up to melt the PCM, simultaneously triggering the release and decomposition of AIPH. The free radicals derived from the decomposition of AIPH resulted in tumor cell apoptosis. As shown in Figure 5b, the amount of AIPH released is positively correlated with the intensity and duration of the laser. Furthermore, AIPH-induced reactive oxygen species (ROS) can be detected in A549 cancer cells through 2′,7′-dichlorodihydrofluorescein diacetate (DCFHDA) staining even under tumor hypoxia conditions (Figure 5c).
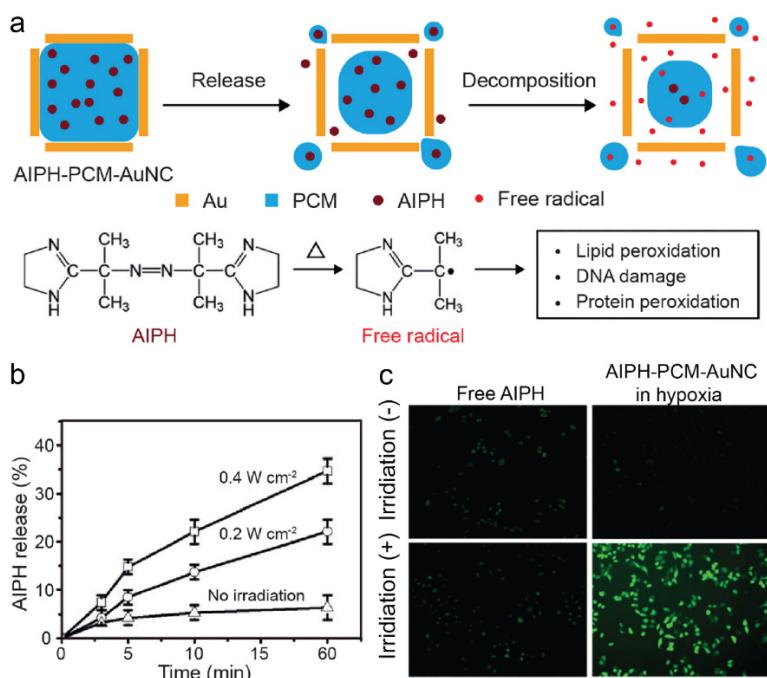
Figure 5. Use of Au nanocages for controlling the release of a therapeutic agent. (**a**) Schematic illustrating the controlled release of AIPH from the PCM loaded in the interior of Au nanocages upon laser irradiation. (**b**) Release profiles of AIPH upon laser irradiation at different irradiances. (**c**) Detection of AIPH-induced ROS in A549 cells by DCFHDA after laser irradiation for 30 min. (**a**) Reproduced with permission from [18]. Copyright 2020 the Royal Society of Chemistry. (**b**–**c**) Reproduced with permission from [28]. Copyright 2017 Wiley-VCH.

Silver is a common element used in biomedical applications. The antimicrobial activity of AgNPs has been extensively investigated. It is well-established that the nanoparticles could serve as effective growth inhibitors for various microorganisms, rendering them suitable for a range of medical devices and antimicrobial control systems. One study investigated AgNPs ranging from 5–25 nm in size while being supported on graphene oxide sheets, as confirmed by X-ray diffraction and electron microscopy [29]. The AgNPs effectively combat Gram-negative bacteria, with their effectiveness linked to their size and shape, showing promise for use in antimicrobial applications. As a relatively new modality, SERS imaging has benefited from AgNPs in biomedical applications such as the detection of specific biomarkers on cell surfaces for cancer diagnosis or tracking drug delivery [30]. Upon irradiation of AgNPs with a laser, enhanced electromagnetic fields are created in the vicinity of the nanoparticles to increase the Raman scattering cross-sections of molecules adsorbed on or near the nanoparticles, enabling highly sensitive detection through the fingerprinting of vibrational modes.

Among the radionuclides used for nanoparticle-based positron emission tomography (PET), ^{64}Cu occupies a unique position as it can be directly incorporated into Au nanocrystals through co-deposition, enabling precise control of radioactivity [31]. In one study, ^{64}Cu-doped AuNCs have been developed to enable image-guided therapy by combining the long half-life of ^{64}Cu for PET and the strong absorption of Au nanostructures in the NIR region for photothermal therapy. In a cancer mice model, both tumor targeting and PET imaging contrast enhancement were demonstrated, highlighting the potential of this unique class of Au-Cu alloy nanostructures for preclinical and translational applications (Figure 6) [32].
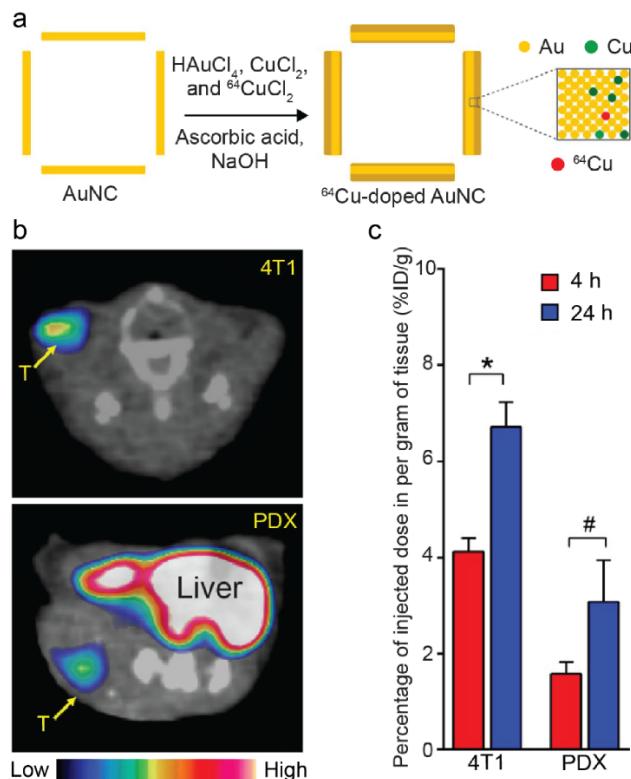
Figure 6. Use of ^{64}Cu-doped Au nanocages for PET. (**a**) Schematic illustrating the synthesis of ^{64}Cu-doped Au nanocages through co-deposition of Au, Cu, and ^{64}Cu atoms onto the walls of Au nanocages. (**b**) Transverse PET/CT images of the PEGylated, ^{64}Cu-doped Au nanocages in mice 4T1 and PDX tumor models recorded 24 h after injection. (**c**) Quantification of tumor uptake in both models, demonstrating effective accumulation of the nanocrystals at the tumor site. * $p < 0.0005$, # $p < 0.005$. Reproduced with permission from [32]. Copyright 2016 Wiley-VCH.

Due to the large atomic number, Ir nanocrystals have found use as a contrast agent for X-ray-based imaging and as an enhancer for radiotherapy. Small Ir nanoparticles (IrNPs) can be prepared using an aqueous method by reducing IrCl3 with NaBH4 without involving any surfactant or capping agent [33]. The as-obtained nanoparticles have promising potential for medical applications involving X-ray radiation. In vitro tests using Alamar Blue assay with liver and immune cells suggested that the IrNPs could be used safely in living organisms at concentrations of up to 100 μM.

In a set of studies, Pt-nanocluster assemblies (PtNAs) comprising a pH-sensitive polymer (octadecylamine-p(API-Asp)$_{10}$) and a liver cancer cell-targeting peptide have been demonstrated to successfully combat drug resistance and stem-like properties in liver cancer [34]. Significant death of liver cancer cells and the overcoming of chemotherapy medication resistance were achieved by PtNAs via the induction of DNA damage. The mechanism of these effects at the molecular level has also been investigated, suggesting that PtNAs hold promise for clinical treatment through the downregulation of highly expressed genes in liver cancer patients.

4. Conclusions and Outlook

The past two decades have witnessed remarkable advancement in the controlled synthesis of noble-metal nanocrystals, particularly Au and Ag, enabling precise manipulation of their sizes and morphologies. With their unique physiochemical properties and tunable architecture, engineered noble-metal nanostructures now serve as versatile tools in biomedical applications, supporting advanced bioimaging, stimuli-responsive drug delivery, and

antimicrobial or anticancer therapies. Despite this progress, challenges remain in improving synthesis scalability and investigating their long-term biocompatibility for successful clinical translation. By addressing the current limitations and exploring new research avenues, we can fully realize the immense promises noble-metal nanocrystals hold for improving diagnostics and therapies.

References

1. Cho, E.C.; Glaus, C.; Chen, J.; Welch, M.J.; Xia, Y. Inorganic Nanoparticle-Based Contrast Agents for Molecular Imaging. *Trends Mol. Med.* **2010**, *16*, 561–573. https://doi.org/10.1016/j.molmed.2010.09.004.

2. Yang, X.; Yang, M.; Pang, B.; Vara, M.; Xia, Y. Gold Nanomaterials at Work in Biomedicine. *Chem. Rev.* **2015**, *115*, 10410–10488. https://doi.org/10.1021/acs.chemrev.5b00193.

3. Xia, Y.; Xiong, Y.; Lim, B.; Skrabalak, S.E. Shape-Controlled Synthesis of Metal Nanocrystals: Simple Chemistry Meets Complex Physics? *Angew. Chem., Int. Ed.* **2009**, *48*, 60–103. https://doi.org/10.1002/anie.200802248.

4. Nguyen, Q.N.; Wang, C.; Shang, Y.; Janssen, A.; Xia, Y. Colloidal Synthesis of Metal Nanocrystals: From Asymmetrical Growth to Symmetry Breaking. *Chem. Rev.* **2022**, *123*, 3693–3760. https://doi.org/10.1021/acs.chemrev.2c00468.

5. Ji, X.; Song, X.; Li, J.; Bai, Y.; Yang, W.; Peng, X. Size Control of Gold Nanocrystals in Citrate Reduction: The Third Role of Citrate. *J. Am. Chem. Soc.* **2007**, *129*, 13939–13948. https://doi.org/10.1021/ja074447k.

6. Zheng, Y.; Ma, Y.; Zeng, J.; Zhong, X.; Jin, M.; Li, Z.-Y.; Xia, Y. Seed-Mediated Synthesis of Single-Crystal Gold Nanospheres with Controlled Diameters in the Range 5–30 nm and their Self-Assembly upon Dilution. *Chem. Asian J.* **2013**, *8*, 792–799. https://doi.org/10.1002/asia.201201105.

7. Zheng, Y.; Zhong, X.; Li, Z.; Xia, Y. Successive, Seed-Mediated Growth for the Synthesis of Single-Crystal Gold Nanospheres with Uniform Diameters Controlled in the Range of 5–150 nm. *Part. Part. Syst. Charact.* **2014**, *31*, 266–273. https://doi.org/10.1002/ppsc.201300256.

8. Huo, D.; Kim, M.J.; Lyu, Z.; Shi, Y.; Wiley, B.J.; Xia, Y. One-Dimensional Metal Nanostructures: From Colloidal Syntheses to Applications. *Chem. Rev.* **2019**, *119*, 8972–9073. https://doi.org/10.1021/acs.chemrev.8b00745.

9. Wang, Y.; Zheng, Y.; Huang, C.Z.; Xia, Y. Synthesis of Ag Nanocubes 18–32 nm in Edge Length: The Effects of Polyol on Reduction Kinetics, Size Control, and Reproducibility. *J. Am. Chem. Soc.* **2013**, *135*, 1941–1951. https://doi.org/10.1021/ja311503q.

10. Sun, Y.; Xia, Y. Shape-Controlled Synthesis of Gold and Silver Nanoparticles. *Science* **2002**, *298*, 2176–2179. https://doi.org/10.1126/science.1077229.

11. Zhang, Q.; Li, W.; Wen, L.-P.; Chen, J.; Xia, Y. Facile Synthesis of Ag Nanocubes of 30 to 70 nm in Edge Length with CF_3COOAg as a Precursor. *Chem. Eur. J.* **2010**, *16*, 10234–10239. https://doi.org/10.1002/chem.201000341.

12. Siekkinen, A.R.; McLellan, J.M.; Chen, J.; Xia, Y. Rapid Synthesis of Small Silver Nanocubes by Mediating Polyol Reduction with a Trace Amount of Sodium Sulfide or Sodium Hydrosulfide. *Chem. Phys. Lett.* **2006**, *432*, 491–496. https://doi.org/10.1016/j.cplett.2006.10.095.

13. Wiley, B.; Herricks, T.; Sun, Y.; Xia, Y. Polyol Synthesis of Silver Nanoparticles: Use of Chloride and Oxygen to Promote the Formation of Single-Crystal, Truncated Cubes and Tetrahedrons. *Nano Lett.* **2004**, *4*, 1733–1739. https://doi.org/10.1021/nl048912c.

14. Lyu, Z.; Shang, Y.; Xia, Y. Shape-Controlled Synthesis of Copper Nanocrystals for Plasmonic, Biomedical, and Electrocatalytic Applications. *Acc. Mater. Res.* **2022**, *3*, 1137–1148. https://doi.org/10.1021/accountsmr.2c00134.

15. Lyu, Z.; Xie, M.; Aldama, E.; Zhao, M.; Qiu, J.; Zhou, S.; Xia, Y. Au@Cu Core–Shell Nanocubes with Controllable Sizes in the Range of 20–30 nm for Applications in Catalysis and Plasmonics. *ACS Appl. Nano Mater.* **2019**, *2*, 1533–1540. https://doi.org/10.1021/acsanm.9b00016.

16. Mayer, M.; Scarabelli, L.; March, K.; Altantzis, T.; Tebbe, M.; Kociak, M.; Bals, S.; Garcia de Abajo, F.J.; Fery, A.; Liz-Marzan, L.M. Controlled Living Nanowire Growth: Precise Control over the Morphology and Optical Properties of AgAuAg Bimetallic Nanowires. *Nano Lett.* **2015**, *15*, 5427–5437. https://doi.org/10.1021/acs.nanolett.5b01833

17. Yang, M.; Wang, W.; Qiu, J.; Bai, M.-Y.; Xia, Y. Direct Visualization and Semi-Quantitative Analysis of Payload Loading in the Case of Gold Nanocages. *Angew. Chem. Int. Ed.* **2019**, *58*, 17671–17674. https://doi.org/10.1002/anie.201911163

18. Qiu, J.; Xie, M.; Wu, T.; Qin, D.; Xia, Y. Gold Nanocages for Effective Photothermal Conversion and Related Applications. *Chem. Sci.* **2020**, *11*, 12955–12973. https://doi.org/10.1039/D0SC05146B.

19. Mieszawska, A.J.; Mulder, W.J.; Fayad, Z.A.; Cormode, D.P. Multifunctional Gold Nanoparticles for Diagnosis and Therapy of Disease. *Mol. Pharmaceutics* **2013**, *10*, 831–847. https://doi.org/10.1021/mp3005885.

20. Gnoth, C.; Johnson, S. Strips of Hope: Accuracy of Home Pregnancy Tests and New Developments. *Geburtshilfe Frauenheilkd.* **2014**, *74*, 661–669. https://doi.org/10.1055/s-0034-1368589.

21. Wikipedia: Pregnancy Test. Available online: https://en.wikipedia.org/wiki/Pregnancy_test#/media/File:Pregnancy_Test_Positive.jpg (accessed on 22 February 2025).

22. Moitra, P.; Alafeef, M.; Dighe, K.; Frieman, M.B.; Pan, D. Selective Naked-Eye Detection of SARS-CoV-2 Mediated by N Gene Targeted Antisense Oligonucleotide Capped Plasmonic Nanoparticles. *ACS Nano* **2020**, *14*, 7617–7627. https://doi.org/10.1021/acsnano.0c03822.

23. Cobley, C.M.; Chen, J.; Cho, E.C.; Wang, L.V.; Xia, Y. Gold nanostructures: a class of multifunctional materials for biomedical applications. *Chem. Soc. Rev.* **2011**, *40*, 44–56. https://doi.org/10.1039/B821763G.

24. Hu, M.; Chen, J.; Li, Z.-Y.; Au, L.; Hartland, G.V.; Li, X.; Marquez, M.; Xia, Y. Gold Nanostructures: Engineering Their Plasmonic Properties for Biomedical Applications. *Chem. Soc. Rev.* **2006**, *35*, 1084–1094. https://doi.org/10.1039/b517615h.

25. Li, W.; Brown, P.K.; Wang, L.V.; Xia, Y. Gold Nanocages as Contrast Agents for Photoacoustic Imaging. *Contrast Media Mol. Imaging* **2011**, *6*, 370–377. https://doi.org/10.1002/cmmi.439

26. Kim, C.; Cho, E.C.; Chen, J.; Song, K.H.; Au, L.; Favazza, C.; Zhang, Q.; Cobley, C.M.; Gao, F.; Xia, Y. In Vivo Molecular Photoacoustic Tomography of Melanomas Targeted by Bioconjugated Gold Nanocages. *ACS Nano* **2010**, *4*, 4559–4564. https://doi.org/10.1021/nn100736c.

27. Yavuz, M.S.; Cheng, Y.; Chen, J.; Cobley, C.M.; Zhang, Q.; Rycenga, M.; Xie, J.; Kim, C.; Song, K.H.; Schwartz, A.G.; et al. Gold Nanocages Covered by Smart Polymers for Controlled Release with Near-Infrared Light. *Nat. Mater.* **2009**, *8*, 935–939. https://doi.org/10.1038/nmat2564.

28. Shen, S.; Zhu, C.; Huo, D.; Yang, M.; Xue, J.; Xia, Y. A Hybrid Nanomaterial for the Controlled Generation of Free Radicals and Oxidative Destruction of Hypoxic Cancer Cells. *Angew. Chem., Int. Ed.* **2017**, *56*, 8801–8804. https://doi.org/10.1002/anie.201702898.

29. Das, M.R.; Sarma, R.K.; Saikia, R.; Kale, V.S.; Shelke, M.V.; Sengupta, P. Synthesis of Silver Nanoparticles in an Aqueous Suspension of Graphene Oxide Sheets and Its Antimicrobial Activity. *Colloids Surf. B* **2011**, *83*, 16–22. https://doi.org/10.1016/j.colsurfb.2010.10.033.

30. Schlücker, S. SERS Microscopy: Nanoparticle Probes and Biomedical Applications. *ChemPhysChem* **2009**, *10*, 1344–1354. https://doi.org/10.1002/cphc.200900119.

31. Zhao, Y.; Sultan, D.; Detering, L.; Cho, S.; Sun, G.; Pierce, R.; Wooley, K.L.; Liu, Y. Copper-64-Alloyed Gold Nanoparticles for Cancer Imaging: Improved Radiolabel Stability and Diagnostic Accuracy. *Angew. Chem. Int. Ed.* **2013**, *53*, 156–159. https://doi.org/10.1002/ange.201308494.

32. Yang, M.; Huo, D.; Gilroy, K.D.; Sun, X.; Sultan, D.; Luehmann, H.; Detering, L.; Li, S.; Qin, D.; Liu, Y.; et al. Facile Synthesis of 64Cu-Doped Au Nanocages for Positron Emission Tomography Imaging. *ChemNanoMat* **2017**, *3*, 44–50. https://doi.org/10.1002/cnma.201600281.

33. Brown, A.L.; Winter, H.; Goforth, A.M.; Sahay, G.; Sun, C. Facile Synthesis of Ligand-Free Iridium Nanoparticles and Their In Vitro Biocompatibility. *Nanoscale Res. Let.* **2018**, *13*, 1–6. https://doi.org/10.1186/s11671-018-2621-3.

34. Xia, H.; Li, F.; Hu, X.; Park, W.; Wang, S.; Jang, Y.; Du, Y.; Baik, S.; Cho, S.; Kang, T. pH-Sensitive Pt Nanocluster Assembly Overcomes Cisplatin Resistance and Heterogeneous Stemness of Hepatocellular Carcinoma. *ACS Cent. Sci.* **2016**, *2*, 802–811. https://doi.org/10.1021/acscentsci.6b00197.

Review

# Quantification of Nanomaterial Surfaces

Harshit Kumar and Mingdi Yan *

Department of Chemistry, University of Massachusetts Lowell, 1 University Avenue, Lowell, MA 01854, USA
* Correspondence: Mingdi_Yan@uml.edu

Abstract: Quantification of nanomaterial surfaces is critical in the design of nanomaterials with predictable and tailored functions. Nanomaterials exhibit unique surface properties, such as high surface-to-volume ratios and tunable chemistry, which govern their stability, reactivity, and functions in a wide range of applications including catalysis, drug delivery, bioimaging, and environmental remediation. However, quantitative analysis of the nanomaterial surface is challenging due to the inherent heterogeneity, which affects the surface structure, ligand density and presentation. This mini review discusses several important aspects of surface quantification, including ligand structure, ligand density, functional groups, and surface reactions. Traditional analytical methods, such as nuclear magnetic resonance (NMR) spectroscopy, mass spectrometry (MS), and UV-vis spectroscopy, as well as emerging techniques that offer higher spatial resolution and sensitivity are discussed, and examples are given.
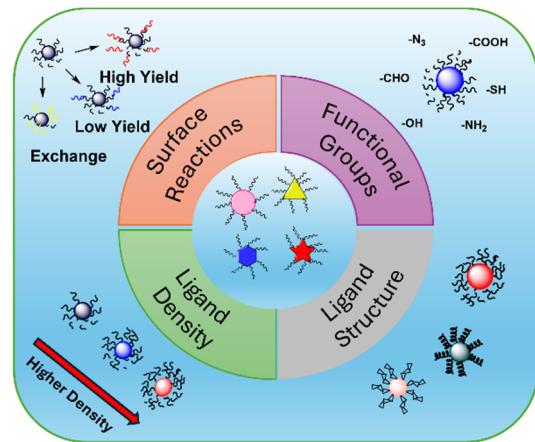
Keywords: nanomaterial surface; quantification; ligand structure; surface reactions

1. Introduction

Nanomaterials have gained wide uses in both fundamental research and for applications in catalysis, drug delivery, bioimaging, electronic devices, and energy owing to their extraordinary properties. Many of these applications originate from their surface properties such as high surface area-to-volume ratios and tunable surface chemistry [1,2]. The surface of nanomaterials plays a central role in determining their interactions with the surrounding environment, which directly influences their stability, reactivity, and functional performance [3,4]. Understanding and controlling these surface properties is essential for optimizing nanomaterials for the desired applications.

Nanomaterials are generally capped with ligands, which are molecules or ions that bind to the surface of the nanomaterial. Ligands on the surface of nanomaterials serve a number of important roles. (1) Reducing high-energy nanomaterial surfaces by passivating surface atoms. Without the surface ligands, nanomaterials are prone to aggregate or undergo unwanted reactions as they minimize surface energy [5,6]. (2) Controlling nanomaterial size and shape during synthesis. Surface ligands can influence the nucleation and growth rates, and dictate the final particle size through steric stabilization and surface charge [7]. When ligands preferentially bind to certain crystallographic facets, the facet-specific binding allows for precise control over the structural features of nanomaterials, such as anisotropic shapes and hierarchical assemblies [8–10]. (3) Tuning surface properties of nanomaterials. Through functional groups such as carboxy (-COOH), amine (-NH$_2$), or azide (-N$_3$), surface ligands enable further chemical modifications of the nanomaterial to improve the chemical reactivity, environmental stability, and biocompatibility [11]. Detailed understanding of the nanomaterial surfaces is therefore essential for the rational design of nanomaterials with predictable and tailored properties.

Ligands can be introduced to nanomaterial surfaces via non-covalent or coordination interactions, or by covalent bond formation [12,13]. In non-covalent interactions, ligands adhere to nanomaterial surfaces through hydrogen bonding, electrostatic forces, or hydrophobic interactions. For example, ligands such as polymers or

long-chain surfactants physisorb onto the nanomaterial surface via multivalent non-covalent interactions, which strengthen the ligand-nanomaterial interface. In coordination interactions, ligands such as amines, phosphines, and carboxylates coordinate with metals via dative bonds. Covalent bond formation provides strong ligand attachment, resulting in stable ligand-nanomaterial interface. Common examples include thiols/disulfides on metal or semiconductor nanomaterials, and silanes on oxide nanomaterials. Additional ligands can be introduced to nanomaterial surface through ligand exchange or post-synthesis modification. In ligand exchange, the original capping ligand is replaced by a ligand having higher affinity for the nanomaterials. For instance, citrate-capped gold nanomaterials can be modified by replacing citrate with thiol ligands, as the S-Au bond is stronger than the ionic citrate-gold interaction. Post-synthesis modification involves covalently conjugating a new ligand to the nanomaterial surface through reactions such as amine-carboxy amidation and azide-mediated click reactions.

However, quantifying nanomaterial surfaces remains a significant challenge due to their inherent heterogeneity. Nanomaterial surfaces often exhibit varying crystalline facets, structural defects, and curvatures, which influence ligand attachment, presentation, density, and reactivity [14,15]. Crystalline facets determine the surface energy, where high energy facets result in stronger ligand binding than low-energy facets, leading to uneven ligand attachments across the surface. Structural defects such as vacancies, dislocations, and grain boundaries are also high-energy sites that can cause ligands to cluster around them and leave other areas under-functionalized [14]. Curvature introduces another complexity [16,17]. On high curvature surfaces, e.g., small nanoparticles, ligands are spaced further apart, resulting in lower packing efficiency. This leads to reduced steric hindrance and enhanced functional group accessibility, potentially enhancing surface reactivity. On the other hand, flat and concave surfaces result in denser ligand packing, which can lead to stronger intermolecular interactions, reduced ligand mobility, and decreased reactivity. Collectively, these characteristics lead to non-uniform surfaces, making it challenging to characterize nanomaterial surfaces especially at the molecular level.

This mini review discusses four aspects of surface quantification: ligand structure, ligand density, functional groups, and surface reactions. We discuss traditional analytical methods such as NMR and UV-vis spectroscopy as they are well-established and widely accessible, as well as chemical assays that are ligand specific. We also discuss advanced analytical techniques that offer enhanced spatial resolution, sensitivity, and the ability to probe nanomaterial surfaces at the single-particle level. Since nanoparticles are the most studied nanomaterials, the terms nanomaterials and nanoparticles will be used interchangeably throughout the discussions.

2. Determination of Ligand Structure

Knowledge of the structure and spatial distribution of surface ligands is an important aspect that directly impacts the stability, reactivity, and functions of nanomaterials. High-resolution transmission electron microscopy (HR-TEM) can determine the crystalline structure of the nanoparticle core and visualize the nanoparticle-ligand interface, but the organic ligand shell often lacks sufficient contrast for its structure to be resolved directly [18]. The state-of-art cryogenic electron microscopy (cryo-EM) can provide 3–5 Å resolution and has been extensively used to solve the structures of proteins. Cryo-EM has been used to identify the binding location of nanoparticles within proteins, but it could not identify explicitly which atoms or functional groups in the protein are bound to the nanoparticle [19].

X-ray crystallography, NMR, and MS are commonly used to determine the precise structure of organic compounds. X-ray crystallography is a powerful technique for determining the atomic structure of crystalline materials including small molecules, proteins, and ordered solids. However, its application in determining the structure of ligands on nanoparticles is more challenging and less common due to the complex and heterogeneous nature of nanomaterials. Nanoparticles with disordered or mixed ligand shells often fail to crystallize into high-quality crystals required for X-ray crystallography. While X-ray crystallography has been used to determine the structure of ligands on nanoparticles, its application is primarily limited to crystalline systems, ordered superlattices, or atomically precise nanoclusters. For instance, when nanoparticles and ligands form highly ordered superlattices or crystalline assemblies, X-ray crystallography can be used to determine ligand packing and orientation, providing insights into how ligands mediate interparticle interactions and stabilize the lattice [20,21]. Atomically precise nanoclusters, nanoparticles having diameters of <2 nm and well-defined structures, are particularly suitable for X-ray crystallography. When single crystals can be obtained, X-ray diffraction can determine the complete structure of atomically precise nanoclusters, including the core structure as well as the conformation and orientation of the ligand shell [22,23]. This level of precision is impossible to achieve for large heterogeneous nanomaterials.

NMR, the workhorse for structure determination of organic compounds, is highly useful for analyzing the structure and dynamics of ligands on nanomaterials [24,25]. Ligands bound to nanomaterials exhibit distinct spectral

features compared to the free ligand, including line broadening and peak shift. Line broadening is commonly observed for ligands on the nanomaterial surface, attributed to factors such as restricted motions in surface-bound ligands, heterogeneous chemical environment, and altered relaxation dynamics, which lead to decreased spin-spin relaxation time and increased dipolar relaxation. Nuclei closer to the nanoparticle surface show greater peak broadening than those further away. When the rotational restriction becomes more severe, it leads to significant line broadening, often causing the peak to appear as if it has disappeared. These can be seen in the studied by Murphy and coworkers who investigated the NMR spectra of 11-mercaptohexadecyl)trimethylammonium bromide (MTAB) conjugated to gold nanospheres (AuNS) of different sizes (Figure 1A) [26]. The peak at ~1.2 ppm, which corresponds to the main chain (mc) protons of MTAB, is broader than the peak of the head group (hg) protons at ~3.1 ppm, which are further away from AuNS surface (Figure 1B). Protons ω and ψ, the closest to AuNS, appear completely disappeared in MTAB-AuNS. Results in Figure 1B also show that the line broadening became more pronounced with increasing AuNS size. With regard to peak shift, ligands tethered to nanomaterial surfaces generally shift downfield, and several factors contribute to this. For interacting surfaces such as metals or semiconductors, electron density can be partially withdrawn from the ligand, deshielding nearby protons and causing a downfield shift. Additionally, these surfaces can create a paramagnetic or polarizable environment, altering the magnetic shielding of adjacent protons and further contributing to the downfield shift [27,28]. Protons near the nanoparticle surface may also interact with neighboring ligands, thus enhancing deshielding effects. Protons closest to the nanoparticle surface experience the strongest deshielding, resulting in the largest downfield shifts. In the example in Figure 1B, the hg protons shifted downfield from 2.99 ppm in the free MTAB to 3.05 ppm for 1.2 ± 0.3 nm AuNS. The results also showed that the downfield shift increased with increasing particle size, to 3.23 ppm for 10.8 ± 0.8 nm AuNS and then plateaued for larger AuNS (Figure 1C). Larger nanoparticles exhibit increased ability to alter electron density, reduced ligand mobility, and increased ligand-nanoparticle interactions due to larger surface area, all of which contribute to stronger deshielding and larger peak shifts.
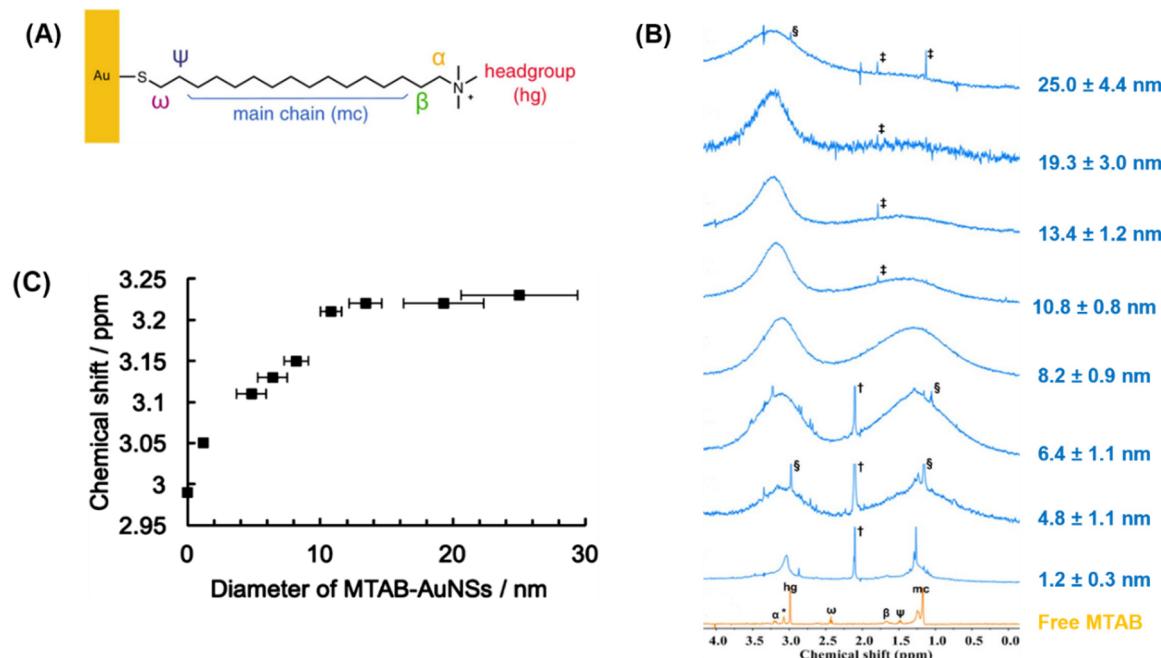
Figure 1. NMR analysis of ligand structure on gold nanospheres. (**A**) MTAB-functionalized AuNS. (**B**) ^{1}H NMR spectra of the free and AuNS-bound MTAB in D$_2$O, showing increased line broadening with increasing particle diameter. †: Residual acetone signal. ‡: Signals from impurities of plastic centrifugation tubes. §: Residual MTAB signal. *: Signal from the headgroup protons in MTAB. (**C**) Chemical shift of hg headgroup protons in AuNS-bound MTAB vs. the diameter of AuNS, showing increased downfield shift with increasing particle size. Reprinted with permission [26]. Copyright 2019, American Chemical Society.

The results in Figure 1 demonstrate that NMR spectroscopy for ligand structure analysis becomes more challenging for larger nanoparticles due to significant line broadening. Additionally, NMR requires milligram scale materials in order to obtain measurable signals. For ligands on nanoparticles, the weight percent of the surface ligand decreases exponentially as the nanoparticle size increases [29]. As a result, a larger amount of nanomaterials

is required, which is challenging for nanomaterials having low solubility or are difficult to synthesize in large quantities. In contrast, nanoclusters with particle sizes smaller than 2 nm give a higher concentration of surface ligands, and as such, NMR has been extensively used in the structural analysis of nanoclusters to obtain precise ligand structure, particularly for atomically precise nanoclusters. In a remarkable work, Jin and coworkers employed ^{1}H NMR spectroscopy to determine the ligand structure, including the detailed bonding modes of the surface ligands, of a glutathione (SG)-capped atomically precise gold nanocluster, $Au_{25}(SG)_{18}$ [30]. The ^{1}H NMR spectrum of $Au_{25}(SG)_{18}$ revealed two distinct doublets (7 and 7′, Figure 2B), which are assigned to the alpha protons of the thiolate (-CH_2S) in the ligand. The peak integration ratio was 2:1, indicating that the protons experience two different chemical environments. The integration ratio, 2:1, aligns with the proposed two-mode ligand structure on the Au_{25} core: Mode I with 12 ligands and Mode II with 6 ligands (Figure 2A). Furthermore, NMR revealed differences in the reactivity of the two ligand modes in $Au_{25}(SG)_{18}$. Upon treating with an oxidizing reagent, $Ce(SO_4)_2$, Mode II peaks disappeared first before Mode I (Figure 2B), indicating higher stability of the Mode I than the Mode II ligands. When treated with a lower concentration of $Ce(SO_4)_2$, Mode I ligands remained unchanged even after 5 days, further supporting the higher stability of Mode I ligands.
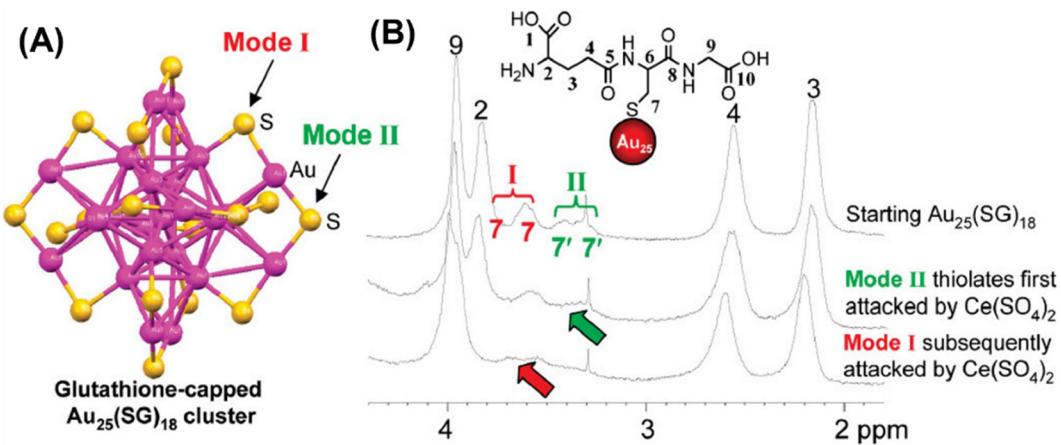
Figure 2. Determining ligand structure of Au25(SG)18 nanocluster by NMR. (**A**) Struture of Au25(SG)18. Only S of the ligand is shown for clarity. Au: purple; S: yellow. Each Mode I ligand coordinates to one inner and one outer Au, and each Mode II ligand coordinates to two outer Au. (**B**) 1H NMR spectra of Au25(SG)18 in D2O before and after treating with Ce(SO4)2 over time. Oxidation affected Mode II ligands (7′) first, and then Mode I ligands (7). Reproduced with permission [30]. Copyright 2009, American Chemical Society.

Mass spectrometry is a powerful technique for the characterization of chemical composition, molecular structure, and elemental distribution on nanomaterial surface. MS determines the structure and composition by analyzing the mass-to-charge ratio (*m/z*) of the fragments generated from the material. The accuracy of MS in surface analysis is governed by the type of the ionization method and the sensitivity of the mass analyzer [31]. Several MS techniques have been used to analyze nanomaterial surfaces. High-resolution electrospray ionization mass spectrometry (ESI-MS) is effective in determining the structure of small nanoclusters, offering high sensitivity and resolution for low molecular weight ligands [32]. For large nanoparticles and nanoparticles with more complex organic ligands, soft ionization techniques such as laser desorption/ionization (LDI) and matrix-assisted laser desorption/ionization (MALDI) are commonly used. For nanomaterials, however, the ionization efficiency of LDI or MALDI can be affected by the interaction of the ligand on the nanomaterial surface, which may hinder ligand release during analysis and lead to weak or undetectable signals. Also, ligands that bond strongly to nanomaterials may not be completely released, resulting in incomplete detection of surface species. Other challenges in using MS to characterize nanomaterial ligands include sample preparation, such as incomplete purification of nanoparticles or porous nanomaterials that may trap impurities, which can introduce artifacts and complicate data analysis.

Chiodo and coworker employed a Fourier transform ion cyclotron resonance (FTICR) mass spectrometer with high resolution and high mass accuracy to characterize complex surface ligand structures [33]. Using multiple MS techniques, including LDI-MS, MALDI-MS, MS/MS and FTICR combined with MALDI/LDI-MS (LDI/MALDI−FTICR MS), the authors characterized the ligand structure and the S-Au bond of a ~2 nm gold nanoparticle (AuNP). Figure 3 shows the mass spectra and analysis of ovalbumin peptide (OVA)-functionalized AuNPs. Using LDI-FTICR MS, a low intensity pseudomolecular ion, [M + Na]+, was detected (Figure 3A), supporting the conjugation of the OVA ligand on AuNP. During the analysis by MALDI-FTICR MS, the authors

found that using 1,5-diaminonaphthalene (1,5-DAN) as the matrix improved the signal intensity by >80 times and enabled the detection of additional pseudomolecular ions such as $[M + Au]^+$ and $[M + 2\,Au - H]^+$ (Figure 3B). The detection of these unique Au-bound species provides strong evidence for the presence of thiol-gold coordination on AuNP surface, which is impossible to characterize using other traditional analytical techniques like NMR. Further MS/MS analysis of Au-containing fragmentations (Figure 3C) suggested preferential binding site of Au^+ (Figure 3D).
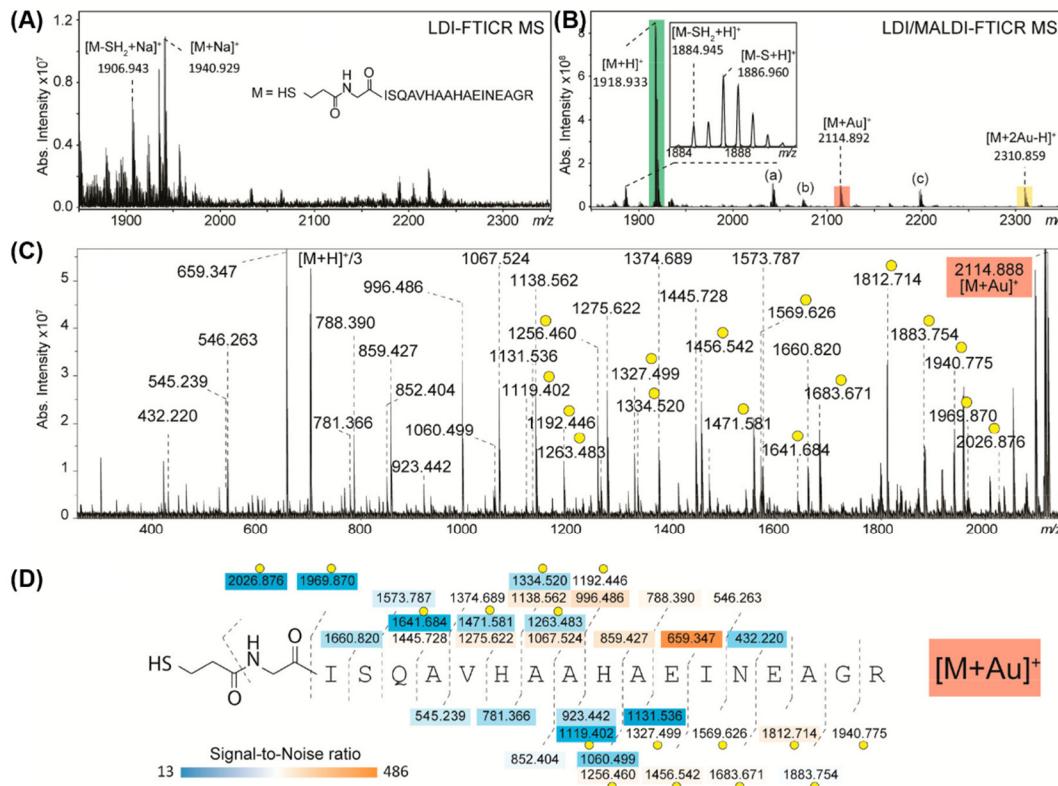
Figure 3. Ligand structure analysis of OVA-functionalized AuNPs by mass spectroscopy. (**A**) LDI-FTICR MS spectrum, showing pseudomolecular ion $[M + Na]^+$. (**B**) LDI/MALDI-FTICR MS spectrum using 1,5-DAN matrix, showing additional pseudomolecular ions: $[M + H]^+$, $[M + Au]^+$ and $[M + 2\,Au - H]^+$. (**C**) MS/MS spectrum of $[M + Au]^+$ showing detailed fragmentation. (**D**) Collision-induced dissociation (CID) analysis of the MS/MS spectrum in (**C**), showing sequence coverage and Au-coordinated fragment ions (highlighted with yellow circles). Reproduced with permission [33]. Copyright 2017, American Chemical Society.

3. Quantification of Ligand Density

Ligand density is defined as the quantity or mass of ligands per unit area of the nanomaterial surface or the unit mass of the nanomaterial, typically expressed as weight/mole/molecules per nm^2 or mg. The amount of ligands on nanomaterial can directly impact the physicochemical properties and the functions of nanomaterials [11]. Calculating ligand density requires two pieces of information: the quantity of ligands and the total surface area or weight of the nanomaterial. The total surface area of the nanomaterial is often estimated from the size and shape of the nanomaterial measured by microscopy techniques such as TEM. Direct measurement by techniques such as gas adsorption gives the total surface area, which includes not only the external surface area but also surface areas of accessible internal pores.

A number of methods have been used to quantify the ligand density on nanomaterial [25,34]. Thermogravimetric analysis (TGA) is widely used for quantifying ligand density on nanomaterials for its convenience and straightforward operation [35]. It measures the mass loss as the nanomaterial is heated, and the mass loss is directly correlated to the amount of ligand desorbed or decomposed from the nanomaterial. TGA is particularly well-suited for analyzing ligand density on nanomaterials having thermal decomposition behavior distinct from their surface ligands, such as organic ligands on metal or inorganic nanomaterials. However, the mass measured by TGA does not provide structural information of the surface ligands. Also, the technique is sensitive to impurities such as solvents, unbound ligands or organic contaminants, which can contribute to observed mass loss. Additionally, TGA requires milligrams of sample to give accurate measurements, which can be difficult to

obtain for certain nanomaterials. Despite these limitations, TGA is valuable for quantifying ligand density, especially when used together with other techniques to provide a more comprehensive understanding of nanomaterial surfaces. Below, we discuss structure-specific methods for the quantification of ligand densities on nanomaterials, including traditional analytical techniques such as quantitative NMR (qNMR) and UV-vis spectroscopy, chemical assays, as well as emerging techniques that offer spatial resolution on single nanoparticles or measure functional ligands available for receptor binding.

The qNMR spectroscopy is specifically developed for quantitative measurements [36]. By using a reference compound with known concentration as the calibration, qNMR can accurately determine the concentration of a sample. When applied to nanomaterials, qNMR can quantify organic ligands with high specificity when the sample and preparation requirements can be met. Since NMR requires milligram-scale quantity of samples, sufficiently high ligand concentrations are needed in order to obtain reliable results. Additionally, sufficient solubility is required to ensure proper dispersion of nanomaterials in the NMR solvent. For larger nanoparticles having low ligand concentrations and displaying greater line broadening, qNMR experiments can become more difficult. A possible solution is to cleave the ligands from the nanoparticles prior to qNMR analysis, provided that the protocol does not degrade the ligands or introduce additional impurities.

On the other hand, if the ligands contain F or P which are absent in the nanomaterial itself, ^{19}F qNMR or ^{31}P qNMR can be used without having to go through complicated sample separation. We applied ^{19}F qNMR to determine the ligand density on large nanoparticles, 87 ± 8.0 nm diameter silica nanoparticles (SNPs) [37]. [19]F is a 100% naturally abundant nuclei and ^{19}F NMR has comparable sensitivity (~88%) to ^{1}H NMR. The ligands, D-mannose (Man) and D-galactose (Gal), were conjugated on SNPs via azide-alkyne click reaction using perfluorophenyl azide (PFPA, Figure 4A). As the F atoms are present only in PFPA and not in SNPs, using ^{19}F qNMR simplifies the quantification process as no complex separation is needed. The samples can be directly subjected to ^{19}F qNMR without background interference from SNPs. The ligand density obtained from ^{19}F qNMR, 6.4 ± 0.2 nmol/nm^2 for Man-SNP, was also compared with the results from TGA (13.0 ± 3.4 nmol/nm^2). The higher values measured by TGA could be from trapped solvents and other organic impurities in the nanoparticles.
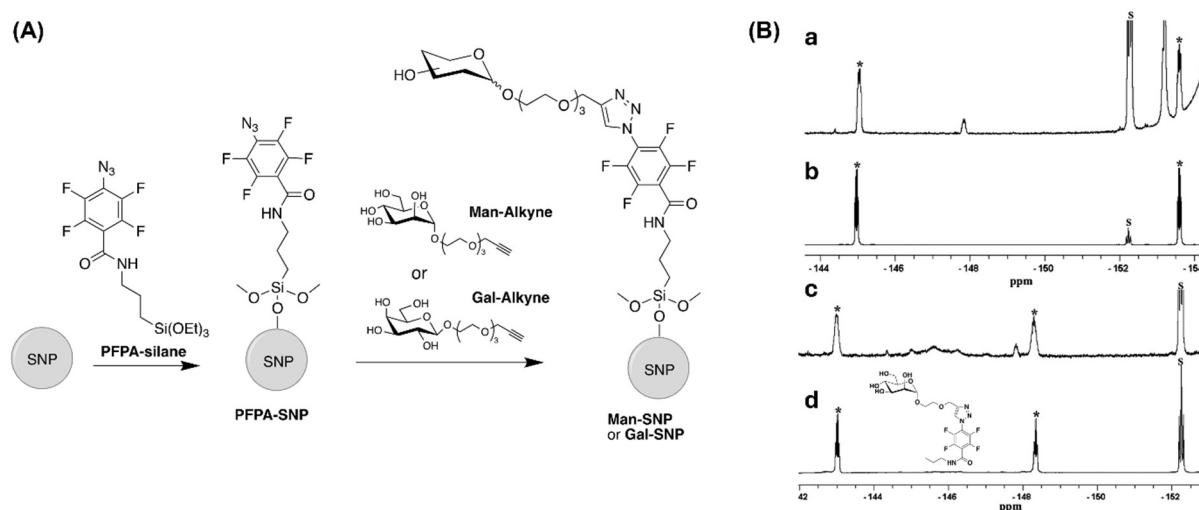
Figure 4. Determining ligand density on nanoparticles by ^{19}F qNMR. (**A**) Conjugation of Man or Gal to SNPs via PFPA-click reaction. (**B**) ^{19}F NMR spectra of (**a**) PFPA-SNP after treating with HF, (**b**) PFPA-silane, (**c**) Man-SNP after treating with HF, (**d**) a model compound. Nanoparticle samples were treated with 5% HF for 1 h, lyophilized in the presence of an in-line trap with CaO, and the residual was dissolved in methanol with methyl pentafluorobenzoate as the internal standard. Marked as "*" are F-2,6 and F-3,5 in the tetrafluorophenyl group, and "S" are from the methyl pentafluorobenzoate standard. Reproduced with permission [37]. Copyright 2015, American Chemical Society.

When multiple ligands are present on a nanomaterial, accurate quantification of each surface ligand can be challenging. Pérez-García et al. employed UV-vis spectroscopy combined with spectral deconvolution to quantify the densities of mixed ligands on AuNPs [38]. The sample was prepared via ligand exchange reactions from citrate-capped AuNPs, first with thiol-PEG-COOH and then with cytochrome C (Cyt C) and zinc porphyrin (Zn Porph) to give AuNP-PEG-Cyt C/Zn Porph (Figure 5A). The UV-vis spectrum of AuNP-PEG-Cyt C/Zn Porph showed overlapping peaks from Cyt C and Zn Porph, making it impossible to identify each ligand for quantification. To overcome this, the authors used CASA-XPS software and the Levenberg–Marquardt algorithm to deconvolute the

absorption spectra. Using this approach, the authors were able to identify bound Zn Porph and Cyt C and unbound Zn Porph (Figure 5B), from which the concentration of each bound as well as unbound ligand were determined. For ~20 nm AuNPs, the concentrations of conjugated Cyt C and Zn Porph were 0.42 μM and 1.3 μM, respectively, corresponding to 346 Cyt C and 1073 Zn Porph molecules per nanoparticle. For ~50 nm AuNPs, higher ligand densities were obtained, with the concentrations of Cyt C and Zn Porph at 0.11 mM and 1.3 mM, corresponding to 23,259 Cyt C and 35,168 Zn Porph molecules per nanoparticle.
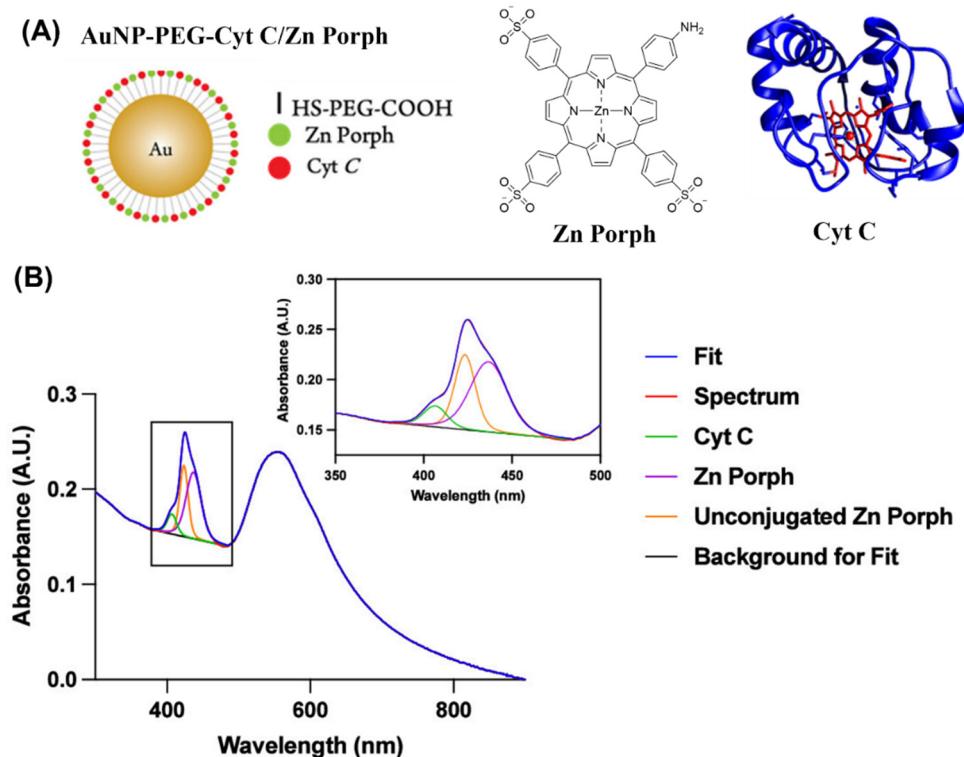
Figure 5. Quantification of mixed ligands using UV−vis spectroscopy combined with spectral deconvolution. (**A**) AuNPs functionalized with Zn Porph and Cyt C. (**B**) Deconvolution of Soret band in the UV−vis spectrum of AuNP-PEG-Cyt C/Zn Porph identified bound Zn Porph and Cyt C and unbound Zn Porph. Reproduced with permission [38]. Copyright 2023, American Chemical Society.

Surface-sensitive MS techniques, such as time-of-flight secondary ion mass spectrometry (ToF-SIMS), has also been used to quantify ligand density on nanoparticles [39]. ToF-SIMS utilizes a primary ion beam (e.g., Bi^+, Ga^+, C_{60}^+) to bombard a sample, ejecting secondary ions from ligands or ligand fragments within the top 5−10 nm surface layer of the sample. While ToF-SIMS is traditionally applied to flat surfaces due to potential topographical effects, recent advancement has enabled the analysis of surface ligands on individual nanoparticles. For instance, Schweikert and coworkers used $Au400^{4+}$ clusters as projectiles to determine ligand density on DNA-functionalized anisotropic gold nanostars and isotropic gold nanospheres of comparable surface areas but different morphologies [40]. The $Au400^{4+}$ clusters produced abundant secondary ions, with each impact probing a 10–15 nm diameter area, giving sampling density of $2–4 \times 10^6$ projectiles across a 125 μm radius area to ensure statistically robust data collection. Results showed higher DNA density on gold nanostars than on gold nanospheres. Furthermore, nanostars with ~3 branches per particle had the highest DNA density whereas nanostars with more branches showed reduced DNA loading, likely due to steric hindrance at branch-core junctions.

Chemical assays, when specific to certain ligand types, can be a powerful method for the quantification of ligand density. The anthrone-sulfuric acid or phenol-sulfuric acid assays, for example, is highly specific for carbohydrates. It works by converting carbohydrates into furfural derivatives under acidic conditions, which then react with anthrone to form a blue-green complex (l_{max} = 620 nm) (Figure 6A) [29], or with phenol to form a yellow-orange complex (l_{max} = 490 nm) [41]. The assay has been employed to quantify carbohydrate density on nanoparticles. In the example shown in Figure 6B, we conjugated carbohydrates to AuNPs via a photoconjugation reaction using PFPA, and determined the ligand density by treating carbohydrate-capped AuNPs with anthrone/sulfuric acid and comparing the absorption to a standard calibration [42]. By comparing the amount of Man conjugated on AuNPs with the amount of Man initially added, the photoconjugation yield can be calculated. Results showed decent coupling yields for all samples tested (53–85%, Figure 6C), demonstrating high efficiency

of the photoconjugation reaction. Even at low ligand concentrations, high yields were achieved (78–85%), although the overall surface coverage was low (0.11–1.1%) due to low amount of Man initially added (0.1–1 nmol/mg).

(C)

| Mannose added (nmol/mg NPs)	Mannose coupled (nmol/mg NPs)	Coupling yield (%)[a]	Surface coverage (%)[b]
0.1	0.081	85	0.11
0.5	0.40	80	0.56
1	0.78	78	1.1
5	3.1	61	4.3
10	5.3	53	7.4
50	30	59	41
80	44	56	62
100	57	57	80
120	58	N/A	80
150	57	N/A	80

[a] Coupling yield = mannose coupled/mannose added × 100%. [b] Surface coverage = mannose coupled/max. mannose computed × 100%. The max. mannose computed is 71.7 nmol/mg NPs for 20 nm Au NPs (see ESI† for detailed calculation).

Figure 6. Anthrone-sulfuric acid assay to quantify carbohydrate ligands on nanoparticles. (**A**) Reaction of D-glucose with sulfuric acid followed by anthrone to give a colored anthracenone product. (**B**) Photochemical conjugation of carbohydrates on AuNPs. (**C**) Ligand density, conjugation yield, and surface coverage of Man-AuNPs. Reproduced with permission [42]. Copyright 2009, Royal Society of Chemistry.

Nanomaterials often have heterogeneous surfaces with varying crystalline facets, defects, and curvature, which can lead to non-uniform ligand attachment [14,15]. Heterogeneity in nanoparticle size, shape, surface morphology, and ligand distribution can also cause variations in ligand density both among and within individual nanoparticles. In addition, factors such as ligand presentation and ligand-ligand interactions through functional groups and/or spacer linker further contribute to this variation. The ability to map ligand density with high spatial resolution is thus important for understanding the ligand attachment patterns, distribution, and reactivity across nanomaterial surface. The common quantification methods discussed above give the global average and cannot resolve particle-to-particle variations in ligand density. Below, we discuss two examples that used emerging microscopy techniques to achieve single particle analysis and high spatial resolution.

Huang et al. exploited electron energy loss spectroscopy (EELS) combined with aberration-corrected dark-field scanning transmission electron microscopy (ADF-STEM) to quantify and image ligand density on cetyltrimethylammonium bromide (CTAB)- or MTAB-capped gold nanorods (AuNRs) at sub-nanometer spatial resolution [43]. Samples were prepared by depositing AuNRs on single-layer graphene grids to reduce background noise and enhance detection sensitivity. Following baking the samples in vacuum at 130 °C, EELS maps were generated by integrating the signals and dividing them by the nanorod surface area (Figure 7). The authors found that the ligand density was anisotropic on CTAB-AuNR, with lower ligand coverage at the nanorod ends at 0.88 ± 0.4 molecules/nm^2 compared to the nanorod sides at 1.03 ± 0.4 molecules/nm^2. On the other hand, the ligand density was more uniform across the surface of MTAB-AuNR, with 1.04 ± 0.2 molecules/nm^2 at the ends and 0.97 ± 0.2 molecules/nm^2 at the sides.

Yan and coworkers employed nanoflow cytometry (nFCM) to quantify ligand density on liposomes at the single-particle level, achieving high throughput with analysis of up to 10,000 liposomes per minute (Figure 8) [44]. For ligand density determination, the authors used fluorescently labeled recombinant receptors as probes that bind specifically to ligands on liposomes. nFCM simultaneously measured side-scattering for particle size and fluorescence for ligand quantification. Using this method, the authors identified optimal ligand density for effective cell targeting: 0.5–2.0 ligands/100 nm^2 for folate, 0.7 ligands/100 nm^2 for transferrin, and (0.2 ligands/100 nm^2) for HER2 antibody. Note that this method only detects ligands available for receptor binding, not the total ligand density. Ligands having undesired orientation, shielded by PEG, and denatured or overcrowded ligands were not detected.
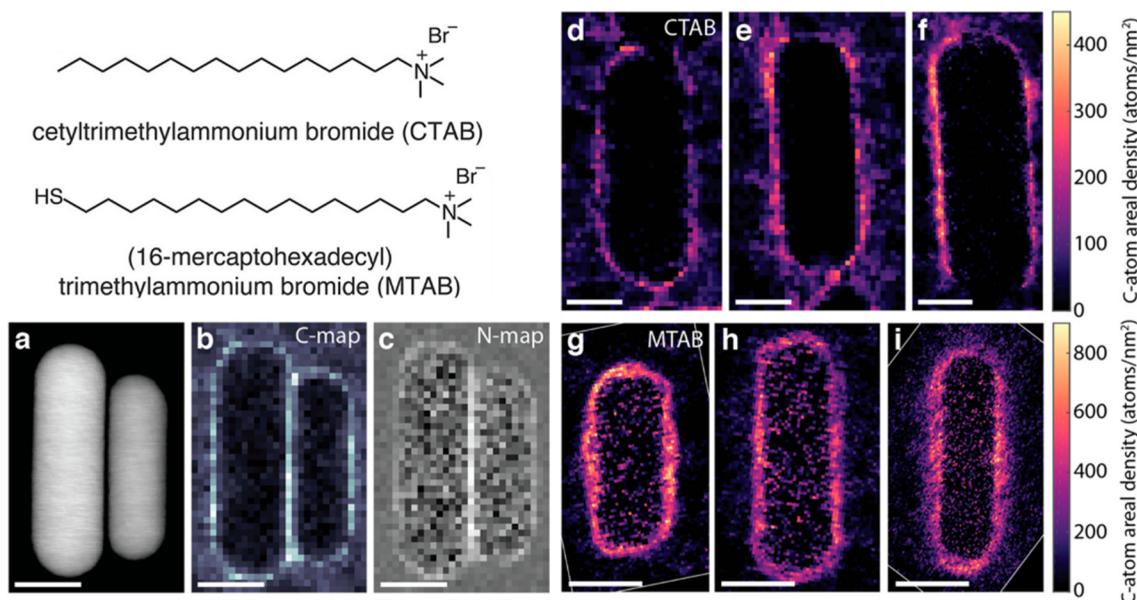
Figure 7. Mapping ligand density on CTAB-AuNR and MTAB-AuNR using ADF-STEM and EELS. (**a**) ADF-STEM image of CTAB-AuNRs. (**b**) Carbon and (**c**) nitrogen EELS maps of the two CTAB-AuNRs in (**a**). (**d–i**) EELS carbon density maps of (**d–f**) CTAB-AuNRs and (**g–i**) MTAB-AuNRs. The atomic areal intensity is the 2D projected areal density of C atoms after subtracting the graphene background. Scale bars are 15 nm in (**a–c**), and 10 nm in (**d–i**). Reproduced with permission [43]. Copyright 2019, American Chemical Society.
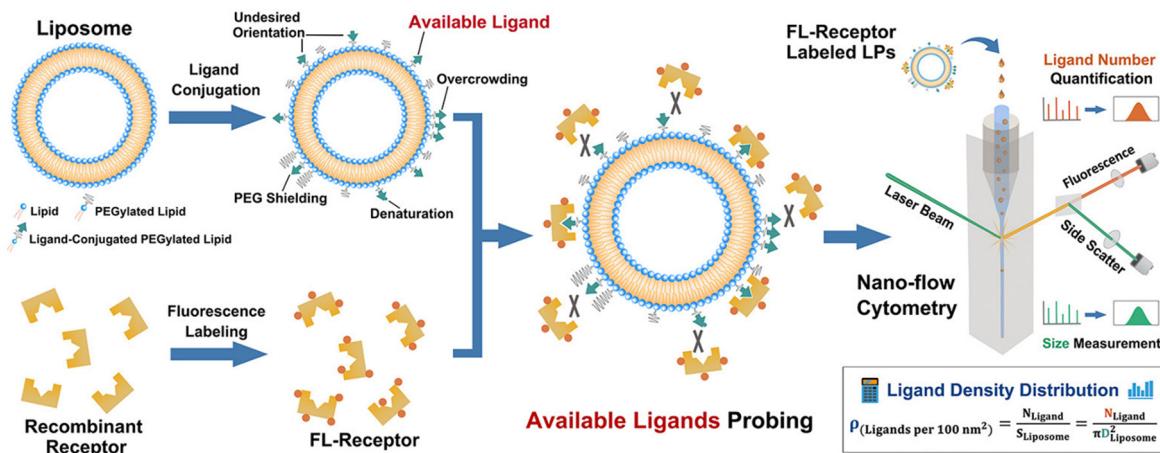
Figure 8. Quantification of ligand density on single liposomes: Sample preparation and quantification of available ligands by nFCM. Reproduced with permission [44]. Copyright 2022, American Chemical Society.

4. Quantification of Surface Functional Groups

A number of analytical techniques have been employed and developed to quantify functional groups on nanomaterials [45–47]. Titration methods, qNMR, MS, and various spectroscopy methods are used to quantify total functional groups on nanomaterials. Quantification using these methods focuses on detecting the intrinsic chemical properties of functional groups or elements in the nanomaterial, eliminating the need for external labels or probes. On the other hand, probe-based methods use chromophore-based probes or cleavable probes that interact or react with functional groups on the nanomaterial to produce measurable changes in absorbance or emission. Quantification is achieved by comparing the measured signals to a standard calibration curve. Probe-based methods measure functional groups that are accessible to the probe molecules, referred to as derivatizable functional groups. As such, differences in the relative size, steric hindrance, and reactivity contribute to inaccuracies in these methods.

Table 1 summarizes the working principle, type and quantifiable functional groups of various methods that have been used to quantify functional groups on nanomaterials. Readers are referred to a recent review on this topic by Resch-Genger and coworkers for comprehensive discussions of the techniques and examples [45]. Each method offers its own advantages, limitations, and contexts of application, and multiple complementary techniques

are often necessary to gain a comprehensive characterization. Here, we discuss cleavable probes and give an example where the total and derivatizable functional groups were measured using different probes and quantification techniques.

Table 1. Working principle, type and quantifiable functional groups (FGs) of methods for quantification of functional groups on nanomaterials.

Method	Working Principle	Type of FGs	Total vs. Derivatizable FGs	Examples of Quantifiable FGs
Potentiometric Titration	Measures electrochemical potential changes; determines equivalence points for (de)protonable groups.	(De)protonable groups	Total	-COOH, -NH$_2$, -SH
Conductometric Titration	Measures conductivity changes during acid/base titration.	Charged groups	Total	-COOH, -NH$_2$
Boehm Titration	Neutralizes acidic FGs on carbon materials; calculates density from back titration of unreacted FGs.	Acidic oxygen-containing FGs	Total	-COOH, phenols, lactonic groups
Optical Assays	Dye-based reporters interact or react with FGs, yielding measurable absorption/emission signals.	Dye interacting or reactive FGs	Derivatizable; limited by dye size and steric effects	-NH$_2$, -SH, -CHO, -N$_3$
Cleavable Probes	Reporter molecules react with FGs, which is then cleaved, and quantified using photometric or fluorometric assays.	Dye reactive FGs	Derivatizable; limited by dye size and steric effects	-NH$_2$, -COOH, -CHO
Adsorption/Desorption Assays	Reporter molecules electrostatically interact with surface FGs; desorbed reporters are quantified.	Reporter interacting FGs	Accessible FGs; Relies on stoichiometry factor calibration	Charged groups: -COOH, -NH$_2$, sulfates
NMR Spectroscopy	Analyzes chemical shifts of nuclei; high chemical specificity.	FGs containing NMR active nuclei; distinguishes surface-bound and free species.	Total	H-, C-, N-, F-, P-containing FGs
Inductively Coupled Plasma (ICP)-MS/ICP-OES (Optical Emission Spectroscopy)	Measures elemental concentrations to infer FG or ligand counts, often labeled with detectable elements, high sensitivity	Most FGs, except those containing only light elements of H, C, N, O, F	Total or derivatizable	S- and P-containing FGs, metal-complexing FGs
Vibrational Spectroscopy	Measures molecular vibrations corresponding to specific FGs, e.g., IR and Raman, including surface-enhanced variants for increased sensitivity.	FGs with strong dipoles (IR), or containing bonds with high polarizability (Raman)	Total	-COOH, -NH$_2$, -SH, -OH, -SiOH, -CHO, C-C, S-S, etc.

Cleavable probes typically consist of three parts: a reactive group that binds to or reacts with the functional group, a cleavable linker that facilitates the release of the reporter, and a reporter molecule for detection [48,49]. The linker is designed with cleavable covalent bonds such as disulfide, pH sensitive hydrazone or protecting groups such as fluorenylmethoxycarbonyl (Fmoc) which is a base-labile protecting group for amines. Upon cleavage, the reporter molecule is released, and the functional group is quantified by measuring the concentration of the released reporter. An advantage of using cleavable probes is that the indirect quantification of the cleaved reporter improves accuracy by eliminating errors caused by light scattering, which can occur in the direct measurements on nanoparticles.

Johnston and coworkers employed several methods to quantify the density of amino groups on silica nanoparticles, including using a dye-based reporter, a cleavable probe, and qNMR [50]. For the dye-based reporter

method, the amine-functionalized silica nanoparticles were allowed to react with ninhydrin to produce a colored product, Ruhemann's purple (Figure 9A). The density of surface amino groups was quantified by measuring the concentration of Ruhemann's purple (l_{max} = 570 nm) using UV-vis spectroscopy, giving 47–320 µmol g^{-1} depending on the nanoparticle size and surface coverage. In the cleavable probe approach, the amine on the nanoparticle first reacted with 4-nitrobenzaldehyde (4-NBA) to form an imine, which was then hydrolyzed to regenerate 4-NBA (l_{max} = 275 nm) for quantification by UV-vis spectroscopy (Figure 9B). This method resulted in higher amine density, 53–459 µmol g^{-1} (Figure 9D), than the dye-based reporter method, hypothesized as reduced steric hindrance of 4-NBA compared to ninhydrin. In the third method, amines were labeled with a fluorinated probe, trifluoromethylated benzaldehyde, via a reaction between the amine and the aldehyde to form an imine product (Figure 9C). Quantifcation using solid-state ^{19}F NMR gave amine density of 40–380 µmol g^{-1}, which is similar to the results obtained from the 4-NBA assay (Figure 9D). Finally, the amine was quantified by dissolving silica nanoparticles in a solution of 0.4 M NaOD in D$_2$O at 45 °C for 3 h and analyzing by ^{1}H qNMR using maleic acid as the internal standard. The result, 57–655 µmol g^{-1}, is the highest of all methods as ^{1}H qNMR measures the total amines. On the other hand, the probe-based methods in Figures 9A–9C only measure amines accessible to the probes. The larger size of the probes compared to the amine means that not all amines are able to react with the probes in a 1:1 stoichiometry. This leads to lower measured concentrations than that obtained by ^{1}H qNMR. In fact, the largest probe, ninhydrin, generally gave the lowest result (Figure 9D).
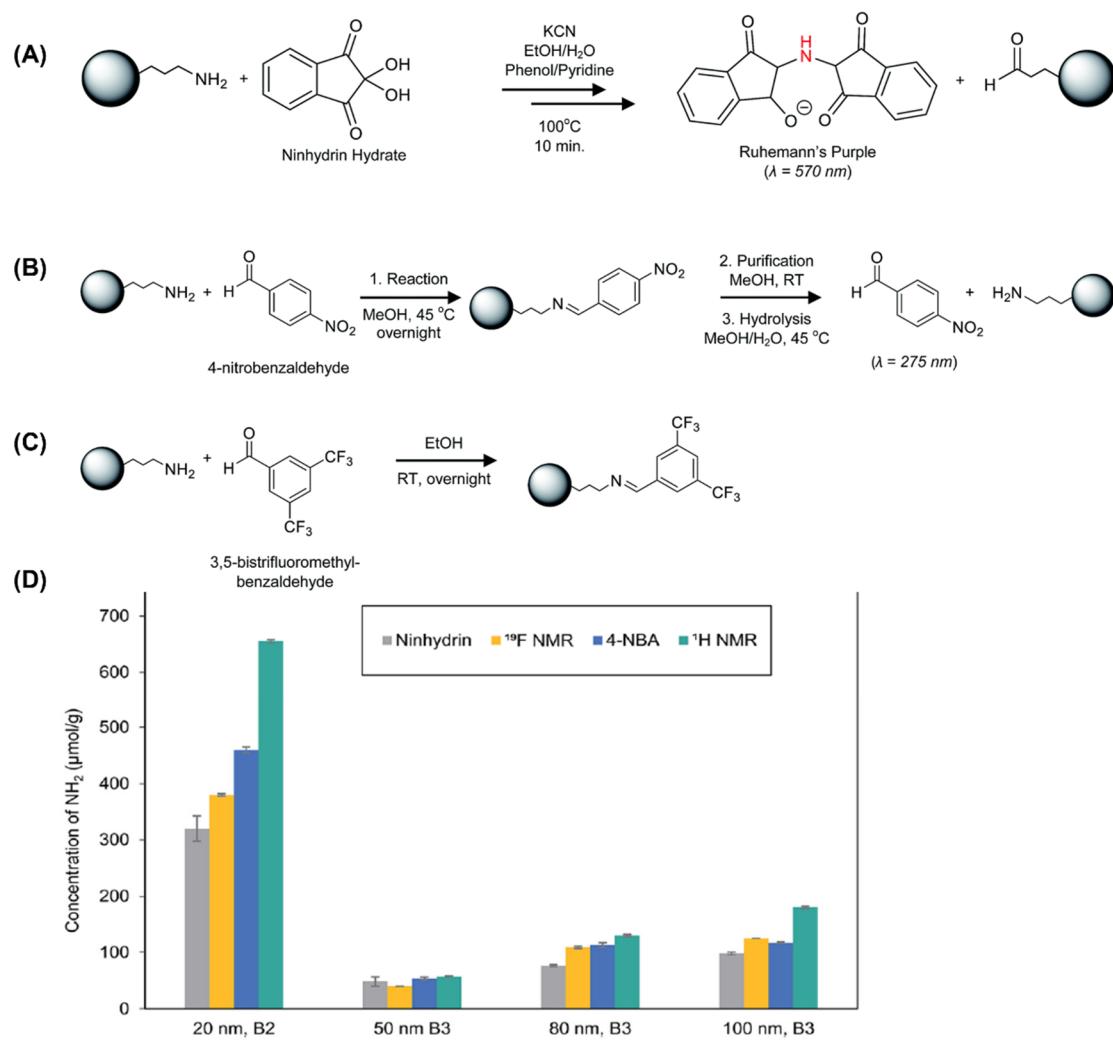
Figure 9. Probe-based methods for the quantification of amine density on silica nanoparticles. (**A**) Dye-based reporter method using ninhydrin to give Ruhemann's purple for quantification by UV-vis spectroscopy. (**B**) Cleavable probe method using 4-NBA and UV-vis spectroscopy. (**C**) Quantification by ^{19}F NMR using an F-containing reporter, trifluoromethylated benzaldehyde. (**D**) Comparison of amine density determined by methods (**A**–**C**) and ^{1}H qNMR. Reproduced with permission [50]. Copyright 2019, Royal Society of Chemistry.

5. Quantification of Surface Reactions

Quantitative analysis of reactions on nanomaterial surfaces is necessary for both fundamental understanding of the surface reaction and for optimizing nanomaterial properties and performance [51,52]. Like any chemical reactions, quantitative analysis of reactions on nanomaterial surfaces provides insights into reaction stoichiometry, kinetics, thermodynamics, and yield, enabling the identification of active sites and mechanisms unique to nanomaterials. Quantitative analysis also provides means to compare across nanomaterials under identical reaction conditions, ensuring batch-to-batch reproducibility and scalability of nanomaterials for commercial applications. Surface reactions are generally carried out by way of direct functionalization of nanomaterials, ligand exchange, or through conjugation reactions with complementary functional groups [53].

NMR is again a powerful tool to determine the product structure of surface reactions, particularly for small nanomaterials like nanoclusters. In the example shown in Figure 10, we carried out a ligand exchange reaction on $[Au_{11}(PPh_3)_8Cl_2]Cl$ (TPP: triphenylphosphine) using triphenylphosphine monosulfonate (TPPMS) as the incoming ligand [54]. $[Au_{11}(PPh_3)_8Cl_2]Cl$ undergoes nuclearity conversion to give $[Au_9(TPPMS)_8]Cl_3$ as confirmed by high-resolution ESI-MS (Figure 10A). Characterizations of the product using a combination of NMR techniques, including ^1H, ^{31}P, 2D COSY (correlation spectroscopy) and 2D DOSY (diffusion-ordered spectroscopy), collectively confirmed the product structure. The results also revealed the purity of the product, with no evidence of free ligands or other impurities (Figure 10C).
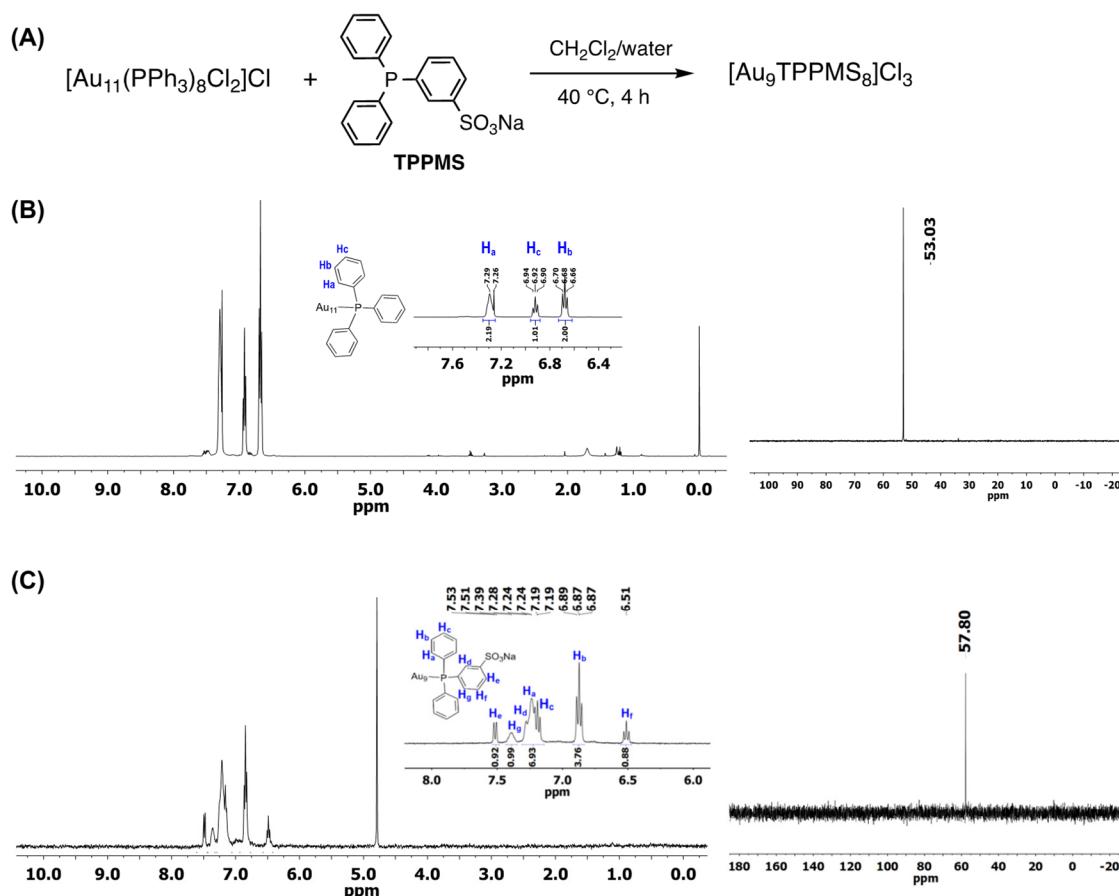
Figure 10. Studying surface reaction by NMR. (**A**) The ligand exchange reaction of $[Au_{11}(PPh_3)_8Cl_2]Cl$ with TPPMS to give $[Au_9(TPPMS)_8]Cl_3$. (**B**) ^1H and ^{31}P NMR spectra of starting material $[Au_{11}(PPh_3)_8Cl_2]Cl$ in CDCl$_3$. (**C**) ^1H and ^{31}P NMR spectra of product $[Au_9(TPPMS)_8]Cl_3$ in D$_2$O (0.6 mM). Peak assignments were confirmed by 2D COSY NMR. Reproduced with permission [54]. Copyright 2021, Royal Society of Chemistry.

Epple and coworkers used qNMR and other spectroscopy techniques to quantify surface reactions on AuNPs [55]. The authors first converted the amino groups on glutathione (GSH)-capped AuNPs (~2 nm) to azide via a copper-catalyzed N_2 transfer reaction (Figure 11A). Subsequent click reaction of N_3-AuNP with alkyne-functionalized dyes (FAM-alkyne and AlexaFluor-647-alkyne) gave FAM-AuNP and AlexaFluor-647-AuNP (Figure 11B). The number of surface ligands was determined using atomic absorption spectroscopy (AAS) and qNMR. AAS measurements gave the molar concentration of AuNPs. The ^1H qNMR analysis of GS-AuNP,

calibrated with maleic acid, gave ~125 GSH molecules per nanoparticle. After azidation, 118 GSH were converted to azido groups, giving a 94% reaction yield (Figure 11C). By measuring the concentration of dye molecules by UV-vis spectroscopy and the concentration of nanoparticles by AAS, the click reaction yield was calculated as 13% for FAM-AuNP (~6 FAM molecules/nanoparticle) and 23% for AlexaFluor-647-AuNP (~11 AlexaFluor-647 molecules/ nanoparticle), respectively. The low yields were attributed to steric hindrance due to the large dye molecules and electrostatic interactions between dye molecules on the nanoparticle surface.
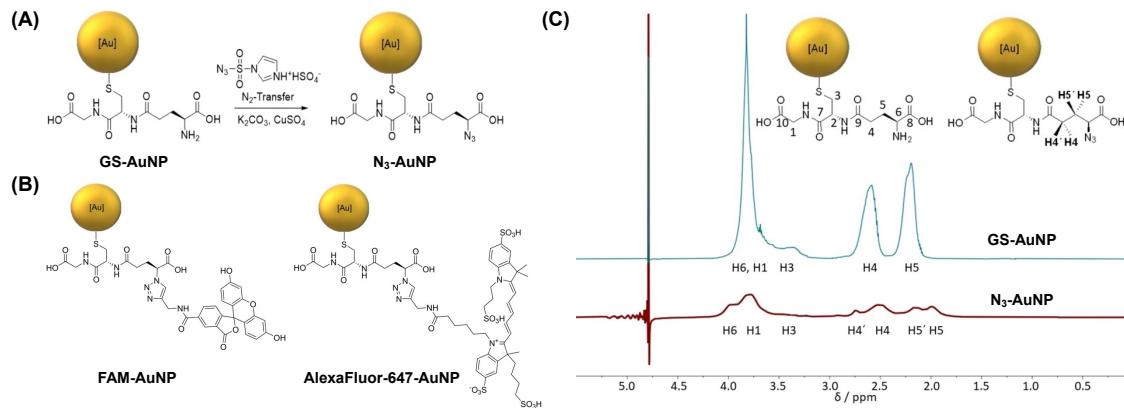
Figure 11. Determining the yield of surface reactions on nanoparticles by qNMR. (**A**) Azidation of GS-AuNPs to give N₃-AuNP. (**B**) FAM-AuNP and alexaFluor-647-AuNP. (**C**) ^{1}H NMR spectra of GS-AuNP and N₃-AuNP, in 90% H_2O/10% D_2O at pH 8 with water suppression. Reproduced with permission [55]. Copyright 2021, Wiley.

We employed Raman spectroscopy to determine the kinetics of the Diels-Alder reactions on graphene supported on different substrates [56,57]. Monolayer pristine graphene has a characteristic Raman G band at ~1580 cm^{-1}. When the sp^2 carbons in graphene are converted to sp^3 carbons after chemical functionalization, the D band at ~1350 cm^{-1} appears in its Raman spectrum. At low degree of functionalization, the intensity ratio of the Raman D and G bands, I_D/I_G, serves as an indicator of the extent of functionalization (Figure 12A). To quantify reaction kinetics, a pseudo-first-order kinetic model was applied. Plotting $-ln\left[1 - 0.067\frac{I_D}{I_G}\right]$ against time yielded linear fits (Figure 12B), from which the rate constants were obtained. Results of the reaction between maleic anhydride (MAH) and graphene showed that Ni-supported graphene had the highest rate, 1.8–2.4 times higher than graphene supported on silicon wafer (SiO₂/Si, Figure 12C).
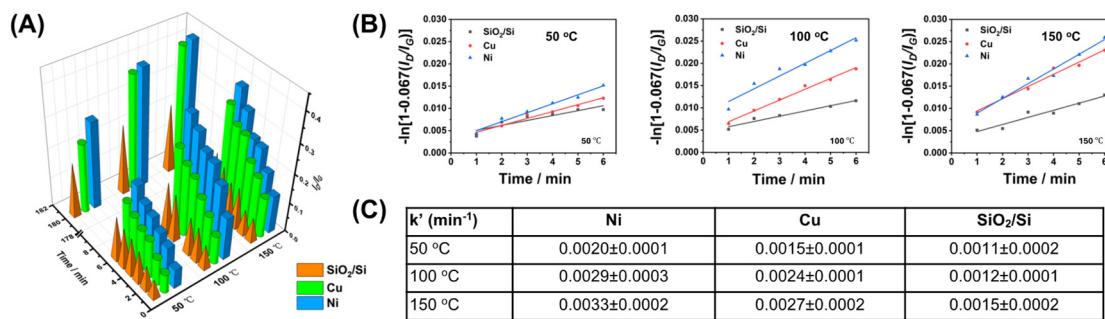
Figure 12. Determining rate constant of reactions on graphene by Raman spectroscopy. (**A**) I_D/I_G vs. reaction time and temperature for graphene supported on Ni, Cu or silicon wafer. (**B**) $-ln\left[1 - 0.067\frac{I_D}{I_G}\right]$ vs. time, and (**C**) the apparent rate constant k' (min^{-1}) for reaction of MAH with graphene supported on Ni, Cu or silicon wafer at 50 °C, 100 °C, and 150 °C. Reproduced with permission [56]. Copyright 2022, Royal Society of Chemistry.

Alivisatos and coworkers employed a combination of isothermal titration calorimetry (ITC), ^{1}H qNMR spectroscopy, X-ray diffraction, and modified Ising model to study the ligand exchange of myristate- or stearate-capped indium phosphide (InP) quantum dots (QDs) by zinc chloride [58]. The ligand exchange involves breaking van der Waals interactions between aliphatic chains of the ligands and forming new bonds with Zn^{2+}. ITC results support the proposed mechanism, showing that ligand exchange reactions became more endothermic with increasing QD size and longer ligand chains. ^{1}H qNMR with mesitylene as the internal standard was used to track the ligand density before and after ligand exchange. Stearate-capped QDs generally have lower ligand densities

than myristate-capped QDs of similar sizes, at 1.9 ± 0.5–3.7 ± 0.9 ligands/nm^2 and 2.7 ± 0.7–5.1 ± 1.0 ligands/nm^2, respectively. For both ligand types, smaller QDs (e.g., 2.7 nm) gave higher ligand densities compared to larger QDs (e.g., 3.4 nm). After the ligand exchange, the ligand coverage decreased more for myristate-capped QDs to a normalized coverage of ~0.2–0.4 of the original density than for stearate-capped QDs, which decreased to ~0.3–0.5 of the initial density.

A recent work by Choi and coworkers quantified interparticle ligand exchange kinetics of thiol ligands on AuNPs using the technique of time-resolved small-angle neutron scattering (TR-SANS) [59]. Hydrogenated (hDDT) and deuterated dodecanethiol (dDDT) were used to functionalize AuNPs, which provide neutron contrast. Changes in scattering intensity over time were monitored at different temperatures to detect ligand exchange, and the normalized relaxation function, R(t), was calculated to quantify the extent of ligand exchange. Further, an exponential decay model was applied to estimate exchange kinetics and rate constants. Results showed that at 25 °C, there was minimal ligand exchange even after 40 h. The ligand exchange was 11%, 34%, and 74% at 50, 60, and 70 °C, respectively after 40 h, and reached ~100% at 80 °C within 20 h (Figure 13A). First-order kinetic was observed, indicating that the ligand desorption was the rate-determining step (Figure 13B). The rate of ligand exchange increased with temperature, ranging from 3.4×10^{-5} min^{-1} at 50 °C to 1.6×10^{-3} min^{-1} at 80 °C. Arrhenius analysis yielded an activation energy of 29.1 kcal/mol (Figure 13C).
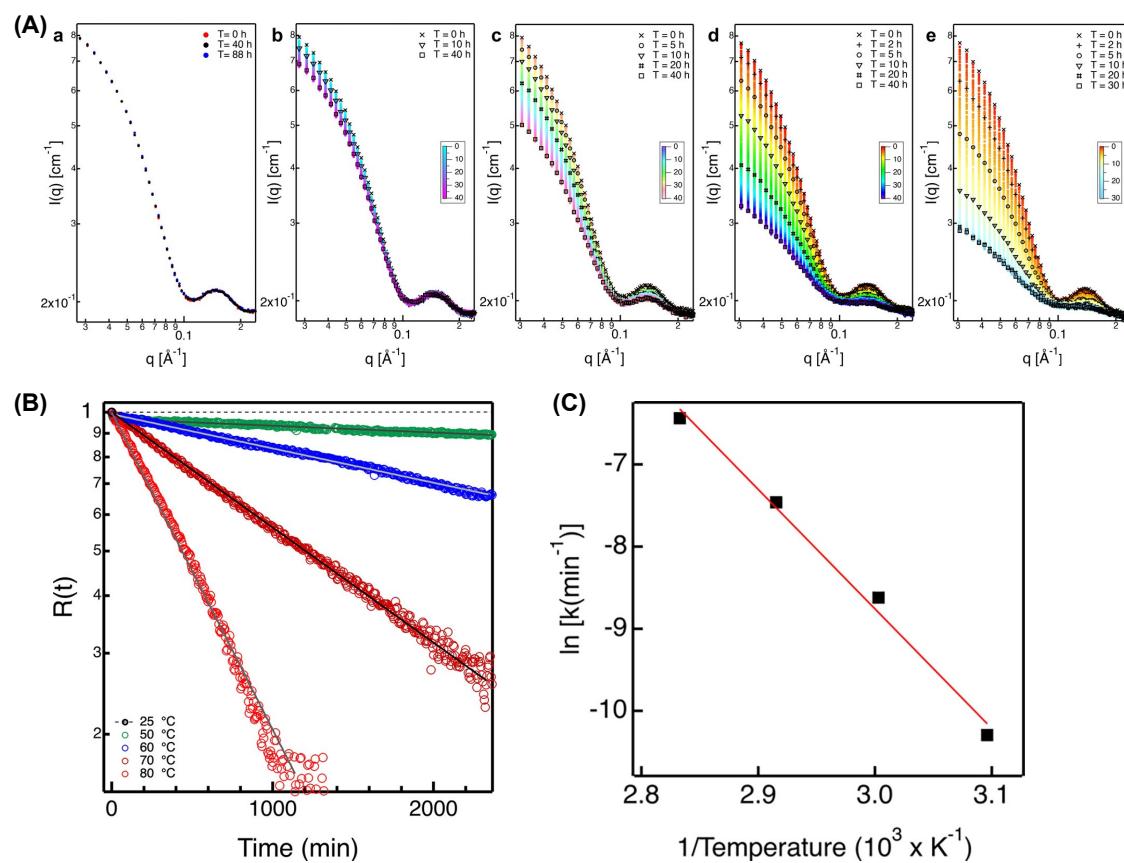
Figure 13. Quantification of interparticle ligand exchange kinetics of thiol ligands on AuNPs using TR-SANS. (**A**) TR-SANS intensity of Au-hDDT and Au-dDDT mixture at different reaction times at (**a**) 25, (**b**) 50, (**c**) 60, (**d**) 70, and (**e**) 80 °C. (**B**) Normalized relaxation function R(t) vs. time, showing first-order kinetic. (**C**) Arrhenius plot showing the relationship between the rate constant and temperature for the interparticle ligand exchange reaction. Reproduced with permission [59]. Copyright 2024, American Chemical Society.

6. Conclusions and Outlook

Detailed understanding of nanomaterial surfaces is essential for the rational design of nanomaterials with consistent, predictable, and tailored functions. In this mini review, we discussed traditional and advanced techniques to quantify ligand structure, ligand density, functional groups, and surface reactions on nanomaterials. NMR spectroscopy is a key method to determine the ligand structure on nanomaterials, providing insights into ligand dynamics and ligand-nanoparticle interface through characteristic spectral features such as peak broadening and chemical shifts, which are influenced by the proximity of ligands to the nanomaterial surface. MS, particularly

when combined with advanced analyzers like FTICR, is another powerful tool that can identify ligand structures through fragmentation patterns and molecular ion analysis. Techniques such as X-ray crystallography are used for ordered systems and can solve the complete structure of atomically precise nanoclusters at atomic resolution.

Multiple methods are available to determine ligand density on nanomaterials. TGA is widely used, offering a straightforward estimate of ligand density but is limited regarding structural specificity and sensitivity to impurities. qNMR spectroscopy provides quantitative measurements and is particularly effective for small nanoparticles or when ligands are cleaved for analysis; however, it requires sufficient sample quantities and solubility in the NMR solvent. UV-vis spectroscopy, in conjunction with spectral deconvolution, enables the quantification of mixed ligand systems by resolving overlapping absorption peaks. Advanced techniques such as nanoflow cytometry allow single-particle analysis of ligand densities and accessible ligands, while EELS offers spatial resolution for imaging ligand density variations across single nanomaterials.

Quantification of functional groups on nanomaterials can be done by a variety of methods depending on specific chemical reactivity or physical property. Titration-based techniques apply primarily to acids, bases or ionizable species. Optical assays using dye-based reporters or cleavable probes offer a straightforward way to quantify accessible functional groups by measuring absorbance or emission changes, although steric effects can limit the accuracy. IR and Raman spectroscopy detects molecular vibrations associated with functional groups. NMR spectroscopy and ICP-MS/ICP-OES analyze functional groups by identifying specific elements or structural features for quantification.

Quantifying reactions on nanomaterial surfaces employs methods that can determine reaction kinetics, rates, energetics, and yields. NMR spectroscopy is widely used to analyze reaction products and monitor ligand conversions, and qNMR can further quantify reaction yields. Advanced technique of TR-SANS provides ligand exchange kinetics, rate constants and activation energy of nanomaterial surface reactions.

Each analytical technique has unique strengths and limitations. For example, NMR and MS provide detailed molecular structure information but lack spatial resolution, while techniques like TEM, EELS, and super-resolution microscopy offer high spatial resolution but are less suited for bulk quantification. Given the complexity and heterogeneity of nanomaterials, no single method can address the full range of challenges associated with their characterizations. Employing multiple complementary techniques is therefore recommended to reduce the likelihood of measurement errors or artifacts, to cross-validate, and to ensure reliability of the results. For instance, ligand densities determined by TGA should be validated with qNMR or other spectroscopic methods for potential inclusion of contaminants. As methods for measuring the total functional groups may not accurately reflect the functional groups available for bioconjugation or receptor binding, employing multiple analytical methods such as qNMR and optical reporter probes would provide a more comprehensive quantification of both the total and accessible functional groups for receptor binding.

Beyond molecular structure, functional groups, ligand density, and surface reactions, other important surface characteristics, such as ligand presentation and the ligand-nanomaterial interface, remain poorly understood. Ligand presentation refers to the three-dimensional arrangement of ligands on the nanomaterial surface, including the conformation, spatial orientation and distribution. Factors, such as nanoparticle size, shape, spacer linker length and structure, influence the ligand presentation [60,61], which in turn affects ligand accessibility, reactivity, interactions, and binding strength with receptor molecules in applications like cell targeting. Current analytical techniques generally give the global average. Significant gap exists in the ability to characterize the conformation and spatial orientation of ligands as well as the distribution and spacing of ligands on the nanomaterial surface. Additionally, surface ligands are often in a dynamic equilibrium of various conformations especially in solution. This dynamic behavior is further influenced by interactions between neighboring ligands, adding complexity to the characterization. Furthermore, functional nanomaterials frequently carry multiple ligand types. For instance, nanoparticles for drug delivery are often functionalized with multiple ligands, including antifouling ligands to prevent non-specific protein adsorption and targeting ligands for specific cell type. The presence of different ligand types can lead to complex and ambiguous surface structures, resulting in diverse orientations and binding conformations. Similarly, the precise nature of the ligand-nanomaterial interface, including the bond type (covalent, ionic, hydrogen bonding, or van der Waals interactions), strength, and binding dynamics, also remains poorly understood. For example, in one of the most widely studied systems, thiols on Au, the nature, strength, and mechanism of formation of the Au-S bond under different conditions are still challenging to characterize [62,63]. The ligand-nanomaterial bonding directly impacts the stability of surface ligands with respect to environmental changes in pH, temperature, and ionic strength, which in turn govern the overall stability, reactivity, and properties of the nanomaterial.

The ultimate goal of nanomaterial characterization is to determine the complete structure of the nanomaterial at the molecular and atomic levels, including not only the structures of the core, ligand-nanomaterial interface and

surface ligands, but also the dynamic conformation, spatial orientation and distribution of the surface ligand. For crystallizable atomically precise nanoclusters, single-crystal X-ray diffraction has been successfully used to resolve their total structures and assemblies, including the conformation and arrangement of the ligand shell as well as the interactions between nanoclusters within crystal lattices. However, for heterogeneous nanomaterials, techniques for characterizing nanomaterial surfaces at molecular or atomic levels are lacking. Current microscopy and spectroscopy methods often lack the resolution, surface sensitivity, or scalability required to map ligand distribution or surface heterogeneity at molecular level. Additional challenges include the ability to characterize complex samples and the dynamics of nanomaterial surfaces in different environments. Emerging techniques, such as super-resolution microscopy and single-particle tracking, offer promising avenues for studying nanomaterial surfaces in unprecedented details. Combined with computational modeling and machine learning, these tools could potentially allow precise mapping of nanomaterial surfaces and ligand interactions. Looking forward, integrating conventional analytical and chemical methods with advanced characterization techniques could potentially provide a comprehensive understanding of nanomaterial surfaces with spatial resolution, surface sensitivity, and molecular specificity, facilitating the rational design of nanomaterials for diverse applications.

References

1. Pozzi, M.; Jonak Dutta, S.; Kuntze, M.; Bading, J.; Rüßbült, J.S.; Fabig, C.; Langfeldt, M.; Schulz, F.; Horcajada, P.; Parak, W.J. Visualization of the High Surface-to-Volume Ratio of Nanomaterials and Its Consequences. *J. Chem. Educ.* **2024**, *101*, 3146–3155.

2. Liu, P.; Qin, R.; Fu, G.; Zheng, N. Surface Coordination Chemistry of Metal Nanomaterials. *J. Am. Chem. Soc.* **2017**, *139*, 2122–2131.

3. Singh, R.; Srinivas, S.P.; Kumawat, M.; Daima, H.K. Ligand-based surface engineering of nanomaterials: Trends, challenges, and biomedical perspectives. *OpenNano* **2024**, *15*, 100194.

4. Nam, J.-M.; Owen, J.S.; Talapin, D.V. The Ligand–Surface Interface and Its Influence on Nanoparticle Properties. *Acc. Chem. Res.* **2023**, *56*, 2265–2266.

5. Cetin, A.; Ilk Capar, M. Functional-Group Effect of Ligand Molecules on the Aggregation of Gold Nanoparticles: A Molecular Dynamics Simulation Study. *J. Phys. Chem. B* **2022**, *126*, 5534–5543.

6. Shrestha, S.; Wang, B.; Dutta, P. Nanoparticle processing: Understanding and controlling aggregation. *Adv. Colloid Interface Sci.* **2020**, *279*, 102162.

7. Thanh, N.T.K.; Maclean, N.; Mahiddine, S. Mechanisms of Nucleation and Growth of Nanoparticles in Solution. *Chem. Rev.* **2014**, *114*, 7610–7630.

8. An, K.; Somorjai, G.A. Size and Shape Control of Metal Nanoparticles for Reaction Selectivity in Catalysis. *ChemCatChem* **2012**, *4*, 1512–1524.

9. Shi, Y.; Lyu, Z.; Zhao, M.; Chen, R.; Nguyen, Q.N.; Xia, Y. Noble-Metal Nanocrystals with Controlled Shapes for Catalytic and Electrocatalytic Applications. *Chem. Rev.* **2021**, *121*, 649–735.

10. Kumar, S.; Saha, D.; Kohlbrecher, J.; Aswal, V.K. Interplay of interactions for different pathways of the fractal aggregation of nanoparticles. *Chem. Phys. Lett.* **2022**, *803*, 139808.

11. Heuer-Jungemann, A.; Feliu, N.; Bakaimi, I.; Hamaly, M.; Alkilany, A.; Chakraborty, I.; Masood, A.; Casula, M.F.; Kostopoulou, A.; Oh, E.; et al. The role of ligands in the chemical synthesis and applications of inorganic nanoparticles. *Chem. Rev.* **2019**, *119*, 4819–4880.

12. Bhattacharjee, K.; Prasad, B.L.V. Surface functionalization of inorganic nanoparticles with ligands: A necessary step for their utility. *Chem. Soc. Rev.* **2023**, *52*, 2573–2595.

13. Sperling, R.A.; Parak, W.J. Surface modification, functionalization and bioconjugation of colloidal inorganic nanoparticles. *Philos. Trans. A Math. Phys. Eng. Sci.* **2010**, *368*, 1333–1383.

14. Mishra, R.K.; Verma, K.; Singh, D.S. Defect engineering in nanomaterials: Impact, challenges, and applications. *Smart Mater. Manuf.* **2024**, *2*, 100052.

15. Baumler, K.J.; Schaak, R.E. Tutorial on Describing, Classifying, and Visualizing Common Crystal Structures in Nanoscale Materials Systems. *ACS Nanosci. Au* **2024**, *4*, 290–316.

16. Xi, Z.; Zhang, R.; Kiessling, F.; Lammers, T.; Pallares, R.M. Role of Surface Curvature in Gold Nanostar Properties and Applications. *ACS Biomater. Sci. Eng.* **2024**, *10*, 38–50.

17. Walker, D.A.; Leitsch, E.K.; Nap, R.J.; Szleifer, I.; Grzybowski, B.A. Geometric curvature controls the chemical patchiness and self-assembly of nanoparticles. *Nat. Nanotechnol.* **2013**, *8*, 676–681.

18. Pedrazo-Tardajos, A.; Claes, N.; Wang, D.; Sánchez-Iglesias, A.; Nandi, P.; Jenkinson, K.; De Meyer, R.; Liz-Marzán, L.M.; Bals, S. Direct visualization of ligands on gold nanoparticles in a liquid environment. *Nat. Chem.* **2024**, *16*, 1278–1285.

19. Sen, S.; Thaker, A.; Sirajudeen, L.; Williams, D.; Nannenga, B.L. Protein–Nanoparticle Complex Structure Determination by Cryo-Electron Microscopy. *ACS Appl. Bio Mater.* **2022**, *5*, 4696–4700.

20. Shevchenko, E.V.; Talapin, D.V.; Kotov, N.A.; O'Brien, S.; Murray, C.B. Structural diversity in binary nanoparticle superlattices. *Nature* **2006**, *439*, 55–59.

21. Zhou, W.; Li, Y.; Partridge, B.E.; Mirkin, C.A. Engineering Anisotropy into Organized Nanoscale Matter. *Chem. Rev.* **2024**, *124*, 11063–11107.

22. Jadzinsky, P.D.; Calero, G.; Ackerson, C.J.; Bushnell, D.A.; Kornberg, R.D. Structure of a Thiol Monolayer-Protected Gold Nanoparticle at 1.1 Å Resolution. *Science* **2007**, *318*, 430–433.

23. Li, Y.; Jin, R. Seeing Ligands on Nanoclusters and in Their Assemblies by X-ray Crystallography: Atomically Precise Nanochemistry and Beyond. *J. Am. Chem. Soc.* **2020**, *142*, 13627–13644.

24. Marbella, L.E.; Millstone, J.E. NMR Techniques for Noble Metal Nanoparticles. *Chem. Mater.* **2015**, *27*, 2721–2739.

25. Jayawardena, H.S.N.; Liyanage, S.H.; Rathnayake, K.; Patel, U.; Yan, M. Analytical Methods for Characterization of Nanomaterial Surfaces. *Anal. Chem.* **2021**, *93*, 1889–1911.

26. Wu, M.; Vartanian, A.M.; Chong, G.; Pandiakumar, A.K.; Hamers, R.J.; Hernandez, R.; Murphy, C.J. Solution NMR Analysis of Ligand Environment in Quaternary Ammonium-Terminated Self-Assembled Monolayers on Gold Nanoparticles: The Effect of Surface Curvature and Ligand Structure. *J. Am. Chem. Soc.* **2019**, *141*, 4316–4327.

27. Novotný, J.; Vícha, J.; Bora, P.L.; Repisky, M.; Straka, M.; Komorovsky, S.; Marek, R. Linking the Character of the Metal–Ligand Bond to the Ligand NMR Shielding in Transition-Metal Complexes: NMR Contributions from Spin–Orbit Coupling. *J. Chem. Theory Comput.* **2017**, *13*, 3586–3601.

28. Vícha, J.; Novotný, J.; Komorovsky, S.; Straka, M.; Kaupp, M.; Marek, R. Relativistic Heavy-Neighbor-Atom Effects on NMR Shifts: Concepts and Trends Across the Periodic Table. *Chem. Rev.* **2020**, *120*, 7065–7103.

29. Ndugire, W.; Liyanage, S.H.; Yan, M. Carbohydrate-Presenting Metal Nanoparticles: Synthesis, Characterization and Applications. In *Comprehensive Glycoscience*, 2nd ed.; Barchi, J.J., Ed.; Elsevier: Amsterdam, The Netherlands, 2021; pp. 380–405.

30. Wu, Z.; Jin, R. Stability of the Two Au−S Binding Modes in Au25(SG)18 Nanoclusters Probed by NMR and Optical Spectroscopy. *ACS Nano* **2009**, *3*, 2036–2042.

31. Ghosh, J.; Cooks, R.G. Mass spectrometry in materials synthesis. *Trends Anal. Chem.* **2023**, *161*, 117010.

32. Comby-Zerbino, C.; Dagany, X.; Chirot, F.; Dugourd, P.; Antoine, R. The emergence of mass spectrometry for characterizing nanomaterials. Atomically precise nanoclusters and beyond. *Mater. Adv.* **2021**, *2*, 4896–4913.

33. Nicolardi, S.; van der Burgt, Y.E.M.; Codée, J.D.C.; Wuhrer, M.; Hokke, C.H.; Chiodo, F. Structural Characterization of Biofunctionalized Gold Nanoparticles by Ultrahigh-Resolution Mass Spectrometry. *ACS Nano* **2017**, *11*, 8257–8264.

34. Smith, A.M.; Johnston, K.A.; Crawford, S.E.; Marbella, L.E.; Millstone, J.E. Ligand density quantification on colloidal inorganic nanoparticles. *Analyst* **2017**, *142*, 11–29.

35. Mansfield, E.; Tyner, K.M.; Poling, C.M.; Blacklock, J.L. Determination of Nanoparticle Surface Coatings and Nanoparticle Purity Using Microscale Thermogravimetric Analysis. *Anal. Chem.* **2014**, *86*, 1478–1484.

36. Choi, K.; Myoung, S.; Seo, Y.; Ahn, S. Quantitative NMR as a Versatile Tool for the Reference Material Preparation. *Magnetochemistry* **2021**, *7*, 15.

37. Kong, N.; Zhou, J.; Park, J.; Xie, S.; Ramström, O.; Yan, M. Quantitative Fluorine NMR To Determine Carbohydrate Density on Glyconanomaterials Synthesized from Perfluorophenyl Azide-Functionalized Silica Nanoparticles by Click Reaction. *Anal. Chem.* **2015**, *87*, 9451–9458.

38. Potts, J.C.; Jain, A.; Amabilino, D.B.; Rawson, F.J.; Pérez-García, L. Molecular Surface Quantification of Multifunctionalized Gold Nanoparticles Using UV–Visible Absorption Spectroscopy Deconvolution. *Anal. Chem.* **2023**, *95*, 12998–13002.

39. Senoner, M.; Unger, W.E.S. SIMS imaging of the nanoworld: Applications in science and technology. *J. Anal. At. Spectrom.* **2012**, *27*, 1050–1068.

40. Eller, M.J.; Chandra, K.; Coughlin, E.E.; Odom, T.W.; Schweikert, E.A. Label Free Particle-by-Particle Quantification of DNA Loading on Sorted Gold Nanostars. *Anal. Chem.* **2019**, *91*, 5566–5572.

41. Masuko, T.; Minami, A.; Iwasaki, N.; Majima, T.; Nishimura, S.-I.; Lee, Y.C. Carbohydrate analysis by a phenol–sulfuric acid method in microplate format. *Anal. Biochem.* **2005**, *339*, 69–72.

42. Wang, X.; Ramström, O.; Yan, M. A photochemically initiated chemistry for coupling underivatized carbohydrates to gold nanoparticles. *J. Mater. Chem.* **2009**, *19*, 8944–8949.

43. Janicek, B.E.; Hinman, J.G.; Hinman, J.J.; Bae, S.H.; Wu, M.; Turner, J.; Chang, H.-H.; Park, E.; Lawless, R.; Suslick,

K.S.; et al. Quantitative Imaging of Organic Ligand Density on Anisotropic Inorganic Nanocrystals. *Nano Lett.* **2019**, *19*, 6308–6314.

44. Chen, C.; Zhou, Y.; Chen, C.; Zhu, S.; Yan, X. Quantification of Available Ligand Density on the Surface of Targeted Liposomal Nanomedicines at the Single-Particle Level. *ACS Nano* **2022**, *16*, 6886–6897.

45. Geißler, D.; Nirmalananthan-Budau, N.; Scholtz, L.; Tavernaro, I.; Resch-Genger, U. Analyzing the surface of functional nanomaterials—How to quantify the total and derivatizable number of functional groups and ligands. *Microchim. Acta* **2021**, *188*, 321.

46. Kunc, F.; Balhara, V.; Brinkmann, A.; Sun, Y.; Leek, D.M.; Johnston, L.J. Quantification and Stability Determination of Surface Amine Groups on Silica Nanoparticles Using Solution NMR. *Anal. Chem.* **2018**, *90*, 13322–13330.

47. Kunc, F.; Balhara, V.; Sun, Y.; Daroszewska, M.; Jakubek, Z.J.; Hill, M.; Brinkmann, A.; Johnston, L.J. Quantification of surface functional groups on silica nanoparticles: Comparison of thermogravimetric analysis and quantitative NMR. *Analyst* **2019**, *144*, 5589–5599.

48. Moser, M.; Nirmalananthan, N.; Behnke, T.; Geißler, D.; Resch-Genger, U. Multimodal Cleavable Reporters versus Conventional Labels for Optical Quantification of Accessible Amino and Carboxy Groups on Nano- and Microparticles. *Anal. Chem.* **2018**, *90*, 5887–5895.

49. Roloff, A.; Nirmalananthan-Budau, N.; Rühle, B.; Borcherding, H.; Thiele, T.; Schedler, U.; Resch-Genger, U. Quantification of Aldehydes on Polymeric Microbead Surfaces via Catch and Release of Reporter Chromophores. *Anal. Chem.* **2019**, *91*, 8827–8834.

50. Sun, Y.; Kunc, F.; Balhara, V.; Coleman, B.; Kodra, O.; Raza, M.; Chen, M.; Brinkmann, A.; Lopinski, G.P.; Johnston, L.J. Quantification of amine functional groups on silica nanoparticles: A multi-method approach. *Nanoscale Adv.* **2019**, *1*, 1598–1607.

51. Konsolakis, M. Surface Chemistry and Catalysis. *Catalysts* **2016**, *6*, 102.

52. Somorjai, G.A.; Li, Y. *Introduction to Surface Chemistry and Catalysis*, 2nd ed.; Wiley: NewYork, NY, USA, 2010.

53. Sanità, G.; Carrese, B.; Lamberti, A. Nanoparticle surface functionalization: How to improve biocompatibility and cellular internalization. *Front. Mol. Biosci.* **2020**, *7*, 587012.

54. Ndugire, W.; Yan, M. Synthesis and solution isomerization of water-soluble Au9 nanoclusters prepared by nuclearity conversion of [Au11(PPh3)8Cl2]Cl. *Nanoscale* **2021**, *13*, 16809–16817.

55. Klein, K.; Loza, K.; Heggen, M.; Epple, M. An efficient method for covalent surface functionalization of ultrasmall metallic nanoparticles by surface azidation followed by copper-catalyzed azide-alkyne cycloaddition (click chemistry). *ChemNanoMat* **2021**, *7*, 1330–1339.

56. Yang, X.; Chen, F.; Kim, M.A.; Liu, H.; Wolf, L.M.; Yan, M. Using metal substrates to enhance the reactivity of graphene towards Diels–Alder reactions. *Phys. Chem. Chem. Phys.* **2022**, *24*, 20082–20093.

57. Tu, J.; Yan, M. Enhancing the chemical reactivity of graphene through substrate engineering. *Small* **2024**, e2408116.

58. Calvin, J.J.; Sedlak, A.B.; Brewer, A.S.; Kaufman, T.M.; Alivisatos, A.P. Evidence and Structural Insights into a Ligand-Mediated Phase Transition in the Solvated Ligand Shell of Quantum Dots. *ACS Nano* **2024**, *18*, 25257–25270.

59. Lee, S.-J.; Jang, J.D.; Choi, S.-M. Interparticle Ligand Exchange Kinetics Revealed by Time-Resolved SANS. *Nano Lett.* **2025**, *25*, 981–986.

60. Wang, X.; Ramström, O.; Yan, M. Quantitative Analysis of Multivalent Ligand Presentation on Gold Glyconanoparticles and the Impact on Lectin Binding. *Anal. Chem.* **2010**, *82*, 9082–9089.

61. Wang, X.; Ramström, O.; Yan, M. Glyconanomaterials: Synthesis, Characterization, and Ligand Presentation. *Adv. Mater.* **2010**, *22*, 1946–1953.

62. Rashid, U.; Bro-Jørgensen, W.; Harilal, K.B.; Sreelakshmi, P.A.; Mondal, R.R.; Chittari Pisharam, V.; Parida, K.N.; Geetharani, K.; Hamill, J.M.; Kaliginedi, V. Chemistry of the Au–Thiol Interface through the Lens of Single-Molecule Flicker Noise Measurements. *J. Am. Chem. Soc.* **2024**, *146*, 9063–9073.

63. Inkpen, M.S.; Liu, Z.F.; Li, H.; Campos, L.M.; Neaton, J.B.; Venkataraman, L. Non-chemisorbed gold–sulfur binding prevails in self-assembled monolayers. *Nat. Chem.* **2019**, *11*, 351–358.

Article

Chameleon-Inspired Color-Changeable Colloidal Photonic Crystal Films Sensitive to Human Body Temperature

Toshimitsu Kanai *, Mari Sato, and Yuna Hirano

Graduate School of Engineering Science, Yokohama National University, 79-5 Tokiwadai, Hodogaya-ku, Yokohama 240-8501, Japan
* Correspondence: tkanai@ynu.ac.jp

Abstract: Artificial chameleon skins have been developed using advanced materials, such as photonic crystals, for camouflage and thermoregulation. However, to respond to subtle changes in human body temperature, the thermosensitivity, quality, and color response of these biomimetic films need to be improved. We report the development of chameleon-inspired

color-changeable films with enhanced sensitivity to changes in the human body temperature. Non-close-packed colloidal photonic crystals were immobilized in a thermosensitive poly(*N*-isopropylacrylamide) (PNIPAM) hydrogel film and simultaneously attached to a flexible polyethylene terephthalate (PET) sheet by photopolymerization. The attachment to the PET sheet ensured high thermosensitivity and film quality besides ease of use. The film displayed full color spectrum from red to violet within a small range (~3 °C) of human body temperature without any change in the film area and film distortion. The temperature range of the full color spectrum was easily tuned by adding a poor solvent, ethylene glycol, to PNIPAM. The film attached to a human arm exhibited color changes from red to yellow, light green, and blue in response to changes in the body temperature without external heat. This study could contribute to the basic research and practical applications of artificial chameleon skins.
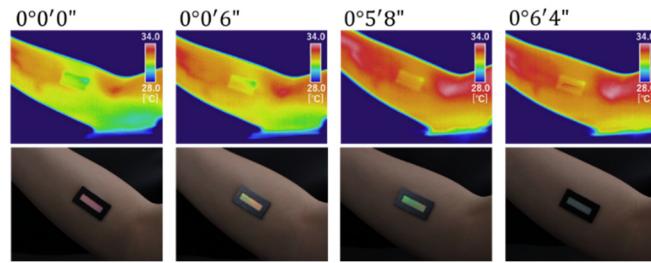
Keywords: structural color; colloidal photonic crystal; tunable color; chameleon; thermosensitive hydrogel

1. Introduction

Panther chameleons change their body color for camouflage, communication, and thermoregulation [1–5]. Their unique changeable color originates from the periodic nanostructure of guanine particles present in skin cells. Although guanine particles are colorless, the periodic nanostructure generates color by reflecting or scattering a specific wavelength of light depending on the spacing of the guanine particles. Chameleons can change the spacing of guanine particles, resulting in a color change. The color generated by the periodic nanostructure is called structural color [6–12]. Color-changeable films that mimic chameleon skins have been studied for applications such as artificial camouflage and sensors that detect changes in environmental conditions based on color changes. An important example is the elastomer-immobilized colloidal photonic crystal film, which comprises a non-close-packed particle array of submicron-sized monodisperse colloids embedded in an elastic polymer film [13–17]. When the film is attached to a human elbow and the elbow is bent, the film color changes according to the change in the particle spacing of the colloidal photonic crystals in the stretched elastomer [13]. However, this type of stress-responsive color change is limited to nearby joints because the film must be elongated or contracted to change the particle spacing.

Thermoresponsive hydrogel-immobilized colloidal photonic crystal films are promising color-changeable films that mimic chameleon skins [18–20]. The color changes are based on the change in the particle spacing of the non-close-packed colloidal photonic crystals, which is caused by the volume change of the surrounding hydrogel in response to a temperature change. In particular, the poly(*N*-isopropylacrylamide) (PNIPAM) hydrogel

undergoes significant volume change near its phase transition temperature of 32 °C [21]; i.e., the PNIPAM hydrogel-immobilized colloidal photonic crystal film changes color within a temperature range that encompasses human body temperature. However, a significant color change in response to temperature changes (i.e., higher thermosensitivity) is required because changes in the human body temperature are small. In addition, the film quality must be preserved after the color change. The generation of various colors involves a significant volume change in the hydrogel, which generally results in a significant change in the film area and film distortion. Furthermore, easy color customization is indispensable because the human body temperature differs between individuals and body parts [22]. Although color tuning of thermoresponsive colloidal photonic crystal film is possible by varying the particle diameter, particle volume fraction, and thermosensitive monomer concentration, this approach is impractical because the laborious and time-consuming preparation must be repeated for the individual.

We previously found that the linear thermosensitivity of a PNIPAM-poly(*N*-methylolacrylamide) hydrogel-immobilized colloidal photonic crystal film can be increased 1.6-fold by bonding the film to a glass substrate using a silane coupling agent [23]. Furthermore, the film area does not change; no waving or warping occurs during the temperature change owing to the attachment of the film to the glass substrate. Herein, we report the preparation of chameleon-inspired color-changeable films that respond to small changes in the surface temperature of the human body without any change in the film area or distortion.

2. Materials and Methods

2.1. Materials

An ion-exchange resin (AG501-X8(D), Bio-Rad, Hercules, CA, USA) was added to an aqueous suspension of monodisperse polystyrene particles with a diameter of 200 nm (5020 B, Thermo Fisher Scientific, Waltham, MA, USA) and gently stirred to form charge-stabilized colloidal photonic crystals by deionization. The obtained colloidal photonic crystals were concentrated using a centrifuge (5702 RH, Eppendorf Corporate, Hamburg, Germany). Thereafter, a gelation reagent comprising *N*-isopropylacrylamide (NIPAM) monomer (FUJIFILM Wako Pure Chemical Corp., Tokyo, Japan), *N*,*N*′-methylene*bis*-acrylamide (BIS) crosslinker (FUJIFILM Wako Pure Chemical Corp., Tokyo, Japan), and 2,2′-azo*bis*[2-methyl-*N*-(2-hydroxyethyl)propionamide] (VA) photopolymerization initiator (FUJIFILM Wako Pure Chemical Corp., Tokyo, Japan) were added. Ultrapure water (Milli-Q system, Merck KGaA, Darmstadt, Germany) was added to adjust the concentrations of the polystyrene particles, NIPAM, BIS, and VA to 10 vol.%, 800 mM, 40 mM, and 0.4 mM, respectively.

2.2. Immobilization and Photopolymerization of the Film

A PET sheet (Lumirror T60, thickness: 250 μm, Toray Industries, Inc., Tokyo, Japan) was cut into a rectangular piece (7.5 cm × 2.5 cm), and the surface was treated with a plasma ion bombarder (PIB-20, Vacuum Device, Mito, Japan) for 90 s to attach a PNIPAM hydrogel film to the PET sheet by graft polymerization [24]. The PET sheet was sandwiched between a quartz substrate with a flow channel (channel height: 0.1 mm; width: 9 mm; length: 50 mm) and a plain quartz substrate to assemble the cell (Figure 1). The cells were fixed between metal frames and screws. The charge-stabilized colloidal photonic crystals with a gelation reagent were bubbled with Ar gas for 5 min and subsequently shear-flowed into the cell to form a single-crystalline structure [25,26]. The top and bottom of the cell were irradiated with ultraviolet (UV) light (MBRL-CUV7530, MORITEX Corporation, Saitama, Japan) for 90 min to photopolymerize the gelation reagent. The cells were then disassembled to obtain the PET-attached PNIPAM hydrogel-immobilized colloidal photonic crystal film. A 500-μm thick silicone spacer was placed on the PET sheet to surround the film. Thereafter, ethylene glycol aqueous solution with different ethylene glycol concentrations, C_{EG}, was added to the film as the swelling solvent and covered with a 250-μm thick PET sheet (Lumirror T60, Toray Industries, Inc., Tokyo, Japan) or a glass slide. For comparison, a PNIPAM hydrogel-immobilized colloidal photonic crystal film without the PET sheet was prepared. The film was cut into a 3-mm diameter disk and sandwiched between 250-μm thick PET sheets (Lumirror T60, Toray Industries, Inc., Tokyo, Japan) along with ultrapure water using a 500-μm thick silicone spacer.
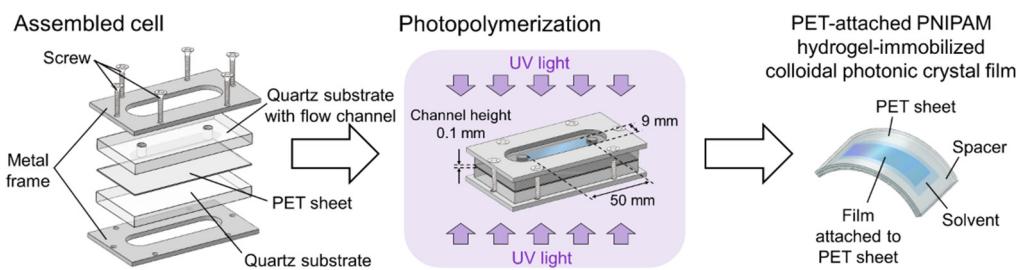
Figure 1. Schematic of the preparation process of the polyethylene terephthalate-attached poly(*N*-isopropylacrylamide) hydrogel-immobilized colloidal photonic crystal film.

2.3. Characterization

The reflection spectra of the colloidal photonic crystals at normal incidence were measured before and after UV light irradiation using a fiber spectrometer (Fastevert S-2630, Soma Optics, Ltd., Tokyo, Japan). The samples were placed on a thermal stage (KM-1, Kitazato Corporation, Tokyo, Japan) and the temperature was increased. The photograph and reflection spectrum at normal incidence were recorded at various temperatures using a charge-coupled device camera (XCD-V60CR, Sony, Tokyo, Japan) and fiber spectrometer (Fastevert S-2630 or S-2431 model II, Soma Optics, Ltd., Tokyo, Japan), respectively. The temperature distribution on the film surface was measured using an infrared thermal imaging camera (R300SR, Nippon Avionics Co., Ltd., Yokohama, Japan).

3. Results and Discussion

Figure 2a shows the reflection spectrum (at normal incidence) of the colloidal photonic crystals on the PET sheet in the cell before and after UV light irradiation. Before irradiation, a strong reflection peak is observed at 867 nm. Considering the Bragg condition, this peak originates from the (111) lattice planes of a face-centered cubic (FCC) structure aligned parallel to the cell surface [27]. The Bragg equation is as follows:

$$\lambda_{111} = 2n_c d_{111}, \tag{1}$$

where λ_{111} and d_{111} are the Bragg wavelength and lattice spacing of FCC (111) planes, respectively, and n_c is the refractive index of the colloidal photonic crystals. The value of n_c can be approximated as the volume-weighted average of the refractive indexes of the components [28]:

$$n_c = n_p \phi_p + n_{pol} \phi_{pol} + n_w \phi_w, \tag{2}$$

where n_p, n_{pol}, and n_w are the refractive indexes of polystyrene particles ($n_p = 1.59$), polymer ($n_{pol} = 1.45$), and water ($n_w = 1.33$), respectively. The volume fractions of the polystyrene particles (ϕ_p), polymer (ϕ_{pol}), and water (ϕ_w) exhibit the relationships $\phi_w = 1 - \phi_p - \phi_{pol}$ and $\phi_{pol} = 1.03\,\phi_p$ [29]. Furthermore, ϕ_p was determined from the geometrical properties of the FCC structure using d_{111} and particle diameter d as:

$$\phi_p = \frac{2\pi}{9\sqrt{3}} \left(\frac{d}{d_{111}} \right)^3. \tag{3}$$

By substituting $\phi_p = 0.1$ (determined from the particle concentration of the preparation) in Equations (2) and (3), λ_{111} was calculated as 871 nm using Equation (1), which is in good agreement with the observed Bragg wavelength.

Under UV light irradiation, the NIPAM monomer and BIS crosslinker were photopolymerized to immobilize the non-close-packed colloidal photonic crystals almost intact in the PNIPAM hydrogel film and were simultaneously attached to the PET sheet by graft polymerization [24]. A slight reduction in the intensity and blue shift of the Bragg reflection peak are observed after UV irradiation, probably because of the evaporation of water during photopolymerization. When the cell was disassembled, a PET-attached PNIPAM hydrogel-immobilized colloidal photonic crystal film was obtained. The film was easy to handle and exhibited good flexibility because of the support of the PET sheet, as shown in Figure 2b.

Figure 3a,b show the photographs and reflection spectra at normal incidence, respectively, of the PET-unattached and PET-attached PNIPAM hydrogel-immobilized colloidal photonic crystal films at various temperatures. As the temperature increases, the PET-unattached film shrinks and exhibits a red color at 31.5 °C. With further increase in the temperature, the film shrinks more and warps above 32.4 °C. The film ceases to shrink above 34.0 °C. In the reflection spectrum, the Bragg peak markedly blueshifts with increasing temperature and then saturates to approximately 600 nm above 34.0 °C. These behaviors are typical of PNIPAM hydrogel-immobilized colloidal photonic crystals [18,19]. In contrast, the PET-attached film exhibits better color changes

without any change in the film area or warping. The full color spectrum from red to violet was displayed in a temperature range of approximately 3 °C (31.0–34.2 °C). Figure 3c shows the Bragg wavelengths of the PET-unattached and PET-attached films as a function of temperature. The Bragg wavelength of the PET-attached film is consistently lower than that of the PET-unattached film. While the Bragg wavelength of the PET-unattached film saturates to approximately 600 nm above 34.0 °C, that of the PET-attached film decreases further and reaches 332 nm at 35.1 °C. The thermosensitivities, $\Delta\lambda/\Delta T$, of the PET-unattached and PET-attached films were calculated from the Bragg wavelengths at different temperatures (Figure 3d). The thermosensitivity was enhanced by attaching the PNIPAM hydrogel-immobilized colloidal photonic crystal film to the PET sheet. While the maximum thermosensitivity of the PET-unattached film is −76 nm/°C at 31.5 °C, that of the PET-attached film is enhanced to −171 nm/°C at 32.8 °C.
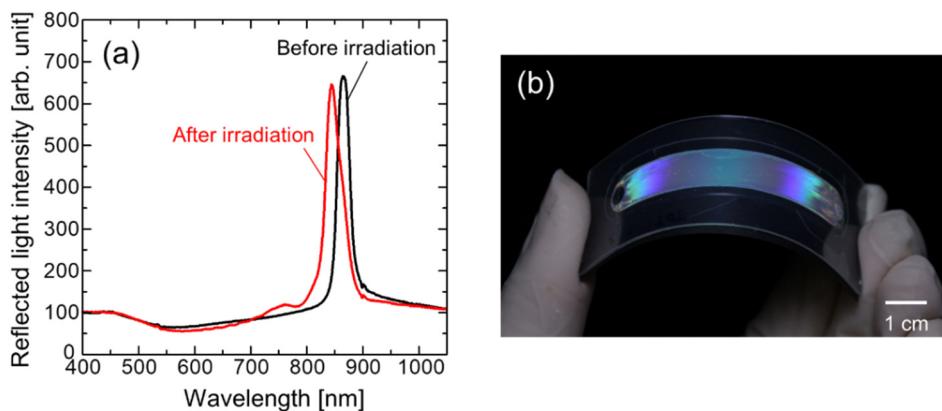
Figure 2. (**a**) Reflection spectrum (at normal incidence) of the non-close-packed colloidal photonic crystals on the polyethylene terephthalate (PET) sheet in the cell before and after ultraviolet light irradiation. (**b**) Photograph of the PET-attached poly(*N*-isopropylacrylamide) hydrogel-immobilized colloidal photonic crystal film covered with the PET sheet.
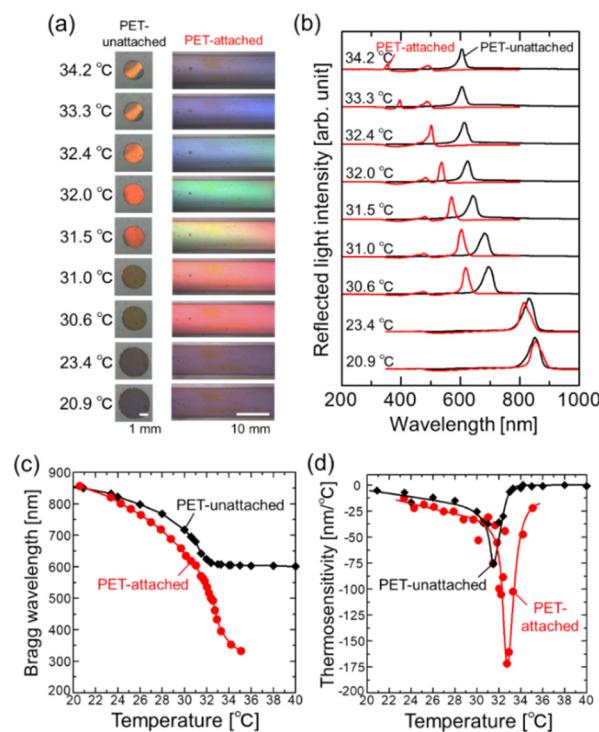
Figure 3. (**a**) Photographs and (**b**) reflection spectra of the polyethylene terephthalate (PET)-unattached and PET-attached poly(*N*-isopropylacrylamide) (PNIPAM) hydrogel-immobilized colloidal photonic crystal films at various temperatures. (**c**) Bragg wavelengths and (**d**) thermosensitivities of the PET-unattached and PET-attached PNIPAM hydrogel-immobilized colloidal photonic crystal films as a function of temperature.

The enhanced thermosensitivity of the PET-attached PNIPAM hydrogel-immobilized colloidal photonic crystal film arises from the anisotropic contraction of the PNIPAM hydrogel [23,29]. The PET-unattached PNIPAM hydrogel-immobilized colloidal photonic crystal film maintained the FCC structure during contraction with increasing temperature. However, for the PET-attached PNIPAM hydrogel-immobilized colloidal photonic crystal film, the contraction in the thickness direction increased because the in-plane shrinkage was suppressed. The observed color or Bragg wavelength is derived from the lattice spacing parallel to the thickness direction; hence, the Bragg wavelength exhibited a greater blue shift. Furthermore, the colloids in the lattice planes perpendicular to the thickness direction remained apart and did not interfere with each other during contraction. This resulted in a smaller lattice spacing parallel to the thickness direction in the maximum shrinkage state. Thus, the ultimate Bragg wavelength of the PET-attached PNIPAM hydrogel-immobilized colloidal photonic crystal film reached a much smaller value of 332 nm.

The temperature range in which the full color spectrum from red to violet is displayed can be easily tuned by adding a poor solvent such as ethylene glycol to PNIPAM. The lattice spacing of the colloidal crystals embedded in the PNIPAM hydrogel reduces with an increase in the C_{EG}. Therefore, the temperature range exhibiting the full color and Bragg wavelength of the PET-attached PNIPAM hydrogel-immobilized colloidal photonic crystal film shifts to lower values with increase in the C_{EG}, as shown in Figure 4a,b. A film with $C_{EG} = 20$ wt.% exhibited the full color spectrum between 24.3 and 27.9 °C. Although the maximum thermosensitivity decreased to -122 nm/°C at $C_{EG} = 20$ wt.% and 27.4 °C, the value is considerably high (Figure 4c).
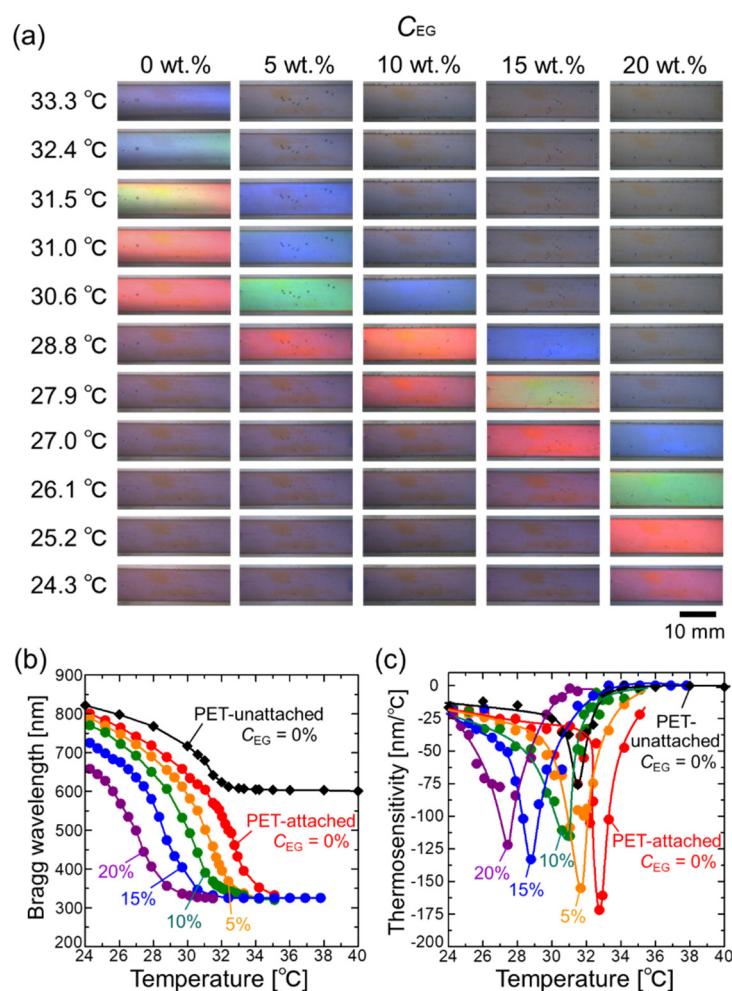
Figure 4. (**a**) Photographs of the polyethylene terephthalate (PET)-attached poly(*N*-isopropylacrylamide) (PNIPAM) hydrogel-immobilized colloidal photonic crystal films with different ethylene glycol concentrations (C_{EG}) at various temperatures. (**b**) Bragg wavelengths, and (**c**) thermosensitivities of the PET-attached PNIPAM hydrogel-immobilized colloidal photonic crystal films with different C_{EG} as a function of temperature.

The PET-attached PNIPAM hydrogel-immobilized colloidal photonic crystal film was used to visualize the temperature distribution. When a copper wire heated to 40 °C was brought closer to the film, the film displayed the full color spectrum from violet to red spreading radially outward close to the copper wire (Figure 5). The

temperatures marked at different positions in Figure 5 were determined using thermography. The correspondence between the color and temperature at each position is in reasonable agreement with that shown in Figure 4a.
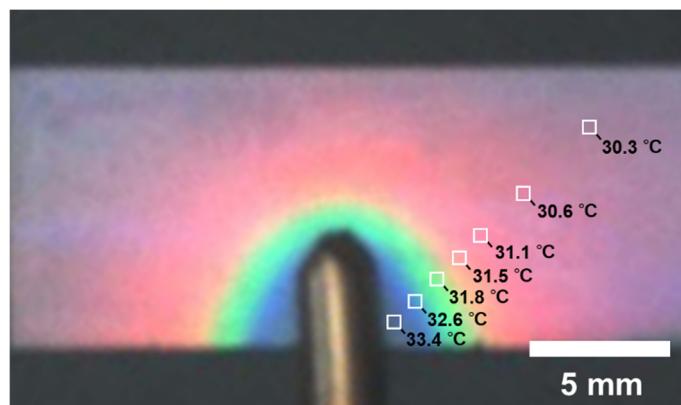
Figure 5. Photograph showing the color change of the polyethylene terephthalate-attached poly(*N*-isopropylacrylamide) hydrogel-immobilized colloidal photonic crystal film (prepared with ethylene glycol concentration of 0 wt.%) when a copper wire heated to 40 °C was brought closer to the film.

The PET-attached PNIPAM hydrogel-immobilized colloidal photonic crystal film changes color in response to changes in the surface temperature of the human body without the application of external heat. Figure 6 shows the color changes occurring in the film attached to a human arm while the arm was swinging. After resting for 30 min in a room maintained at a temperature of 23.0 °C, the surface temperature of the film (as measured by thermography) stabilized to 31.1 °C. In the initial state, the film color was red. When the arm was swung from side to side using the elbow as a fulcrum, the film temperature increased to 31.5 °C after 6 s, and the film color began changing to yellow. After 5 and 6 min, the film temperature increased to 31.9 and 32.6 °C, and the film color changed to light green and blue, respectively. When the arm stopped swinging, the film color returned to light green, yellow, and red, in that order, over approximately 77 min, corresponding to a decrease in the surface temperature of the arm.
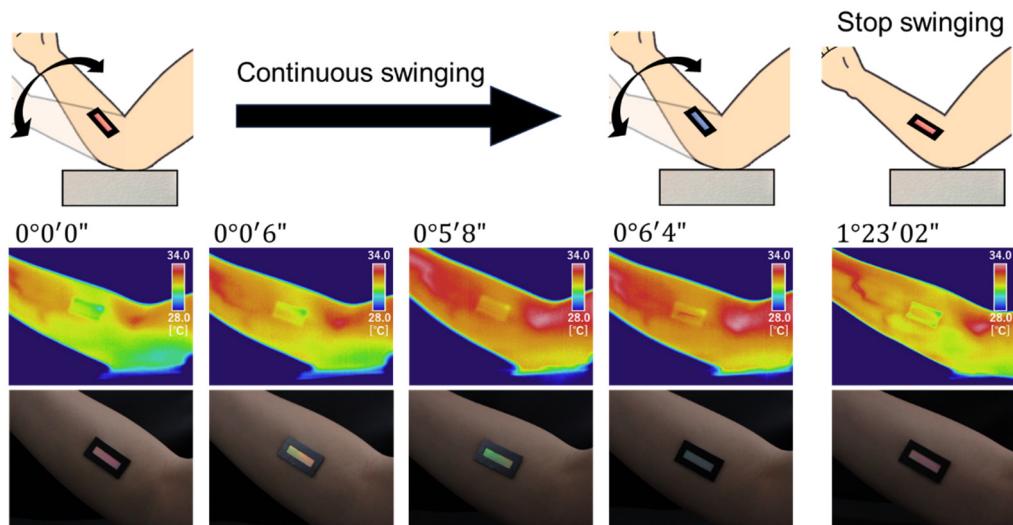
**Figure 6.** Photographs and thermography images of the polyethylene terephthalate-attached poly(*N*-isopropylacrylamide) hydrogel-immobilized colloidal photonic crystal film (prepared with ethylene glycol concentration of 0 wt.%) attached to the human arm when the arm was continuously swung from side to side and then stopped.

4. Conclusions

We demonstrated chameleon-inspired color-changeable films that respond to small changes in the surface temperature of the human body. The films were successfully prepared by immobilization of non-close-packed colloidal photonic crystals in a thermosensitive PNIPAM hydrogel film and simultaneous attachment to a flexible PET sheet through photopolymerization. Attaching the film to the PET sheet ensured high thermosensitivity and film quality; the full color spectrum from red to violet was displayed without any change in the film area and film distortion in a small temperature range of approximately 3 °C, which encompasses the surface temperature of the human body. Furthermore, the temperature range of the full color spectrum was easily tuned by adding a poor solvent such as ethylene glycol to PNIPAM. The color-changeable film supported by the PET sheet was easy to handle and exhibited excellent flexibility. When attached to a human arm, the film exhibited color changes in response to the changes in the body temperature without the application of external heat. Although the PET-attached film is sandwiched between PET sheets, tight sealing is necessary for long-term use to prevent evaporation of the swelling solvent. This study is expected to advance fundamental research and applications of artificial chameleon skins.

Author Contributions: T.K.: conceptualization, data curation, funding acquisition, supervision, writing—original draft, writing—review & editing. M.S.: data curation, investigation, visualization. Y.H.: data curation, investigation, validation, visualization. All authors have read and agreed to the published version of the manuscript.

Data Availability Statement: The data that support the findings of this study are available from the corresponding authors upon reasonable request.

References

1. Ligon, R.A.; McGraw, K.J. Chameleons communicate with complex colour changes during contests: Different body regions convey different information. *Biol. Lett.* **2013**, *9*, 20130892.

2. Teyssier, J.; Saenko, S.V.; van der Marel, D.; Milinkovitch, M.C. Photonic crystals cause active colour change in chameleons. *Nat. Commun.* **2015**, *6*, 7368.

3. Wang, G.; Chen, X.; Liu, S.; Wong, C.; Chu, S. Mechanical chameleon through dynamic real time-plasmonic tuning. *ACS Nano* **2016**, *10*, 1788–1794.

4. Kim, H.; Choi, J.; Kim, K.K.; Won, P.; Hong, S.; Ko, S.H. Biomimetic chameleon soft robot with artificial crypsis and disruptive coloration skin. *Nat. Commun.* **2021**, *12*, 4658.

5. Liu, J.; Zhou, J.; Meng, Y.; Zhu, L.; Xu, J.; Huang, Z.; Wang, S.; Xia, Y. Artificial skin with patterned stripes for color camouflage and thermoregulation. *ACS Appl. Mater. Interfaces* **2023**, *15*, 48601−48612.

6. Rezaei, S.D.; Dong, Z.; Chan, J.Y.E.; Trisno, J.; Ng, R.J.H.; Ruan, Q.; Qiu, C.-W.; Mortensen, N.A.; Yang, J.K.W. Nanophotonic structural colors. *ACS Photonics* **2021**, *8*, 18–33.

7. Xuan, Z.; Li, J.; Liu, Q.; Yi, F.; Wang, S.; Lu, W. Artificial structural colors and applications. *Innovation* **2021**, *2*, 100081.

8. Feng, L.; Wang, F.; Luo, H.; Qiu, B. Review of recent advancements in the biomimicry of structural colors. *Dyes Pigment.* **2023**, *210*, 111019.

9. Wang, H.; Zhang, H.; Chen, Z.; Zhao, Y.; Gu, Z.; Shang, L. Polymer-based responsive structural color materials. *Prog. Mater. Sci.* **2023**, *135*, 101091.

10. Liu, Y.; Luo, W.; Fan, Q.; Ma, H.; Yin, Y.; Long, Y.; Guan, J. Polyphenol-mediated synthesis of superparamagnetic magnetite nanoclusters for highly stable magnetically responsive photonic crystals. *Adv. Funct. Mater.* **2023**, *33*, 2303470.

11. Du, X.; Cui, H.; Xu, T.; Huang, C.; Wang, Y.; Zhao, Q.; Xu, Y.; Wu, X. Reconfiguration, camouflage, and color-shifting for bioinspired adaptive hydrogel-based millirobots. *Adv. Funct. Mater.* **2020**, *30*, 1909202.

12. Huang, C.; Shang, Y.; Hua, J.; Yin, Y.; Du, X. Self-destructive structural color liquids for time–temperature indicating. *ACS Nano* **2023**, *17*, 10269–10279.

13. Lee, G.H.; Choi, T.M.; Kim, B.; Han, S.H.; Lee, J.M.; Kim, S.-H. Chameleon-inspired mechanochromic photonic films composed of non-close-packed colloidal arrays. *ACS Nano* **2017**, *11*, 11350–11357.

14. Wang, Y.; Yu, Y.; Guo, J.; Zhang, Z.; Zhang, X.; Zhao, Y. Bio-Inspired stretchable, adhesive, and conductive structural color film for visually flexible electronics. *Adv. Funct. Mater.* **2020**, *30*, 2000151.

15. Tajima, H.; Amano, A.; Kanai, T. Elastomer-immobilized tunable colloidal photonic crystal films with high optical qualities and high maximum strain. *Mater. Adv.* **2021**, *2*, 3294–3299.

16. Fudouzi, H.; Sawada, T. Photonic rubber sheets with tunable color by elastic deformation. *Langmuir* **2006**, *22*, 1365–1368.

17. Hu, Y.; Wei, B.; Yang, D.; Ma, D.; Huang, S. Chameleon-inspired brilliant and sensitive mechano-chromic photonic skins for self-reporting the strains of earthworms. *ACS Appl. Mater. Interfaces* **2022**, *14*, 11672–11680.

18. Takeoka, Y.; Watanabe, M. Tuning structural color changes of porous thermosensitive gels through quantitative adjustment of the cross-linker in pre-gel solutions. *Langmuir* **2003**, *19*, 9104–9106.

19. Sugiyama, H.; Sawada, T.; Yano, H.; Kanai, T. Linear thermosensitivity of gel-immobilized tunable colloidal photonic crystals. *J. Mater. Chem. C* **2013**, *1*, 6103–6106.

20. Li, X.; Li, X.; Shi, X.; Peng, M.; Lu, X. PNIPAM-based colloidal photonic crystals above phase transition temperature and its application in naked-eye glucose-detection. *Eur. Polym. J.* **2019**, *120*, 109230.

21. Saunders, B.R.; Vincent, B. Microgel particles as model colloids: Theory, properties and applications. *Adv. Colloid Interface Sci.* **1999**, *80*, 1–25.

22. Neves, E.B.; Salamunes, A.C.C.; de Oliveira, R.M.; Stadnik, A.M.W. Effect of body fat and gender on body temperature distribution. *J. Therm. Biol.* **2017**, *70*, 1–8.

23. Kanai, T.; Kobayashi, N.; Tajima, H. Enhanced linear thermosensitivity of gel-immobilized colloidal photonic crystal film bound on glass substrate. *Mater. Adv.* **2021**, *2*, 2600–2603.

24. Sugiyama, K.; Kato, K.; Kido, M.; Shiraishi, K.; Ohga, K.; Okada, K.; Matsuo, O. Grafting of vinyl monomers on the surface of a poly(ethylene terephthalate) film using Ar plasma post polymerization technique to increase biocompatibility. *Macromol. Chem. Phys.* **1998**, *199*, 1201–1208.

25. Sawada, T.; Suzuki, Y.; Toyotama, A.; Iyi, N. Quick fabrication of gigantic single-crystalline colloidal crystals for photonic crystal applications. *Jpn. J. Appl. Phys.* **2001**, *40*, L1226–L1228.

26. Kanai, T.; Sawada, T.; Toyotama, A.; Kitamura, K. Air-pulse-drive fabrication of photonic crystal films of colloids with high spectral quality. *Adv. Funct. Mater.* **2005**, *15*, 25–29.

27. Kanai, T.; Sawada, T.; Kitamura, K. Optical determination of the lattice constants of colloidal crystals without use of the refractive index. *Langmuir* **2003**, *19*, 1984–1986.

28. Hiltner, P.A.; Krieger, I.M. Diffraction of light by ordered suspensions. *J. Phys. Chem.* **1969**, *73*, 2386–2389.

29. Kanai, T.; Yano, H.; Kobayashi, N.; Sawada, T. Enhancement of thermosensitivity of gel-immobilized tunable colloidal photonic crystals with anisotropic contraction. *ACS Macro Lett.* **2017**, *6*, 1196–1200.

Article

Magnetically-Driven Reconfigurable Cilium Array with Tunable Wettability for Dynamic Display and Controllable Microreaction

Zijing Quan [1], Yuhan Zhang [1,*], You Pan [1], Zhongyi Yang [1], You Chen [1], Fawei Rui [1], Letian Li [1], Bo Li [1,2,*], Shichao Niu [1,2,3,*], Zhiwu Han [1,2,3], and Luquan Ren [1,2,3]

[1] Key Laboratory of Bionic Engineering (Ministry of Education), Jilin University, Changchun 130022, China
[2] National Key Laboratory of Automotive Chassis Integration and Bionics, Jilin University, Changchun 130022, China
[3] Institute of Structured and Architected Materials, Liaoning Academy of Materials, Shenyang 110167, China
* Correspondence: yhzhang9922@mails.jlu.edu.cn (Y.Z.); boli@jlu.edu.cn (B.L.); niushichao@jlu.edu.cn (S.N.)

Abstract: Efficient droplet transport plays an important role in many fields such as liquid collection, microfluidic management, and reaction control. However, it remains a key challenge to achieve fast and precise droplet motion control along a predetermined path. Herein, a magnetically driven cilium array (MDCA) was developed by a

simple one-step spraying method. The MDCA exhibits both upright and prostrated states under a programmable magnetic field, achieving in-situ pinning and driving of the droplets, respectively. In particular, the MDCA modified by the silicone oil can not only be used for precise droplet manipulation on the spatio-temporal scale (S-shaped trajectory transport, selective control of target droplets, and velocity control) but also provides a self-enclosed space for droplet fusion for chemical microreactions, allowing fine-tuning of reaction parameters and isolation from external contamination. Based on the theoretical analysis of droplet transport, MDCA can be applied to the development of dynamic digital displays and chemical microreactors and provides inspiration for the development of environmental monitoring, drug delivery, and energy purification.
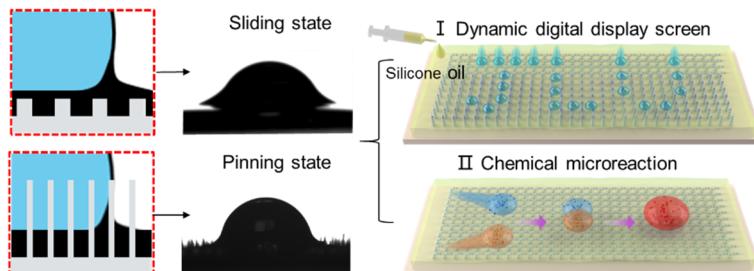
Keywords: magnetically driven; cilium array; tunable wettability; droplet motion control

1. Introduction

Dynamic programmable regulation of droplet motion [1,2] is of great scientific importance and application value in the fields of droplet transport [3], reaction control, environmental monitoring [4], 3D printing [5–8] and biomedicine [9,10]. However, it is difficult for conventional droplet regulation methods to achieve effective switching between in-situ pinning and fast sliding of droplets on a single surface, limiting their application in complex motion path scenarios [11,12]. Therefore, it remains a key challenge to achieve fast and precise motion manipulation of droplets along a programmable path through simplified design.

To improve droplet controllability [13], researchers have attempted to achieve controllable liquid dynamics through the design of material surface energy gradients [14–16] and the construction of hierarchical micro-nanostructures [17,18], aided by external fields such as heat [19], light [20,21], acoustic [22], electric [23,24], and magnetic fields [16,25,26]. In particular, magnetic drive offers unique advantages, including non-contact real-time control, fast response, and no specific environmental requirements. The design principles can be summarised in two different categories: (1) Direct actuation [27] of droplets by adding magnetic particles directly to the droplet [28]; (2) Indirect actuation of droplets by deforming the magnetic particle assemblies wrapped in flexible membranes in response to the magnetic field [29–31]. However, the direct addition of magnetic particles to a droplet limits the types of droplets that can be driven. Meanwhile, the deposition of magnetic particles tends to deteriorate

the driveability. On the contrary, for the typical indirect liquid manipulation method driven by an external magnetic field, the magnetic cilia [32] produce a directional motion [33–35] that enables the control of the liquid's directional rolling. This technique provides controlled directional transport of liquids while also demonstrating adaptability to different droplet actuation and magnetic field conditions, making it a promising solution for microfluidic [30], biomedical engineering, and environmental monitoring applications. However, conventional magnetically controlled cilia exhibit limitation: The inertial rolling of droplets on cilia makes tuning of the adhesion properties [36,37] difficult, affecting the precision of programmable pathway transport of droplets.

In this work, a magnetically driven cilium array (MDCA) was developed by a simple one-step spraying method. The MDCA achieves fast switching between two states (upright and prostrated) driven by a magnetic field, leading to pinning and sliding behaviours of droplets, respectively. This design not only simplifies the preparation process but also significantly improves the flexibility of droplet manipulation. To further optimise the droplet motion performance, silicone oil [38,39] was used for surface modification of MDCA. The silicone oil formed spontaneously a closed environment at the periphery of the droplet, which created a smooth start-up of MDCA when it switched from the upright state to the prostrated state, thus overcoming the detrimental effect of inertia on the accuracy of droplet manipulation. The SOMDCA reduces the impact of natural cilia defects on droplet driving. Specifically, silicone oil-modified MDCA (SOMDCA) was capable of driving droplets in programmable pathways (inversed S-shape motion, in-situ selective drive of the target droplet, and velocity control) based on droplet static thermodynamic mechanism and dynamic slippage principle. In addition, the proposed optimal SOMDCA is critical for the design of digital display screens and chemical microreactors that isolate the outside environment. This superwettable surface provides new research ideas and technical guidance for the development of magnetic fluid manipulation technology, environmental monitoring, microfluidic chips and biomedicine.

2. Methodology

2.1. Fabrication of the MDCA

To fabricate the MDCA, a 4 cm × 4 cm neodymium magnet (~0.5 T), an airbrush, and polyethylene terephthalate (PET) substrates were prepared. The PET substrate was fixed at a 6 mm precise distance above the magnet to ensure the vertical alignment of the magnetic particles encased in liquid during the spraying process. The detailed fabrication procedure is described as follows: The precursor solution was prepared by adding 2.4 g polydimethylsiloxane (PDMS), 0.17 g curing agent and 2.4 g carbonyl iron powder (CIP, 5 μm in diameter) to 5 g ethyl acetate (EA). The solution was thoroughly stirred with a glass rod for 30 min to ensure uniform dispersion of CIPs within the PDMS and EA matrix. The prepared solution was then transferred into an airbrush, maintaining PDMS in a 30 cm distance between the airbrush nozzle and the PET substrate (Figure 1a), which is to ensure that the magnetic particles encased in liquid were evenly deposited parallel to the substrate surface. The spraying process was conducted for 50 s, after which the magnet and coated PET substrate were immediately placed in an oven and dried at 60 °C for 5 h. This process resulted in the successful fabrication of the MDCA surface.
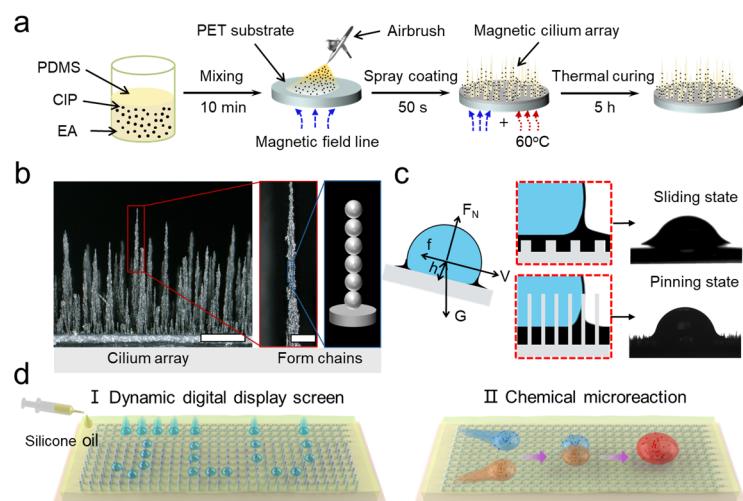
Figure 1. Dynamically reconfigurable SOMDCA design and working Principle. (**a**) Preparation diagram of MDCA. (**b**) Optical UDFM images of MDCA. The interpolated scales are 500 μm and 100 μm respectively. (**c**) Mechanical force analysis of droplets and schematic diagrams illustrating the mechanisms of the sliding and pinning states. (**d**) Applications of SOMDCA surface (**I**: Dynamic digital display screen; **II**: Chemical microreaction).

2.2. Droplet Adhesion Property on SOMDCA

The centrifugation was utilized to measure the maximum adhesion strength of a 10 μL droplet on the MDCA surface which was modified with silicone oils of varying viscosities, in an upright state. The experimental procedure was as follows: the SOMDCA was placed directly above the magnet to maintain the cilia in an upright orientation. This combination was placed at a radial distance of R from the rotation center. By systematically varying the rotational velocity and employing an external camera to capture the instant of droplet detachment, the adhesion strength of the droplet under the influence of silicone oils with different viscosities was evaluated. The adhesive force of the droplet on the SOMDCA was calculated using the equations $\omega = 2\pi n/60$ and $F = m\omega^2 R$, where ω represents the angular velocity, n is the rotational velocity, m is the mass of the droplet, and R is the radial distance from the rotation center.

2.3. Chemical Microreaction

The droplets of $FeCl_3 \cdot 6H_2O$ and KSCN were prepared at a concentration of 1 M and 3 M each. The chemical equation is as follows: $Fe^{3+} + 3SCN^- = Fe(SCN)_3$. The temperature of the chemical reaction was measured using a thermal imager (Hti HT-18, made in Zhejiang, China). Gaussian 16 is used to measure molecular energy values before and after chemical reactions. The red droplets (10 μL) are consist of a mixture of carminic acid and water at a weight ratio of 1:50.

2.4. Characterization

The morphological characteristics of the MDCA were characterized using the Ultra-deep Field Microscope (UDFM, Keyence VHX-6000, made in Osaka, Japan) and Laser Scanning Confocal Microscope (LSCM, Zeiss LSM 980, made in Oberkochen, Germany). The water contact angle and sliding angle were obtained by a contact angle measurement system (Sindin SDC-100, made in Shenzhen, China). Magnetic force simulation tests of magnets were conducted by Comsol 6.0.

3. Results and Discussion

3.1. Design and Working Principle of Dynamically Reconfigurable SOMDCA

To achieve stable droplet pinning and sliding behaviors, a surface capable of rapid switching between two states (upright and prostrated state) under magnetic actuation has been developed. In this work, a simple spray-coating method was employed, leveraging the unique magnetic responsiveness of magnetic particles. By systematically adjusting the ratios of PDMS, CIP, and EA, the formulation with high spray-coating uniformity was optimized. The detailed preparation method has been comprehensively described in the experimental section, as illustrated in Figure 1a. Specifically, the magnetic particles produce a magnetic force in the presence of a magnetic field. As the system tends to reach its minimum energy state, the magnetic dipole interactions between the particles cause them to align into chain-like structures within the magnetic field. This ordered arrangement of particles in the magnetic field reduces the system's magnetic energy, thereby promoting CIPs upward growth. The magnetic moment of CIPs can be described by the following formula: $M = \chi H$. M is the magnetization (A/m), χ is the magnetic susceptibility of the CIPs, and H is the applied magnetic field strength (A/m). The growth direction is determined by the magnetic field gradient and the magnetic moment of the particles. After the PDMS encapsulating the magnetic particles has been cured, the magnetic particles maintain an upright configuration even in the absence of an applied magnetic field. Figure 1b presents the topographic characteristic of the MDCA under UDFM, revealing that the magnified single magnetic cilium exhibits a stacked growth pattern of magnetic particles to minimize energy.

After the surface modification of the MDCA with silicone oil, the force analysis of droplets, as well as the mechanisms underlying the pinned and sliding states, along with their contact angles respectively, were further investigated (Figure 1c). Due to the low surface energy (21.2 mN/m, 1000 cP) of silicone oil, when the droplet was deposited on the superwetting surface of the prostrated cilium array, the silicone oil may spread and "mask" the droplet. As the silicone oil infiltrates and submerges the microstructure surface, the SOMDCA exhibits an extremely low roll-off angle, with negligible contact line pinning. In this case, the total interfacial energy per unit area: $E = \gamma_{ow} + r\gamma_{os}$. Where γ is the interfacial tension between the two phases designated by subscripts water (w), oil (o), and air (a). And r is the ratio of the total surface area to the projected area of the solid. Different from the prostrated state, when a droplet resides on a superwetting surface with upright cilia, despite the droplet's tendency to slide forward due to gravitational force, the array of upright cilia with a high aspect ratio obstructs the

droplet's sliding progression, macroscopically manifesting as a pinned state. On this basis, dynamically reconfigurable MDCA can achieve the switching between the pinning and sliding states of droplets under the actuation of a magnetic field thereby enhancing the programmed design and precise control of droplets. Specifically, by utilizing the surfaces with super wettability, a new generation of digital dynamic display screens and chemical microreactors (Figure 1d) was designed. These innovations hold promising prospects for various fields, including magnetic fluid manipulation technology, environmental monitoring, drug delivery, and energy purification.

3.2. Characterization and Optimization of MDCA

To further optimize the driving performance, the MDCAs and the magnetically controlled properties were characterized and refined. Six kinds of MDCAs were prepared based on varying contents of PDMS and CIP. Specifically, three grades (high (H), middle (M), and low (L)) were set for both PDMS and CIP content. The first letter of the abbreviation is PDMS content and the last letter is CIP content. Detailed content information is provided in Table S1. Utilizing UDFM, an investigation was conducted into the height, magnetic compliance, and uniformity of MDCA distribution fabricated using various contents (Figure 1b). As illustrated in Figure 2a, the cilia comply with the magnetic field direction, regardless of whether the magnetic field is designed to be orientated perpendicular or parallel to the substrate. The magnetic cilia compliance to the magnetic field is shown in Figure S1. The growth and alignment of MDCA are significantly influenced by the PDMS and CIP concentrations in the solution, as well as the strength of the external magnetic field. Based on the experimental results and relevant theories, the following analysis is conducted. The viscosity η of the PDMS solution can be described by the equation: $\eta = \tau/\gamma$. Where η is solution viscosity (Pa·s), τ is the shear stress (Pa), γ is the shear rate (1/s). Specifically, PDMS serves as the structural matrix of the cilium array, providing flexibility and strength. The PDMS concentration has a substantial impact on the solution viscosity, which in turn affects the spraying process and the subsequent cilia morphology. For sample LM with lower PDMS concentrations, the solution exhibits reduced viscosity, leading to a more uniform spray pattern and the formation of taller cilia. However, this lower viscosity also results in weaker adhesion between the cilia and substrate, causing an increased propensity for cilia detachment (Figure S2b). As the concentration of PDMS increases in sample HH, the solution becomes more viscous, which can hinder the uniform distribution of particles during the spraying process leading to a decrease in cilia height (Figure S2c). Higher viscosity results in poorer particle dispersion, as predicted by the particle deposition model. Thus, an excessive PDMS concentration leads to a reduction in cilia height due to non-uniform particle distribution during the spraying process.

The magnetic responsiveness of cilia is attributed to CIPs. The concentration of CIPs directly influences the magnetic alignment of cilia in an external magnetic field. At lower CIP concentrations, the limited number of magnetic particles tends to adhere more closely to the substrate, resulting in shorter cilia growth heights. At higher CIP concentrations of the sample MH, the enhanced magnetic responsiveness leads to increased interparticle interactions, potentially causing agglomeration and uneven particle distribution. This effect, commonly referred to as magnetic agglomeration, results in higher average cilium heights but reduced uniformity. At moderate CIP concentrations of sample MM, the cilia effectively align under the magnetic field, leading to uniform growth and optimal height. The magnetic field facilitates the directional alignment of CIPs, promoting uniform self-assembly of cilia. The sample MM exhibits the most uniform cilium distribution and optimal magnetic compliance.

Subsequently, LSCM was employed to conduct an in-depth investigation into the morphological characteristics and distribution patterns of cilia (Figure 2b). This process successfully obtained height simulation distribution maps of magnetic cilium arrays in both upright and prostrated states, agreeing with the results obtained by UDFM. A detailed quantitative analysis using Abbott curve simulations was further conducted on the cross-sectional area fractions of the MDCA (Figure 2c–e). Figure 2c illustrates the trend of cross-sectional area fraction varying with height in the upright state. Specifically, the highest cross-sectional occupancy is gradually increasing, possibly due to the increasing diameter and height of the cilia with increasing CIP concentration, which is consistent with the results of previous analyses. Notably, PDMS and CIP at middle concentrations exhibit dual peak cross-sectional areas, suggesting probably the presence of two types of cilia: tall cilia and short cilia. This situation not only increases the retention capacity of silicone oil on the surface of the cilia but also reduces the height of the cilia in the prostrated state and decreases the surface roughness. In contrast, the simulation results for the samples LL and MM do not reflect the presence of these two types of cilia. Similarly, Figure 2d demonstrates the variation of cross-sectional area fraction changing with height in the prostrated state. With the increase in CIP concentration, the prostrated cilia height also increases. Notably, the sample MM exhibits a more marked prostrated effect, which may be attributed to the dual height peaks of cilia in Figure 2c. Ultimately, based on the

analysis in Figure 2e, the samples MM in the prostrated state have the highest percentage of cross-sectional integration, which suggests a certain degree of homogeneity of the cilia, a property that positively affects droplet sliding.
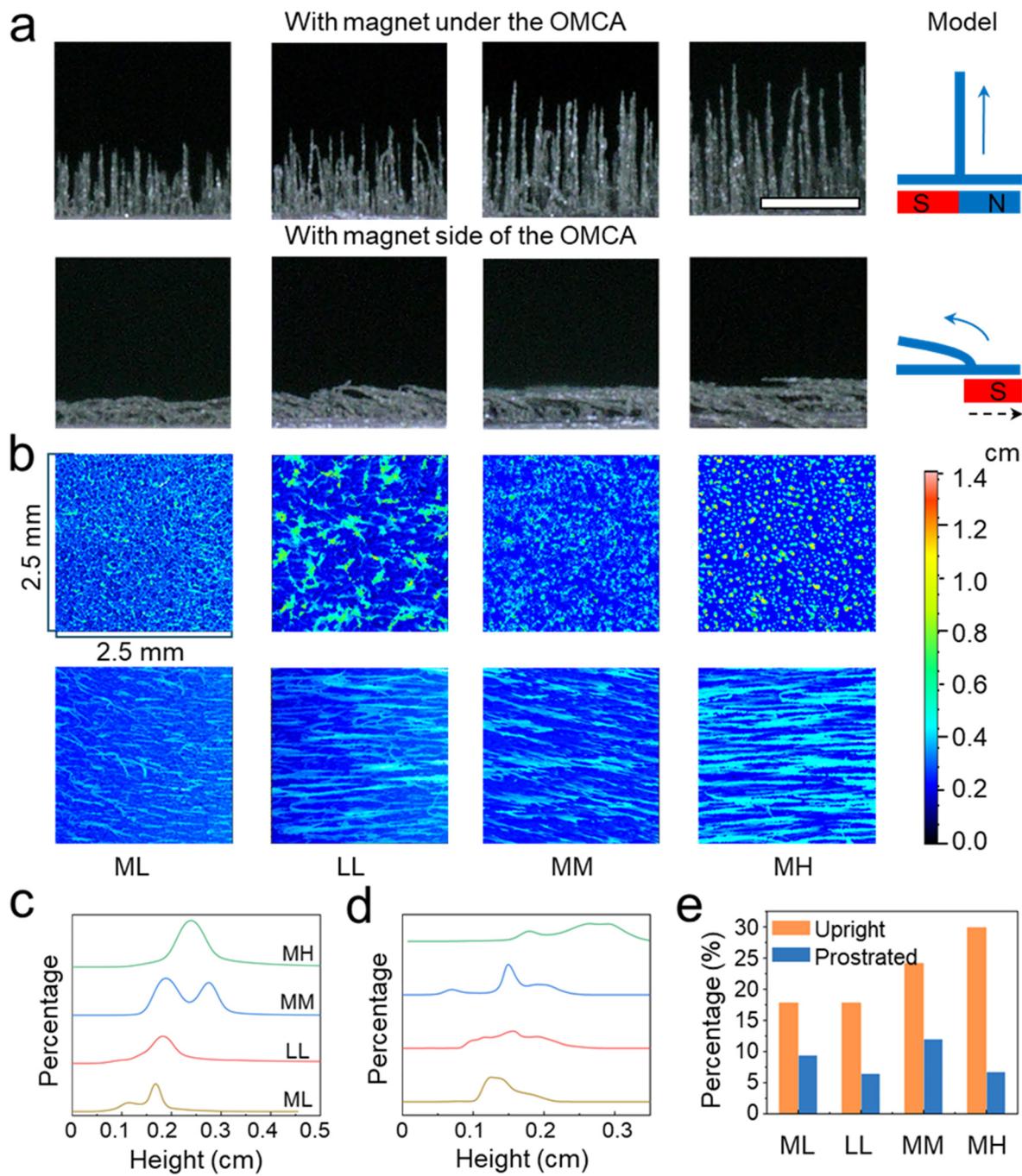
Figure 2. Characterization and optimization of MDCA. (**a**) UDFM images of the upright and prostrated MDCA. The interpolated scale is 1 cm. (**b**) LSCM images of the upright and prostrated MDCA. Cross-section proportion of (**c**) upright and (**d**) prostrated. (**e**) Cross-section proportion diagram of four kinds of MDCAs.

3.3. Magnetically Driven Droplet Transport Performance and Optimization

To demonstrate that the prepared SOMDCA surface possesses tunable droplet adhesion, a centrifuge was utilized to characterize the adhesion force of droplets on the SOMDCA surface with varying viscosities, based on the action of centrifugal force, as shown in Figure 3a.
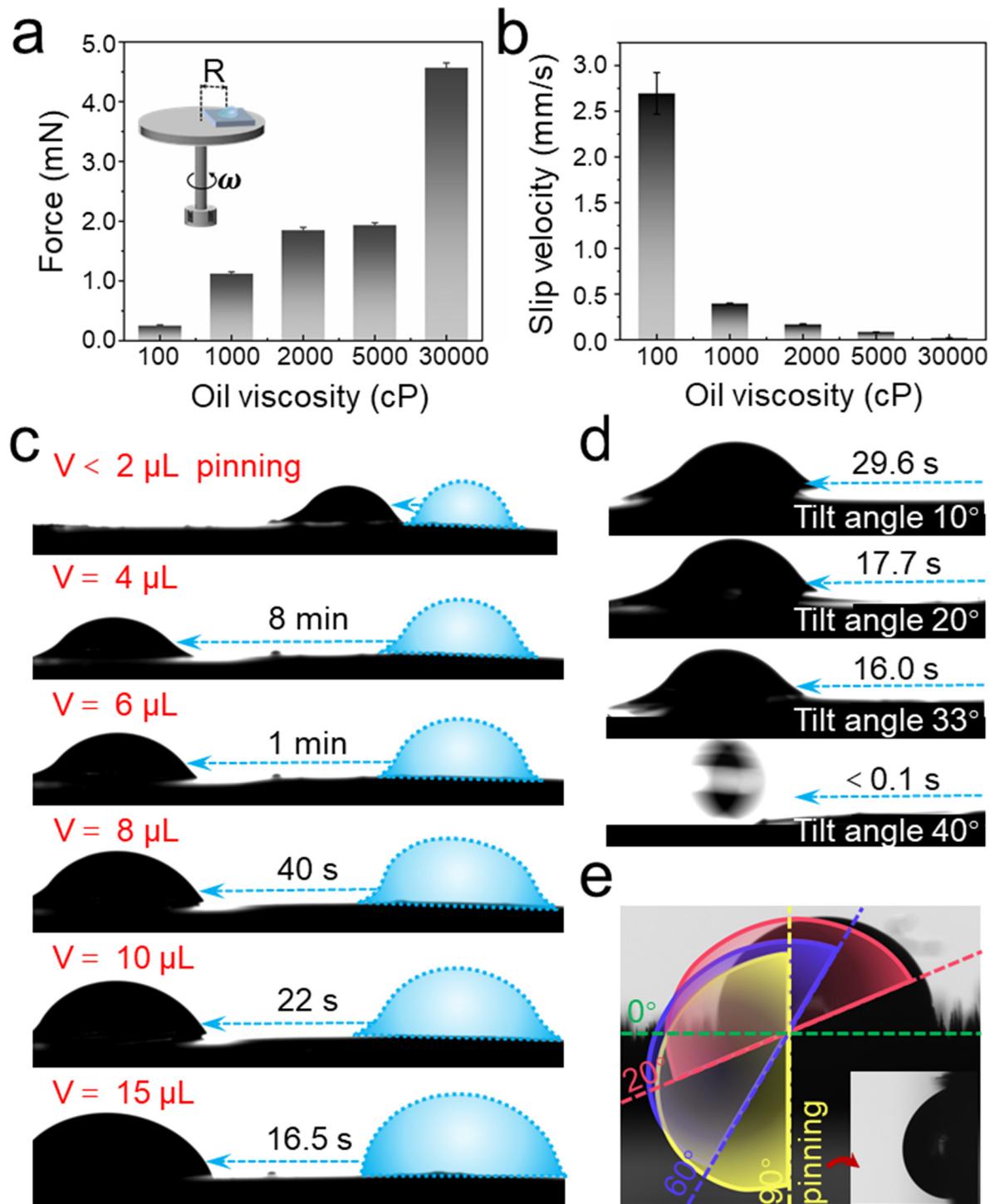
Figure 3. Optimization of magnetically driven droplet transport performance. (**a**) The critical adhesion of droplet adhesion on SOMDCA surface under different viscosity of silicone oils. (**b**) The sliding velocity of 10 μm droplet under different viscosity of silicone oils. (**c**) Effect of volume on droplet sliding ability. (**d**) The sliding ability of droplets at different obliquity angles of SOMDCA surface. (**e**) The droplet pinning state diagram of at different angles of SOMDCA surface.

The experimental results indicate that after placing a cylindrical permanent magnet beneath the SOMDCA surface, the pinning force of droplets on the SOMDCA surface increased with the viscosity of the silicone oil. The adhesion force of the silicone oil with a viscosity of 1000 cP on the SOMDCA surface reached 1.2 mN, which is 12 times the mass of the droplet itself. Subsequently, MDCA surfaces were modified with silicone oils of different viscosities, which significantly influenced the sliding velocity of the droplets (Figure 3b). As the viscosity of the silicone oil increased, the droplet sliding velocity changed from 0.019 mm/s to 2.7 mm/s, which illustrates the high viscosity of silicone oil significantly reducing droplet mobility. At a 30,000 cP viscosity, droplet movement on the SOMDCA surface was negligible. An appropriate droplet viscosity should enable control over droplet pinning and

precise manipulation of droplet movement under fast sliding conditions. The SOMDCA with a viscosity of 100 cP exhibited excessively fast sliding velocities, making it difficult to precisely control the motion trajectory of the droplets, while those with viscosities above 2000 cP resulted in excessively slow droplet sliding, neither of which were considered to possess excellent precision control over droplet movement. Therefore, silicone oil with a viscosity of 1000 cP was selected for subsequent droplet manipulation experiments. Although droplets can also be driven at 0°, the velocity is too slow (Figure S7). To demonstrate the superior droplet control performance of the prepared SOMDCA surface, the sliding capability of droplets with varying volumes was explored on the SOMDCA in a prostrated state at a 10° tilt angle. The driving magnets effect model for droplets on SOMDCA is shown in Figure S3. As shown in Figure 3c, a 2 μL droplet, even on the prostrated SOMDCA surface, only slid a short distance before pinning to the surface. This is because when the droplet falls onto the surface, its gravitational potential energy is partially converted into kinetic energy, causing a brief sliding phenomenon. After this energy is expended, the droplet, with insufficient gravitational force, cannot overcome the resistance of the higher parts of the prostrated cilia, resulting in complete pinning on the surface. Secondly, when the droplet volume reached 4 μL, the droplet exhibited sliding capability on the surface, but the sliding velocity was relatively slow, taking approximately 8 min to cover a distance of 10 mm. When the droplet volume reached 15 μL, the sliding velocity (0.61 mm/s) significantly increased, being 29 times that of the 4 μL droplet. Additionally, the sliding capability of the droplets varied at different tilt angles, as shown in Figure 3d. The greater the tilt angle, the faster the sliding velocity of the droplets. At a 40° tilt angle, the droplets could roll rapidly off the surface, instead of being pinned or sliding on the SOMDCA surface for silicone oil struggling to capture droplets with an excessively large gravitational potential energy component. In contrast, when the magnetic field causes the cilia to stand upright, a 10 μL droplet remains firmly fixed on the surface even as the SOMDCA is tilted from 0° to 90° (Figure 3e), which is different from sample LL for droplet sliding off the upright SOMDCA surface with a 10° tilt angle (Figure S4 and Video S1). This observation underscores the robust adhesion and stability of the SOMDCA over the droplet under the influence of the magnetic field, highlighting the effective control over droplet immobilization achieved through the upright cilia configuration. To ensure controlled droplet movement, a 10° inclination was selected for subsequent experiments.

3.4. Droplet Programmed Manipulation

Utilizing the gravitational force of droplets to facilitate their sliding or pinning on inclined surfaces represents a traditional methodology. Nonetheless, the challenge of achieving controllable regulation of droplet pinning and sliding in situ is not easily surmounted through mere material and structural design. Intriguingly, magnetically actuated droplet sliding emerges as a microfluidic technology underpinned by magnetic field modulation, which enables rapidly dynamic regulation with minimal energy expenditure. By judiciously designing the magnetic field distribution and changing surface characteristics, it is feasible to effectuate in situ toggling between sliding and pinning of droplets on inclined surfaces. However, this technique typically confines droplet propulsion to the direction dictated by gravity, thereby presenting challenges for precise manipulation and the customization of droplet trajectories. This research employs magnets to customize droplet sliding paths by modulating droplet slippage and pinning, demonstrating significant advantages in the field of micro-droplet manipulation.

During the experiment, the SOMDCA surface was tilted at 10°, and the droplet moved along a predetermined inverted S-shaped trajectory under the influence of a magnetic field. The superwetting surface properties changed with the magnetic field gradient, enabling the droplet to overcome the effects of gravity and slide precisely along the inverted S-shaped path. This method not only exceeds the limitations of traditional droplet sliding, which relies solely on gravity for directional movement, but also the ability of SOMDCA to switch between in-situ anchoring and sliding provides new possibilities for precise droplet control on complex paths. As shown in Figure 4a and Video S2, the droplet exhibited an inverted S-shaped curved slide under the driving action of two small magnets. To detail the driving method and principle of this path, a simulation of two small magnets (N35) was conducted using Comsol. Combining finite element analysis, the spatial distribution of the magnetic field, as well as the direction and intensity of their magnetization vectors, were obtained by solving Maxwell's equations (Figure 4e). During the preparation of MDCA, the magnetic particles were influenced by the magnetic field, causing the magnetic poles to align directionally. This alignment allows the cilia to bend towards the direction of the magnetic field lines under the influence of an external magnetic field, overcoming their inherent elastic force. According to the distribution characteristics of the magnetic field, the magnetic cilia above the two magnets stand upright, while those between the two magnets collapse. Therefore, by continuously adjusting the position of the magnets, the droplet is positioned between 1.5 mm magnets, allowing the droplet's sliding path to be altered, thus enabling the droplet to slide along the predetermined inverted S-shaped path. Similarly, using the magnet shown in Figure 4b,e2 and Video S3 demonstrate

the droplet's ability to slide along a programmed path at an inclination of 30°, and Figure 4c and Video S4 show the ability to switch between selective in-situ pinning and droplet sliding for two droplets. Additionally, the sliding velocity of the droplet can be controlled based on the distance between the magnet and the droplet (Figure 4d,f and Video S5). This phenomenon arises because the closer the droplet is to the magnet, the greater the compliance of the cilia, resulting in reduced surface roughness and consequently lower resistance to droplet sliding. Conversely, when the magnet is farther from the droplet, the magnetic force struggles to overcome the inherent elastic force of PDMS, resulting in greater surface roughness, which limits the droplet's sliding velocity. In comparison, silicone oil with a viscosity of 100 cP cannot achieve precise droplet control solely through gravitational force. However, with an appropriate 3D printing platform (Figure S5), it is possible to facilitate the C-shaped and S-shaped motions (Figure S6) sliding of droplets by adjusting platform tilt angle.
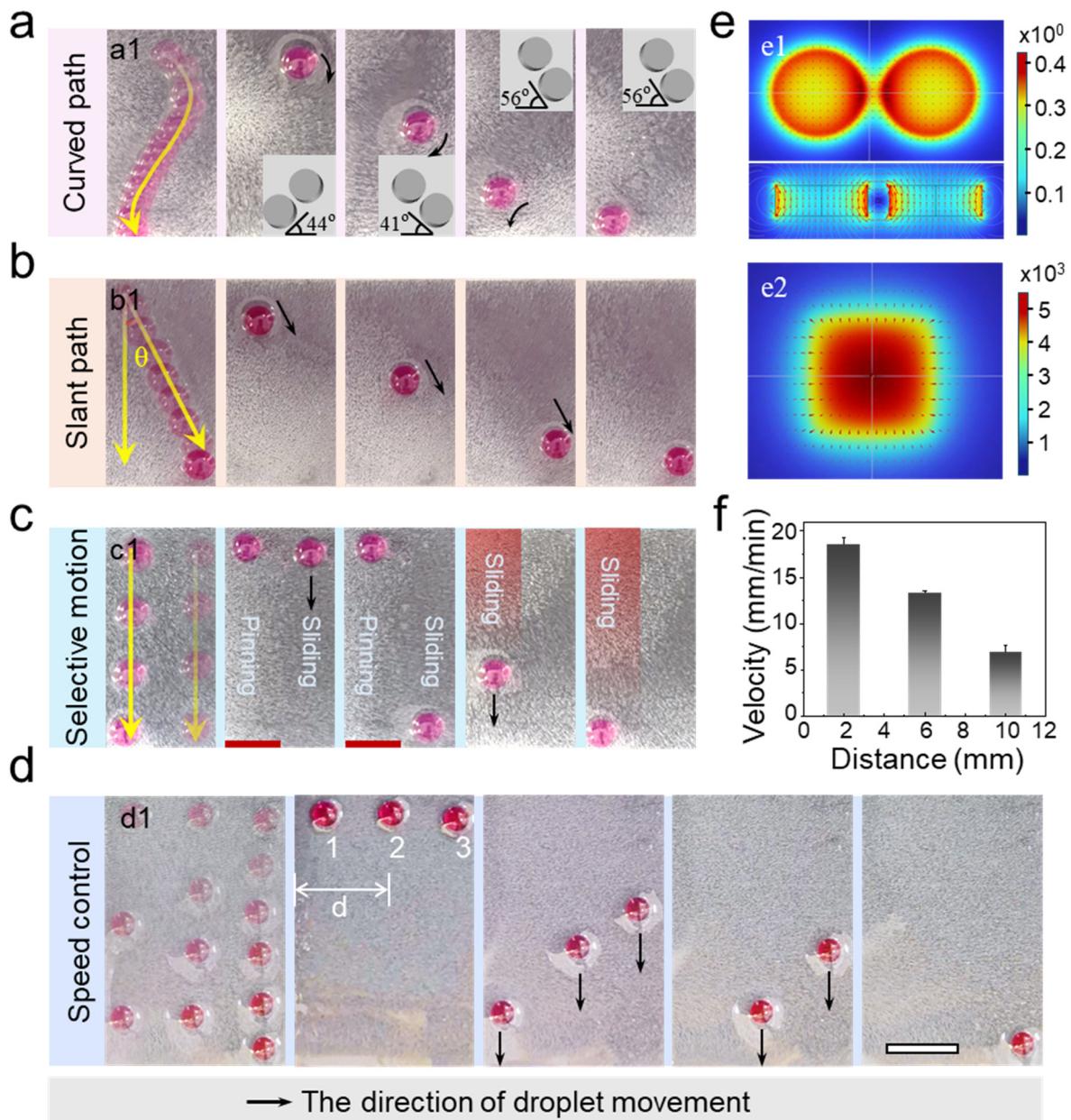
Figure 4. The precise control and path programmability by SOMDCA over droplets. (**a**) The magnet guides the droplet through the inverted S shape. (**b**) The magnet guides the droplet through the 30° inclination. (**c**) Selective pinning and sliding of droplets. (**d**) Effect picture of distance between magnet and droplet on droplet sliding velocity. (**e**) Magnetic line distribution of double round magnet and square magnet. The unit is Gs. (**f**) Effect of distance between magnet and droplet on droplet sliding velocity. The interpolated scale bars of all pictures are 2 cm.

3.5. Application Demonstration of the SOMDCA

Based on the aforementioned principles and phenomena of droplet programmed manipulation, the magnetic field-regulated microfluidic control technology demonstrates broad application prospects in multiple fields due to its non-contact nature, high precision, and programmable characteristics.

In this work, by controlling the pinning and sliding of droplets on the SOMDCA surface, dynamic digital display functionality and the driving of droplet coalescence for chemical microreactions can be achieved. Specifically, the number and position of droplets along the x-axis are pre-designed and allocated to the upright cilia at the top of the sample. Subsequently, the droplets are allowed to slide under the influence of gravity from the prostrated SOMDCA surface to the pre-designed positions, where they are anchored by the upright SOMDCA surface. This process is then repeated multiple times to stack the droplets layer by layer along the y-axis, akin to building blocks, until the formation of the letters "JLU" is achieved (Figure 5a and Video S6). Based on the standard deviation of the path, the deviations of the x-axis and y-axis are $\sigma_x = 1.2\%$ mm^2 and $\sigma_y = 2.3\%$ mm^2 respectively (Table S2). The specific locations of the letters "JLU" are illustrated in Figure 5b. Notably, based on the influence of SOMDCA on the sliding velocity of droplets with varying sizes and distances, more sophisticated dynamic patterns could be engineered in future designs to address more stringent requirements. This capability of dynamic droplets to perform digital stacking, with each droplet acting as a new unit sliding along a pre-designed path, provides novel insights for the design of next-generation dynamic digital displays.

Precision manipulation of droplets exhibits significant applications not only in dynamic digital displays but also in various areas such as droplet fusion, chemical microreactions in a self-enclosed environment, and reducing energy loss rate (Figure 5c and Video S7). Typically, in a silicone oil-enclosed environment, the fusion process of two droplets involves overcoming their surface tension and regulating interfacial dynamics. When magnetically driven to gradually approach each other, a sudden rapid movement towards each other occurs between the droplets, which is attributed to the attractive force between molecules, prompting the two droplets coated with oil to approach each other. Subsequently, as the droplets approach, the silicone oil film between them gradually thins. When the film thickness reaches a critical value (typically at the nanoscale), the film becomes unstable and ruptures. Mechanisms leading to film rupture encompass van der Waals forces, thermal fluctuations, or external perturbations. Upon film rupture, direct contact between the droplets results in a reduction in interfacial energy, thereby driving the fusion process. A chemical reaction occurs between 1 M Fe^{3+} and 3 M SCN^-, resulting in the transformation of the droplets from pale yellow and colorless to a blood-red color, accompanied by the generation of energy. Furthermore, Figure 5d demonstrates energy generation by employing the density functional theory method within the Gaussian 16 to conduct energy simulations before and after the reaction, as well as experiments on heat loss rates in a self-contained environment in Figure 5e. Theoretical calculations indicate that the sum of the energies of 1 M Fe^{3+} and 3 M SCN^- is higher than the energy of $Fe(SCN)_3$ (Figure 5d), with an energy difference of -2.165 Hartree. Typically, the reaction primarily releases energy in the form of thermal energy. Based on this, an infrared thermography camera was utilized to record the changes in thermal energy on microdroplet chemical reactors of oil-free MDCA surfaces and microdroplet chemical reactors of oil-loaded MDCA surfaces (Figure 5e). On the MDCA surface, the temperature at the center of the droplet was the lowest, with the ambient temperature surrounding the droplet being higher. As the chemical reaction progressed, the temperature at the droplet's center increased by 2.6 °C over 5 s and returned to normal after 10 s. In contrast, due to the encapsulation by the silicone oil layer, the baseline temperature of the droplet was approximately 6°C higher than that of the unencapsulated droplets, and the infrared thermography camera had a lower sensitivity to temperature changes the droplets on the SOMDCA surface compared to the droplets on the MDCA. The exothermic duration of the reaction lasted for 9 s, with an energy retention capacity approximately 1.8 times higher than that of the droplets without silicone oil encapsulation. In conclusion, the performance of SOMDCA in droplet fusion and reduction of energy loss within a confined environment holds significant potential across various fields. In chemical reaction engineering, it can optimize reaction conditions, minimize the occurrence of side reactions, and enhance product purity as well as experimental reproducibility. In the energy sector, it contributes to improving energy storage density and conversion efficiency. Within the realm of 3D printing and material synthesis, it ensures the uniformity and stability of materials post-fusion, thereby enhancing printing precision and material performance. In the food and cosmetics industry, droplet fusion and emulsification help maintain product stability and the efficacy of active ingredients. Furthermore, in the fields of dynamic displays and smart materials, it improves display quality and the responsiveness of materials. Finally, Table S2 shows the superiority of SOMDCA compared to other articles.
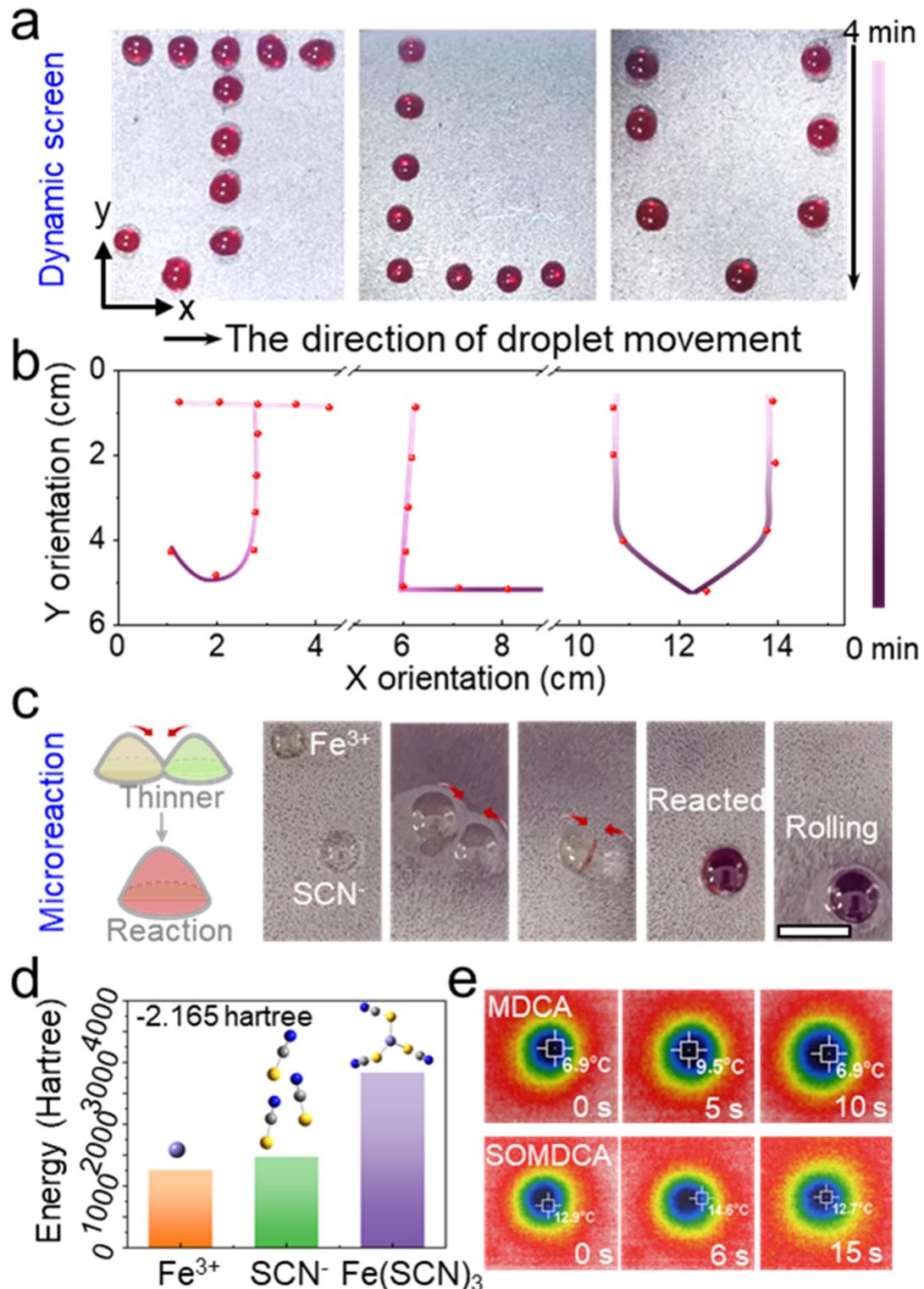
Figure 5. Dynamic screen and microreaction application of the SOMDCA. (**a**) SOMDCA manipulates the droplet for display instances. (**b**) SOMDCA manipulates the time profile of the droplets. (**c**) SOMDCA controls the droplet for microfluidic reactions. The interpolated scale bar is 1 cm. (**d**) Gauss 16 software simulates molecular energy maps. (**e**) Heat distribution diagram of chemical reaction with or without silicone oil coating.

3.6. Mechanism Analysis of Droplet Driven

The stable configuration of droplets on the surface of SOMDCA can be predicted through a thermodynamic framework: for the external interface (in an air environment), the oil spreads across the entire droplet as a thin covering layer, forming an oil-water interface, where $E_{oa} < E_{wa}$. For the internal interface (the droplet-substrate contact layer), a "wetting ridge" exists at the bottom of the droplet, where $E_{os} < E_{ws}$. The subscripts denote oil, air, water and substrate. The influence of structure on sliding behavior can be modelled by balancing gravitational

force and pinning force. When a droplet undergoes motion, its behavior can be characterized by the roll-off angle model. On a lubricant-infused surface, the roll-off angle is governed by the pinning force along the contact line, particularly influenced by contact angle hysteresis. The movement and rolling angle of the droplet are affected by the surface microstructure and the viscosity of the liquid. The equilibrium of forces at the point of tangency on the surface, which corresponds to the stable configuration of droplets on a surface wetted by a lubricant, is formulated based on the force balance principle: $\rho_w V g \sin\alpha = R_b \Phi^{1/2}[\gamma_{ow}(\cos\theta_{rec,os(w)} - \cos\theta_{adv,os(w)}) + \gamma_{oa}(\cos\theta_{rec,os(a)} - \cos\theta_{adv,os(a)})]$, Where ρ_w is the liquid density, g is the gravitational acceleration, V is the droplet volume, R_b is the droplet base radius, $\Phi^{1/2}$ is the fraction of R_b, $\theta_{adv,ws(a)}$ and $\theta_{rec,ws(a)}$ are the advancing and receding contact angles of the droplet in air on the smooth solid surface, $\gamma_{oil-water}, \gamma_{oil-air}$ denote the oil-water and oil-air interfacial tensions, α represents the inclination angle of the substrate. In the presence of silicone oil, the triple contact line or the quadruple contact line does not exist, which is the reason why droplets can slide down with a low rolling angle even on MDCA surfaces with certain structures.

Furthermore, once the gravity of the droplet overcomes the pinning force, the droplet acquires a certain velocity to slide or roll off. For a droplet of volume it is anticipated that this velocity will depend on the contact line pinning and the viscosity of the lubricant. According to the research by J. David Smith et al. [40], $V^{2/3}\rho_w g/\gamma_{wa}(\sin\alpha - \sin\alpha^*) V^{1/3}/R_b = \mu_w v/\gamma_{wa}$, where μ_w is water dynamic viscosity, v is the steady-state shedding velocity, and R_b is the droplet base radius. This model suggests that the gravitational potential energy of the rolling droplet is primarily consumed in the viscous dissipation around the wetting ridge at the base of the droplet's slide. The thin layer covering the droplet has negligible inertial and gravitational forces. Therefore, the velocity is uniform along the streamline, and viscous dissipation can be ignored.

4. Conclusions

In summary, based on the principle that CIPs are magnetized and arranged in an orderly manner under the influence of a magnetic field, MDCA with strong subcompliance was developed in this paper. The Abbott curve simulation results of MDCA showed that the optimized MDCA had two types of heights of cilium array as well as excellent spatial distributability, which reduces the roughness of the cilia in a prostrated state and enhances the droplet slipperiness. Particularly, the presence of the micro-cilia increases the retention time of the silicone oil to a certain extent. In addition, under the drive of the programmable magnetic field, the droplets showed two states, upright and prostrated, which realized in situ fixation and actuation of the droplets, respectively. In order to further optimize the slippage performance of the droplets, the MDCA was surface modified with silicone oil. The SOMDCA can be not only used for precise manipulation of droplets on both spatial and temporal scales (S-trajectory transport, selective control, and velocity control of target droplets), but also provide a self-enclosed space for droplet fusion in chemical microreactions, thus enabling fine-tuning of reaction parameters and isolation from external contamination.

References

1. Zhou, M.; Wu, Z.; Zhao, Y.; Yang, Q.; Huang, X. Droplets as Carriers for Flexible Electronic Devices. *Adv. Sci.* **2019**, *6*, 1901862. https://doi.org/10.1002/advs.201901862.

2. Li, J.; Han, X.; Li, W.; Yang, L.; Li, X.; Wang, L. Nature-Inspired Reentrant Surfaces. *Prog. Mater. Sci.* **2023**, *133*, 101064. https://doi.org/10.1016/j.pmatsci.2022.101064.

3. Sun, Q.; Wang, D.; Li, Y.; Zhang, J.; Ye, S.; Cui, J.; Chen, L.; Wang, Z.; Bütt, H.; Vollmer, D. Surface Charge Printing for Programmed Droplet Transport. *Nat. Mater.* **2019**, *18*, 936–941. https://doi.org/10.1038/s41563-019-0440-2.

4. Peng, W.; Lin, S.; Guan, D.; Chen, Y.; Wu, H.; Cao, L.; Huang, Y.; Li, F. Cactus-Inspired Photonic Crystal Chip for Attomolar Fluorescence Multi-analysis. *Anal. Chem.* **2023**, *95*, 2047–2053. https://doi.org/10.1021/acs.analchem.2c04729.

5. Hwang, Y.H.; Um, T.; Hong, J.; Ahn, G.N.; Qiao, J.; Kang, I.; Qi, L.; Lee, H.; Kim, D.P. Robust Production of Well-Controlled Microdroplets in a 3D-Printed Chimney-Shaped Milli-Fluidic Device. *Adv. Mater. Technol.* **2019**, *4*, 1900457. https://doi.org/10.1002/admt.201900457.

6. Plog, J.; Jiang, Y.; Pan, Y.; Yarin, A.L. Electrostatic Charging and Deflection of Droplets for Drop-on-Demand 3D Printing within Confinements. *Addit. Manuf.* **2020**, *36*, 101400. https://doi.org/10.1016/j.addma.2020.101400.

7. Zhang, Y.; Dong, Z.; Li, C.; Du, H.; Fang, N.; Wu, L.; Song, Y. Continuous 3D Printing from One Single Droplet. *Nat. Commun.* **2020**, *11*, 4685. https://doi.org/10.1038/s41467-020-18518-1.

8. Ma, S.; Liu, D.; Sheng, W.; Ma, Y.; Li, B.; Zhao, X.; Wang, X.; Zhou, F.; Liu, W. Bio-Inspired Wet/Lubricious/Adhesive Soft Matter and Performance Control in-between. *Adv. Bionics* **2024**, *1*, 29–56. https://doi.org/10.1016/j.abs.2024.09.002.

9. Zhang, S.; Chi, M.; Liu, T.; Luo, B.; Cai, C.; Wang, J.; Liu, Y.; Gao, C.; Wang, S.; Nie, S. Spontaneous Charging-induced Droplets Directional Steering. *Nano Energy* **2024**, *127*, 109766. https://doi.org/10.1016/j.nanoen.2024.109766.

10. Ferraro, D.; Serra, M.; Filippi, D.; Zago, L.; Guglielmin, E.; Pierno, M.; Descroix, S.; Viovy, J.-L.; Mistura, G. Controlling the Distance of Highly Confined Droplets in a Capillary by Interfacial Tension for Merging on-demand. *Lab Chip* **2019**, *19*, 136–146. https://doi.org/10.1039/c8lc01182f.

11. Zhang, X.; Sun, L.; Wang, Y.; Bian, F.; Wang, Y.; Zhao, Y. Multibioinspired Slippery Surfaces with Wettable Bump Arrays for Droplets Pumping. *Proc. Natl. Acad. Sci. USA* **2019**, *116*, 20863–20868. https://doi.org/10.1073/pnas.1912467116.

12. Li, G.; Zhang, Y.; Zhang, X.; Zhu, B.; Lei, Y.; Chen, D.; Shui, L.; Wu, G.; Xue, L. Filiform Papillae-Inspired Wearable Pressure Sensor with High Sensitivity and Wide Detection Range. *Adv. Funct. Mater.* **2024**, *35*, 2414465 https://doi.org/10.1002/adfm.202414465.

13. Wang, L.; Zhang, C.; Wei, Z.; Xin, Z. Bioinspired Fluoride-Free Magnetic Microcilia Arrays for Anti-Icing and Multidimensional Droplet Manipulation. *ACS Nano* **2023**, *18*, 526–538. https://doi.org/10.1021/acsnano.3c08368.

14. Gao, Z.; Lin, G.; Chen, Y.; Zheng, Y.; Sang, N.; Li, Y.; Chen, L.; Li, M. Moth-eye Manostructure PDMS Films for Reducing Reflection and Retaining Flexibility in Ultra-thin c-Si solar cells. *Sol. Energy* **2020**, *205*, 275–281. https://doi.org/10.1016/j.solener.2020.05.065.

15. Zhang, B.; Liao, X.; Chen, Y.; Xiao, H.; Ni, Y.; Chen, X. Rapid Programmable Nanodroplet Motion on a Strain-Gradient Surface. *Langmuir* **2019**, *35*, 2865–2870. https://doi.org/10.1021/acs.langmuir.8b03774.

16. Tian, L.; Dou, H.; Shao, Y.; Yi, Y.; Fu, X.; Zhao, J.; Fan, Y.; Ming, W.; Ren, L. Magnetically Controlled Super-wetting Surface Switching between Ultra-low and Ultra-high Droplet Adhesion. *Chem. Eng. J.* **2023**, *456*, 141093. https://doi.org/10.1016/j.cej.2022.141093.

17. Shao, K.; Jiang, S.; Hu, Y.; Zhang, Y.; Li, C.; Zhang, Y.; Li, J.; Wu, D.; Chu, J. Bioinspired Lubricated Slippery Magnetic Responsive Microplate Array for High Performance Multi-Substance Transport. *Adv. Funct. Mater.* **2022**, *32*, 2205831. https://doi.org/10.1002/adfm.202205831.

18. Ko, J.; Zhao, Z.; Hwang, S.H.; Kang, H.; Ahn, J.; Jeon, S.; Bok, M.; Jeong, Y.; Kang, K.; Cho, I.; et al. Nanotransfer Printing on Textile Substrate with Water-Soluble Polymer Nanotemplate. *ACS Nano* **2020**, *14*, 2191–2201. https://doi.org/ 10.1021/acsnano.9b09082.

19. Song, Y.; Yang, J.; Zhang, X.; Zhang, Z.; Hu, X.; Cheng, G.; Liu, Y.; Lv, G.; Ding, J. Temperature-Responsive Peristome-Structured Smart Surface for the Unidirectional Controllable Motion of Large Droplets. *Microsyst. Nanoeng.* **2023**, *9*, 119. https://doi.org/10.1038/s41378-023-00573-5.

20. Rao, Q.; Tong, Z.; Song, L.; Ali, A.; Hou, Y.; He, Q.; Lu, J.; Gao, X.; Zhan, X.; Zhang, Q. NIR-driven Fast Construction of Patterned-Wettability on Slippery Lubricant Infused Surface for Droplet Manipulation. *Chem. Eng. J.* **2022**, *428*, 131141. https://doi.org/10.1016/j.cej.2021.131141.

21. Liang, X.; Karnaukh, K.; Zhao, L.; Seshadri, S.; DuBose, A.; Bailey, S.; Cao, Q.; Cooper, M.; Xu, H.; Haggmark, M.; et al. Dynamic Manipulation of Droplets on Liquid-Infused Surfaces Using Photoresponsive Surfactant. *Acs Cent. Sci.* **2024**, *10*, 684–694. https://doi.org/10.1021/acscentsci.3c00982.

22. Zhang, Q.; Bai, X.; Li, Y.; Zhang, X.; Tian, D.; Jiang, L. Ultrastable Super-Hydrophobic Surface with an Ordered Scaly Structure for Decompression and Guiding Liquid Manipulation. *ACS Nano* **2022**, *16*, 16843–16852. https://doi.org/10.1021/acsnano.2c06749.

23. Huo, X.; Li, L.; Yang, Y.; Liu, X.; Yu, Q.; Wang, Q. The Dynamics of Directional Transport of a Droplet in Programmable Electrowetting Channel. *Phys. Fluids* **2023**, *35*, 032105. https://doi.org/10.1063/5.0139965.

24. Li, N.; Yang, P.; Bai, Z.; Shen, T.; Liu, Z.; Qin, S.; Hu, J.; Yu, C.; Dong, Z.; Chen, X. Bioinspired Electrostatic Capture-and-Release System for Precise Microdroplet Manipulation. *Adv. Mater.* **2025**, *37*, 2418711. https://doi.org/10.1002/adma.202418711.

25. Kravanja, G.; Kriegl, R.; Hribar, L.; Glavan, G.; Drevensek-Olenik, I.; Shamonin, M.; Jezersek, M. Magnetically Actuated Surface Microstructures for Efficient Transport and Tunable Separation of Droplets and Solids. *Adv. Eng. Mater.* **2023**, *25*, 2301000. https://doi.org/ 10.1002/adem.202301000.

26. Chi, Y.; Evans, E.; Clary, M.R.; Qi, F.; Sun, H.; Cantu, S.N.; Capodanno, C.M.; Tracy, J.; Yin, J. Magnetic Kirigami

Dome Metasheet with High Deformability and Stiffness for Adaptive Dynamic Shape-Shifting and Multimodal Manipulation. *Sci. Adv.* **2024** *10*, eadr8421. https://doi.org/10.1126/sciadv.adr8421.

27. Wang, W.; Timonen, J.; Carlson, A.; Drotlef, D.; Zhang, C.; Kolle, S.; Grinthal, A.; Wong, T.S.; Hatton, B.; Kang, S.H.; et al. Multifunctional Ferrofluid-Infused Surfaces with Reconfigurable Multiscale Topography. *Nature* **2018**, *559*, 77–82. https://doi.org/10.1038/s41586-018-0250-8.

28. Han, K.; Snezhko, A. Programmable Chiral States in Flocks of Active Magnetic Rollers. *Lab Chip* **2021**, *21*, 215–222. https://doi.org/10.1039/d0lc00892c.

29. Park, S.; Choi, G.; Kang, M.; Kim, W.; Kim, J.; Jeong, H.E. Bioinspired Magnetic Cilia: From Materials to Applications. *Microsyst. Nanoeng.* **2023**, *9*, 153. https://doi.org/10.1038/s41378-023-00611-2.

30. Yang, C.; Wu, L.; Li, G. Magnetically Responsive Superhydrophobic Surface: In Situ Reversible Switching of Water Droplet Wettability and Adhesion for Droplet Manipulation. *ACS Appl. Mater. Interfaces* **2018**, *10*, 20150–20158. https://doi.org/10.1021/acsami.8b04190.

31. Kim, J.; Kang, S.; Lee, B.; Ko, H.; Bae, W.; Suh, K.; Kwak, M.; Jeong, H. Remote Manipulation of Droplets on a Flexible Magnetically Responsive Film. *Sci. Rep.* **2015**, *5*, 17843. https://doi.org/10.1038/srep17843.

32. Chen, Y.; Quan, Z.; Xie, H.; Li, B.; Zhao, J.; Niu, S.; Han, Z.; Ren, L. Bioinspired Active Dynamic Dust Remover for Multiscale Stardust Repelling of Unmanned Probe Surface. *Nano Lett.* **2024**, *25*, 553–561. https://doi.org/10.1021/acs.nanolett.4c05480.

33. Lu, G.; Cui, H.; Zhao, T.; Yang, W.; Wang, M.; Liu, Z.; Niu, S.; Ren, L. Cilia-Inspired Functional Channels for High-Speed and Directional PEMFC Drainage. *Adv. Funct. Mater.* **2024**, *35*, 2416005. https://doi.org/10.1002/adfm.202416005.

34. Zhang, X.; Ben, S.; Zhao, Z.; Ning, Y.; Li, Q.; Long, Z.; Yu, C.; Liu, K.; Jiang, L. Lossless and Directional Transport of Droplets on Multi-bioinspired Superwetting V-shape Rails. *Adv. Funct. Mater.* **2023**, *33*, 2212217. https://doi.org/10.1002/adfm.202212217.

35. Feng, S.; Zhu, P.; Zheng, H.; Zhan, H.; Chen, C.; Li, J.; Wang, L.; Yao, X.; Liu, Y.; Wang, Z. Three-Dimensional Capillary Ratchet-Induced Liquid Directional Steering. *Science* **2021,** *373*, 1344–1348. https://doi.org/10.1126/science.abg7552.

36. Li, Y.; Liu, X.; Wang, R.; Jiao, S.; Liu, Y.; Lai, H.; Cheng, Z. Triple-Bioinspired Shape Memory Microcavities with Strong and Switchable Adhesion. *ACS Nano* **2023**, *17*, 23595–23607. https://doi.org/10.1021/acsnano.3c06651.

37. Li, Y.; Wang, R.; Jiao, S.; Lai, H.; Liu, Y.; Cheng, Z. Beetle-Inspired Oil-Loaded Shape Memory Micro-Arrays with Switchable Adhesion to Both Solid and Liquid. *Chem. Eng. J.* **2023**, *461*, 141927. https://doi.org/10.1016/j.cej.2023.141927.

38. Hev, Z.; Mu, L.; Wang, N.; Su, J.; Wang, Z.; Luo, M.; Zhang, C.; Li, G.; Lan, X. Design, Fabrication, and Applications of Bioinspired Slippery Surfaces. *Adv. Colloid Interface* **2023**, *318*, 102948. https://doi.org/10.1016/j.cis.2023.102948.

39. Yue, T.; Bloomfield-Gadêlha, H.; Rossiter, J. Snail-Inspired Water-Enhanced Soft Sliding Suction for Climbing Robots. *Nat. Commun.* **2024**, *15*, 4038. https://doi.org/10.1038/s41467-024-48293-2.

40. Smith, J.; Dhiman, R.; Anand, S.; Reza-Garduno, E.; Cohen, R.; McKinley, G.; Varanasi, K. Droplet Mobility on Lubricant-Impregnated Surfaces. *Soft Matter* **2013**, *9*, 1772–1780. https://doi.org/10.1039/c2sm27032c.

41. Manabe, K.; Saito, K.; Nakano, M.; Ohzono, T.; Norikane, Y. Light-Driven Liquid Conveyors: Manipulating Liquid Mobility and Transporting Solids on Demand. *ACS Nano* **2022**, *16*, 16353–16362. https://doi.org/10.1021/acsnano.2c05524.

42. Wang, Z.; Xu, Q.; Wang, L.; Heng, L.; Jiang, L. Temperature-induced switchable interfacial interactions on slippery surfaces for controllable liquid manipulation. *J. Mater. Chem. A* **2019**, *7*, 18510–18518. https://doi.org/10.1039/c9ta05164c.

43. Ichimura, K.; Oh, S.; Nakagawa, M. Light-Driven Motion of Liquids on a Photoresponsive Surface. *Science* **2000**, *288*, 1624–1626. https://doi.org/10.1126/science.288.5471.1624.

44. Hwang, H.; Papadopoulos, P.; Fujii, S.; Wooh, S. Driving Droplets on Liquid Repellent Surfaces via Light-Driven Marangoni Propulsion. *Adv. Funct. Mater.* **2022**, *32*, 2111311. https://doi.org/10.1002/adfm.202111311.

45. Tang, B.; Meng, C.; Zhuang, L.; Groenewold, J.; Qian, Y.; Sun, Z.; Liu, X.; Gao, J.; Zhou, G. Field-Induced Wettability Gradients for No-Loss Transport of Oil Droplets on Slippery Surfaces. *ACS Appl. Mater. Interfaces* **2020**, *12*, 38723–38729. https://doi.org/10.1021/acsami.0c06389.

46. Chen, C.; Huan, Z.; Jiao, Y.; Shi, L.; Zhang, Y.; Li, J.; Li, C.; Lv, X.; Wu, S.; Hu, Y. In Situ Reversible Control between Sliding and Pinning for Diverse Liquids under Ultra-Low Voltage. *ACS Nano* **2019**, *13*, 5742–5752. https://doi.org/10.1021/acsnano.9b01180.

47. Feng, S.; Hou, Y.; Zheng, Y. Programmable Curvilinear Self-Propelling of Droplets without Preset Channels. *Droplet* **2025**, *3*, e138. https://doi.org/10.1002/dro2.138.

Review

Polymer-Patched Plasmonic Nanoparticles

Chansong Kim [1], Xiaoying Lin [1], Jiyeon Kim [1], Yangming Wang [1], and Qian Chen [1,2,3,4,*]

[1] Department of Materials Science and Engineering, the Grainger College of Engineering, University of Illinois, Urbana, IL 61801, USA
[2] Materials Research Laboratory, University of Illinois, Urbana, IL 61801, USA
[3] Department of Chemistry, University of Illinois, Urbana, IL 61801, USA
[4] Beckman Institute for Advanced Science and Technology, University of Illinois, Urbana, IL 61801, USA
* Correspondence: qchen20@illinois.edu

Abstract: In this work, we discuss advancements at the intersection of surface patchiness design and plasmonic nanoparticles. Surface patchiness design, inspired by nature's strategy to encode complex functions by spatially distributed surface patterns, has become increasingly popular in nanoparticle research. The surface patterns lead to their nonuniformity in chemical and physical properties, enabling not only their application as functional hybrid nanomaterials but as building blocks for self-assembly through directional interactions for applications in catalysis, biomedicine, sensing, robotics, and metamaterials. When surface patchiness design is implemented on plasmonic nanoparticles, interesting coupling of plasmonic resonance emerges from self-assembly structures not easily available from non-patchy nanoparticles. This direction is rapidly evolving and we review efforts in the synthesis, self-assembly, and applications of plasmonic patchy nanoparticles. We conclude with outlook discussions of the future opportunities of this field.
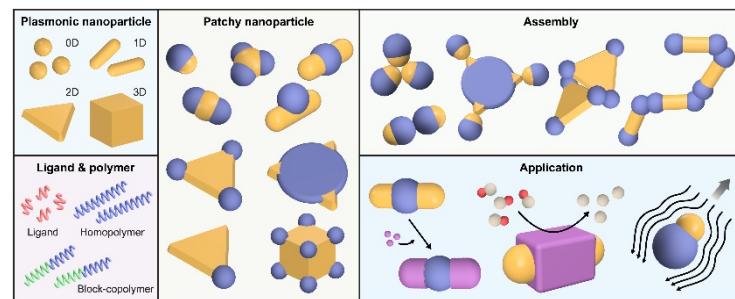
Keywords: patchy nanoparticles; plasmonic particles; polymer ligands; surface chemistry; self-assembly

1. Introduction

Inorganic nanoparticles (NPs) such as metal oxides and noble metals have been extensively studied over the last few decades due to their chemical stability against oxidation and degradation, the convenience to achieve surface modification for attachments of functional groups, and size-dependent electromagnetic properties [1–4]. In particular, plasmonic NPs, such as Au and Ag, exhibit localized surface plasmon resonance (LSPR), which arises from the collective oscillation of free electrons in the metal resonating upon excitation of electromagnetic wave at a specific wavelength [5,6]. Based on LSPR effect, plasmonic NPs are widely used in catalysis [7], sensing [8], and photothermal therapy [9]. Furthermore, self-assembly of these plasmonic NPs can have plasmon coupling dependent on the details of assembly structure, involving both local and global symmetry, which are distinctive from a simple sum of the SPRs of individual NPs [10]. Take a dimeric assembly of NPs—the simplest assembly of two NPs—as an example. For Au nanospheres (NSs), the LSPRs are sensitively dependent on the distance of the two NPs, which is the design principle of plasmonic rulers [11,12] capable of measuring local chemical reactions and distances at nanometer precision. For shape-anisotropic NPs, such as Au triangular prisms, the "bow-tie" configuration of dimers [13], where the sharp tips of each prism are positioned close or in contact with each other, can have a "hot spot", namely an immensely enhanced electromagnetic field around the tip regions, useful for nanoantenna arrays, near field optics, and sensing. It is for the importance of assembly structures in plasmonic coupling that researchers have extended different strategies of making self-assembly structures. One strategy that has gained increasing attention is through surface patchiness design on plasmonic NPs to make the patches repulsive or attractive for directing the self-assembly into nonconventional structures such as non-closely packed structures, and for controlling the relative orientation of contacting pairs of NPs, thereby expanding the

applications of NP assemblies. Moreover, surface patterning of NPs by ligand molecules is a powerful strategy to introduce functionalities in addition to those of the core NPs, allowing more dimensions of control in properties such as wettability, surface charge density, bio-specificity, host-guest interaction, and mechanical stiffness.

For plasmonic patchy NPs, a key challenge has been on the synthesis, as it is hard to achieve high precision in patterning ligand molecules on a NP surface with nanometer precision. For colloidal particles that are micrometer in size, various top-down methods such as electron beam lithography and deposition have been utilized to coat the particles with surface patches [14–16], thereby enabling directional self-assembly [16,17] and diverse applications such as biomedicine [18], sensing [19], self-propelling motors [20,21], and anti-counterfeiting [22]. However, most of these methods have a resolution that is around tens to hundreds of nanometer resolution [23,24], not sufficient for NPs. In the field of microelectronics, surface chemistry patterning has been vigorously pushed for advancements in spatial resolution, for ever-smaller and fast chip technology. Yet even aided with bottom-up assemblies such as polymer microphase separation, current patterning on these chip-based microelectronics has a pitch size of 7 nm and are mostly applied to flat substrates [25].

Thus, the focus of this article (Figure 1) is on highlighting achievements in the synthesis of patchy plasmonic NPs with high precision, particularly on polymer-coated patchy NPs. The formation of polymer patches is intricate, considering both the ligand−NP interactions through chemisorption or physisorption, as well as the polymer−polymer, polymer−solvent interactions which determine the chain configurations, patch dimension, and patch shape. Next, we discuss efforts on the self-assembly of polymer-patched NPs directed through either patch−patch attraction or repulsion. We also discuss current effort to utilize patchy plasmonic NPs in practical applications Finally, we provide our perspectives of the remaining challenges and opportunities for the areas of plasmonic patchy NPs.
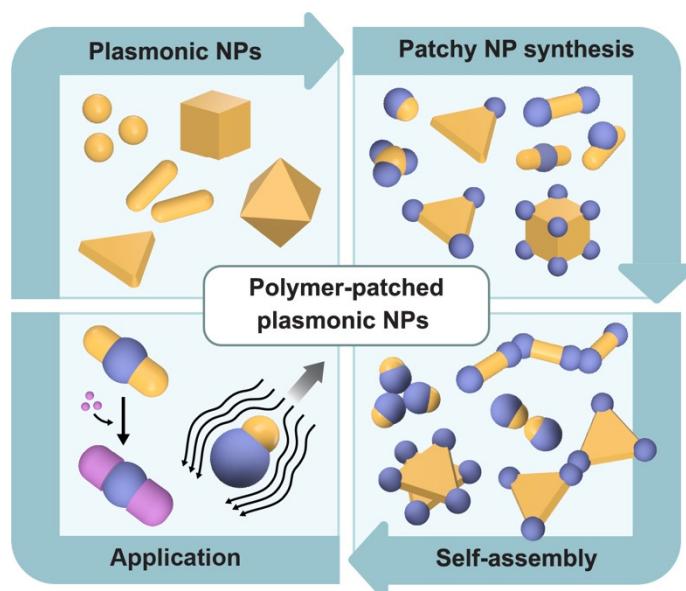
Figure 1. Schematic illustration of the overview of this work. Plasmonic NPs with various shapes can be used to synthesize patchy NPs. These patchy NPs can serve as building blocks for assemblies via directional interactions into a diversity of assembly structures. Due to the surface patchiness, patchy NPs can be used for practical applications such as templates for site-selective depositions and self-propelling nanomotors.

2. Synthesis of Patchy Plasmonic NPs

This section covers the methods used in synthesizing polymer-patched plasmonic NPs, mostly Au NPs, classified into six categories based on the synthesis mechanisms: (1) solvent-mediated segregation of homopolymer ligands, (2) solvent-mediated segregation of block copolymer ligands, (3) microphase separation of ligands, (4) heat-induced transformation of polymer ligands, (5) site-selective binding of ligands, and (6) other strategies such as plasmonic-induced patch formation and templated surface modification.

2.1. Solvent-Mediated Segregation of Homopolymers

Polymer molecules with a functional group that can chemically bind to noble metal NPs, through Au−thiol and Au−amine bonds, are widely used to synthesize polymer-coated NPs since the strong chemical bonds ensure stable surface modification of NPs. These polymer ligands can exhibit different phase behaviors such as swelling

and collapsing, depending on the solvents, to balance polymer−solvent interfacial energy and polymer−polymer interaction [26]. Thus for the synthesis of polymer-patched NPs, the phase transition of polymer ligands collapsing into segregated surface patches was among the first successful strategies.

This strategy was pioneered by Kumacheva and coworkers, when they reported a milestone in the synthesis of patchy plasmonic Au and Ag NPs by utilizing solvent-mediated polymer segregation of homopolymer ligands [27]. Specifically, they first grafted NPs with hydrophobic thiol-terminated polystyrene (HS-PS) ligands in dimethylformamide (DMF), which is a good solvent for the ligands. In DMF, the ligands fully cover the NP surface and are extended with favored solvent−polymer contact. Then the solvent quality was reduced by adding controlled portion of poor solvent, water, for the polymer ligands, to cause collapsing of the grafted polymer ligands into spatially discrete, pinned micelles as polymer patches on the NP surface. These pinned micelles consisted of dense cores of aggregated polymers and stretched surface-tethered 'legs', the latter of which serve as polymer bridges between core NPs and densely collapsed patches. This polymer segregation was governed by the balance between the polymer−solvent interfacial energy and the stretching energy of the micellar 'legs.' In the Au NS system, for example, transition from core−shell to patchy structures is favored at decreasing polymer grafting density (σ) and core NP diameter (D). At high σ, the extended polymer chains minimize their interfacial and stretching energies by forming a smooth layer, which resulted in homogeneously coated Au core−polymer shell NPs. In contrast, at lower σ, the polymer coating becomes thinner, and the interfacial energy is lowered by polymer segregation into pinned micelles. Additionally, the competition between the polymer–solvent interfacial energy (favoring segregation) and the elastic energy of stretched micellar 'legs' (favoring core−shell coating) determines the optimized pinned micelle footprint area (A), which is proportional to $(N^2/\sigma)^{2/5}$, where N is the polymer degree of polymerization. It was demonstrated that the number of pinned micelles per NP (n) is proportional to the ratio between the surface area of Au NS (πD^2) and A, which suggests that the ratio of D to polymer chain size (R, defined as the root-mean-square end-to-end distance of a polymer in its ideal conformation) (D/R) determine the number and spatial distribution of patches.

After this pioneering work, similar strategies were extended to different anisotropically shaped NPs. One prominent example is one-dimensional (1D) Au nanorods (NRs), which unlike Au NSs, exhibit different local surface curvatures along the Au NP in two principal axis directions: a cylindrical segment with zero curvature along the longitudinal axis and positive curvature along the transverse axis [28]. By reducing solvent quality, Kumacheva and coworkers show that Au NRs with polymer ligands uniformly grafted can form diverse NP structures, such as core−shells, discrete random patches, and helicoidal patch arrangements, depending on the lN, where l is monomer length, surface curvature ($1/r$, where r is radius of the fitted circle of the Au NR surface), and σ (Figure 2a,b). Notably, the formation of the helicoidal patches with handedness was a surprise and differs from uniformly collapsed patches in most cases.

This breaking of symmetry was rationalized by the two different curvature values, which govern the formation of polymer-pinned micelles upon reduced solvent quality on Au NRs. On one hand, the footprint of pinned micelles elongates in the direction parallel to the Au NR long axis. On the other, perpendicular to the Au NR long axis, the stretched polymer micelles experience a high local curvature and become connected with each other at the centers of the nearest micelles. With these two effects combined, in the end, the patches twist at an angle with respect to the long axis, and coalesce along the line of the shortest distance between the neighboring patches, resulting in the helicoidal patch structure (Figure 2c).

Given the importance of local surface curvature of the core NP in determining the patch patterns, more follow-up studies focused on the gradual evolution of patch patterns occurred while the shape of the core NPs changes, accompanied by changes in local surface curvature [29]. When Au NPs are exposed to Au^{3+} ions in an aqueous solution of cetyltrimethylammonium bromide (CTAB), Au^{3+}−CTAB complexes form, and they can etch the Au NPs through comproportionation reaction [30]. Kumacheva and coworkers used this straightforward chemistry to induce the etching of patchy Au nanocubes (NCs) after the patchy particles were synthesized following solvent quality-induced polymer segregation strategy. During this etching process, Au NCs gradually transformed into Au NSs, leading to changes in the shape and number of patches on the NPs. The patch patterns on the etched Au NCs resemble those on patchy Au NSs directly synthesized via the polymer segregation of polymer ligands. While Au NCs exhibited eight corner patches from the transmission electron microscopy (TEM) images (only four shown due to two-dimensional projection, Figure 2d), three patches were observed on both etched Au NCs and Au NSs (Figure 2e). This similarity of patch patterns between the etched Au NCs and Au NSs highlighted again the critical role of local surface curvature of the core NPs on determining the patch patterns.

In addition to in-situ etching, the patch pattern changes can also occur through the ligand migration. In the examples above, thiol-terminated polymer ligands, such as HS-PS, have been utilized to exploit Au−thiol bonds. It is well known that the barrier for desorption of thiol-terminated molecules on Au surfaces are 20–50 k_BT in

solution [31,32], with the barrier for lateral migration of the molecules along Au surface even lower. Thus it was hypothesized that thermal treatment can induce the migration of polymer patches. Indeed, work by Kumacheva and coworkers show that the polymer patterns on Au NPs can change upon heating [33]. In this study, Au NSs with two patches were firstly prepared and then incubated for different time durations at varying temperatures to observe the patch shape transformation. While no obvious change was found at low temperature (25 and 40 °C) even after 96 h of incubation due to insufficient thermal energy, gradual transformation of polymer patterns into one-patch and even complete loss of patches (due to thiol desorption) after 2 days and 4 days of incubation at 80 °C, respectively (Figure 2f).
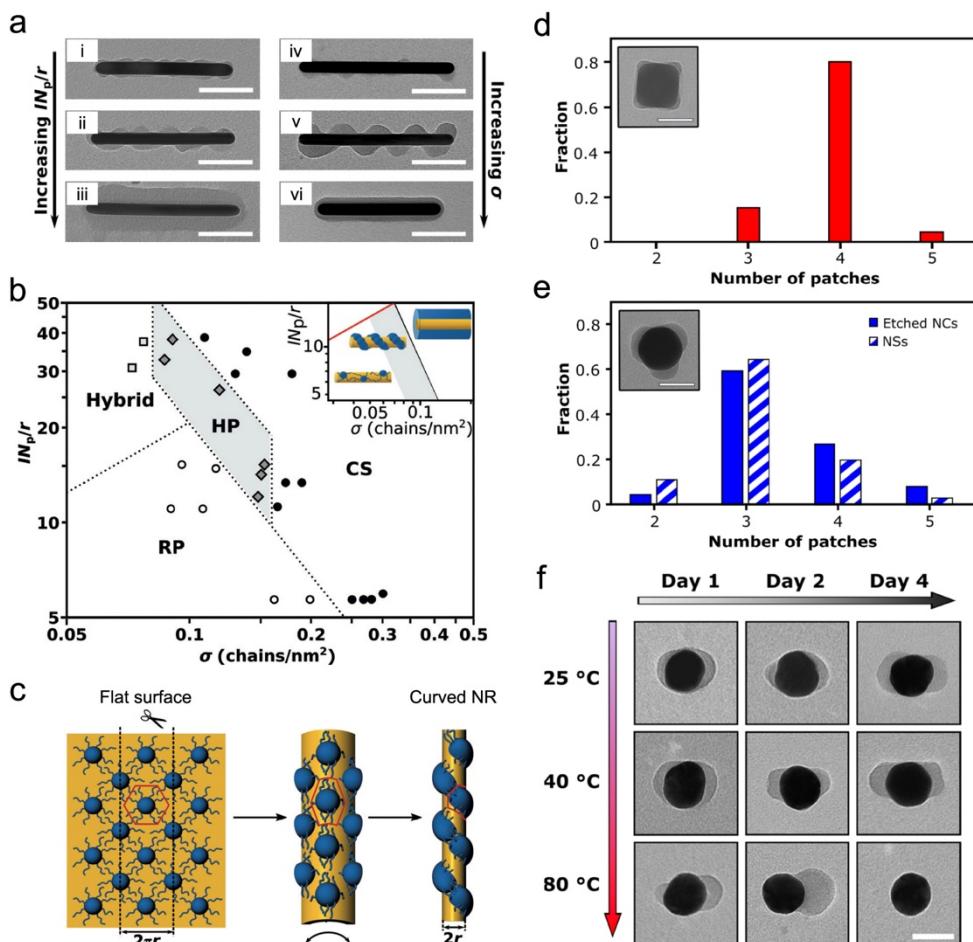
Figure 2. Solvent-mediated segregation of homopolymer ligands on anisotropically shaped Au NPs. (**a**) Representative TEM images of patchy Au NRs synthesized under varying lN/r and σ. (**b**) Experimental diagram of polymer pattern states as a function of lN/r and σ for the Au NRs. (**c**) Schematic illustrating the formation of the helicoidal patches on NRs. (**d,e**) Histograms of patchy Au NCs (**d**), as well as etched Au NCs and Au NSs (**e**) with different n. (**f**) Representative TEM images of patchy Au NSs after thermal treatment at different temperatures for varying durations. Scale bars: (**a**) 100 nm, (**d,e**) 50 nm, and (**f**) 40 nm. (**a–c**) Reproduced with permission from ref. [28]. Copyright 2019, Wiley-VCH. (**d,e**) Reproduced with permission from ref. [29]. Copyright 2017, American Chemical Society. (**f**) Reproduced with permission from ref. [33]. Copyright 2020, American Chemical Society.

2.2. Solvent-Mediated Segregation of Block Copolymers

The above early synthetic efforts of patchy NPs using the solvent-mediated polymer segregation strategy primarily employed homopolymer ligands such as HS-PS for patch formation. However, when polymer ligands segregate due to reduced solvent quality, the stability of the NPs can also be compromised. This reduced stability can lead to agglomeration of polymer-patched NPs due to the lack of inter-NP repulsion. Consequently, these patchy NPs often require precise control over the solvent quality and are typically synthesized under low NP concentrations, with relatively low yield. To mitigate these challenges, block copolymer ligands were used as a good ligand candidate for synthesizing patchy NPs using the polymer segregation strategy, with the ligands consisting of at least two blocks: a NP-adjacent block that forms patches, and a NP-remote block that stabilizes

the patchy NP in the solvent. Furthermore, since this NP-remote block governs the stability of patchy NPs, they also determine the subsequent assembly of the patchy NPs.

Kumacheva and coworkers pioneered the usage of end-grafted block copolymer ligands to synthesize patchy Au NPs with enhanced stability [34]. A trithiocarbonate-terminated block copolymer, consisting of a PS block (a NP-adjacent block for patchy formation) and a poly(4-vinylbenzoic acid) (P4VBA) block (a NP-remote block for the stabilization and subsequent self-assembly) was used to coat Au NPs uniformly first, followed by a reduction in solvent quality. A trithiocarbonate-terminated PS homopolymer ligand was also used as a control sample for comparison. Under poor solvency conditions, Janus structures formed for both ligands through polymer segregation. However, the reduced solvent quality compromised the stability of homopolymer ligand-grafted Au NPs, leading to simultaneous formation of merged patchy Au NPs, with limited control over synthesis. In contrast, block copolymer ligand-grafted Au NPs exhibited stable patchy structures and good NP dispersibility in poor solvents, allowing subsequent self-assembly (Figure 3a).

Since this pioneering work, various block copolymers have been used for synthesizing patchy NPs to utilize the functionality of different polymer blocks. He and coworkers synthesized patchy NPs using a mixture of homopolymer ligands and block copolymers [35–37]. Hydrophobic HS-PS and amphiphilic block copolymer, such as PS-*b*-poly(acrylic acid) (PS-*b*-PAA) and PS-*b*-poly(ethylene oxide) (PS-*b*-PEO), were introduced into Au NSs in a mixture of DMF and water [35,36]. When HS-PS was first grafted on the Au surface, water in the solvent mixture induced polymer segregation and site-selective surface decoration. The block copolymer with a PS block then bound to the pre-attached HS-PS via hydrophobic attractions, thereby forming Janus patches (Figure 3b). Importantly, these block copolymer-coated NPs can stay stabilized due to the hydrophilic block, even in water which is a poor solvent for PS block. The polymer patterns on the NPs were determined by the concentration of the polymer ligand. Under low HS-PS concentrations, Janus structures formed, while fully covered NPs were observed under high HS-PS concentration. Patch coverage decrease, showing gradual transitions from core−shell to patchy structures, was observed as the polymer ligand concentration decreased (Figure 3c). This synthesis method was also applied to other shaped particles. Interestingly, when using NRs, a dumbbell-like patch pattern with two patches at both NR ends formed at low HS-PS concentrations [37]. The higher local curvature at the ends than those along the rods resulted in a smaller polymer−solvent interface, leading to site-selective polymer grafting at the NR ends (Figure 3d). Furthermore, as the concentration of anchoring HS-PS decreased further, a gradual transition from individual dumbbell-like structures to interlinked 1D chain-like assemblies were formed, with decreasing end-to-end distances due to lower σ (Figure 3d). Notably, this decreased end-to-end distance resulted in a red shift of the longitudinal LSPR due to the plasmon coupling effect.

In addition to block copolymers, patchy Au NPs have been also synthesized with a thiol-terminated block-random copolymer ligand, consisting of three different segments—hydrophilic PEO, hydrophobic PS, and a randomly copolymerized blocks [38]. By using this block-random copolymer ligands, Nie and coworkers achieved not only enhanced stability of patchy Au NPs while reducing solvent quality but also a broader library of patch patterns, which were difficult to achieve using diblock copolymers. The structural evolution from fully coated polymer ligands to patches was attributed to the molecular exchange between the polymers on Au NP surface and the free polymer micelles in the solution upon sequential reducing solvent quality and heating at 110 °C. When water, a poor solvent for the hydrophobic PS block, was added to the solution of fully coated Au NPs, patchy structures were formed by polymer segregation. Upon heating, dynamic ligand exchange led to the evolution of patch shapes, making patch sizes more uniform and distributing them more symmetrically on the Au NP surface over time (Figure 3e). Notably, the presence of the randomly copolymerized block regulated this dynamic molecular exchange, acting as a buffering region between the hydrophilic and hydrophobic blocks. Through this method, diverse patchy Au NPs with controlled morphology and different n, such as beanlike patches, one-, two-, three-, and multiple-patches ($n > 3$), were formed (Figure 3f).
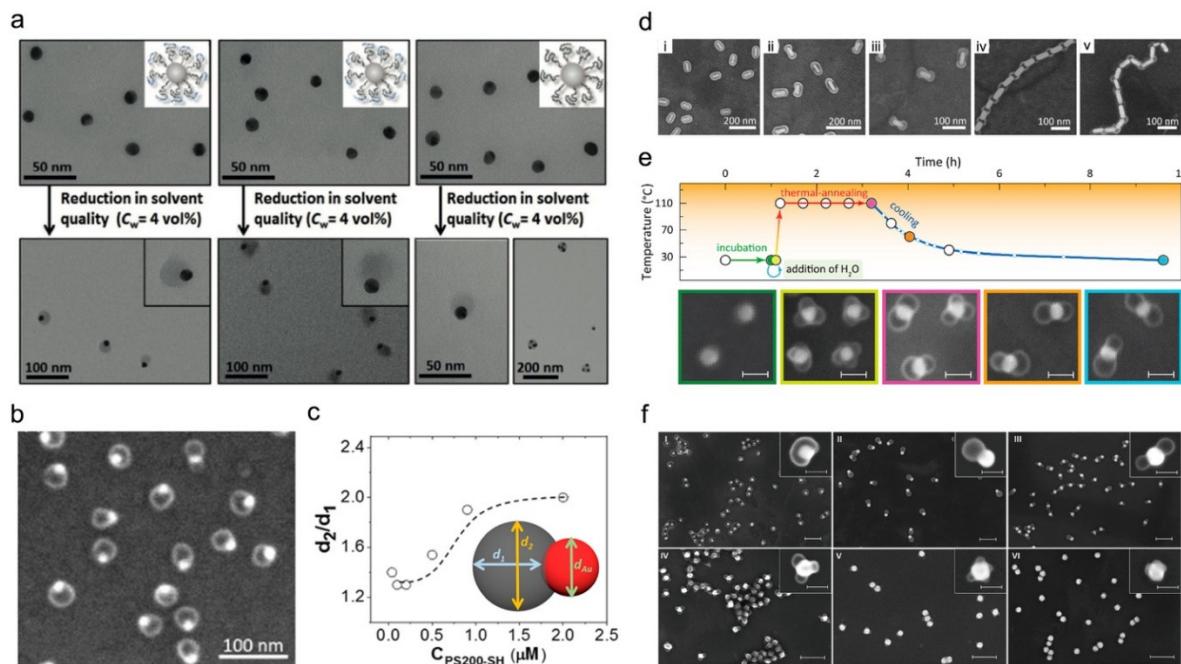
**Figure 3.** Solvent-mediated segregation of block copolymer ligands on Au NPs for patch formation. (**a**) Representative TEM images of Au NPs coated with short (left) and long (middle) PS-*b*-P4VPA block copolymer ligands, and a PS homopolymer ligand (right), before and after reducing solvent quality. (**b**) Representative scanning electron microscopy (SEM) image of Janus Au NPs with PS-*b*-PEO patches. (**c**) The changes in the d_2/d_1 ratio of the Janus Au NPs shown in (**b**) under varying HS-PS ligand concentrations. The inset schematic defines d_1 and d_2. (**d**) Representative SEM images of patchy Au NRs prepared at decreasing HS-PS polymer ligand concentrations (from left to right). (**e**) Schematic of the patch formation process and SEM images showing the morphological evolution of the patches. The colored boxes in each SEM image correspond to the experimental conditions indicated by data points of the same color in the schematic. (**f**) Low- and high-magnification (insets) SEM images of patchy Au NPs with different morphologies synthesized using a block-random copolymer. Scale bars: (**e**) 50 nm and (**f**) 200 nm (insets: 50 nm). (**a**) Reproduced with permission from ref. [34]. Copyright 2019, Wiley-VCH. (**b,c**) Reproduced with permission from ref. [35]. Copyright 2021, American Chemical Society. (**d**) Reproduced with permission from ref. [37]. Copyright 2023, American Chemical Society. (**e,f**) Reproduced with permission from ref. [38]. Copyright 2021, American Chemical Society.

2.3. Microphase Separation-Induced Patch Formation

Even though controllability of patch patterns was achieved using copolymers, most solvent-mediated strategies for patchy NP synthesis utilizing one kind of ligand still exhibited limited patch patterns. Usually, only a single type of patch structure could be formed on a given core NP shape, such as Janus for NSs and end-grafting for NRs. Furthermore, the solvent-mediated synthesis method utilizes polymer strand collapse on fully polymer-coated NPs grafted with a single type of polymer. Thus efforts reviewed in this section focused on having more than one ligand.

When multiple thiol-terminated ligands are grafted on one NP, spontaneous microphase separation of the mixed polymer ligands can occur through their lateral diffusion to maximize their conformational entropy gain as well enthalpic attraction sites. The number, size, and spatial distribution of each polymer domain are determined by the structural properties of the core NPs such as surface curvature, the chemical structures of ligands such as length and bulkiness, and the molecular ratio of each species [39,40]. This microphase separation has been utilized to synthesize patchy NPs. Chen and coworkers reported the patchy Au NSs synthesized using a binary mixture of thiol-terminated ligands with different hydrophilicities (2-dipalmitoyl-*sn*-glycero-3-phosphothioethanol for a hydrophobic ligand and either diethylamine or 2-mercaptoacetic acid for a hydrophilic ligand) along with block copolymer [41]. The two ligands bound to the Au NP surface, forming separated ligand domains. The PS-*b*-PAA block copolymer then attached site-selectively to the hydrophobic ligand-coated regions via hydrophobic attraction. Notably, it was demonstrated that the concentration ratio of hydrophobic to hydrophilic ligands (L_A/L_B) determined the morphology of polymer patch patterns on the NP surface. The homocentric core–shell structure gradually transitioned into a slightly eccentric and then a highly eccentric Janus shape as the L_A/L_B ratio decreased (Figure 4a). This transition was attributed to the formation of small hydrophobic domain on the surface under relatively

deficient hydrophobic ligand concentrations, where the PS block of the PS-*b*-PAA molecules can attach via hydrophobic attraction. Interestingly, sequential addition of a hydrophobic ligand after the incubation of Au NPs with a hydrophilic ligand, instead of using a mixture of hydrophobic and hydrophilic ligands for ligand grafting, resulted in flower-like patchy structures exhibiting multiple patches on NP surfaces. This was attributed to uneven distribution of hydrophobic ligands on Au NPs, resulting from the kinetically controlled dissociation of pre-attached hydrophilic ligands from the Au NPs and ligand exchange with hydrophobic ligands in solutions.

The underlying mechanism of microphase separation-driven patchy NP formation was proposed based on a three-phase wetting problem, which involves the balance of three interfacial free energies: NP–solvent, NP–polymer, and polymer–solvent [42]. Depending on their relative magnitudes, the polymer chains either completely or partially covered the NP surface. This resulted in different polymer patch patterns, as they preferentially coated on the hydrophobic ligand domains to minimize the overall free energy. Specifically, NP–solvent interfacial energy is determined by the hydrophilicity of the NP, which is governed by the ligand chemistry, namely the L_A/L_B ratio. When the NP surface was coated with hydrophobic ligands exclusively in a polar solvent, the NP–solvent interfacial energy increased, resulting in a fully polymer-coated core–shell structure to minimize interfacial area between NP and solvent. In contrast, as more hydrophilic ligands covered the NP surface, the lower NP–solvent interfacial energy led to partial coverage, thereby forming patchy structures. Based on this wetting-induced microphase separation, structural diversity in patchy Au NPs was achieved by controlling the L_A/L_B ratio. This microphase separation for synthesizing patchy NPs effective for different ligand mixtures, yielding distinct patch patterns such as periodic patches on Au NRs when using a mixture of HS-PS and HS-methoxy PEO (mPEO) (Figure 4b) [43], and differently shaped core Au NPs including spheres, rods, triangular prisms, cubes, and octahedra [42,44].

In addition to microphase separation induced only by physical, non-covalent interactions, in situ self-polymerization of dithiol ligands can induce patch formation on NPs through microphase separation by using it along with other ligands [45]. For example, benzene-1,4-dithiol (BDT) can create a polymer layer on Au NPs via self-polymerization. Specifically, when BDT molecules attach to the Au surface, additional BDT molecules subsequently bind to the pre-attached BDT through disulfide bridging, thereby forming polymerized BDT (pBDT). This process also facilitates further polymerization on pre-attached BDT and/or pBDT via π−π stacking. The Au NPs used in this study were initially stabilized by sodium dodecyl sulfate (SDS) in solution. Thus, the BDT polymerization on the Au NPs was initiated through ligand exchange between SDS on the Au NP surface and BDT in solution, making a similar scenario to that in which multiple ligands showing different hydrophilicity induce microphase separation on the surface. Consequently, this process, akin to microphase separation, resulted in Janus Au NPs. Moreover, beyond this BDT unary ligand system, binary and ternary ligand systems incorporating multiple ligands were also employed with varying ligand types and molar ratios (Figure 4c–h). The use of BDT alongside multiple ligands, such as 4-methylbenzenethiol (MBT), 4-mercaptophenol (MCP), 4-mercaptobenzoic acid (MBA), and 4-aminothiophenol (ATP), enabled various patch structures. These patch patterns were governed by the ligand types and molar ratio of each species, ranging from simple Janus structures to complex patch shapes with different n. Additionally, the study on the time-dependent transformation of polymer patterns using a binary system of BDT and ATP confirmed the underlying mechanism of self-polymerization-driven patch formation. After creating multiple patches on the Au NP at the beginning of the reaction, the number of patches gradually decreased over time, eventually resulting in two-patch structure (Figure 4g). It is likely that the electrostatic repulsion between patches on the confined Au NP surface increased as the patches grew larger, thereby limiting their further growth. To overcome this barrier, existing small patches dissociated and reorganized into a larger patch to lower the surface energy. This demonstrated that, in addition to surface binding energy (between core NP and grafting ligands) and π−π interaction (between ligands), which are known to govern microphase separation, additional interactions, such as patch−patch electrostatic repulsion, can also influence the patching reaction.
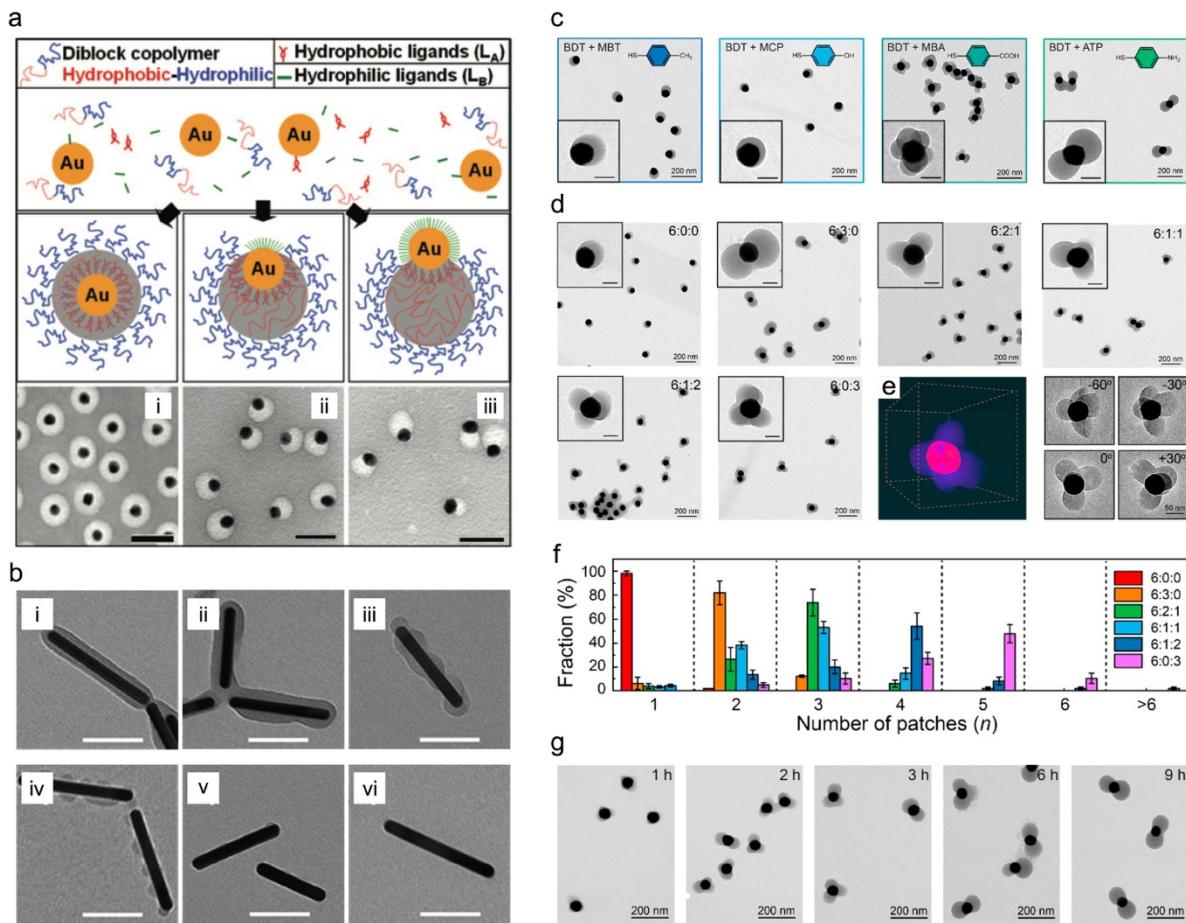
Figure 4. Microphase separation of ligands inducing patch formation on Au NPs. (**a**) Schematic and representative TEM images showing the formation of homocentric (**left**) and eccentric (**middle** and **right**) polymer patterns on Au NPs at increasing L_A/L_B ratios (from **left** to **right**). (**b**) TEM images of patchy Au NRs synthesized using a mixed hydrophobic HS-PS and hydrophilic HS-mPEO at increasing L_A/L_B ratios (from **i** to **vi**). (**c,d**) Low- and high-magnification TEM images of pBDT patchy Au NSs synthesized under a binary (with varying ligand type) (**c**) and a ternary (at varying molar ratios between ATP and MBA) (**d**) ligand systems. The values in (**d**) represent the molar ratio of BDT:ATP:MBA. (**e**) 3D electron tomography reconstruction of a patchy Au NS coated with four patches obtained with a stoichiometric ratio of 6:1:2, along with corresponding TEM images at different tilting angles. (**f**) Histogram of patchy Au NSs with different n in each stoichiometric ratio. (**g**) TEM images of patchy Au NSs at different time of reaction, showing the transition of patch configurations. Scale bars: (**a**) 50 nm, (**b**) 100 nm, and (**c,d**) 50 nm. (**a**) Reproduced with permission from ref. [41]. Copyright 2008, American Chemical Society. (**b**) Reproduced with permission from ref. [43]. Copyright 2019, American Chemical Society. (**c–g**) Reproduced with permission from ref. [45]. Copyright 2021, American Chemical Society.

2.4. Heat-Induced Transformation of Polymer Coatings on NPs to Form Patches

As noted in Section 2.1, the patch patterns formed from solvent quality reduction in homopolymer ligands of HS-PS can be changed upon heat treatment. The same principle can be applied to other more complex systems. For example, when polymer coatings are formed on the Au NP surface using thiol-terminated hydrophobic ligands and amphiphilic block copolymers, the ligands first bind to Au NP surfaces, followed by the attachment of the block copolymers through hydrophobic attractions between ligands and the hydrophobic block of block copolymers. In this case, sufficient thermal energy at elevated temperature can "liquefy" the polymer coating by weakening the ligand–polymer attractions, leading to the formation of polymer patch patterns on NPs. Therefore, this heat-induced transformation of polymer coatings has been broadly used for synthesizing patchy Au NPs.

Chen and coworkers used this strategy to synthesize patchy Au NRs which formed with diverse types of thiol-terminated ligands alongside PS-*b*-PAA, at sufficiently high temperature [46]. Upon heating above 90 °C, polymers increase their mobility, leading to different transformation, such as contraction, dissociation, and winding depending on the ligand types. The controllability achieved by the hydrophobic ligand types is made possible due to variations in intermolecular interactions between polymer and ligands. Specifically, 2-

naphthalenethiol (2-NAT) (Figure 5a) and biphenyl-4-thiol (Figure 5b) ligands have strong attractions with PS-*b*-PAA, making the polymers difficult to dissociate and thus persist on the NP surface even heated at 115 °C. Instead, the contraction of the polymer coating occurs in this case, leading to smaller sized patches (Figure 5c, left). In contrast, aliphatic (1-dodecanethiol and 1-octadecanethiol) or bulky ligands (HS-PS) have weaker attraction with PS-*b*-PAA. As a result, even heating at 90 °C, the polymers can dissociate from the ligands, with patches dislodging and moving into the aqueous phase (Figure 5c, middle). On the other hand, amphiphilic 2-dipalmitoyl-*sn*-glycero-3-phosphothioethanol interacts with PS-*b*-PAA block polymers to form micelle-like polymer domains upon heating at 60 °C, leading to winding cylinder structures (Figure 5c, right). In addition to ligand types, heating temperature and ligand concentration also influence the final patch structures.
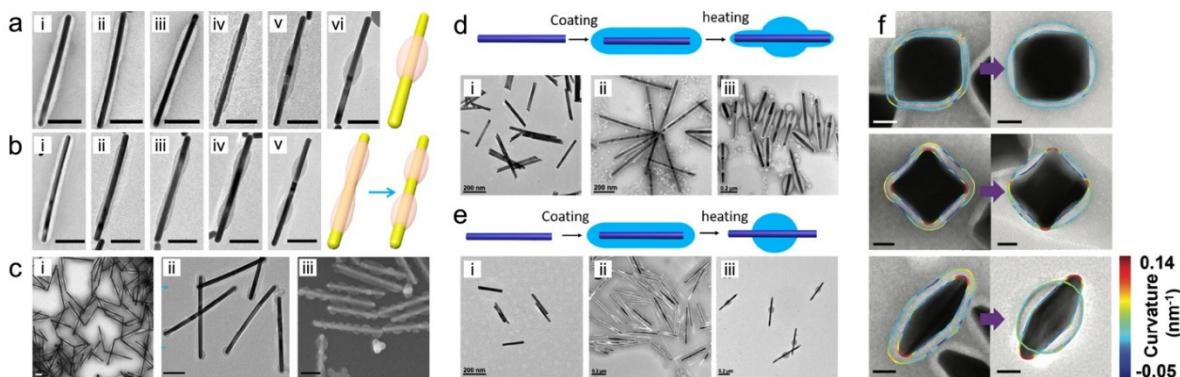

Figure 5. Heat-induced transformation of polymer coating for patch formation on NPs. (**a**,**b**) Schematics and TEM images of the initial core–shell structures and the transformation of polymer layers on Au NRs based on contraction mode, forming one- (**a**) and two-patch (**b**) structures, through thermal treatment at a temperature range of 105 to 115 °C and at 90 °C, respectively. Increased thermal energy was supplied from left to right by either extending the heating time or raising the temperature. (**c**) Representative TEM and SEM images of NRs with one-patch structure (**left**, contraction mode), two-patch at both ends (**middle**, dissociation mode), and helicoidal patch (**right**, winding mode) structures. (**d**,**e**) Schematics and TEM images of polymer shell transformation on Te NWs coated with long (**d**) and short (**e**) HS-PS polymer ligands upon heating at 80 °C. (**f**) TEM images of PS-*b*-PAA-coated NPs with different Au core shapes—octahedron (**top**), concave cube (**middle**), and bipyramid (**bottom**)—before (**left**) and after (**right**) heating. Scale bars: (**a**–**c**) 100 nm and (**f**) 20 nm. (**a**–**c**) Reproduced with permission from ref. [46]. Copyright 2018, Springer Nature. (**d**,**e**) Reproduced with permission from ref. [47]. Copyright 2019, American Chemical Society. (**f**) Reproduced with permission from ref. [48]. Copyright 2018, Wiley-VCH.

The heat-induced patch formation mechanism using thiol-terminated ligands and physisorbed polymers onto them extends to NPs of another composition, Te nanowires (NWs) (Figure 5d,e) [47], and other Au NP shapes including bipyramid, octahedron, and concave cube (Figure 5f) [48]. Notably, when one extends the patching strategy to other shapes, characterization of the patch patterns becomes non-trivial. TEM and SEM images are usually used to classify the products. Chen and coworkers customized an automated workflow to analyze many TEM images of polymer-coated Au NPs before and after segregation by recognizing the patch domain (lighter contrast in TEM images) and the core NP domain (darker contrast TEM images) first through thresholding [48]. After segmenting the core Au NP and polymer regions, they quantified a series of geometric metrics such as the thickness and local surface curvature of the polymer patches (Figure 6a). Polymer segregation into patches measures a broad range of both positive and negative values in the local curvature distribution of the patches, as a means to quantify the patch shape. From the quantitative analysis, in this work, both the thickness and local curvature of the polymer patches were higher at the high curvature regions of core Au NPs, such as the vertices of octahedra and the vertices and edges of cubes, indicating that patches were preferentially formed in NP surface regions with high surface curvature during solvent-mediated polymer segregation (Figure 6b,c).
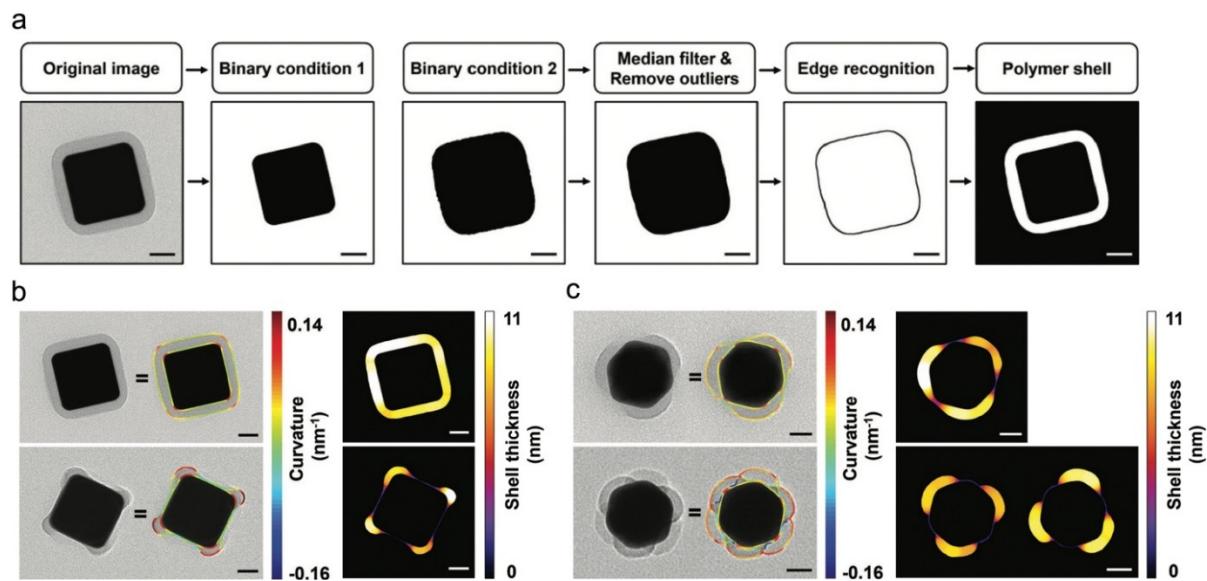
Figure 6. Image analysis of polymer-grafted NPs. (**a**) Image processing workflow for the TEM images of polymer-coated Au NPs. Analysis of local surface curvature and thickness of polymer layers based on TEM images for (**b**) cube and (**c**) octahedron system before (**top**) and after (**bottom**) segregation. The local surface curvature was defined as the inverse of the radius of the best-fitted circle to the local arc. The patch thickness was defined as diameter of the largest circle that incorporates the pixel belonging to the polymer patches. Scale bars: (**a**) 20 nm. Reproduced with permission from ref. [48]. Copyright 2018, Wiley-VCH.

2.5. Site-Selective Ligand Binding onto NPs to Form Patchy NPs

For the strategies discussed in Sections 2.1, 2.2, and 2.4, polymers uniformly adsorb onto the NP surface first and then rely on different mechanisms to either change their configurations to cluster into patches or migrate to form into domains. In this section, we focus on the methods that allow polymers to adsorb in a site-selective manner from the beginning for patchy NP formation.

Site-selective binding of ligands (small molecules or polymers), even in the absence of the microphase separation mechanism discussed in Section 2.3 was predicted to be possible given a generic balance between entropic and enthalpic effects for the ligand molecules. Glotzer and coworkers theoretically demonstrated that ligands packed at different curvature sites on a NP surfaces exhibit different configurational entropy, leading to curvature-dependent site-selective grafting of ligands on NP surfaces [49]. When ligands are tethered to different sites on polyhedral NP surface—faces, edges, and vertices—they exhibit different sizes of free volume, defined as the volume of the Voronoi cell within which they move freely in a self-avoiding random walk. Among these sites, ligands tend to attach to vertices, which exhibit the highest surface curvature, with the greatest entropy gain due to the largest Voronoi cell, compared to those attached to the edges and faces (Figure 7a). Consequently, this preference leads to a heterogenous ligand coating on NPs, which can be exploited for synthesizing patchy NPs.

In efforts translating this theoretical calculation to practical effects, the entropically-favored vertex patches were first demonstrated. For example, Chen and coworkers synthesized tip-patched Au triangular nanoprisms using a hydrophobic ligand (2-NAT) and PS-*b*-PAA block copolymer [50]. Similarly to the studies discussed in Section 2.4, the thiol-terminated ligands bind to the Au NP surface first, and the PS-*b*-PAA adsorbs onto the thiol ligands due to hydrophobic attraction. The difference is that the ligands preferentially bound to the tips of Au nanoprisms from the beginning, which exhibit significantly higher surface curvature than the rest of the prisms, to maximize the entropy gains of ligands. Subsequent adsorption of the PS-*b*-PAA polymers to the hydrophobic ligand-coated sites led to a high yield of tip-patched Au nanoprisms (Figure 7b). The patch coverage was finely controlled by ligand concentration. As the ligand concentration increased under a fixed concentration of NPs, the lateral size of the patches grew larger, leading to a gradual transformation in the patch patterns, from small tip-patches, large tip-patches to T-shaped, and eventually Reuleaux triangular patch shapes (Figure 7c). This increase in patch coverage was attributed to the expansion of ligand islands from the initial adsorption site (tips), which provided more binding sites for polymer strands as the ligand concentration increased.

As a follow-up study, Chen, Glotzer, and coworkers further studied the enthalpic effects. In this 2-NAT and PS-*b*-PAA block copolymer system, the enthalpy, or chain–chain attraction of PS-*b*-PAA is more dominant under certain reaction conditions [51]. It was demonstrated that the reaction temperature governed the symmetricity of patch shapes by controlling n on Au nanoprisms. While symmetric three tip-patches are formed at high

temperature of 110 °C, a gradual decrease in n was observed as the reaction temperature decreased to finally 90 °C, which result in asymmetric one- or two-patchy structures (Figure 7d). A theoretical model based on polymer scaling theory rationalized this temperature-dependence of the patch shapes. This model incorporated both entropic and enthalpic energies resulted from the polymer chain localization on NP surfaces. The Flory-Huggins parameter, χ parameter, which is inversely proportional to temperature, was predicted to exhibit a critical value χ_c for patch patterning. Physically, polymer chain−chain attraction increased with increasing χ parameter. When $\chi > \chi_c$, the chain−chain attractions became strong enough to overcome both competing enthalpic gains associated with chain–solvent interaction and the entropic costs arising from local chain confinement of polymer strands, resulting in asymmetric one- or two-patch structures. When $\chi < \chi_c$, the chain−solvent attraction increases, and the contribution of entropy gains becomes dominant which led to all three tips of Au nanoprisms simultaneously occupied by polymer strands, thereby forming symmetric three-patch structure. This scaling theory-based model effectively explained the temperature dependence of patch formation and provides a thorough understanding of the balance between entropic and enthalpic effects, which governs polymer patterning on NPs.
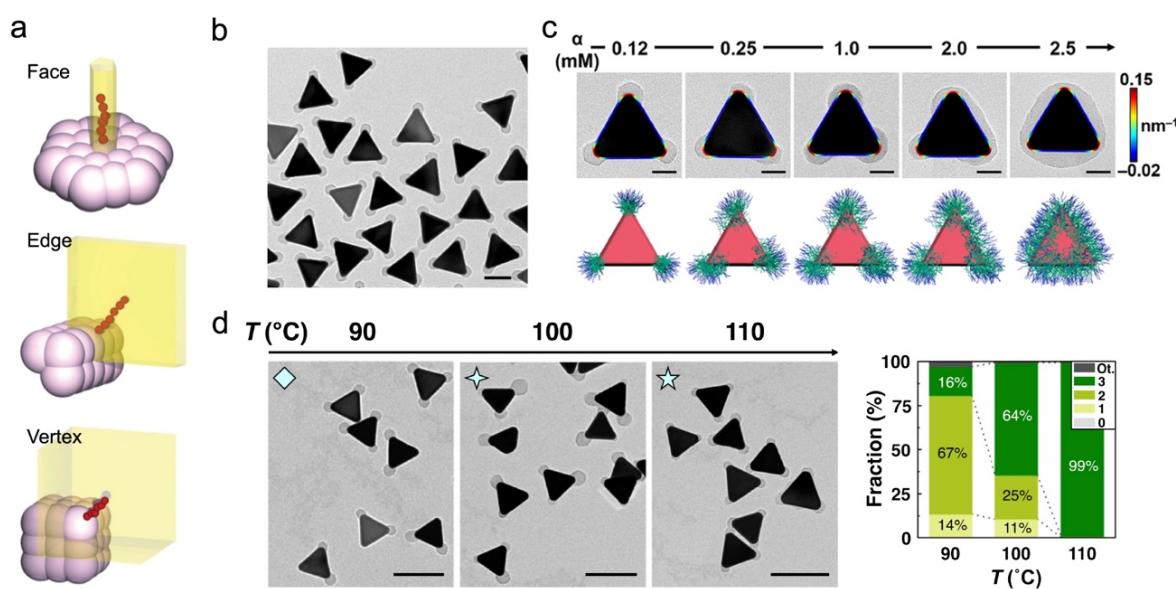

Figure 7. Site-selective ligand grafting for patch formation in NPs. (**a**) Voronoi cells for ligands grafted on the face (**top**), edge (**middle**), and vertex (**bottom**). (**b**) Representative TEM images of symmetric tip-patched Au nanoprisms. (**c**) TEM images and the corresponding schematics of patchy Au nanoprisms synthesized at increasing α (defined as the ratio of ligand molar concentration to optical density of the Au nanoprism suspension at its maximum extinction wavelength). (**d**) TEM images and histograms of patchy Au nanoprisms with the different n, synthesized at varying reaction temperature (α = 50 nM). Scale bars: (**b**) 50 nm, (**c**) 20 nm, and (**d**) 100 nm. (**a**) Reproduced with permission from ref. [49]. Copyright 2012, The Royal Society of Chemistry. (**b,c**) Reproduced with permission from ref. [50]. Copyright 2019, American Chemical Society. (**d**) Reproduced with permission from ref. [51]. Copyright 2022, Springer Nature.

In order to generalize such studies of patch formation, Chen and coworkers further advanced automatic TEM images by involving the machine learning (ML)-based convolutional neural networks to analyze patch shapes on Au nanoprisms [52]. A pixel in the TEM image was classified as a non-overlaying part of a NP (Channel 1), an overlaying part of NPs (Channel 2), and the background (Channel 3) by a trained U-net with three output channels. The three-channel U-Net predicted both the Au core and patches at pixel-wise accuracy as high as 99.5% (Figure 8a). Additionally, based on the shape fingerprints, described as $d(\theta)$ (defined in Figure 8b) of both the Au cores and patches, the patch shapes were classified into six groups using the Gaussian mixture model (GMM) after principal component analysis. The GMM-based classification was carried out based on patch coverage (defined as the angular range θ of the Au core covered by a polymer patch) and the symmetricity of individual patches relative to the Au nanoprism tip (Figure 8c,d). Consequently, the ML-based TEM image analysis statistically demonstrated patch coverage increased with α, which is consistent with their previous work (Figure 8e,f) [50].
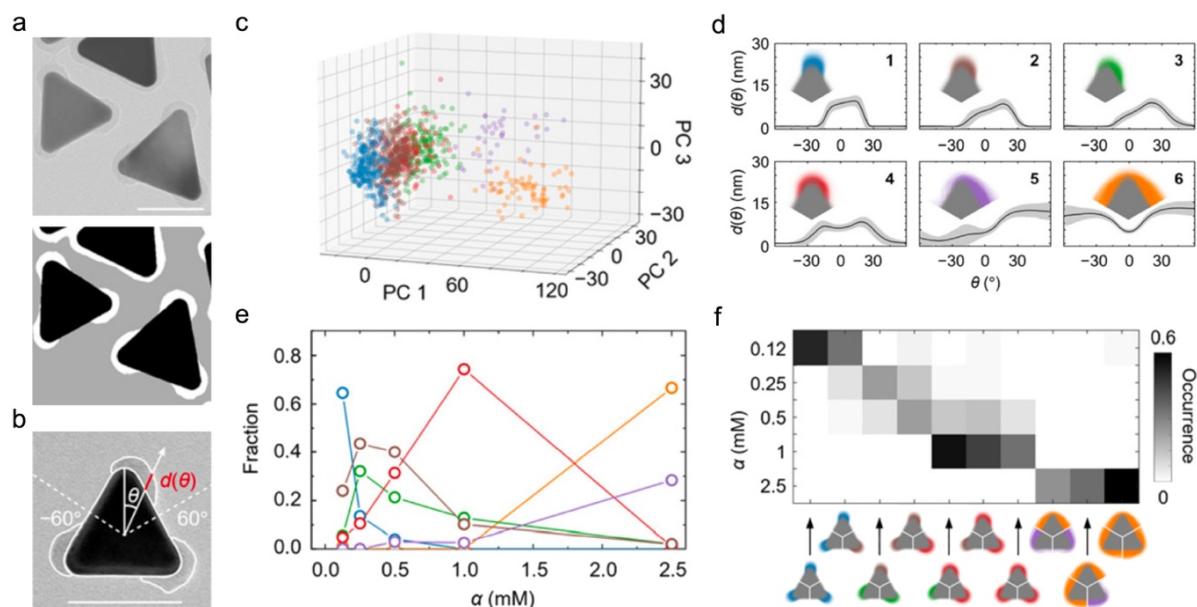
Figure 8. ML-based image analysis of polymer-grafted Au nanoprisms. (**a**) TEM image of tip-patched Au nanoprisms (**top**) and the corresponding predicted image (**bottom**), obtained by a trained three-channel U-Net. The black, white, and gray colors indicate Au core, polymer patch, and the background, respectively. (**b**) TEM image overlaid with shape contours and the shape fingerprint. $d(\theta)$ corresponds to the length of the red segment. (**c**) Shape fingerprints projected onto the first three principal components, with each color denoting a shape group predicted by the GMM. (**d**) Averaged shape fingerprint for each group predicted by GMM. Patch coverage increases from groups 1 to 6. The fingerprints of groups 1, 4, and 6 show symmetric patch distributions around $\theta = 0°$, while those of groups 2, 3, and 5 exhibit asymmetric patch distributions. The colors of patches correspond to those of the data points in (**c**). (**e**) Fractions of each GMM group as a function of α. (**f**) Occurrence of patch combinations within a Au nanoprism at different α. Scale bars: (a,b) 50 nm. Reproduced with permission from ref. [52]. Copyright 2022, The Royal Society of Chemistry.

2.6. Other Synthesis Methods for Patchy NPs

Besides the wet chemistry synthesis methods discussed above, there have been efforts combining top-down microfabrication with wet chemistry methods to synthesize patchy Au NPs. Félidj and coworkers achieved patches on the lithographically deposited Au nanodisks by using plasmon-driven reduction of aryl diazonium salts [53]. Aryl radicals, formed by reducing diazonium salt, covalently bound to the Au NP surface, followed by a successive polymerization of aryl radicals on the grafted layers. This reaction only occurs on the exposed top side of the nanodisks, with the other side in contact with substrate uncoated. The polyaryl patch thickness could be controlled from monolayers to multilayers, up to tens of nanometers, by adjusting the laser wavelength and incident polarization. Importantly, the reaction does not occur uniformly on the exposed side of nanodisk but selectively at regions where the local electric field was enhanced due to the excited multipolar plasmon modes. As a result, the polyaryl layers are most dense at the tips, lateral sides, and the apexes, with slight deposition on the edges of the nanodisks under dipolar, quadrupolar, and sextupolar excitations, respectively (Figure 9a,b). In this example, the substrate for the deposited nanodisks served as physical protection to ensure only one side of the nanodisk is exposed to reactants, and then the plasmonic modes determine the lateral distribution of the patches.

Similarly, other templates can be used to selectively coat Au NPs with polymer patches. For example, templated methods have been used for synthesizing patchy micron-sized particles by applying coating techniques, such as atomic layer deposition to embed the particles on substrates [14–16]. He and coworkers reported a templated method for creating patches on NPs [54]. Citrate-stabilized Au NPs were first adsorbed onto positively charged silica microspheres through electrostatic attraction. The exposed surfaces of NPs were modified with poly(N-isopropylacrylamide) (PNIPAM), followed by dissolution of the microsphere templates, resulting in Janus Au NPs (Figure 9c–e). These templated methods described above can strictly limit the regions where polymer is grafted onto the Au NP surface, ensuring that the original surface properties of the core NPs remain intact. This advantage potentially enables exploitation of the unaltered surface chemical properties of Au, such as its capability to form versatile chemical bonds (e.g., Au–thiol, Au–amine, and Au–catechol bonds) with additional ligands, thereby facilitating the formation of multifunctional patchy Au NPs with different types of polymer patches on surfaces.

Lastly, in situ polymerization of monomers onto Au NPs can be used for the synthesis of polymer patches [55,56]. Xia and coworkers modified the PS precipitation polymerization process by adding Au NPs. When citrate-capped Au NPs were introduced after the onset of PS polymerization, asymmetric Janus Au–PS NPs were formed (Figure 9f). PS bumps initially formed on the Au NP surface through heterogeneous nucleation, followed by polymerization on the "nuclei", which resulted in monodisperse Janus structures (Figure 9g). Interestingly, aggregates of multiple Au NPs were contained in the PS patches when the Au NPs were introduced before the onset of polymerization, while "core-free" structures, as well as Janus NPs, formed when the Au NPs were added 30 min after the polymerization was initiated. This observation indicates that the timing of Au NP addition is critical for determining the NP stability during synthesis, suggesting that PS oligomers formed in the early stage of polymerization and possibly stabilized the Au NPs during the patchy NP formation [55]. Furthermore, it was also demonstrated that various core NPs, such as Pt and Pd NPs, can be utilized for the synthesis of Janus NP [56]. This in situ polymerization method is expected to work for as long as the initially formed oligomers can exhibit sufficient attraction to the core NP surface. Therefore, this method potentially expands libraires of patchy NP compositions for both core NPs and polymer patches by fine tuning the surface chemistry of the core NPs, thereby inducing polymer–NP interactions and creating diverse patchy NPs.
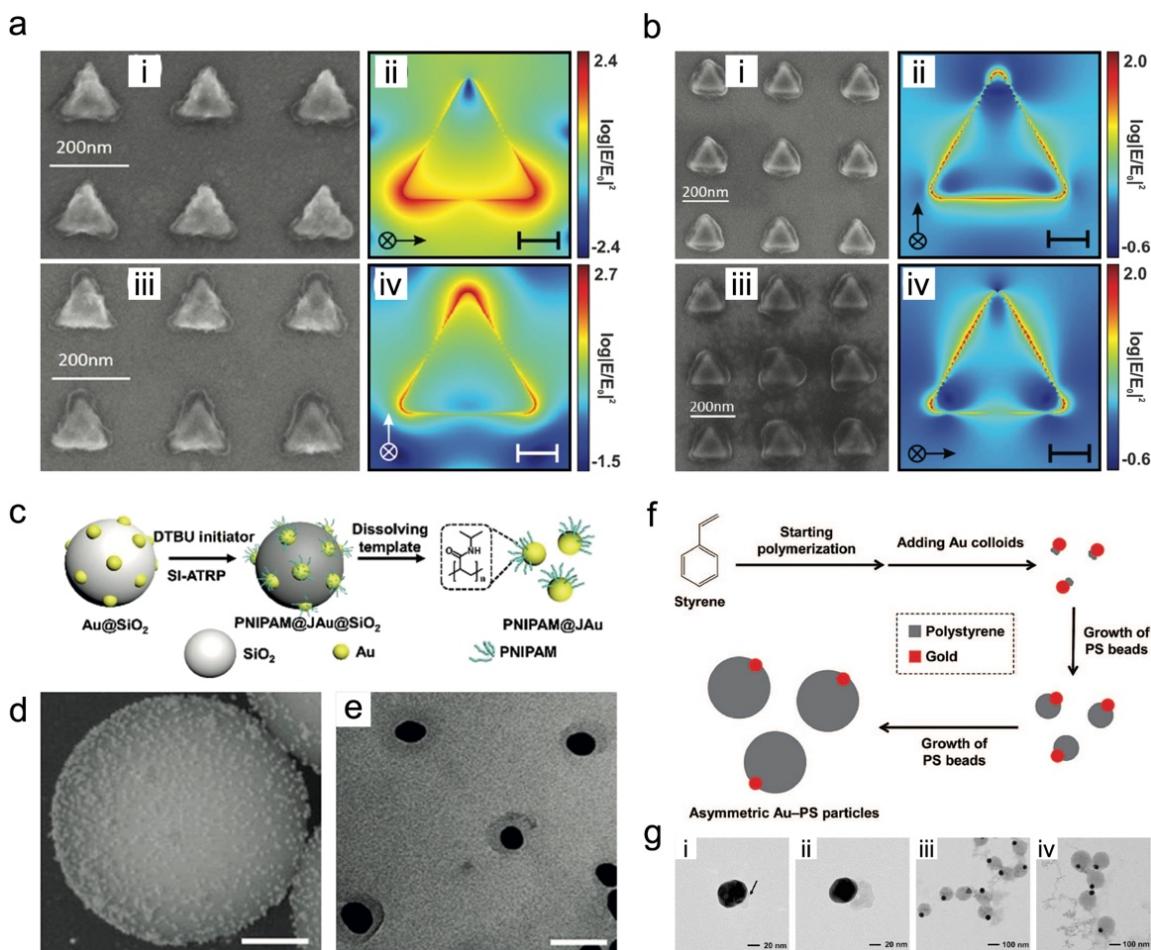

Figure 9. Other methods for the synthesis of patchy Au NPs. (**a**,**b**) SEM images of patchy Au NPs synthesized through a plasmon-induced grafting of polymers with polarization along two different directions (**left**), and the corresponding mapping of the electric field intensity (**right**) under dipolar (**a**) and quadrupolar (**b**) modes. The arrows in the electric field intensity maps indicate the polarization axis. (**c**) Schematic of a templated method for Janus Au NP synthesis. (**d**) SEM image of Au NPs adsorbed on a silica microparticle template. (**e**) TEM image of Janus Au NPs with PNIPAM patches synthesized via a templated method. (**f**) Schematic illustrating the synthesis procedure of Au–PS Janus NPs through the in situ polymerization method. (**g**) TEM images showing the morphology evolution of Au–PS Janus NPs collected at 5 min (black arrow indicates the heterogeneously polymerized PS shell), 10 min, 30 min, and 45 min during synthesis (from left to right). Scale bars: (**a**,**b**) 50 nm, (**d**) 500 nm, and (**e**) 50 nm. (**a**,**b**) Reproduced with permission from ref. [53]. Copyright 2021, The Royal Society of Chemistry. (**c**–**e**) Reproduced with permission from ref. [54]. Copyright 2019, Wiley-VCH. (**f**,**g**) Reproduced with permission from ref. [55]. Copyright 2009, American Chemical Society.

3. Self-Assembly of Patchy NPs

Patchy NPs consist of two types of surfaces—partially exposed core NP surface and polymer patch region—which exhibit different chemical and/or physical properties. This surface heterogeneity of patchy NPs enables the design of complex and programmable assemblies with controlled orientations of building blocks through directional inter-NP interactions. These inter-NP interactions occur in various forms such as van der Waals attraction, electrostatic repulsion, and steric hindrance. This section provides a detailed discussion of diverse strategies for the self-assembly of patchy NPs, categorized into parts based on if the patches are mutually attractive or repulsive. Note that because current synthesis of NPs is not large quantity yet with high uniformity, crystalline assembly of patchy NPs into superlattices has not been achieved yet. The achieved assemblies are limited to small-sized disordered clusters that are composed of fewer than 20 NPs.

3.1. Assembly of Patchy NPs Following Patch−Patch Attractions

Polymer patches on the core NPs can serve as attractive sites, inducing patch−patch attraction for assembly of loosely packed structures. Kumacheva and coworkers first reported a method for assembling tip-patched Au NRs, synthesized using site-selective adsorption of HS-PS ligands to the high curvature ends of Au NRs, by reducing the solvent quality [57]. Solvent quality was intentionally reduced by adding water to create a poor solvent environment for PS blocks. This caused the polymer patches of neighboring Au NRs to connect with each other to minimize the polymer−solvent interfaces. The resulting assembly structures were finely controlled, ranging from rings and chains to side-to-side segregated bundles of chains and spheres, as well as tip-to-tip connected bundles of chains. These structures were determined by solvent types and water fraction, which govern the quality of the solvent mixture. The change in LSPR was observed differently depending on the assembly shape and distance of Au NRs. As the distance between NRs in the end-to-end assembly increased, the longitudinal plasmon mode underwent a significant blue shift due to the decreasing plasmonic coupling. Additionally, variation in the separation between the metal blocks, resulted from controlling the water fraction, also resulted in a shift of the plasmonic band. Following this method, solvent quality-mediated assembly has been applied to various shaped NPs, such as Au NCs, Au NSs, and Ag nanoprisms, leading to diverse loosely packed clusters that cannot be assembled from non-patchy NPs [27].

He and coworkers also demonstrated heat-induced patch−patch attraction for controlled assemblies using dumbbell-like patchy Au NRs synthesized with a polymer ligand mixture (HS-PS) and PS-*b*-PEO [37]. While patchy Au NRs remained stable in solution at room temperature, the dynamics of block copolymers significantly increased at elevated temperatures of 90 °C. At this temperature, polymer solubility is enhanced, resulting in the destabilization of patches on the core Au NR and partial desorption of polymer strands due to weakened hydrophobic interactions between the ligands and polymers. After the desorption of the polymer strands from the Au NR surface, the exposed PS ligands became thermodynamically unfavorable, prompting end-to-end assembly of Au NRs, thereby the formation of chain-like structures to minimize the interfacial area between NR and solvent (Figure 10a). Notably, the formation of end-to-end assemblies between Au NRs was also confirmed by monitoring changes in LSPR. After 1.5 min from the onset of Au NR self-assembly, the UV–vis spectrum exhibited a distinct peak at 805 nm, attributed to plasmonic coupling in short NR chains. As the thermal annealing time increased, the LSPR red-shifted to 830 nm due to the elongation of the chains (Figure 10b). Lastly, since NP−solvent interfacial energy is a key parameter governing the assembly process, the water fraction, which determines solvent quality, also influenced the kinetics of the assembly process (Figure 10c).

When patches are charged, patch−patch attractions can be triggered by complexation of polymer patches and molecular additives. "Bridge" molecules or ions of an opposite charge to the patches can induce self-aggregation between charged polymer patches. For instance, Cu_2^{4+} and Co^{2+} were shown to induce complexation of block copolymer patches on Au NPs containing acrylic acid group, such as P(4VPA) [34] and PAA [38] segments, resulting in assemblies such as elongated chain-like structures (Figure 11a) and clusters (Figure 11b) via patch−patch agglomeration.

Beyond multivalent ions, ionic surfactants can also induce the complexations of charged patches. Chen and coworkers demonstrated complexation of patches by introducing CTAB, a cationic surfactant, into a tip-patched Au nanoprism system, synthesized with thiol-terminated ligands and physisorbed PS-*b*-PAA [51,58]. The patchy Au nanoprisms were suspended in water, with the PAA blocks protruding towards water. The head group of CTAB electrostatically bound to the negatively charged PAA blocks, followed by hydrophobic attractions among the tails, leading to the aggregation of polymeric patches (Figure 11c–f). This CTAB-induced complexation of tip-patchy prisms resulted in diverse assembly structures such as linear, cyclic, and branched chains. The assembled trimer

exhibited symmetric bonding (2.25 eV) and anti-symmetric antibonding (2.29 eV) modes, depending on the excitation energy, due to the plasmonic coupling effect (Figure 11g).
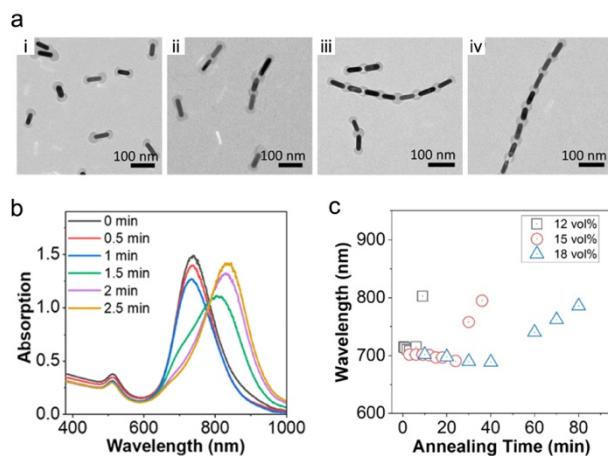

Figure 10. Assembly of patchy Au NPs via patch−patch attractions. (**a**) Representative TEM images of patchy Au NRs at increasing thermal annealing times (from **left** to **right**). (**b**) UV−vis spectra of the self-assemblies at different time points. (**c**) The longitudinal plasmon band of patchy Au NRs during thermal treatment at different water volume fractions as a function of annealing time. Reproduced with permission from ref. [37]. Copyright 2023, American Chemical Society.
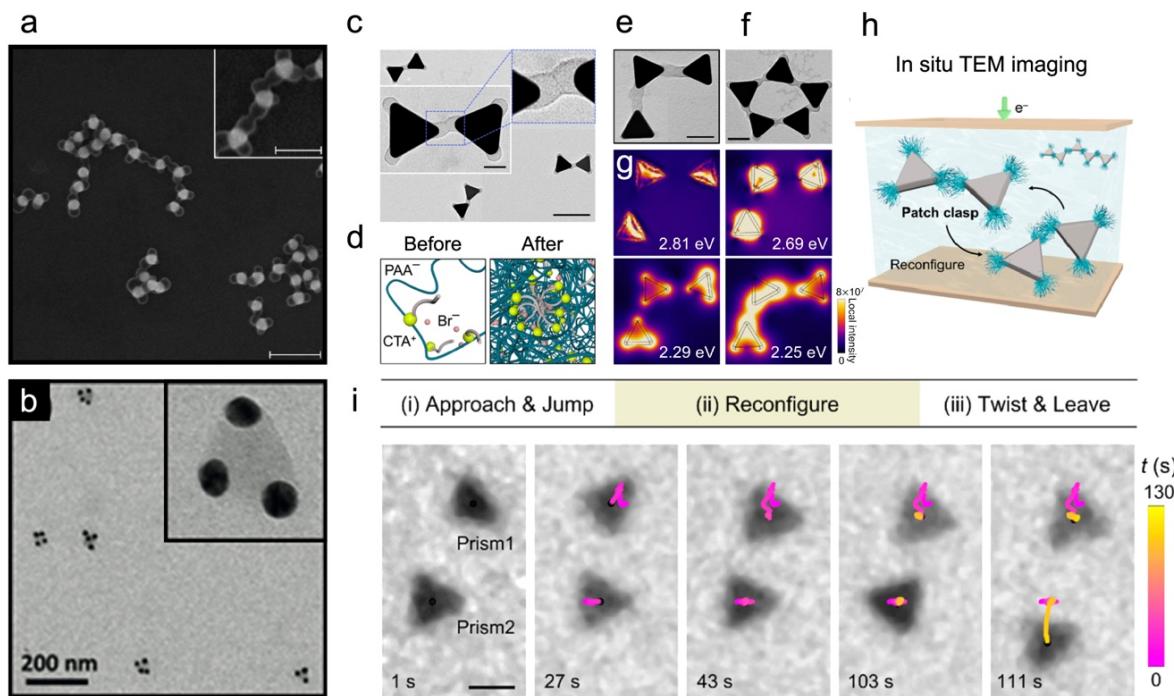

Figure 11. Assembly of patchy Au NPs via patch−patch attractions induced by complexation between polymeric patch and additive moieties. (**a,b**) Self-assembly of patchy Au NPs driven by multivalent cations, forming small clusters and elongated chain-like structures. (**c**) TEM image of patchy Au nanoprism dimers. (**d**) Schematics illustrating CTAB and PAA blocks before (**left**) and after (**right**) complexation. (**e,f**) TEM images of a Au nanoprism trimer (**e**) and multimer (**f**) created through CTAB-induced complexation. (**g**) The spatial electric field distribution maps of the trimer in (**e**) at different excitation energies. (**h**) Schematic illustrating the self-assembly of patchy Au nanoprisms into a dimer in a liquid chamber for in situ TEM imaging. (**i**) Time-lapse liquid-phase TEM images for the assembly and disassembly of patchy Au nanoprisms. Scale bars: (**a**) 200 nm (inset: 100 nm), (**c**) 200 nm (inset: 20 nm), and (**e,f,i**) 50 nm. (**a**) Reproduced with permission from ref. [38]. Copyright 2021, American Chemical Society. (**b**) Reproduced with permission from ref. [34]. Copyright 2019, Wiley-VCH. (**c,d,f,h,i**) Reproduced with permission from ref. [58]. Copyright 2024, American Chemical Society. (**e,g**) Reproduced with permission from ref. [51]. Copyright 2022, Springer Nature.

Such complexation induced self-assembly is often considered as a "soft" bond that is flexible and dynamic. The assembly and disassembly dynamics of the patchy Au nanoprisms discussed above was investigated using liquid-phase TEM in real-time (Figure 11h) at low dose rate to minimize the electron beam damage [58]. At the beginning of patch–patch assembly, patchy Au nanoprisms approached each other by slow crawling, followed by a sudden jump, forming a tip-to-tip assembly. The assembled dimer of the patchy Au nanoprisms then maintained a stable center-to-center distance, indicating a robust longitudinal connection between the patch Au NPs. Meanwhile, each NP exhibited rotational flexibility with a fluctuating tip–tip angle, which was attributed to the dynamic reorganization of polymer chains while maintaining the associations in the linked patches, referred to as the "patch clasping". Finally, when disassembly happened, the NPs twisted against each other, eventually breaking apart into two individual patchy Au nanoprisms (Figure 11i), showing the reversibility of the self-assembly process.

These soft "bridges" linking patchy NPs do not strictly restrict the direction of the bonds in assembly, allowing rotational distortion of the structures without breaking any bonds, and can serve as emerging mechanical metamaterials. Meanwhile, when this patch–patch assembly occurs, complexation of patches proceeds rapidly, not allowing enough time to find the configurations that is thermodynamically most stable, resulting in assembly in cluster-scale consisting of a small number of NPs with low structural crystallinity.

3.2. Assembly Involving Mutually Repulsive Patches

When the patches are repulsive, they can assemble driven by the van der Waals attractions of the core NPs. Chen and coworkers first reported the self-assembly of Janus Au NPs via salt-induced agglomeration, where the electrostatic repulsion between negatively charged PAA blocks of the polymer patches was screened by adding sodium chloride. The weakened repulsion allows the Au NPs to aggregate through van der Waals attraction, preferentially along the uncoated Au surfaces (Figure 12a) [41]. Following this study, Nie and coworkers also utilized salt-induced surface charge screening to assemble other patchy Au NPs with negatively charged patches, leading to petal-like clusters of Janus Au NSs (Figure 12b) [38]. The balance of the electrostatic repulsion of patches and van der Waals attraction between Au has been discussed using the Derjaguin-Landau-Verwey-Overbeek theory [59,60]. The limitation of this method is the relative low level of control in the assembly yield, especially for shape anisotropic NPs where many relative configurations are possible. For example, in the case of tip-patched Au nanoprisms, both star- and slanting diamond-shaped assemblies of tip-patched Au nanoprisms (Figure 12c,d) [50] were formed spontaneously in the same system with very similar levels of free energy.

In addition to ionic additives, solvent variations can also control the surface charge of patchy NPs and induce assembly [36]. He and coworkers synthesized Janus Au NPs with neutral PS-*b*-PEO block copolymers. These NPs were stabilized in water due to both the steric hindrance of polymer patches and the electrostatic repulsion from charges on the polymer-free Au surface originated from CTAB surfactant out of Au NP synthesis. When ethanol was introduced into this Janus Au NP dispersion, selective removal of CTAB was achieved due to its high solubility in ethanol, decreasing the surface charge on Au NPs. This decrease led to the aggregation of patchy Au NPs along the exposed Au surface through Au–Au van der Waals attractions (Figure 12e), while steric patch–patch repulsion was maintained.

Going beyond the generic van der Waals attraction of core NPs, other more specific attractions can be used to counteract with mutually repulsive patches and to induce self-assembly. One of such specific attraction is DNA hybridization. Broadly, Au NPs capped with single-stranded DNAs (ssDNAs) have been studied as building blocks for assemblies since they readily form hydrogen bonds with complementary strands [61–64]. Therefore, the use of ssDNAs, as additional linkers, have also been explored for the assembly of patchy NPs. Lu and coworkers utilized Janus NSs for this DNA hybridization-driven assembly [65]. After synthesizing patches with PS-*b*-PAA on Au NSs, the uncoated Au surfaces were functionalized with thiol-terminated ssDNAs (Figure 12f). These post-functionalized Janus particles were assembled with other NPs (either bare or patchy Au NPs) coated with complementary ssDNAs (Figure 12g,h), or linker strands consisting of the complementary sequence (Figure 12i). In addition to NSs, differently shaped patchy NPs, such as Au NRs and nanoprisms, were also utilized for this complementary DNA-induced assembly, leading to a wide library of assemblies, ranging from small clusters to large chain-like structures [42].
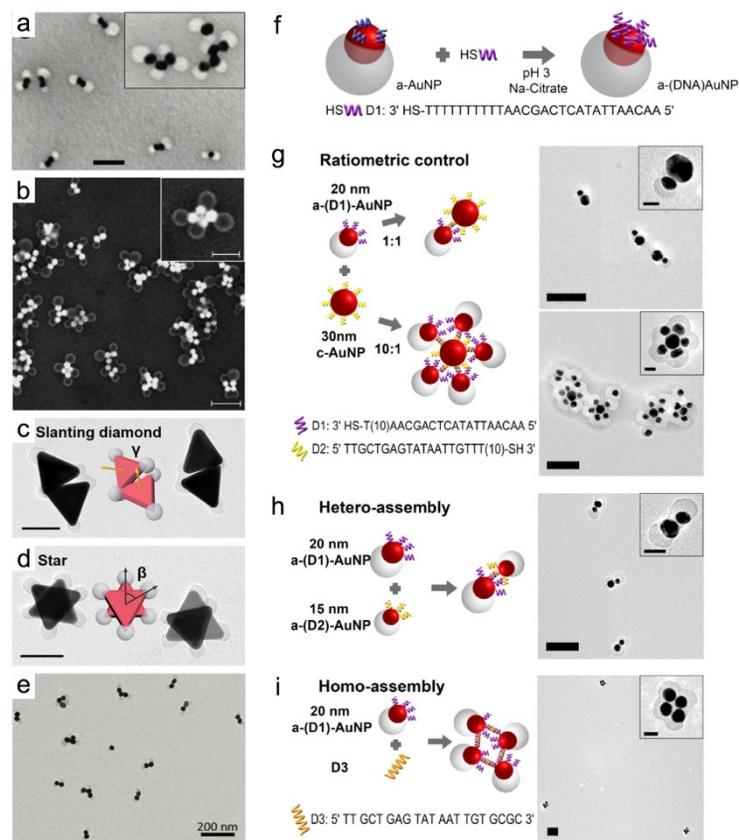
Figure 12. Assembly of patchy Au NPs in the presence of mutually repulsive patches. (**a**,**b**) TEM and SEM images of Janus Au NP assemblies induced by screening the surface charge of the patches using sodium chloride. (**c**,**d**) TEM and SEM images of self-assemblies of patchy Au nanoprisms exhibiting slanting diamond- (**c**) and star-like (**d**) shapes. (**e**) TEM images of Janus Au NP clusters assembled upon the addition of ethanol. (**f**) Schematic illustrating the functionalization of Janus Au NPs with ssDNAs. (**g**) Schematic and TEM images of assemblies of Janus Au NSs and bare NPs functionalized with complimentary ssDNAs. The structures of clusters can be controlled by the ratios of the two building blocks. (**h**,**i**) Schematic and TEM images of hetero-assembly between differently sized Janus Au NSs (**h**), and homo-assembly of Janus Au NSs using linker ssDNA strands (**i**). Scale bars: (**a**) 100 nm, (**b**) 200 nm (inset: 100 nm), (**c**,**d**) 50 nm, and (**g–i**) 100 nm (insets: 25 nm). (**a**) Reproduced with permission from ref. [41]. Copyright 2008, American Chemical Society. (**b**) Reproduced with permission from ref. [38]. Copyright 2021, American Chemical Society. (**c**,**d**) Reproduced with permission from ref. [50]. Copyright 2019, American Chemical Society. (**e**) Reproduced with permission from ref. [36]. Copyright 2022, The Royal Society of Chemistry. (**f–i**) Reproduced with permission from ref. [65]. Copyright 2013, American Chemical Society.

4. Applications of Patchy Plasmonic NPs

Polymer-patched plasmonic NPs are expected to be useful in various application fields due to their spatially heterogeneous and hybrid chemical, physical, and geometrical surface features. Thus efforts on applications have been emerging despite the short history of research on patchy NPs. This section highlights two applications of patchy NPs: one is the use of templates for overgrowth of complex NPs, and the other is self-propelling nanomotors.

4.1. Templates for Overgrowth

The surface heterogeneity of patchy NPs imparts different chemical reactivities for polymer patches and uncoated NP surfaces, enabling their use as unique templates for subsequent reaction via seed-mediated growth. Wang and coworkers demonstrated the site-selective deposition of metals on the uncoated Au surface of patchy Au NPs as the PS-*b*-PAA polymer patches blocked the diffusion of the reactants into contact with the core NPs [46]. A metal precursor and a mild reducing reagent (hydroquinone) were introduced into the patchy Au NP dispersion, followed by overnight overgrowth to facilitate further deposition. This process resulted in two distinct domains— overgrown metal layer and polymer patch regions—on the core Au NP surfaces. The deposition on patchy Au NPs was effective regardless of the polymer patterns and core NP shapes including rods, bipyramids, and triangular prims (Figure 13a). Furthermore, a multi-step overgrowth reaction was also demonstrated. After the initial overgrowth of Pd on both ends of patchy Au NRs, with a polymer patch in the middle, additional heating-induced

transformation was performed, thereby leading to further contraction of the polymer patches. This process created small gaps between Pd (at both ends) and polymer patch (in the middle), where additional Ag can be selectively deposited. Through this multi-step metal deposition, Au NRs with three distinct surface domains—Pd, Ag, and polymer patch—were synthesized (Figure 13b–d). It should be noted that these new metallic domains can be also used for further surface functionalization, which can be easily carried out using sulfide reagents. The applicability of patchy Au NP as templates was further demonstrated through the overgrowth of silica domains using silane coupling reagents (tetraethyl orthosilicate) beyond metals (Figure 13e) [47], and the patchy NP assemblies beyond discrete NPs (Figure 13f,g) [37].

It was also demonstrated that multi-component plasmonic NPs can be synthesized by selectively removing polymer patches from patchy NPs with overgrown domains. Xia and coworkers first synthesized Au–PS Janus NPs through the in situ polymerization method (discussed in Section 2.6), followed by the deposition of Ag onto the Au NPs [66]. The PS patches were then selectively removed using organic solution (tetrahydrofuran containing PVP and ethanol), resulting in Au–Ag Janus NPs (Figure 13h–j). Similarly, since different metallic compositions (Pd and Pt) can be utilized for overgrowth on Au–PS Janus NPs, similar Au–Pd (Figure 13k,l) and Au–Pt (Figure 13m,n) Janus NPs were also synthesized by selective removal of PS patches. Lastly, asymmetric, bowl-like NPs were also achieved by etching of polymer patches from the Janus Au NCs with overgrown metal (Au, Ag, and Pd) domains (Figure 13o) [67].
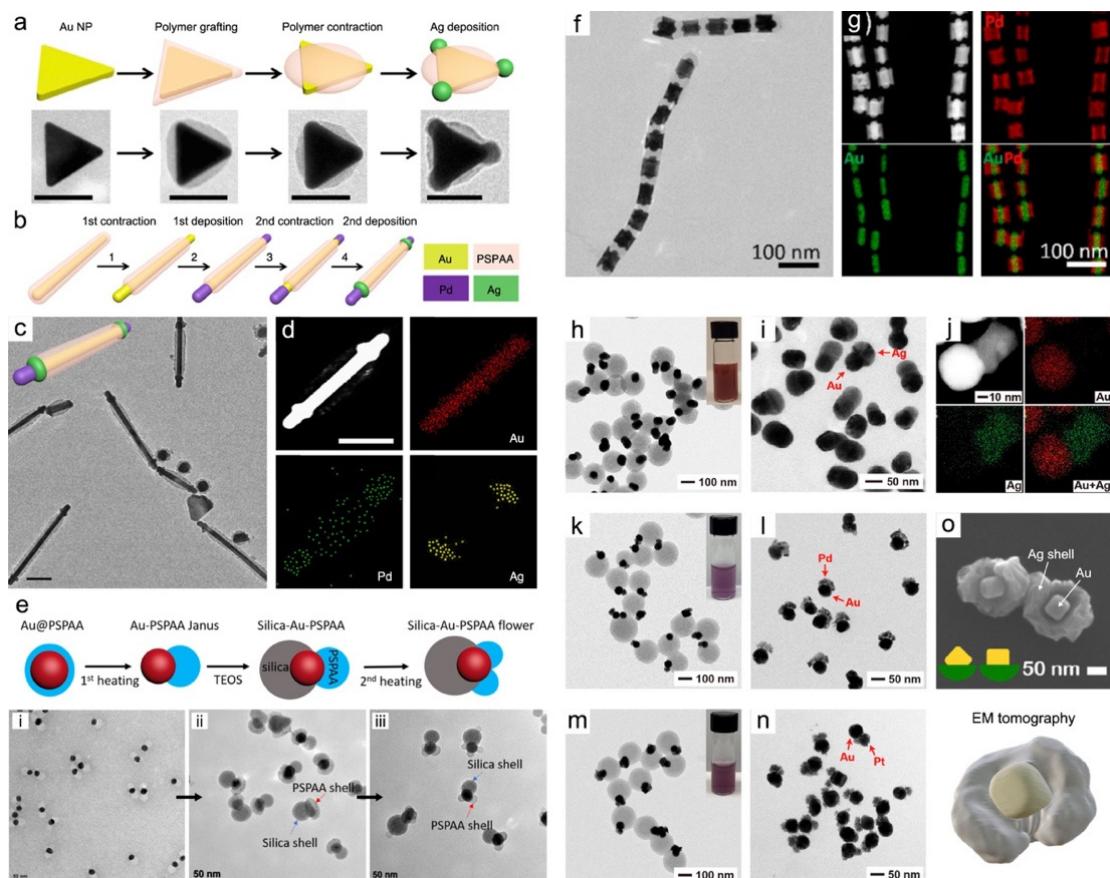

Figure 13. Patchy Au NPs as templates for overgrowth. (**a**) Schematics and TEM images illustrating the overgrowth of Ag on PS-*b*-PAA patchy Au nanoprisms. (**b**–**d**) Schematics (**b**), TEM image (**c**), and energy dispersive X-ray (EDX) mapping (**d**) of patchy Au NRs subsequently deposited with Pd and Ag via multi-step overgrowth. (**e**) Schematics and TEM images of silica-overgrown Janus Au NPs. (**f**) TEM and (**g**) EDX mapping of chain-like assemblies of patchy Au NRs after Pd-overgrowth. (**h**) TEM images of Au−PS Janus NPs after Ag overgrowth. (**i**) TEM and (**j**) EDX mapping of Au−Ag Janus NPs after selective removal of PS patch. (**k,l**) TEM images of Pd-overgrown Au−PS Janus NPs before (**k**) and after (**l**) selective removal of PS patch. (**m,n**) TEM images of Pt-overgrown Au−PS Janus NPs before (**m**) and after (**n**) selective removal of PS patch. The top-right insets in (**h**), (**k**), and (**m**) show Au−PS Janus NP solutions after metal overgrowth. (**o**) SEM image (top) and EM tomography (bottom) of Au−Ag bowl-like NPs after selective removal of PS-*b*-PAA patch. Scale bars: (**a**) 50 nm and (**c,d**) 100 nm. (**a**–**d**) Reproduced with permission from ref. [46]. Copyright 2018, Springer Nature. (**e**) Reproduced with permission from ref. [47]. Copyright 2019, American Chemical Society. (**f,g**) Reproduced with permission from

Furthermore, Nie and coworkers also reported overgrowth of additional composition on patchy Au NPs [68]. The end-grafted patchy Au NRs were first synthesized with HS-PS, based on the high curvature preference of ligand grafting. Then, end-to-end self-assembly was induced by the reducing solvent quality, followed by the introduction of various precursors along with a mild reducing reagent (L-ascorbic acid), which resulted in the overgrowth of different components on the exposed Au surfaces (Figure 14a,b). This overgrown chain-like structure can be dissociated by increasing the solvent quality again, leading to individual coaxial NPs with multiple domains—Au surfaces and overgrown shells. The thickness of the overgrown shell was finely tuned by controlling the amount of precursor, thereby enabling coaxial multi-domain NPs with controlled shell thickness (Figure 14c). Importantly, various compositions can be utilized to form the overgrown shell, including not only pure metals (Pt and Ag) but also metal oxides (Cu_2O and CeO_2) (Figure 14d,e).
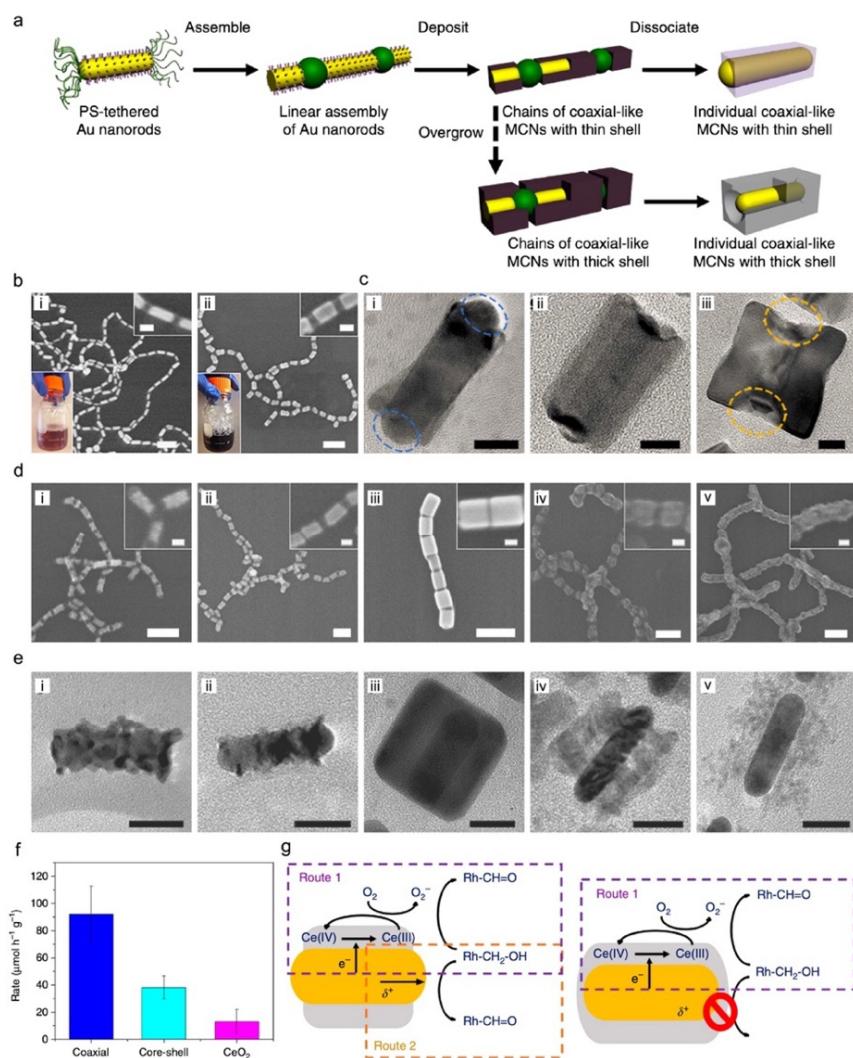

Figure 14. Patchy Au NRs as templates for overgrowth of various components and their catalytic applications. (**a**) Schematic illustrating the overgrowth on chain-like assemblies of patchy Au NRs and their subsequent dissociation into individual coaxial multi-domain NPs. (**b**) High- and low-magnification SEM images of patchy Au NR chains before (**left**) and after (**right**) Pd overgrowth. The bottom-left insets show product solutions with a visible color change upon Pd deposition. (**c**) High-resolution TEM images of individual coaxial multidomain NPs after the dissociation of Pd-overgrown chain-like patchy NR assemblies, showing increase in shell thickness (from **left** to **right**). Blue and yellow circles indicate exposed Au NR and cavities at the tips, respectively. (**d**) SEM and (**e**) high-resolution TEM images of chain-like patchy Au NR assemblies after overgrowth of Pt, Pt/Ni, Ag, Cu_2O, and CeO_2 (from **left** to **right**). (**f**) Rate of benzaldehyde generation for coaxial multi-domain and core–shell of Au–CeO_2, as well as pure CeO_2 NPs. (**g**) Schematics illustrating the proposed photo-oxidation mechanisms for coaxial multi-

domain (**left**) and core–shell (**right**) Au–CeO$_2$. Scale bars: (**b**) 100 nm (insets: 20 nm), (**c**) 10 nm, (**d**) 100 nm (insets: 20 nm), (**e**) 20 nm. Reproduced with permission from ref. [68]. Copyright 2016, Springer Nature.

These individual multi-domain NPs can be used for photocatalysis. The Au–CeO$_2$ coaxial multi-domain NPs exhibited effective photo-oxidization ability of transforming benzyl alcohol to benzaldehyde. Compared to core–shell Au–CeO$_2$ structure and pure CeO$_2$ NPs, the coaxial multi-domain NPs effectively catalyzed this benzyl alcohol transformation (Figure 14f). This improved catalytic effect can be attributed to the efficient utilization of photogenerated charge carriers (hot electrons and holes), facilitated by the exposure of CeO$_2$ shells and Au cores. When using coaxial multi-domain NPs, two reaction pathways can contribute to benzaldehyde generation. First, photogenerated hot electrons are injected from Au core to CeO$_2$, which reduces Ce(IV) to Ce(III). The Ce(III) species react with dissolved oxygen in solution and generate superoxides, which oxidize benzyl alcohol. Second, positive charges accumulated on Au cores can directly oxidize benzyl alcohol on the exposed Au NR tips, while the core–shell can exploit the first pathway only due to the absence of the exposed Au surfaces (Figure 14g). Thus, through the synergistic effect of these two pathways, the coaxial multi-domain NPs effectively oxidized benzyl alcohol, demonstrating the improved catalytic performance.

4.2. Self-Propelling Nanomotors

Plasmonic NPs with a symmetry-broken shapes can also exhibit self-propulsion capability as they have site-dependent reactivity to surrounding chemical reagents [21]. He and coworkers demonstrated the use of Janus Au NPs, synthesized by a templated method (discussed in Section 2.6) for self-propulsion. Glucose oxidase was covalently bound to the exposed Au surface of Janus Au NPs. This chemical enzyme enabled the reduction of glucose in solution, creating local gradients of glucose, gluconic acid, and H$_2$O$_2$ across the NP, which can drive self-propulsion (Figure 15a) [54]. The chemotactic behavior of the symmetry-broken Janus Au NPs was investigated in microfluidic channels with concentration gradient of glucose fuel (Figure 15b). The Janus Au NPs in the reservoir with a low glucose concentration readily moved toward the high-glucose concentration region over time (Figure 15c,d), which indicates their self-propulsion capability.
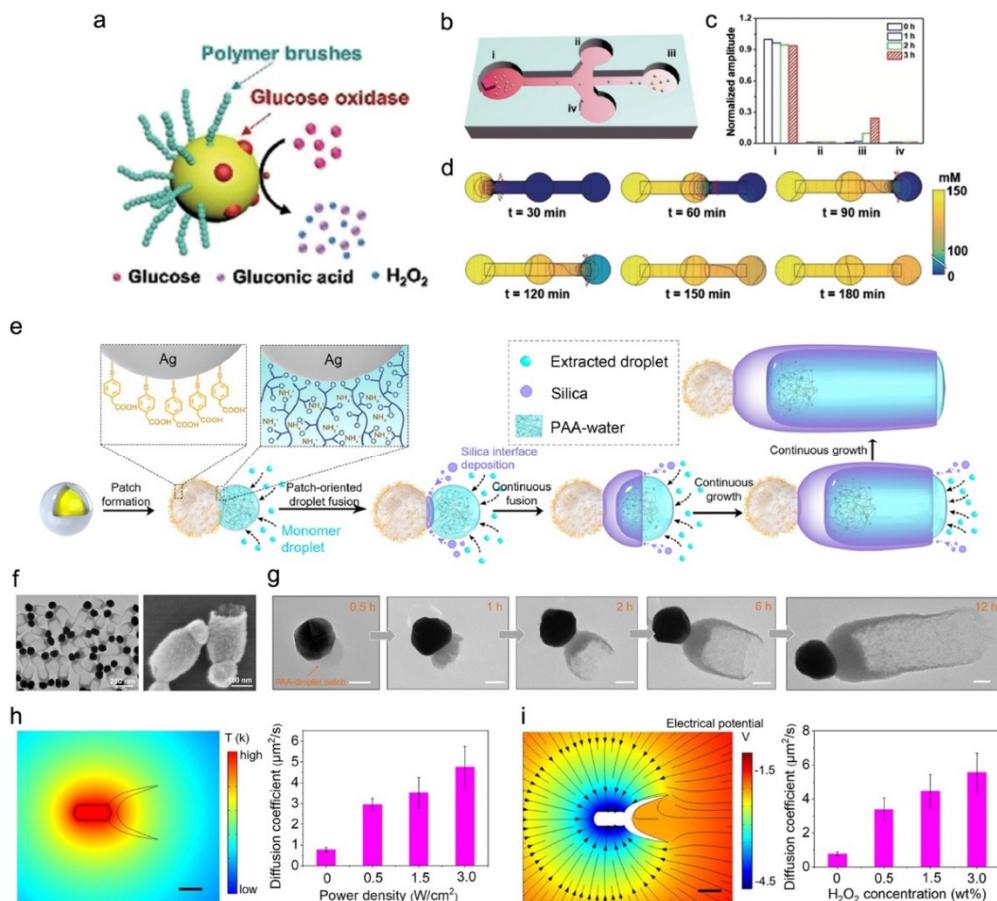

Figure 15. Patchy plasmonic NPs as self-propelling nanomotors. (**a**) Schematic of the motion of glucose oxidase-decorated Janus Au NSs in glucose solutions. (**b**) Schematic of the chemotaxis of the Janus Au NPs towards in a

microfluidic channel with a glucose concentration gradient. After introducing Janus Au NPs into the left reservoir (i), a piece of agarose gel containing glucose was placed in the right reservoir (iii) to make a horizontal glucose concentration gradient. (**c**) Absorbance changes of Janus Au NPs at different time points after the initiation of self-propelling motion. (**d**) Computational simulation showing the diffusion profile of glucose in the microfluidic channel at different time intervals. (**e**) Schematic illustrating the formation of Janus Au@Ag core−shell NPs through directional growth of a hollow silica shell, along with TEM (**left**) and SEM (**right**) images of resulting Janus Au@Ag NPs. (**g**) TEM images showing the morphology evolution of Janus Au@Ag NPs collected at different time points during the synthesis. (**h**) Theoretically calculated steady-state temperature distribution around a Janus Au@Ag NR under 3 W/cm^2 NIR irradiation (**left**), and apparent diffusion coefficients under different laser power densities (**right**). (**i**) Theoretical calculation of the electric potential (color-coded) distribution and electric field (black arrows) around a Janus Au@Ag NR (**left**), and apparent diffusion coefficients at different H$_2$O$_2$ concentrations (**right**). Scale bars: (**g**) 50 nm and (**h,i**) 100 nm. (**a–d**) Reproduced with permission from ref. [54]. Copyright 2019, Wiley-VCH. (**e–i**) Reproduced with permission from ref. [69]. Copyright 2022, American Chemical Society.

Lastly, beyond polymer-patched NPs, Janus NPs with hollow silica patches were also utilized for self-propelling nanomotors. Kong and coworkers synthesized silica patches on Au-core and Ag-shell (Au@Ag) plasmonic core−shell NPs by simultaneously growing a silica shell (Figure 15e–g) [69]. These Au@Ag NPs with structural asymmetry enabled self-propulsion through a dual-mode response to both near-infrared (NIR) irradiation, which generated heat due to photothermal effect, and the formation of H$_2$O$_2$, resulting from the Ag shell. Theoretically computed temperature distributions of the Janus Au@Ag NRs under NIR irradiation showed that heat was concentrated in the exposed Au@Ag region, creating a temperature gradient between two ends. This gradient generated thermo-osmotic flow along the outer surface of the Janus Au@Ag NRs, driving the fluid toward the hotter region and thereby propelling the patchy NRs in the direction of the silica patches via self-thermophoresis (Figure 15h). Furthermore, in the presence of H$_2$O$_2$ in solution, the outmost Ag shell either catalyzed its decomposition into water and oxygen or reacted directly with it, producing HOO$^-$ and Ag$^+$ ions. Due to the significant difference in diffusivity between two ions, an inward electric field formed to maintain charge neutrality in the bulk, leading to self-diffusiophoresis-based propulsion of patchy NRs (Figure 15i). This dual-mode response of patchy Au@Ag NRs enabled their effective use as self-propelling nanomotors. Therefore, the heterogeneous surface chemistry and structural characteristic of patchy NPs make them promising candidates for nanomotors applications, with potential uses in various fields such as targeted delivery and catalysis.

5. Conclusions and Outlook

Patchy plasmonic NPs have attracted interest due to their unique chemical, physical, and geometrical surface heterogeneities, which are expected to be utilized for creating assembled structure as well as diverse practical usages. In this review, we highlight progress in the synthesis and self-assembly strategies of polymer-patched plasmonic NPs and their applications. There is still considerable room for the improvements and innovation in this area.

First, although significant efforts have been made to control the polymer patterns on core NPs, the shape controllability of patchy NPs remains limited. As discussed, while synthesis strategies can be categorized differently based on their underlying mechanism, the positions of polymer patches are mostly similar, since they are governed by only a few parameters, such as local surface curvature, across NP shapes. For example, when diverse NP with different morphologies, such as rods, cubes, triangular prism, were used, high-curvature preference of patch formation is mostly effective regardless of the NP type, resulting in high-curvature region-coated patchy NPs. Even in the case of symmetric spherical NPs, the controllability of the patch configurations, such as shape and number, remained limited. The choice of polymers for patch formation has been limited to those containing PS blocks, likely owing to their hydrophobic and crosslinking properties favoring the patch formation and their chemical and thermal stability. As the hydrophobic ligands spontaneously formed domains based on their chemical properties, this dependency of the ligand within a few candidates restricts the shape diversity of patchy NPs, thereby constraining the range of their assemblies and applications.

Second, current efforts in synthesizing patchy NPs are primarily focused on the Au NP systems utilizing Au−thiol bonds. However, NPs with different compositions exhibit distinct characteristics, such as magnetism (Fe$_2$O$_3$ and Fe$_3$O$_4$) [4,70], catalytic activity (Pd, Pt, and Cu) [1–3], quantum emission (CdSe/CdS) [71], energy storage (MnO$_2$) [72]. These diverse chemical compositions enable different types of bonding with various end-grafted ligands containing functional groups such as thiol [73,74], amine [75], and catechol [76]. Consequently, there is potentially huge opportunity for researchers to facilitate surface coatings on these other core NP materials.

The variations of the core NP composition can also allow the fabrication of multifunctional assemblies through the clustering of two different patchy NPs can further expand their potential applications by synergistic effects.

Third, current studies in the application of patchy NPs have primarily focused on the single NP level. However, self-assembled plasmonic NPs can exhibit distinct optical properties due to the plasmon coupling effect, which depends on inter-NP distances. These newly emerging optical properties of assembled plasmonic NPs can be utilized for potential applications in catalysis and sensing. Polymer patches on NPs can govern the assembly behavior of patchy NPs by balancing various interactions such as van der Waals attraction, electrostatic repulsion, and steric hindrance, thereby forming unique assembled structures with controlled inter-NP gaps. Therefore, studying the unique properties of patchy NP assemblies, beyond those of single NPs, enables the expansion of their potential applications.

Last, the current demonstrations of self-assembled structures of patchy NPs are mostly at the cluster level, consisting of only a few numbers of building blocks. The patchy NPs provide directional and site-specific binding with each other due to additional interactions such as electrostatic forces and steric hindrance, beyond van der Waals attractions, which arise from the surface patches. Therefore, the assembly patterns of patchy NPs, when achieved in large-scale assemblies are expected to differ from those of the bare NPs. However, current strategies for creating assemblies are still in early stage. Therefore, developing an advanced synthesis method for patchy NPs with novel surface capping ligands, along with high uniformity and synthesis yields, can be a key focus for achieving large-scale assembled structure with unique packing geometries. Furthermore, there have been significant efforts in computational ways in designing and optimizing synthesis conditions for unique shapes of plasmonic NPs and predicting their assembly structures. Therefore, in addition to experimental approaches, computational tools can be utilized to establish design rules for the synthesis and make quantitative prediction for patchy NPs based various principles. By combining these computational methods with experiments, it is anticipated that novel methods for synthesizing new patchy NPs with high shape controllability can be achieved, leading to promising candidates for further large-scale self-assemblies with unique lattices. Consequently, these advancements will broaden the applications fields of patchy NPs such as optical and mechanical metamaterials.

References

1. Dong, C.; Lian, C.; Hu, S.; Deng, Z.; Gong, J.; Li, M.; Liu, H.; Xing, M.; Zhang, J. Size-dependent activity and selectivity of carbon dioxide photocatalytic reduction over platinum nanoparticles. *Nat. Commun.* **2018**, *9*, 1252.

2. Lyu, Z.; Shang, Y.; Xia, Y. Shape-controlled synthesis of copper nanocrystals for plasmonic, biomedical, and electrocatalytic applications. *Acc. Mater. Res.* **2022**, *3*, 1137–1148.

3. Miller, M.A.; Askevold, B.; Mikula, H.; Kohler, R.H.; Pirovich, D.; Weissleder, R. Nano-palladium is a cellular catalyst for in vivo chemistry. *Nat. Commun.* **2017**, *8*, 15906.

4. Park, J.; An, K.; Hwang, Y.; Park, J.-G.; Noh, H.-J.; Kim, J.-Y.; Park, J.-H.; Hwang, N.-M.; Hyeon, T. Ultra-large-scale syntheses of monodisperse nanocrystals. *Nat. Mater.* **2004**, *3*, 891–895.

5. Murray, W.A.; Barnes, W.L. Plasmonic materials. *Adv. Mater.* **2007**, *19*, 3771–3782.

6. Zheng, J.; Cheng, X.; Zhang, H.; Bai, X.; Ai, R.; Shao, L.; Wang, J. Gold nanorods: The most versatile plasmonic nanoparticles. *Chem. Rev.* **2021**, *121*, 13342–13453.

7. Lee, H.-E.; Yang, K.D.; Yoon, S.M.; Ahn, H.-Y.; Lee, Y.Y.; Chang, H.; Jeong, D.H.; Lee, Y.-S.; Kim, M.Y.; Nam, K.T. Concave rhombic dodecahedral Au nanocatalyst with multiple high-index facets for CO_2 reduction. *ACS Nano* **2015**, *9*, 8384–8393.

8. Hang, Y.; Wang, A.; Wu, N. Plasmonic silver and gold nanoparticles: Shape-and structure-modulated plasmonic functionality for point-of-caring sensing, bio-imaging and medical therapy. *Chem. Soc. Rev.* **2024**, *53*, 2932–2971.

9. Dreaden, E.C.; Alkilany, A.M.; Huang, X.; Murphy, C.J.; El-Sayed, M.A. The golden age: Gold nanoparticles for biomedicine. *Chem. Soc. Rev.* **2012**, *41*, 2740–2779.

10. García-Lojo, D.; Núñez-Sánchez, S.; Gómez-Graña, S.; Grzelczak, M.; Pastoriza-Santos, I.; Pérez-Juste, J.; Liz-Marzán, L.M. Plasmonic supercrystals. *Acc. Chem. Res.* **2019**, *52*, 1855–1864.

11. Sönnichsen, C.; Reinhard, B.M.; Liphardt, J.; Alivisatos, A.P. A molecular ruler based on plasmon coupling of single gold and silver nanoparticles. *Nat. Biotechnol.* **2005**, *23*, 741–745.

12. Tabor, C.; Murali, R.; Mahmoud, M.; El-Sayed, M.A. On the use of plasmonic nanoparticle pairs as a plasmon ruler: The dependence of the near-field dipole plasmon coupling on nanoparticle size and shape. *J. Phys. Chem. A* **2009**, *113*, 1946–1953.

13. Kim, J.; Ou, Z.; Jones, M.R.; Song, X.; Chen, Q. Imaging the polymerization of multivalent nanoparticles in solution. *Nat. Commun.* **2017**, *8*, 761.

14. Wittmeier, A.; Leeth Holterhoff, A.; Johnson, J.; Gibbs, J.G. Rotational analysis of spherical, optically anisotropic janus particles by dynamic microscopy. *Langmuir* **2015**, *31*, 10402–10410.

15. Han, M.; Yildiz, E.; Bozuyuk, U.; Aydin, A.; Yu, Y.; Bhargava, A.; Karaz, S.; Sitti, M. Janus microparticles-based targeted and spatially-controlled piezoelectric neural stimulation via low-intensity focused ultrasound. *Nat. Commun.* **2024**, *15*, 2013.

16. Chen, Q.; Bae, S.C.; Granick, S. Directed self-assembly of a colloidal kagome lattice. *Nature* **2011**, *469*, 381–384.

17. Wang, Y.; Hollingsworth, A.D.; Yang, S.K.; Patel, S.; Pine, D.J.; Weck, M. Patchy particle self-assembly via metal coordination. *J. Am. Chem. Soc.* **2013**, *135*, 14064–14067.

18. Garbuzenko, O.B.; Winkler, J.; Tomassone, M.S.; Minko, T. Biodegradable Janus nanoparticles for local pulmonary delivery of hydrophilic and hydrophobic molecules to the lungs. *Langmuir* **2014**, *30*, 12941–12949.

19. Luong, H.M.; Pham, M.T.; Guin, T.; Madhogaria, R.P.; Phan, M.-H.; Larsen, G.K.; Nguyen, T.D. Sub-second and ppm-level optical sensing of hydrogen using templated control of nano-hydride geometry and composition. *Nat. Commun.* **2021**, *12*, 2414.

20. Archer, R.J.; Parnell, A.J.; Campbell, A.I.; Howse, J.R.; Ebbens, S.J. A Pickering emulsion route to swimming active Janus colloids. *Adv. Sci.* **2018**, *5*, 1700528.

21. Lyu, Z.; Yao, L.; Wang, Z.; Qian, C.; Wang, Z.; Li, J.; Liu, C.; Wang, Y.; Chen, Q. Nanoscopic imaging of self-propelled ultrasmall catalytic nanomotors. *ACS Nano* **2024**, *18*, 14231–14243.

22. Wang, X.; Liu, B. Molecular alignment-induced chemically patchy uniaxial nanoparticles and their applications in anti-counterfeiting and self-assembled superstructures. *Angew. Chem. Int. Ed.* **2023**, *62*, e202218399.

23. Cao, Q.; Han, S.-J.; Tersoff, J.; Franklin, A.D.; Zhu, Y.; Zhang, Z.; Tulevski, G.S.; Tang, J.; Haensch, W. End-bonded contacts for carbon nanotube transistors with low, size-independent resistance. *Science* **2015**, *350*, 68–72.

24. Qin, D.; Xia, Y.; Whitesides, G.M. Soft lithography for micro-and nanoscale patterning. *Nat. Protoc.* **2010**, *5*, 491–502.

25. Suh, H.S.; Kim, D.H.; Moni, P.; Xiong, S.; Ocola, L.E.; Zaluzec, N.J.; Gleason, K.K.; Nealey, P.F. Sub-10-nm patterning via directed self-assembly of block copolymer films with a vapour-phase deposited topcoat. *Nat. Nanotechnol.* **2017**, *12*, 575–581.

26. De Gennes, P. *Scaling Concepts in Polymer Physics*; Cornell University Press: Ithaca, NY, USA, 1979.

27. Choueiri, R.M.; Galati, E.; Thérien-Aubin, H.; Klinkova, A.; Larin, E.M.; Querejeta-Fernández, A.; Han, L.; Xin, H.L.; Gang, O.; Zhulina, E.B.; et al. Surface patterning of nanoparticles with polymer patches. *Nature* **2016**, *538*, 79–83.

28. Galati, E.; Tao, H.; Tebbe, M.; Ansari, R.; Rubinstein, M.; Zhulina, E.B.; Kumacheva, E. Helicoidal patterning of nanorods with polymer ligands. *Angew. Chem. Int. Ed.* **2019**, *58*, 3123–3127.

29. Galati, E.; Tebbe, M.; Querejeta-Fernández, A.; Xin, H.L.; Gang, O.; Zhulina, E.B.; Kumacheva, E. Shape-specific patterning of polymer-functionalized nanoparticles. *ACS Nano* **2017**, *11*, 4995–5002.

30. Rodríguez-Fernández, J.; Pérez-Juste, J.; Mulvaney, P.; Liz-Marzán, L.M. Spatially-directed oxidation of gold nanoparticles by Au(III)−CTAB complexes. *J. Phys. Chem. B* **2005**, *109*, 14257–14261.

31. Schlenoff, J.B.; Li, M.; Ly, H. Stability and self-exchange in alkanethiol monolayers. *J. Am. Chem. Soc.* **1995**, *117*, 12528–12536.

32. Yang, G.; Amro, N.A.; Starkewolfe, Z.B.; Liu, G.-y. Molecular-level approach to inhibit degradations of alkanethiol self-assembled monolayers in aqueous media. *Langmuir* **2004**, *20*, 3995–4003.

33. Galati, E.; Tao, H.; Rossner, C.; Zhulina, E.B.; Kumacheva, E. Morphological transitions in patchy nanoparticles. *ACS Nano* **2020**, *14*, 4577–4584.

34. Rossner, C.; Zhulina, E.B.; Kumacheva, E. Staged surface patterning and self-assembly of nanoparticles functionalized with end-grafted block copolymer ligands. *Angew. Chem. Int. Ed.* **2019**, *58*, 9269–9274.

35. Duan, H.; Luo, Q.; Wei, Z.; Lin, Y.; He, J. Symmetry-broken patches on gold nanoparticles through deficient ligand exchange. *ACS Macro Lett.* **2021**, *10*, 786–790.

36. Duan, H.; Malesky, T.; Wang, J.; Liu, C.-H.; Tan, H.; Nieh, M.-P.; Lin, Y.; He, J. Patchy metal nanoparticles with polymers: Controllable growth and two-way self-assembly. *Nanoscale* **2022**, *14*, 7364–7371.

37. Duan, H.; Jia, Z.; Liaqat, M.; Mellor, M.D.; Tan, H.; Nieh, M.-P.; Lin, Y.; Link, S.; Landes, C.F.; He, J. Site-specific chemistry on gold nanorods: Curvature-guided surface dewetting and supracolloidal polymerization. *ACS Nano* **2023**, *17*, 12788–12797.

38. Yang, Y.; Yi, C.; Duan, X.; Wu, Q.; Zhang, Y.; Tao, J.; Dong, W.; Nie, Z. Block-random copolymer-micellization-mediated formation of polymeric patches on gold nanoparticles. *J. Am. Chem. Soc.* **2021**, *143*, 5060–5070.

39. Singh, C.; Ghorai, P.K.; Horsch, M.A.; Jackson, A.M.; Larson, R.G.; Stellacci, F.; Glotzer, S.C. Entropy-mediated patterning of surfactant-coated nanoparticles and surfaces. *Phys. Rev. Lett.* **2007**, *99*, 226106.

40. Ghorai, P.K.; Glotzer, S.C. Atomistic simulation study of striped phase separation in mixed-ligand self-assembled monolayer coated nanoparticles. *J. Phys. Chem. C* **2010**, *114*, 19182–19187.

41. Chen, T.; Yang, M.; Wang, X.; Tan, L.H.; Chen, H. Controlled assembly of eccentrically encapsulated gold nanoparticles. *J. Am. Chem. Soc.* **2008**, *130*, 11858–11859.

42. Chen, G.; Gibson, K.J.; Liu, D.; Rees, H.C.; Lee, J.-H.; Xia, W.; Lin, R.; Xin, H.L.; Gang, O.; Weizmann, Y. Regioselective surface encoding of nanoparticles for programmable self-assembly. *Nat. Mater.* **2019**, *18*, 169–174.

43. Tao, H.; Chen, L.; Galati, E.; Manion, J.G.; Seferos, D.S.; Zhulina, E.B.; Kumacheva, E. Helicoidal patterning of gold nanorods by phase separation in mixed polymer brushes. *Langmuir* **2019**, *35*, 15872–15879.

44. Song, X.; Zhang, X.; Ou, Z.; Zhang, Y.-Q.; Li, M. Controlling the anisotropic surface wetting of metal nanoparticles by a competitive ligand packing strategy: Implications for encapsulation. *ACS Appl. Nano Mater.* **2021**, *4*, 11458–11465.

45. Zhou, J.; Creyer, M.N.; Chen, A.; Yim, W.; Lafleur, R.P.; He, T.; Lin, Z.; Xu, M.; Abbasi, P.; Wu, J. Stereoselective growth of small molecule patches on nanoparticles. *J. Am. Chem. Soc.* **2021**, *143*, 12138–12144.

46. Wang, Z.; He, B.; Xu, G.; Wang, G.; Wang, J.; Feng, Y.; Su, D.; Chen, B.; Li, H.; Wu, Z. Transformable masks for colloidal nanosynthesis. *Nat. Commun.* **2018**, *9*, 563.

47. Song, X.; Liu, C.; Liu, X.; Liu, S. Investigating polymer transformation during the encapsulation of metal nanoparticles by polystyrene-*b*-poly(acrylic acid) in colloids. *ACS Appl. Mater. Interfaces* **2019**, *12*, 3969–3975.

48. Kim, J.; Song, X.; Kim, A.; Luo, B.; Smith, J.W.; Ou, Z.; Wu, Z.; Chen, Q. Reconfigurable polymer shells on shape-anisotropic gold nanoparticle cores. *Macromol. Rapid Commun.* **2018**, *39*, 1800101.

49. Santos, A.; Millan, J.A.; Glotzer, S.C. Facetted patchy particles through entropy-driven patterning of mixed ligand SAMS. *Nanoscale* **2012**, *4*, 2640–2650.

50. Kim, A.; Zhou, S.; Yao, L.; Ni, S.; Luo, B.; Sing, C.E.; Chen, Q. Tip-patched nanoprisms from formation of ligand islands. *J. Am. Chem. Soc.* **2019**, *141*, 11796–11800.

51. Kim, A.; Vo, T.; An, H.; Banerjee, P.; Yao, L.; Zhou, S.; Kim, C.; Milliron, D.J.; Glotzer, S.C.; Chen, Q. Symmetry-breaking in patch formation on triangular gold nanoparticles by asymmetric polymer grafting. *Nat. Commun.* **2022**, *13*, 6774.

52. Yao, L.; An, H.; Zhou, S.; Kim, A.; Luijten, E.; Chen, Q. Seeking regularity from irregularity: Unveiling the synthesis–nanomorphology relationships of heterogeneous nanomaterials using unsupervised machine learning. *Nanoscale* **2022**, *14*, 16479–16489.

53. Kherbouche, I.; MacRae, D.; Jourdain, T.G.; Lagugné-Labarthet, F.; Lamouri, A.; Biraud, A.C.; Mangeney, C.; Félidj, N. Extending nanoscale patterning with multipolar surface plasmon resonances. *Nanoscale* **2021**, *13*, 11051–11057.

54. Ji, Y.; Lin, X.; Wu, Z.; Wu, Y.; Gao, W.; He, Q. Macroscale chemotaxis from a swarm of bacteria-mimicking nanoswimmers. *Angew. Chem. Int. Ed.* **2019**, *58*, 12200–12205.

55. Ohnuma, A.; Cho, E.C.; Camargo, P.H.; Au, L.; Ohtani, B.; Xia, Y. A facile synthesis of asymmetric hybrid colloidal particles. *J. Am. Chem. Soc.* **2009**, *131*, 1352–1353.

56. Ohnuma, A.; Cho, E.C.; Jiang, M.; Ohtani, B.; Xia, Y. Metal−polymer hybrid colloidal particles with an eccentric structure. *Langmuir* **2009**, *25*, 13880–13887.

57. Nie, Z.; Fava, D.; Kumacheva, E.; Zou, S.; Walker, G.C.; Rubinstein, M. Self-assembly of metal−polymer analogues of amphiphilic triblock copolymers. *Nat. Mater.* **2007**, *6*, 609–614.

58. Kim, A.; Akkunuri, K.; Qian, C.; Yao, L.; Sun, K.; Chen, Z.; Vo, T.; Chen, Q. Direct imaging of "patch-clasping" and relaxation in robust and flexible nanoparticle assemblies. *ACS Nano* **2024**, *18*, 939–950.

59. Hiemenz, P.C.; Rajagopalan, R. *Principles of Colloid and Surface Chemistry, Revised and Expanded*; CRC Press: Boca Raton, FL, USA, 2016.

60. Israelachvili, J.N. *Intermolecular and Surface Forces*; Academic Press: Cambridge, MA, USA, 2011.

61. Li, Y.; Zhou, W.; Tanriover, I.; Hadibrata, W.; Partridge, B.E.; Lin, H.; Hu, X.; Lee, B.; Liu, J.; Dravid, V.P. Open-channel metal particle superlattices. *Nature* **2022**, *611*, 695–701.

62. Dong, Y.; Liu, J.; Lu, X.; Duan, J.; Zhou, L.; Dai, L.; Ji, M.; Ma, N.; Wang, Y.; Wang, P. Two-stage assembly of nanoparticle superlattices with multiscale organization. *Nano Lett.* **2022**, *22*, 3809–3817.

63. Lewis, D.J.; Carter, D.J.; Macfarlane, R.J. Using DNA to control the mechanical response of nanoparticle superlattices. *J. Am. Chem. Soc.* **2020**, *142*, 19181–19188.

64. Lu, F.; Vo, T.; Zhang, Y.; Frenkel, A.; Yager, K.G.; Kumar, S.; Gang, O. Unusual packing of soft-shelled nanocubes. *Sci. Adv.* **2019**, *5*, eaaw2399.

65. Tan, L.H.; Xing, H.; Chen, H.; Lu, Y. Facile and efficient preparation of anisotropic DNA-functionalized gold nanoparticles and their regioselective assembly. *J. Am. Chem. Soc.* **2013**, *135*, 17675–17678.

66. Qiu, J.; Xie, M.; Lyu, Z.; Gilroy, K.D.; Liu, H.; Xia, Y. General approach to the synthesis of heterodimers of metal nanoparticles through site-selected protection and growth. *Nano Lett.* **2019**, *19*, 6703–6708.

67. Woessner, Z.J.; Lewis, G.R.; Bueno, S.L.; Ringe, E.; Skrabalak, S.E. Asymmetric seed passivation for regioselective overgrowth and formation of plasmonic nanobowls. *Nanoscale* **2022**, *14*, 16918–16928.

68. Huang, Z.; Liu, Y.; Zhang, Q.; Chang, X.; Li, A.; Deng, L.; Yi, C.; Yang, Y.; Khashab, N.M.; Gong, J.; et al. Collapsed polymer-directed synthesis of multicomponent coaxial-like nanostructures. *Nat. Commun.* **2016**, *7*, 12147.

69. Yan, M.; Liu, T.; Li, X.; Zhou, S.; Zeng, H.; Liang, Q.; Liang, K.; Wei, X.; Wang, J.; Gu, Z. Soft patch interface-oriented superassembly of complex hollow nanoarchitectures for smart dual-responsive nanospacecrafts. *J. Am. Chem. Soc.* **2022**, *144*, 7778–7789.

70. Li, L.; Yang, Y.; Ding, J.; Xue, J. Synthesis of magnetite nanooctahedra and their magnetic field-induced two-/three-dimensional superstructure. *Chem. Mater.* **2010**, *22*, 3183–3191.

71. Coropceanu, I.; Rossinelli, A.; Caram, J.R.; Freyria, F.S.; Bawendi, M.G. Slow-injection growth of seeded CdSe/CdS nanorods with unity fluorescence quantum yield and complete shell to core energy transfer. *ACS Nano* **2016**, *10*, 3295–3301.

72. Chen, W.; Zhan, X.; Luo, B.; Ou, Z.; Shih, P.-C.; Yao, L.; Pidaparthy, S.; Patra, A.; An, H.; Braun, P.V. Effects of particle size on Mg^{2+} ion intercalation into λ-MnO_2 cathode materials. *Nano Lett.* **2019**, *19*, 4712–4720.

73. Cargnello, M.; Wieder, N.L.; Canton, P.; Montini, T.; Giambastiani, G.; Benedetti, A.; Gorte, R.J.; Fornasiero, P. A versatile approach to the synthesis of functionalized thiol-protected palladium nanoparticles. *Chem. Mater.* **2011**, *23*, 3961–3969.

74. Wang, Y.; Im, J.; Soares, J.W.; Steeves, D.M.; Whitten, J.E. Thiol adsorption on and reduction of copper oxide particles and surfaces. *Langmuir* **2016**, *32*, 3848–3857.

75. Melby, E.S.; Lohse, S.E.; Park, J.E.; Vartanian, A.M.; Putans, R.A.; Abbott, H.B.; Hamers, R.J.; Murphy, C.J.; Pedersen, J.A. Cascading effects of nanoparticle coatings: Surface functionalization dictates the assemblage of complexed proteins and subsequent interaction with model cell membranes. *ACS Nano* **2017**, *11*, 5489–5499.

76. Na, H.B.; Palui, G.; Rosenberg, J.T.; Ji, X.; Grant, S.C.; Mattoussi, H. Multidentate catechol-based polyethylene glycol oligomers provide enhanced stability and biocompatibility to iron oxide nanoparticles. *ACS Nano* **2012**, *6*, 389–399.